AUTOMATIC ANALYSIS

OF HOLOGRAPHIC INTERFEROGRAMS

by

J.C. HUNTER

A dissertation submitted to
The City University
in fulfilment of the requirement
for the degree of
Doctor of Philosophy

DECEMBER 1987

Department of Mechanical Engineering,
The City University,
LONDON.

ABSTRACT

Holographic interferometry is a powerful, non-invasive, technique for the investigation of many experimental situations. Typically these include stress/strain investigations of deformed objects, heat transfer studies and compressible flow visualisation. The holographic technique allows a reference object wave to be superposed with some deformed object wave, the two waves being separated in time. This superposition produces an interferogram, subject to various coherence, stability, and polarity requirements. The interferogram takes the form of a series of dark and light fringes superimposed on the object being studied. In the case of heat transfer and compressible flow studies, where a transparent object is being studied, the fringes are superimposed over the test-volume. The fringes represent contours of constant phase difference, the phase distribution being directly related to the type of deformation undergone by the test object.

Several types of holographic interferometry are available, and these include infinite fringe, quasi-heterodyne and heterodyne, and speckle holographic interferometry. All these methods have a similarity in that they produce a system of fringes, often quite complicated, that contain a great deal of quantitative information. It is possible to extract this information by hand, but this is a lengthy, tedious, process, open to misinterpretation and poor accuracy of fringe location. To extract the quantitative information available from a typical interferogram both effectively and rapidly an automatic analysis system is required.

A technique for producing infinite fringe background holographic interferograms is described, and interferograms obtained from a forced conduction heat transfer study, Lockett [1987] and a compressible flow study, Ball et al. [1987] are presented.

The heat transfer study investigated the temperature field and heat transfer distribution over both a heated flat plate, and a number of rib-roughened geometries, located in a wind-tunnel. The fringes produced represented isotherms, with a peak-to-peak temperature change of 2K. A one-dimensional automatic fringe analysis system was devised that allowed such interferograms to be analysed both quickly and accurately. The interferograms were investigated along a series of scan lines that lay essentially perpendicular to the general orientation of the isotherms, and the fringe co-ordinates were extracted using either a bucket-bin technique or a gradient change algorithm. The extracted fringe co-ordinates were then ordered, and the temperature distribution over the scan line determined. From this both the temperature distribution over the heated surface, and the heat transfer distribution, were calculable.

Results obtained from the heat transfer study were compared with those obtained from a Large Eddy Simulation, L.E.S.

The compressible flow study investigated the influence of blade incidence upon the flow within low pressure transonic steam turbine blading. The fringes produced represented iso-densities, and hence isobars.

Because of the complicated nature of the resulting interferograms, a two-dimensional automatic fringe analysis system was devised. This involved the binarisation of the fringe field, followed by detection and tracing of the fringe edges. The extracted fringe co-ordinates are then ordered using a semi-automatic fringe ordering system. In this way a map of the complete density distribution over the cascade section was producable, one blade passage being investigated at a time.

The extracted density maps were used for validating a two-dimensional viscous compressible flow code known as TURBINS.

Some of the material published throughout the course of this project is included in Appendix E in the form of two refereed papers.

The majority of the heat transfer holographic interferograms presented in this thesis were produced by J.Lockett, the author producing the flat plate interferograms, and the three-dimensional holographic interferograms. The compressible flow interferograms were produced by [redacted] of the C.E.G.B. Marchwood Engineering Laboratories. A computer simulation for comparison with the compressible flow interferograms, TURBINS, was produced by [redacted] of M.E.L. A Large Eddy Simulation for comparison with the heat transfer results was run by [redacted] and [redacted] of Queen Mary College, London, and a discussion of this simulation is included.

The major achievement of this research is the successful development of automatic fringe analysis routines to analyse heat transfer and compressible flow holographic interferograms.

LIST OF CONTENTS

LIST OF FIGURES

NOMENCLATURE

A	amplitude of sine function
A_L	average grey-level over a local region
A_r	average grey-level over a reference region
A_s	average grey-level over a scan line
A_T	average grey-level over a total picture
a	amplitude of a wave function
a_{mn}	coefficients of a series expansion
$C\ell_i$	refraction error correction factor
De	equivalent diameter
E	electric field vector
$f(2\pi ft)$	temporal frequency (in context shown)
f	field function
$\bar{f}$	approximated field function
G	Gladstone-Dale constant
H_{mn}	generating functions of a series expansion
h	channel height
h_c	heat transfer coefficient
I	intensity
I_{grad}	currently detected grey-level gradient
k	thermal conductivity
$k(=2\pi/\lambda)$	wavenumber (in context shown)
$\bar{k}$	propagation vector
L	spanwise extent of test section
M	Mach number
Nu	Nusselt number

N	fringe order
n	refractive index
P	mean pressure
P_{grad}	previously detected grey-level gradient
Pr	Prandtl number
q	local heat flux
R	Universal gas constant
Re	Reynolds number
R.M.S.	root mean square value
s	ray pathlength
SNR	signal-to-noise ratio
t	time
T	threshold (in context)
T	mean temperature
U	complex amplitude
U_T	shear velocity
$v(t)$	magnitude of time-dependent sine wave at time t
v	speed of propagation
x	streamwise co-ordinate
$\bar{x}$	position vector
y	height co-ordinate
z	spanwise co-ordinate

Greek symbols

γ	ratio of specific heat constants
Δ	constant
Δz	small step in the spanwise direction (small c.f. z)
δ_o	boundary layer thickness
δ_T	thermal layer thickness
ϵ	electrical permittivity
λ	wavelength
ν	fringe visibility
ρ	density
Φ	ray path
τ	shear stress
ϕ	additional phase change
ψ	phase of ray
ω	circular frequency

Subscripts

Hi	upper limit
i	iteration step
Lo	lower limit
m	integer
max	maximum
min	minimum
n	integer
obj	object wave

rec	reconstruction wave
ref	reference conditions
res	resultant wave
t	stagnation conditions
wall	wall conditions

ACKNOWLEDGEMENTS

This project was conducted with the sponsorship of the Science and Engineering Research Council and the C.E.G.B.'s Marchwood Engineering Laboratories, under award number EB052.

Special thanks go to my supervisor, Dr.M.W. Collins, for all his help and advice during the course of this project, and for the enthusiasm that he generated throughout the work.

Thanks are also due to [redacted] for his help during the course of the work, and especially for providing the basic image acquisition and display software used on the Prime mini-computer, as well as allowing me access to the Image Processing group's equipment in order to digitise the interferograms. In this respect, thanks also go to [redacted]

The help of The City University's support staff has also been greatly appreciated, especially that of [redacted], who kept the laser serviced and lent much optical equipment; [redacted] who produced the excellent photographs in this report and throughout the course of the project; and the Chief Technician, [redacted]

Also, special thanks are due to Dr.John Lockett, both for his help and advice throughout the project, and for allowing me to use many of his holographic interferograms for analysis purposes.

Thanks are also due to many people at Marchwood Engineering Laboratories who supported various aspects of this work.

Firstly, thanks go to [redacted], who lent his support both at The City University and when I was working at Marchwood Engineering Laboratories, and for his keen interest in the work.

Special thanks go to [redacted] for all his help during the Marchwood phase of the project, which ranged from finding me accommodation to collecting all my equipment together so that the work could go on efficiently.

Thanks are also due to [redacted] [redacted] who lent me his computer, and for the help provided, and to [redacted] and [redacted] for their useful input into the project.

Lastly, many of Marchwood's support staff deserve thanks, and these include [redacted]

As a final note I would like to thank everyone in my office and in the office next door at The City University, and [redacted] with whom I share a house, as there is nothing so conducive to success as living and working in a happy environment.

Thanks also go to my parents and [redacted], for their great support throughout the course of this project.

CHAPTER 1

1. INTRODUCTION

The mathematical modelling of turbulent flow heat transfer regimes has been investigated by the Mechanical Engineering Department of The City University since 1978. In 1981 it was recognised that there was a general lack of experimental and theoretical data for flows over rib-roughened surfaces, and so an experimental investigation was initiated to study the effect of such rib-roughened geometries on turbulent forced convective heat transfer. An experimental approach to this problem was chosen for three main reasons: it would provide intrinsically useful data; would give the group experience with a heat transfer visualisation technique; and would provide heat transfer data that could be compared with the theoretical Large Eddy Simulation models (L.E.S.) under development at the time.

1.1. EXPERIMENTAL INVESTIGATION OF FORCED CONVECTIVE HEAT TRANSFER

The experimental approach was undertaken by Lockett [1987] and was a development of the work done by Walklate [1983, 1981]. Walklate investigated the turbulent heat transfer over a rib-roughened surface using double-exposure holographic interferometry.

This technique allowed the temperature field extant at a particular instant in time above a heated surface to be visualised. This visualisation took the form of a two-dimensional series of contours located above the heated surface under study, each contour representing a constant temperature, the temperature difference between each contour being 2 K. From this information, Walklate was able to extract by hand qualitative data such as the temperature field and surface temperatures, and local heat transfer data.

A wind-tunnel adapted from that used by P.J. Walklate was designed and built by Voke, (Fig.(1.1)). The wind-tunnel was constructed over two optical tables which allowed the optical system needed for the holographic flow visualisation technique to have a base of the requisite stability. A 3-Watt Argon-Ion laser was provided as a coherent light source.

A proving exercise was then carried out by Lockett using a flat plate geometry in the wind-tunnel, and a double-exposure and a real-time holographic interferometry technique, see Chapter 4. A flat-plate geometry was used because of the availability of experimental data for comparative purposes. Initial results (Lockett, Hunter, Voke and Collins [1985]), illustrated the heat transfer results from such a smooth surface with a Reynolds number varying between 3,000 and 30,000 (Fig.(1.2)). These smooth plate results were compared with those obtained experimentally by Walklate and with the standard smooth channel relationship of:

$$Nu = 0.023\ Re^{0.8} Pr^{0.4} \qquad (1.1)$$

The comparison of the experimental results with such an empirical definition of the Nusselt number is not strictly valid, as this definition assumes a channel which has all walls heated, as opposed to the experimental case under study in which only the lower wall was heated. However, the reasonable agreement obtained between Lockett's experimentally obtained heat transfer results and those of Walklate and the empirical relationship given in equation (1.1) gave confidence in the visualisation and analysis techniques being used, and the experimental investigation then moved on to the study of the rib-roughened geometries, (Fig.(1.3)).

The square rib geometry (Fig.(1.3a)) is similar to that found on the fuel pins of the Advanced Gas Cooled Reactor, or A.G.R. The ribs act as turbulence promoters, increasing the rate at which turbulent eddies transport momentum from the main flow to the boundary layer, breaking up the laminar sublayer and thereby improving the heat transfer. The limiting factors behind the rib design were, then, that the rib must project beyond the laminar sublayer under standard flow conditions (typically a y^+ value of 30) and come into contact with the main turbulent flow, (with a typical y^+ value of 500). However such a ribbed structure must not increase the flow resistance so that an appreciable increase in the pumping power necessary to maintain a particular bulk flow rate is encountered. The rib-geometry used was the same as that encountered in the A.G.R., that is a rib spacing of 7.2 : 1.

The other rib geometries studied investigated the effect of erosion (rounded-ribs) and deposition (built-up ribs) on the temperature field distribution and heat transfer characterstics of the ribbed surfaces.

The double-exposure and real-time holographic interferometry techniques used in this investigation are described fully in Chapter 4.

1.2. AUTOMATIC ANALYSIS OF INFINITE FRINGE HOLOGRAPHIC INTERFEROGRAMS

The large amount of quantitative data available on each interferogram produced by Lockett, and the great number of interferograms being produced, soon pointed to the fact that a procedure for automatically analysing such interferograms, as opposed to the conventional method of hand analysis, was required. This requirement was especially true if a sequence of real-time interferograms had to be analysed, or statistical heat transfer data was required for comparison with the results obtained from Large Eddy Simulations. For this reason the present project was initiated. The fact that the ultimate aim of the work was to branch out into three-dimensional heat transfer tomography also played a part in the decision to investigate the automatic analysis of such interferograms. This is because the three-dimensional analysis technique requires the analysis of a series of two-dimensional interferograms of the same test object,

taken from a variety of directions, and the combination of these results to produce a three-dimensional map of the test object (see Chapter 9).

Automatic fringe analysis techniques may be applied to any situation in which fringes are used to convey quantitative information about a test object. Such situations may be divided into three main categories:

(1) Conventional interferometry in which the interferometric fringes represent constant value contours of the phenomenon under investigation.

(2) Quasi-heterodyne and heterodyne interferometric methods by which phase information about the test object may be obtained directly.

(3) Speckle techniques, which may be sub-divided into:
(i) speckle interferometry, which makes use of the coherent source phenomena of speckle, and
(ii) speckle photography, in which a series of speckled Young's fringes are produced by coherent interference from point sources created by the movement of seeding particles.

For the sake of completeness Chapter 3 provides a survey of the methods used in the automatic analysis of all three categories. However, this project is only concerned really with category (1), or the automatic analysis of conventional interferograms. Although specifically applied to holographic interferometry, it is readily apparent that such techniques are applicable to all forms of conventional interferometry.

Chapter 2 deals with the theoretical basis behind interferometry, and is included before the literature survey to provide a platform by which the reader can relate to the concepts behind some of the automatic analysis techniques. The first section of the literature survey deals with techniques for the automatic analysis of conventional interferograms. Such techniques themselves may be divided into two main regions of interest, that is image enhancement, and quantitative image analysis.

1.2.1. Image Analysis

The problem in this case is to extract quantitative data from the enhanced interferograms. The basis of these techniques is the determination of fringe co-ordinates, and the consistent ordering of these located fringes. It becomes apparent from the literature survey that this section can itself be separated into two parts, that is (a) one-dimensional and (b) two-dimensional, analysis routines.

The one-dimensional analysis routines operate on the image-data grey-levels over one-dimensional signals which are taken sensibly normal to the fringe direction. A full two-dimensional analysis can be made by combining several of these one-dimensional scan lines, or by using one such scan line to provide the starting co-ordinates for a fringe tracing routine.

The two-dimensional analysis routines operate on the whole fringe-field data, and are useful if full-field data from a complicated fringe pattern is required. most of these routines adopt the same format. Firstly the image data are binarised to produce a two-tone fringe field, white and black grey-level values existing only. A variety of techniques may then be applied to this binarised data, such as fringe thinning techniques or edge-detection methods, for the extraction of fringe co-ordinates. The final stage of this process is the ordering of the extracted fringe co-ordinates to allow quantitative data to be obtained. Grey-level analysis may also be used in 2-D analysis routines but prohibitive computational expense usually thwarts this approach.

The heat transfer interferograms produced by Lockett were analysed using the one-dimensional analysis routines, and the system developed for doing this is described in Chapter 6. The one-dimensional method was chosen in this case because the general orientation of the fringes could be predicted, and so it was possible to work over a scan line that was normal to them. Also, point heat transfer data and temperature profiles were required, and so it was not necessary to produce full-field quantitative data, although this facility was included.

1.3. ANALYSIS OF COMPRESSIBLE FLOW INTERFEROGRAMS

As part of the CASE award it was necessary to do some work for the Co-sponsoring body, and this part of the project consists of such work.

At Marchwood Engineering Laboratories a small two-dimensional cascade had been constructed in order to study the influence of blade incidence upon the flow within low pressure transonic steam turbine blading, (Ball, Gordon, Hunter, Richards and Thompson [1987]). A double-pulse image-plane holographic technique, similar to that used by Lockett in his investigations, was used to obtain a map of the gas density field within the blade passages over a range of blade incidence angles. An automatic analysis system was then required to obtain quantitative data from the resulting complicated interferograms. These experimental results were then compared with a two-dimensional Navier-Stokes solver. TURBINS, which produced computer predictions of the density field existing in the cascade section.

The automatic analysis system that was evolved to tackle this problem is based around the two-dimensional analysis methods described in the latter half of the first section of Chapter 3. A complete description of the system is given in Chapter 7.

1.4. HEAT TRANSFER TOMOGRAPHY

The natural extension of the work done to date is into three-dimensional studies of heat transfer effects, that is heat transfer tomography. A holographic interferometry system similar to that used by Lockett may be used, with the inclusion of a diffusing screen just prior to the test section, to produce holographic

interferograms that retain the three-dimensional properties of holograms. When such a holographic interferogram is viewed through a small aperture from a number of different angles a series of two-dimensional interferograms are produced. These may be analysed individually, and the quantitative results obtained, combined to produce a three-dimensional representation of the heat transfer characteristics of the test object.

An explanation of the experimental aspects of this work including sample three-dimensional holographic interferograms produced by the author, and a discussion of the mathematical techniques involved in producing a tomographic representation of such a test object, are given in Chapter 8. Plans for possible future work are also outlined in this section.

CHAPTER 2

2. THE THEORY OF INTERFEROMETRY

2.1. THE NATURE OF LIGHT

It is now common knowledge that radiant energy is quantum in nature, that is energy is transported as massless elementary "particles" known as photons which are localised quanta of energy. However, this quantum nature of radiant energy is not always readily apparent or of practical concern in optics. In most cases the stream of incident light under consideration carries a relatively large amount of energy, and the granularity is obscured. The energy transported by such a large number of photons is, on average, equivalent to the energy transferred by a classical electro-magnetic wave. It is thus quite practical to use such a treatment when considering light rays mathematically. It should be noted that a consideration of the classical electro-magnetic wave theorem suggests that both a magnetic, or B, field and an electrical, or E, field are present. However, at the atomic level the E field is considerably more effective at exerting forces on electrons than is the B field, and it is usual therefore to refer to E as the optical field. This allows an approximate treatment, such as that of Huygens [1690] and Fresnel [1819] to be considered, without the necessity for a strict solution to Maxwell's equations, Maxwell [1881], Chirgwin [1973].

2.2. WAVES AND WAVEFRONTS

The following analysis is based loosely on that given by Steel [1967], and develops the underlying optics for the treatment of the interference phenomenon. Having concluded that light rays may be considered using simple electro-magnetic theory, it is possible to define a ray in terms of a simple, harmonic oscillation:

$$V(t) = A \cos (2\pi ft - kR) \qquad (2.1)$$

the entire argument of the cosine function being known as the phase. The term $2\pi ft$ is known as the circular frequency, f being the temporal frequency of the wave, and k the wavenumber, given by $k = 2\pi/\lambda$.

In the consideration of the wave motions in light we are concerned with a real function of time that covers a range of frequencies. This function can be represented by the Fourier integral:

$$V^{(r)}(t) = 2 \int_0^\infty a(f) \cos (2\pi ft - kR)\, df \qquad (2.2)$$

This function may be converted to the exponential form, and if only the positive frequencies are considered may be written as:

$$V(t) = \int_0^\infty a(f)\, e^{-kRi} \cdot e^{-2\pi fti} \qquad (2.3)$$

So the actual scalar components of the field vector at a point $\bar{x}$ and a time t are rapidly fluctuating real functions $V^{(r)}(\bar{x},t)$. However, practical detectors such as photographic film, photodiodes or the retina of the eye are not capable of responding to the high frequency of these fluctuations, and they respond instead to the time-average energy flux of the light wave, this measure being known as the intensity I of the incident light. This intensity is given by:

$$I(\bar{x}) = \epsilon V \langle V^*(\bar{x},t).\ V(\bar{x},t)\rangle \qquad (2.4)$$

where ϵ is the electrical permittivity of the medium in which the light travels, and V is the speed of propagation. When concerned only with relative irradiances within the same medium it is quite legitimate simply to neglect these constants and set:

$$I(\bar{x}) = \langle V^*(\bar{x},t).\ V(\bar{x},t)\rangle \qquad (2.5)$$

If we now consider a source which is effectively a point light source of intensity I whose frequency bandwidth is very small compared to the median frequency, i.e. $\Delta f \ll f$ (such as a laser), it may be represented by a train of waves of amplitude $I^{1/2}$. At a distance R measured in the direction of propagation the wave is given by:

$$V(R) = I^{1/2}(R) \cos (2\pi ft - 2\pi R/\lambda) \qquad (2.6)$$

This relationship can be considered in two ways. One is that at any fixed point at this distance R there is a periodic disturbance of this form. The other is that each value of the phase, e.g. $kR = 2\pi N$, defines a surface, the wavefront, that advances with the wave.

The expression for V(R) given by equation (2.6) can also be written in its exponential form, and if we once again artificially allow $f = -f$, and hence $k = -k$, then we can write:

$$V(R) = I^{\frac{1}{2}}(R)\ e^{i(2\pi ft + kR)} \qquad (2.7)$$

One form of this equation that is of particular interest is that defining a plane wave, as this is the waveform produced by a laser. If the wavefront is a plane normal to the unit vector F, the ray vector, and $\bar{x}$ is a position vector of some point in it, the distance travelled, R, is equal to $\bar{F}.\bar{x}$ for all points on the wavefront, as shown in (Fig.(2.1)).

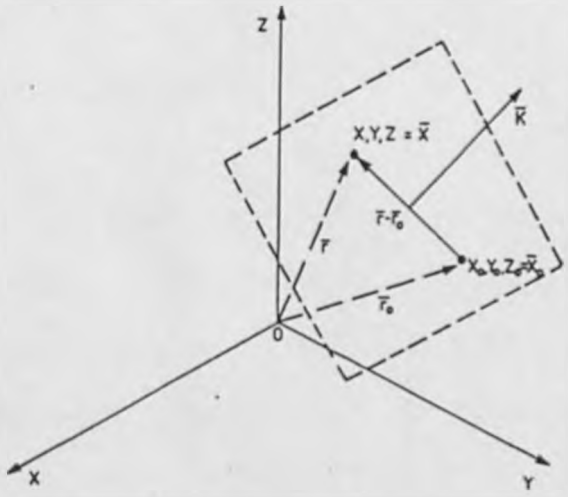

Figure 2.1. The plane wave moving in the $\bar{k}$-direction.

The complex amplitude of a uniform plane wave then has the form:

$$U(\bar{x}) = a\, e^{i(k\bar{r}.\bar{x} + 2\pi ft)} \qquad (2.8)$$

where a is a constant equal to $I^{1/2}$.

In fact it is possible to formulate an expression for a general wave in similar terms:

$$U(\bar{x}) = a(\bar{x})\, e^{i[k\bar{r}.\bar{x} + \psi(\bar{x}) + 2\pi ft]} \qquad (2.9)$$

In this case the non time-dependent phase is written as the sum of two terms, one representing the phase across a best-fit plane, which has a normal F, and the other giving the phase variations from this plane.

2.3. THE PRINCIPLE OF COHERENCE

On studying the equation of the general wave given by equation (2.9) it can be seen quite clearly that the phase at the position vector $\bar{x}$ depends upon the phase of the source. If light beams from two independent sources reach the point $\bar{x}$ there will be no fixed relation between the phases of the two light beams, and so it will not be possible to combine them to form stationary

waves. Such light waves are termed incoherent, and their intensities combine locally. Actually incoherent light waves may produce interference, but these effects are only constant in space for as long as the temporal coherence of the two incoherent light beams lasts, typically 10^{-8} seconds. Thus any interference effects arising occur far too rapidly to be detected. On the other hand two light beams which arrive at $\bar{x}$, from the same source, perhaps by different paths, can superpose and produce visible interference effects because their amplitudes can combine, and not their intensities. This is because there is obviously a fixed relation between the phases of both beams, any phase changes in the one beam originating in source variations being exactly duplicated in the other beam. Thus it is only possible to produce stationary interference effects by using two or more light beams which come from one point of a single source. For this reason all interferometers operate on either a division of wavefront or a division of amplitude basis. So we can say that when such coherent waves pass through a point, the vibrating medium at this point is subjected to the combined superposed effect of the two vibrations and under suitable conditions this leads to stationary waves, or interference fringes.

2.4. POLARISATION

Up to now we have ignored the fact that light is in fact a transverse wave, and hence vectorial in nature. The figure depicts a typical transverse wave travelling in the z-direction.

In this instance the wave motion is confined to a spatially fixed plane called the plane of vibration and the wave is accordingly said to be linearly or plane polarised.

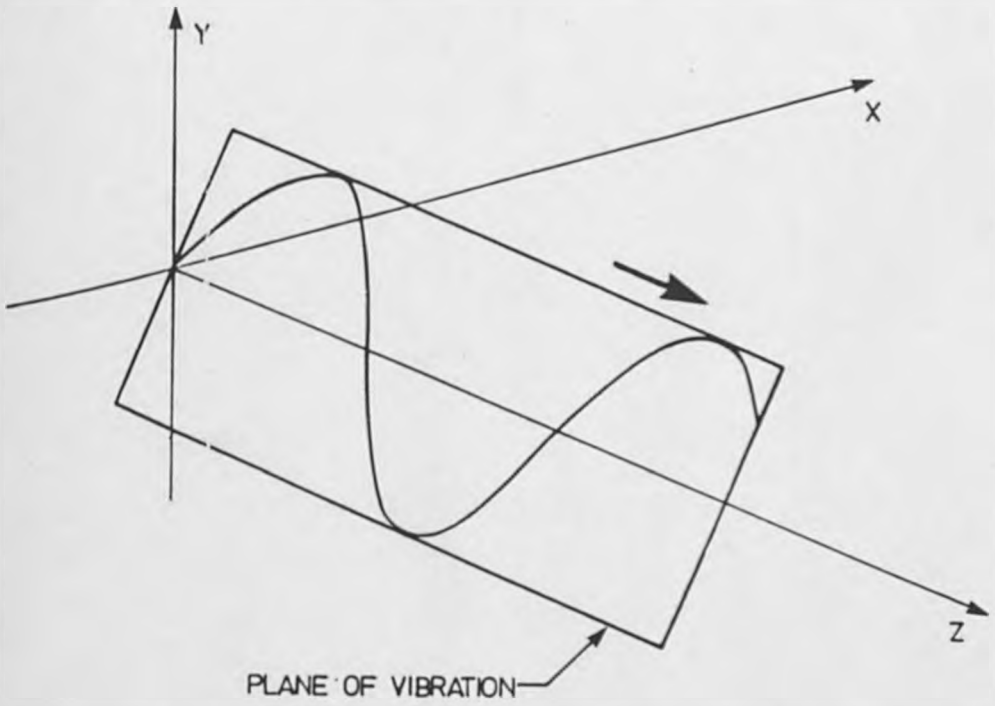

Fig.2.2. Linearly polarised light.

The plane of polarisation contains both E and $\bar{k}$, the electric field vector and the propagation vector in the direction of motion. Plane polarisation is of particular importance in that any polarisation state can be synthesized from two orthogonal p-states (p representing a plane-polarised state), but of course other polarisation states exist. Typical examples are elliptically polarised light, in which the resultant electric field vector E both rotates and changes its magnitude (see Fig.(2.3)), and circularly polarised light in which the vector E traces out a circular

end-path. Elliptically polarised light is said to be in an ϵ-state and circularly polarised light in a right or left, R or L-state.

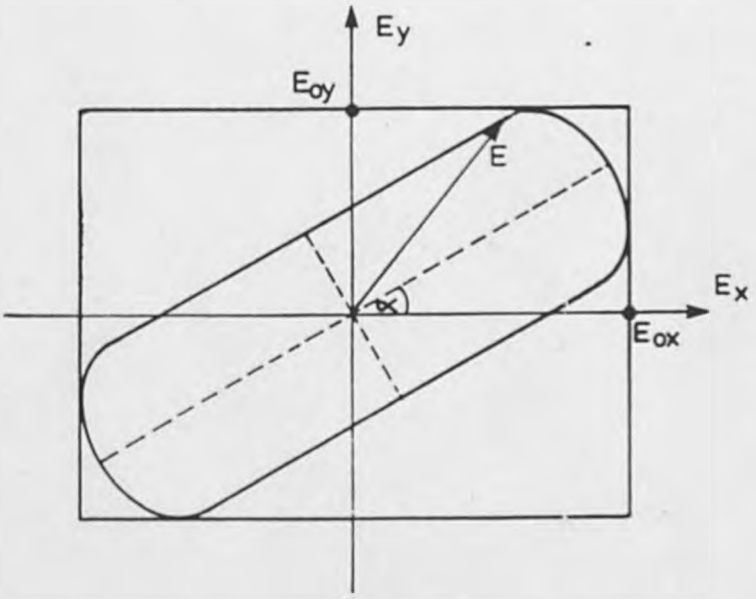

Fig.2.3. Elliptically Polarised Light

In the treatment of the interference of two light rays it is usual to consider them simply as two parallel and linearly polarised wavefronts, the vectorial nature of the waves being neglected. This treatment is acceptable due to the previously mentioned fact that any polarisation state can be synthesized out of two orthogonal p-states. If we suppose that every wave has its propagation vector in the same plane the constituent orthogonal p-states can be labelled with respect to the plane as $E_{\parallel}$ and $E_{\perp}$, as shown in (Fig.(2.4)).

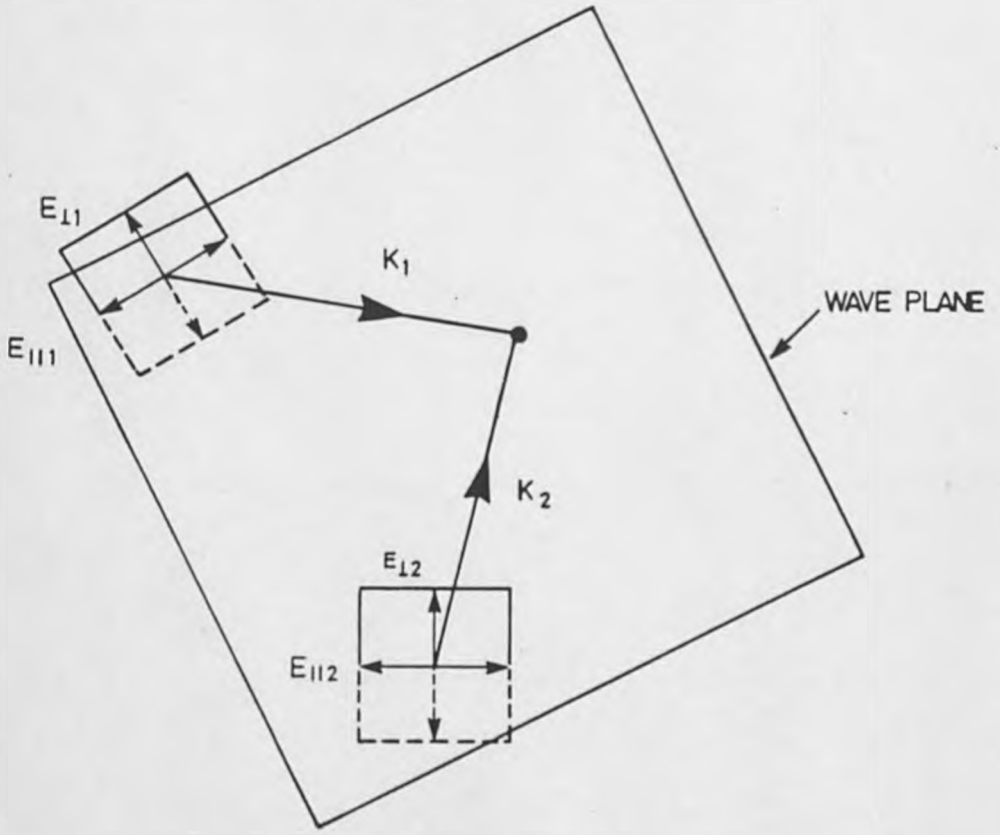

Fig.2.4. Interference of two light waves of any polarisation state, the polarity of each being devolved into the two constituent *p*-states.

If two such plane waves, $E_{1\parallel}$ and $E_{1\perp}$, $E_{2\parallel}$ and $E_{2\perp}$ were to interfere at some point in space, the resulting flux-density distribution would consist of two independent, precisely overlapping interference patterns, given by:

$$\langle (E_{1\parallel} + E_{2\parallel})^2 \rangle \qquad (2.10)$$

and

$$\langle (E_{1\perp} + E_{2\perp})^2 \rangle \qquad (2.11)$$

The conditions under which the interference of polarised light occurs are set out in the Fresnel-Arago laws, namely:

(1) Two orthogonal, coherent *p*-states cannot interfere in the sense that the dot product of the two electric fields $\langle E_1.E_2\rangle=0$ and no fringes result.

(2) Two parallel, coherent *p*-states will interfere in the same way as will natural light.

(3) The two constituent orthogonal *p*-states of natural light cannot interfere to form a readily observable fringe pattern even if rotated into alignment. This is easily understandable as natural light, and hence its *p*-states, are incoherent.

2.5. PRINCIPLE OF SUPERPOSITION

The two interfering light waves will be considered as plane waves emanating from a laser source in this treatment. When the two waves cross, their effects add and the complex amplitude at any point is the sum of those of the separate waves. As both waves will have the same frequency, because we are supposing that they emanate from a single source, a pattern of standing waves is formed, consisting of regions of additive amplitude separated by regions of subtractive amplitude. We will also

consider that there is some change in phase, $\psi_1(\bar{v})$ to $\psi_2(\bar{v})$, over the optical path-lengths travelled.

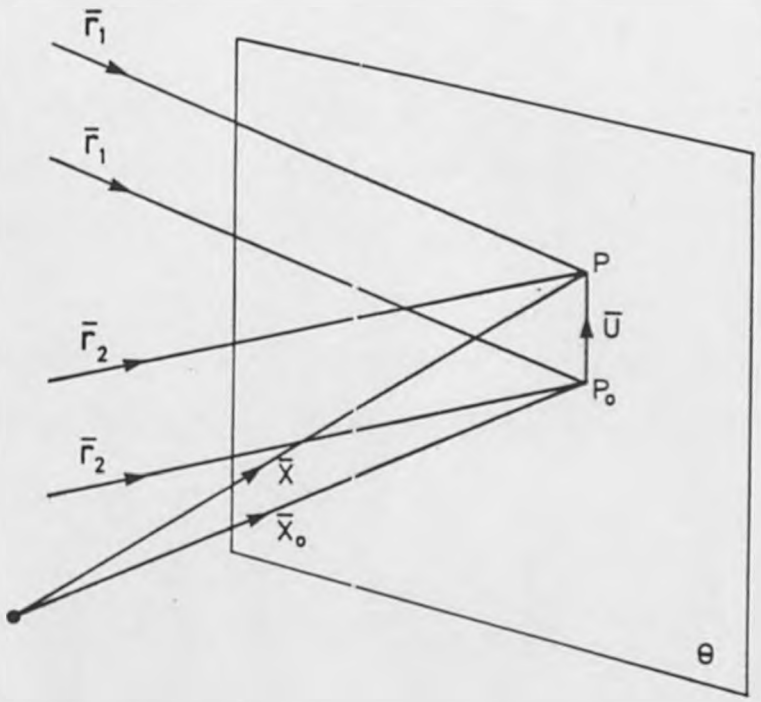

Fig.2.5. Interference of two-plane waves

So the total amplitude at a position $\bar{v} = \bar{x} - \bar{x}_o$ in the plane of observation θ is:

$$U(\bar{u}) = a_1 e^{i(2\pi ft + k\bar{r}_1\bar{u} + \psi_1(\bar{u}))} + a_2 e^{i(2\pi ft + k\bar{r}_2\bar{u} + \psi_2(\bar{u}))} \qquad (2.12)$$

Thus from equation (2.5) we have the intensity at $\bar{u}$ is:

$$I(\bar{u}) = a_1^2 + a_2^2 + 2\, a_1 a_2 \cos\,[k(\bar{r}_2 - \bar{r}_1).\bar{u} + \Psi_2(\bar{u}) - \Psi_1(\bar{u})] \qquad (2.13)$$

It is this varying function, $2a_1a_2 \cos\,[k(\bar{r}_2-\bar{r}_1).\bar{u} + \Psi_2(\bar{u}) - \Psi_1(\bar{u})]$ that provides the modulation necessary to produce an interferogram.

The vector $(\bar{r}_2 - \bar{r}_1)$ is a measure of the angle between the two interfering waves, and is often denoted as an angular tilt term $\bar{\theta}$. Thus equation (2.13) becomes:

$$I(\bar{u}) = a_1^2 + a_2^2 + 2a_1a_2 \cos[k\bar{\theta}.\bar{u} + \Psi_2(\bar{u}) - \Psi_1(\bar{u})] \qquad (2.14)$$

The maxima of the standing waves occur where
$[k\bar{\theta}\bar{u} + \Psi_2(\bar{u}) - \Psi_1(\bar{u})]=N\lambda$, and the minima where
$[k\bar{\theta}\bar{u} + \Psi_2(\bar{u}) - \Psi_1(\bar{u})] = N\lambda/2$, N being the order of interference.

A measure of the fringe contrast is given by Michelson's definition of fringe visibility,

$$V = (I_{max} - I_{min})/(I_{max} + I_{min}) \qquad (2.15)$$

which can be written in terms of wave amplitude or beam intensity as:

$$V = \frac{2a_1 a_2}{a_1^2 + a_2^2} = \frac{2I_1^{\frac{1}{2}} I_2^{\frac{1}{2}}}{I_1 + I_2} \qquad (2.16)$$

2.6. MANIPULATION OF THE EQUATION OF INTERFEROMETRY

(i) Infinite fringe background

The basic equation of interferometry is as stated in equation (2.14). However this can be manipulated in various ways to facilitate the optical technique.

In many cases, such as with holographic interferometry, the object waves propagate in the same direction. Thus the angular tilt $\bar{\theta}$ is reduced to zero, and the interferogram provides a measure of the cosine of the phase difference, $(\Psi_2(\bar{u}) - \Psi_1(\bar{u}))$, provided that the amplitudes of a_1 and a_2 are constant and do not vary with $\bar{u}$. Thus the intensity distribution may be written:

$$I(\bar{u}) = a_1^2 + a_2^2 + 2a_1 a_2 \cos\,(\Psi_2(\bar{u}) - \Psi_1(\bar{u})) \qquad (2.17)$$

The interferogram thus formed is known as an infinite fringe background interferogram, as if no phase change occurs between the interfering beams a field of constant intensity, i.e. one infinite fringe, is formed. It should be noted that there is the possibility of an ambiguity in the sign of the phase difference, when the interferogram takes this form.

ii) Quasi-heterodyne techniques

To resolve this ambiguity and increase the accuracy to which the change in phase of the interfering waves may be assessed, two quasi-heterodyne techniques are available, one spatial and the other temporal.

The first technique, the spatial quasi-heterodyne technique, relies on the introduction of a tilt between the interfering beams, giving us an interference pattern the same as that denoted in equation (2.14). These forms of interferogram are known as finite fringe interferograms, as if no phase change occurs between the interfering beams we have,

$$I(\bar{u}) = \varepsilon_1^2 + a_2^2 + 2a_1a_2 \cos\ [k\bar{\theta}.\bar{u}] \qquad (2.18)$$

giving a series of straight, equally spaced fringes across the interferogram. It is the distortion of these fringes due to phase changes that allows the phase difference between the interfering beams to be determined. The introduction of finite fringes also removes the possible ambiguity in the phase change, i.e. whether an increasing or decreasing phase change is present.

With the temporal quasi-heterodyne technique, a small phase change is artifically introduced into one of the interfering beams, the beams propagating in the same direction. If we consider the introduced phase shift as Φi, then we can write:

$$I(\bar{u}) = a_1^2 + a_2^2 + 2a_1a_2 \cos\ (\Psi_2(\bar{u}) - \Psi_1(\bar{u}) + \Phi i) \qquad (2.19)$$

If three such phase shifts are introduced, such as $0, -2\pi/3$ and $2\pi/3$, separated in time, then a system of simultaneous equations can be formed that allow us to determine the phase difference between the two interfering beams as well as their respective amplitudes.

(iii) True heterodyne technique

It is also possible to utilise a true heterodyne technique in interferometry by the introduction of a small frequency change, Δf, in one of the interfering beams. Thus the time dependent term must be retained in the complex amplitude, and so the total amplitude at a position $\bar{u}$ is given by:

$$U(\bar{u}) = a_1 e^{i(2\pi ft + k\bar{r}_1\bar{u} + \Psi_1(\bar{u}))} + a_2 e^{i(2\pi(f+\Delta f)t + k\bar{r}_2\bar{u} + \Psi_2(\bar{u}))} \qquad (2.20)$$

with the resulting intensity being given by,

$$I(\bar{u}) = a_1^2 + a_2^2 + 2a_1a_2 \cos\ [2\pi\Delta ft + 2\pi\bar{u}\bar{\theta}/\lambda + 2\pi m\Delta f\bar{u}\bar{r}_2/c + \Psi_2(\bar{u}) - \Psi_1(\bar{u})] \qquad (2.21)$$

remembering that $k = 2\pi nf/c$.

The effect of this, as can be seen, is to cause the relative phase of the combined wavefront to increase linearly in time,

making the observed intensity at a point vary sinusoidally with time at a characteristic frequency, the beat frequency. This beat frequency can then be utilised to determine the phase at a point very accurately.

This is because the phase of the introduced modulation corresponds to the optical phase difference between the two interfering object waves. The phase $\Delta\Phi$ can be extracted with respect to a reference signal at the same frequency. A fixed photo-detector is used to supply the required reference signal, and a second photo-detector is stepped across the interferogram, measuring the phase at each point.

Phase measurement accuracies of $2\pi/500$ are obtainable using such a technique, Dändliker [1980].

CHAPTER 3

LITERATURE SURVEY

INTRODUCTION

This chapter is a survey of many of the techniques currently being used for the analysis of fringe systems. It includes methods for analysing infinite fringe background interferograms, the main thrust of this project; heterodyne and quasi-heterodyne techniques; and speckle fringe processing methods. The last two sections are included really for the sake of completeness, giving the reader an overview of the current state of automatic fringe analysis research.

The theory behind the formation of the interferograms looked at in this chapter is discussed in Chapter 2. However to provide a qualitative appreciation of the interferogram analysis problem, a small library of interferograms from various sources is included at this stage. It should be noted that heterodyne and temporal quasi-heterodyne techniques produce interferograms that, at any instant in time, are identical to those produced using the infinite fringe background technique. The only real difference is that the intensity distribution is time dependent. Obviously this difference would not show up in the stills presented, and so no examples of heterodyne and temporal quasi-heterodyne interferograms are included in the library.

Library of Sample Holographic Interferograms

(1) Infinite fringe holographic interferogram showing forced convection heat transfer

(2) Infinite fringe holographic interferogram showing natural convection heat transfer.

(3) Infinite fringe holographic interferogram showing a compressible flow

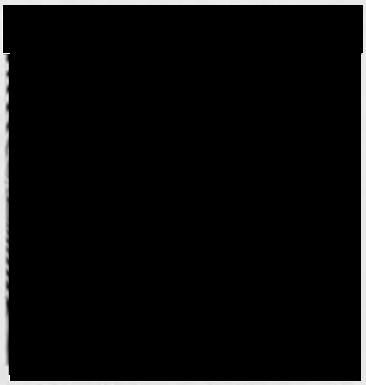

(4) Finite fringe holographic interferogram showing a compressible flow (spatial, quasi-heterodyne technique)

(5) Speckle holographic interferogram showing the stress distribution over a rotating plate

(6) Infinite fringe holographic interferogram of a vibrating bellows

The library of sample interferograms shown highlights some of the problems to be encountered in automatic fringe analysis.

Picture 1 shows a rather poor quality fringe field of low modulation, and with unresolvable fringes in the near wall regions, and around the ribs. Cases such as this require enhancement techniques to improve the fringe modulation, and some capability for analysing enlarged near-wall and rib regions and then merging these results back into the global results. This is necessary to enable sufficient resolution to detect all the fringes present, while still retaining a large enough area to provide useful results.

Picture 2 shows a relatively noise free, well modulated fringe system with few resolution problems. The major problem here for automatic fringe analysis is the closed fringe problem, necessitating a 2-D fringe analysis approach with "a priori" knowledge.

Pictures 3 and 4 show the same flow field with both infinite fringe and finite fringe background interferograms. The finite fringe field is well modulated and has a high signal-to-noise ratio, automatic analysis problems coming with the high frequency fringes due to insufficient resolution, the closed loop fringes, and fringe discontinuities around regions of shock. The finite fringe field, although computationally more intensive to analyse, offers a chance of a more accurate and generally applicable automatic analysis routine. Problems come in the fact that the Fourier analysis technique commonly used breaks down in regions where the fringe frequency is likely to be of the order, or higher, than the carrier frequency.

Picture 5 shows a typical speckle fringe pattern, and highlights the inherent noisiness of such fringe fields, necessitating the use of local area techniques in their automatic analysis.

Picture 6 shows a low modulation infinite fringe background interferogram, where numerous background artefacts make automatic analysis a very difficult job.

3.1. DIRECT UTILISATION OF INTERFEROMETRIC INTENSITY VARIATIONS FOR THE QUANTITATIVE ANALYSIS OF INTERFEROGRAMS

3.1.1. Introduction

The type of interferogram most often produced is the infinite fringe background variety, as described by equation (2.17). This is because extremely good qualitative results can be obtained this way, the fringes on the interferogram corresponding to contours of constant magnitude of the phenomenon under study. Thus, if holographic interferometry is being used to study heat transfer, the fringes obtained are isotherms. If the same technique is used to study compressible flow, the fringes obtained are isobars. So the experimental investigator produces a full-field record of the test-section that is extremely amenable to a qualitative analysis. It is this that makes the infinite fringe background interferogram so attractive to experimental investigators.

The extraction of quantitative data is possible from such interferograms simply by ordering the visible fringes with respect to a known fringe condition, each fringe representing a phase change of 2π, or a change in fringe order of one. Whole fringe orders are assigned to regions of maximum intensity, and half fringe orders to regions of minimum intensity, known as fringe maxima and fringe minima. Thus by knowing the locations of the fringe maxima and minima in the interferogram, and the relative fringe orders, it is possible to extract full-field quantitative data.

At first glance then it would seem a relatively trivial exercise to extract quantitative data automatically, simply locate the regions of maximum and minimum grey-scale intensity and assign fringe orders. However many problems conspire to make this exercise a difficult one to perform successfully. These problems and some of the standard image enhancement techniques used to overcome them are detailed in Chapter 5. This section of the review will therefore just present the fringe location and ordering techniques that have been used by various workers in the field, and will only detail any novel image enhancement techniques that may have been used by a particular author.

The techniques presented may be divided up into three main categories. These are semi-automatic, one-dimensional and two-dimensional fringe analysis procedures. The semi-automatic fringe analysis techniques rely on a large degree of operator interaction for successful application. The one-dimensional approach either analyses the whole fringe system one line at a time, combining the results at the end of the operation, or tackles only specific lines of the fringe data. In both cases the grey-level information tends to be used by the routines. The two-dimensional methods analyse the whole fringe field in one pass, and tend to rely on binarising the image data as an initial step in the procedure. Fringe data is then extracted by either thinning the fringes to produce fringe contours one pixel wide, or by tracing the fringe edges. Special methods have been devised to

store this fringe data in as compact a form as possible, and also to automatically order the resulting, potentially very complicated, fringe systems.

A third category of fringe analysis techniques also exists, and these are those that include a very large degree of manual interaction. Although it could be claimed that these aren't strictly automatic analysis techniques in that the fringe detection and tracing are carried out manually, nevertheless they do provide an important contribution to this field of research, and this section will start with a consideration of such techniques.

3.1.2. Semi-automatic fringe analysis systems

Funnell [1981] makes the remark that any automatic fringe analysis routine needs some degree of operator interaction, especially if that system is to maintain any sort of flexibility in its application. From the author's practical experience this is a very true statement. However, presented in this section are some of those systems that are deemed to have moved away from the spirit at least of automatic fringe analysis; that is those in which the two major operations of either fringe location or fringe tracing are performed manually by some means such as a light pen or a cursor.

Bernal and Loomis [1977] describe a general image processing facility that they developed for analysing fringe patterns in

interferograms. A semi-automatic procedure for locating fringe positions was developed, but this suffered from severe restrictions. If closed fringes were present in the fringe field the interferogram became too complicated for the automatic fringe finding routine to deal with, and it was then necessary to locate the fringes manually using a cursor. For the automatic fringe finding routine to operate effectively the fringes had to be located approximately horizontally on the digitiser screen, orientations of up to 30° being permissible. The program developed then located the fringes along vertical scan lines, and the reliability of the automatic fringe finding process, which relied on a quadratic curve fitting method, were satisfied by having the operator select the first scan line and locate manually the dark fringe centres along that line. The whole system relied quite heavily on the existence on a file editor that allowed for the manual correction of faulty data points with the use of a cursor.

A system for the automated reduction of straight-line and circular fringe patterns was also developed by Glassman and Orr [1979], based around an automated pattern processor (ZAPP, produced by the Zygo Corporation), and a PDP-11/34 mini-computer. The automated pattern processor has been fully described by Augustyn [1978], [1979] in other papers. To analyse straight-line fringes the operator defines an elliptical aperture using a cursor on the digitised data, and then uses the ZAPP to acquire the co-ordinates of the fringe centres, which are displayed superimposed on the interference fringes. Co-ordinates on

alternative fringes are shown by +'s and x's. A major feature of this system is that the operator may change individual points or lines if he is unhappy with them by the use of a cursor. In fact for especially complex patterns it is necessary to enter all the fringe centre points manually.

Ben-Dor et al [1979] developed an interactive system for the evaluation of interferograms that utilised a digital means of storing fringe locations. Initially a very crude system was produced, the interferogram being placed on a digitising tablet and a cursor being used to trace the fringes and extract the x and y co-ordinates. A more advanced system based on this early work was then produced by Ben-Dor and Arzoan [1985] to produce a more fully automated system, based on an Apple micro-computer. Because of the limited system resolution the interferometric data had to be of high quality, that is a high signal-to-noise ratio and good fringe contrast. The fringes were then traced automatically, but it was necessary to provide a great deal of operator input both in providing information about such regions as fringe discontinuities, and also in the fringe ordering procedure.

Yatagi [1984] has developed a semi-automatic fringe analysis system called RIFRAN (Riken Interactive FRinge ANalyser) for analysing Moiré photographs and interferometric patterns in optical shops. A flow diagram for RIFRAN is shown in (Fig.(3.1)), the system allowing for automatic fringe peak detection (described in 3.1.3.1) and interactive correction of false peak points in previously

detected fringe patterns. Most of the operations involved are interactively performed by the use of a light pen connected with a television monitor as an input device. Two-dimensional fringe analysis was not required of the RIFRAN system, but several one-dimensional scan lines could be analysed. The use of fringe order matching and interpolation techniques then allowed these several scan lines to be combined into a two-dimensional analysis. A conceptual configuration for an interactive fringe analysing system making use of a light pen is shown in (Fig.(3.2)).

3.1.3. One-dimensional fringe analysis routines

These routines operate on one-dimensional grey-level signal data; that is either a single scan line across the grey-level fringe field or a grey-level signal formed by temporal or spatial averaging of a number of scan lines to improve the signal quality. For these techniques to be effective the direction of the scan line has to be essentially perpendicular to the fringe direction, giving a data signal that is modulated sinusoidally as it traverses the fringe field. Five distinct techniques may then be applied for the digital determination of fringe co-ordinates. These are:

i) locating the maximum and minimum grey level intensities in the sinusoidal signal.

ii) determining regions of change in the grey-level gradients.

iii) determining the regions of maximum grey-level gradient.

iv) using a floating threshold or hysteresis technique to determine the positions of fringe maxima and minima.

v) the use of a bucket and bin type algorithm to determine the positions of the fringe maxima and minima.

A schematic description of these five methods is shown in (Fig.(3.3)). Such one-dimensional analysis procedures may be extended into two-dimensions either by analysing a series of scan lines and combining the results, or by using such a technique to obtain, say, the locations of the bright fringe centres along a particular scan line and then using a fringe-tracking algorithm to trace these grey-level fringes. Such fringe tracking algorithms all adopt the same format. The grey-level intensity is summed over a series of short vectors and in the case of bright fringe tracking the tracking algorithm moves in the direction of maximum summed intensity.

A more detailed examination of these techniques is now given as various image processing systems developed by researchers in this field are described.

3.1.3.1. Max./Min. fringe detection

Varman [1984] uses a maximum/minimum automatic fringe detection system in the analysis of turbine blade profiles obtained from a Moiré contouring technique. A series of vertical fringes is produced on the surface of the test object by rotating the master

object about a vertical axis and storing this image as the reference grid. The observed fringes are then pure 'wedge' type fringes, and the deflection of the vertical fringe to the right or the left is an indication of the amount and optical phase of the profile error at that point. After the vertical fringes have been produced the image data is enhanced by the use of low-pass filtering techniques, and a linear contrast enhancement is performed so that the grey-level data completely fills the available dynamic range.

A threshold value midway between the intensity extremes is then chosen, and fringe minima searched for along a horizontal scan line at the top of the image data. The threshold level is used as a starting point, and each fringe minimum position is sought by taking the lowest of successive data points until the threshold is again reached.

The procedure is then expanded to a two-dimensional technique, the located fringe minima being used as starting points for a fringe tracking algorithm that traces the dark fringes down the image data. This is done by specifying three pixel vectors, 22.5° apart, as shown in (Fig.(3.4)), and averaging the intensity values over each of these three pixel vectors. The direction of travel for the algorithm is decided by the smallest average over the summed vectors, the centre arm of the vector fan being set to point in the same direction as the previous move. The fringe minima are traced until an operator defined boundary is reached.

Funnell [1981] uses a very similar procedure in the analysis of circular fringe patterns. A single scan is specified which cuts across the circular fringe pattern, and fringe maxima are chosen as the locations where a pixel has a value greater than or equal to both neighbours, with the restriction that neighbouring points may not be considered as a maximum. The located maxima are then used as starting points for a fringe tracking algorithm working on a similar principle to that devised by Varman. In this case also the grey-level values are summed over a number of forward-facing vectors, and the algorithm advances in the direction of the maximum value vector. At this stage Funnell includes the possibility of operator intervention to deal with regions of ambiguity, or at fringe dislocations.

Yatagi [1984] uses a 5 x 5 pixel matrix to detect fringe peaks along a scan line, a data point being considered a fringe maximum if peak conditions are satisfied in two or more directions, that is a maximum grey-level value is found at the centre point of a 5 x 5 pixel neighbourhood along at least two of the four possible crossing vectors. This particular method was incorporated into an interactive fringe analysis system that is detailed further in section (3.1.2).

It should be noted here that of all the possible fringe detection methods this one, the detection of maximum and minimum grey-level intensities, is the worst, due to its susceptibility to failure in the presence of noise. In fact a well modulated, high

contrast signal, with a high signal-to-noise ratio is necessary for the routines detailed in this section to operate effectively.

3.1.3.2. Grey-level gradient change fringe detection

Using this method fringe extrema are detected along a scan line by determining points at which the grey-level gradient over a short vector changes sign with respect to the previous short vector. So for a fringe maximum the preceding vector will show an increasing grey-level, whereas the vector under consideration will show a decreasing grey-level value. If such a gradient change is detected tests for significance then have to be applied to eliminate false gradient changes due to such occurrences as noise or false artefacts in the image data. The rigorousness of these tests is dependent both on image quality and the application being undertaken.

Birch [1976] uses the gradient change method to determine the position of fringes in the interferograms of standard lenses, as formed by a Twyman-Green Interferometer. Approximate fringe positions obtained in this way are accepted subject to the following test criteria;

i) the first detected extreme is a maximum, following by alternately a minimum and a maximum.
ii) all detected extrema should be at least one-half of the preceding semi-period apart.

iii) the maximum intensities must be at least fifty percent of the maximum intensity located previously, and similarly the minimum intensity must be less than twice the previously located minimum intensity.

The exact co-ordinates of the fringe extrema are then located using a least-squares based quadratic filtering routine, using the intensity values at the approximately located fringe extrema and those of the two adjacent data points on each side.

Robinson uses the gradient change method for a number of applications, three-dimensional positional measurement and fault detection in holographic non-destructive testing [1983a], [1983b], and for the determination of components of three-dimensional deformation [1985]. In these cases the tests for fringe extrema significance rely on determining the fringe modulation and the mean threshold over an area local to the suspected extreme. The gradient change located then has to be of the order of the local modulation, and the grey-level intensity of the located extreme has to lie above or below the local mean intensity depending on whether it is a maximum or a minimum respectively. The extremum location is further refined by comparing the local intensity data with a sinusoidal function and performing a correlative fitting procedure over a range of half a fringe spacing either side of the initial estimate. This fitting procedure gives the best value for the fringe spacing.

3.1.3.3. Maximum gradient fringe detection

This technique can be approached in two ways. The first is to search for a grey-scale gradient that is greater than the gradients of the neighbouring vectors on either side, (Fig.(3.3)). Obviously the gradient vectors being compared are of the same length. The second approach is to employ a gradient sensitive operator, and look for regions of maximum response from the operator. Any one of the edge-detection/sharpening techniques discussed in Chapter 5, could be adapted to provide such a gradient sensitive operator. However no literature has been found discussing such an application to fringe analysis techniques.

3.1.3.4. Floating threshold fringe detection

Such a technique was initially proposed by Tichenor [1979] and is alternatively known as hysteresis detection. Tichenor used this method for the analysis of holographic interferograms of stainless steel pressure vessels, any defect in the pressure vessel causing an excessive surface displacement that increases the fringe density around the corresponding point on the interferogram. The digitised image was windowed into several small regions, and the fringe density in each region was estimated based on the number of peaks found in several line scans across the area under study.

To detect a relative minimum the lowest value pixel since the last minimum was detected is accumulated, and this is assigned as MIN. Then, if a pixel value is encountered that exceeds this MIN value by a certain threshold, a minimum is counted. This threshold value, T, is defined as:

$$T = \Delta(A_r + A_s)/2 \qquad (3.1)$$

where Δ is a constant in the region of 0.2 → 0.35 (Tichenor used a Δ of 0.31). A_s is the average pixel value encountered in the line scans, and A_r is the average pixel value encountered over some reference area, which could be the whole image, but in this case was a 64 x 64 pixel square in the centre of the image. The reason for the use of such a threshold was that while adjusting to varying image brightness it does not allow the threshold to approach zero in a predominantly dark region of the interferogram.

Once a minimum has been found a maximum is then searched for in an analogous manner, this time a maximum pixel value, MAX, being accumulated. A relative maximum is counted when a pixel value is encountered that is less than this MAX value by the threshold T. The procedure for maxima and minima detection is then repeated until the end of the scan line.

Tichenor took the maximum number of counts obtained over four scan lines to represent the fringe density in the region of

interest, and compiled a fringe density of the whole object which was then compared to an acceptance profile. If the fringe density map fell into this acceptance profile the part was accepted.

Becker [1982],[1985] adapted this hysteresis procedure into an image segmentation technique, binarising an image by defining a series of step-like functions across the image data. This is dealt with more fully in the two-dimensional analysis section.

3.1.3.5. Bucket-bin fringe detection methods

With this algorithm the fringe data is scanned along one line, sensibly perpendicular to the general fringe orientation. The global intensity average is then determined from the grey-level intensity distribution along this scan line, and the zero-crossing points determined, i.e. PQ in (Fig.(3.4)). All the data points along PHQ define a bucket, and the maximally valued pixel in this bucket defines the bin. This bin pixel may then be used as a definition of the fringe maximum. A similar procedure determines the location of the fringe minimum.

This basic algorithm is improved upon greatly by Choudry [1981] in his analysis of holographic interferograms of a convective heat transport process. In this case a secondary mini-bucket, CHD in (Fig.(3.5)), is constructed around the bin pixel. All subsequent data processing is performed in these mini-buckets, which are made up of pixels having at least a certain percentage of the

grey-level of the bin pixel. Within each of the mini-buckets the choice of an algorithm to determine the fringe extrema is limited by the number of points contained therein. With a small number of points a simple centre of gravity is used. With many points, typically more than five, a parabola or some other higher-order curve is used.

3.1.3.6. Analysis of broad diffuse fringes

The fringe detection algorithms described previously all work well on well defined high quality fringe data. However the analyst is often faced with the problem of broad diffuse fringes, representing a very small change in the physical state of the object being studied. In these cases a different approach to the problem of defining fringe positions has to be adopted.

Schemm and Vest [1983] developed a procedure for smoothing and interpolating fringe position data when the number of fringes is small and there are more than ten irradiance measurements per fringe, and accurate phase values are needed at arbitrary positions in the field. Basically a least-squares error criterion is used to fit the irradiance data obtained over a single scan line running essentially perpendicular to the fringe system to a function of the form:

$$I(x) = A(x) + B(x) \cos \Phi(x) \qquad (3.2)$$

(c.f. equation (2.17))

In this case A(x), B(x) and $\Phi(x)$ are low order polynomials. I(x) represents the intensity data, A(x) the variation in the background irradiance due to such things as non-uniform object illumination and B(x) is an envelope function related to the visibility of the fringes, in other words, it is a measure of the variation in fringe visibility over the scan line of interest. $\Phi(x)$ describes the phase variation over the fringe data, and this is the quantity of interest.

Having fitted such a function to the fringe data it is then a straightforward procedure to determine the fringe co-ordinates and to interpolate between the fringes.

3.1.3.7. Fringe Ordering

With such one-dimensional fringe analysis techniques fringe ordering is usually performed manually, with some form of interactive device such as a light pen or a cursor. It may be performed automatically, but this requires three conditions. The first is that the initial fringe order is manually set, unless it is always constant. The second is that an *a priori* knowledge of the probable fringe order distribution may be built into the ordering algorithm, such as 'the fringe orders will always increase'. The third requirement is that some interactive facility exists so that mis-ordered fringe locations may be corrected. This is because the one-dimensional analysis procedures give no full-field data, and so such instances as the scan line crossing a closed fringe twice may lead to incorrect ordering of the fringes.

3.1.4. Two-dimensional fringe analysis routines

It is often necessary to obtain quantitative data from the whole fringe field, and the two-dimensional fringe analysis routines are designed with this in mind. Such routines can really be divided into four main steps:

(i) Image data pre-processing

This step is necessary to change the data into a form that is more tractable to analysis by the following routines.

(ii) Image binarisation

Image data are nearly always binarised when two-dimensional routines are applied; that is the data are converted from grey-scale data containing as many as 256 possible grey-levels to a simple two-tone data set, the pixel points being either white or black.

(iii) Fringe co-ordinate extraction

This stage is usually the nux of such routines, various methods being available for the determination of the fringe co-ordinates. This stage also includes any special storage features that might be used to reduce the amount of data that need to be stored for full information retrieval.

(iv) Automatic fringe ordering

Because the whole field fringe data are available, automatic fringe ordering systems are possible. However, some *a priori* knowledge is essential if absolute, and not relative fringe orders are to be determined, and some interactive system should be available for fringe order correction, as absolute accuracy is not easy to provide (due to the difficulty of incorporating a priori knowledge).

3.1.4.1. Data pre-processing

Standard image data enhancement techniques are used in these routines, and these are detailed in Chapter 5. Typical pre-processing techniques include:

(i) the averaging of multiple frames of a picture to increase the signal-to-noise ratio, where this is possible.

(ii) spatial smoothing or low-pass filtering to reduce noise usually by the use of a nine-point convolution kernel.

(iii) the removal of background luminance intensity variation. Typically this is done by determining the average grey-level of a number of a large windows distributed over the fringe field. A smooth surface may then be constructed by bilinear interpolation between every four adjacent nodes, and this surface may then be subtracted from the original interferogram, to equalise the intensity distribution.

(iv) the improvement of the grey-level fringe contrast by contrast enhancement techniques.

When an image of sufficient quality has been obtained the fringe data are ready for binarisation.

3.1.4.2. Image Binarisation

Image binarisation, also known as level slicing, is simply the conversion of a grey-scale image containing a number of discrete grey-levels into a two-tone or binary image. For a standard eight-bit resolution system, this usually means that the grey-scale values above a certain threshold value are set to white, a grey-level value of 255. Below this threshold value the pixels are set to black, or a grey-scale value of 0. This can be stated quite simply as:

$$\text{PIXEL}(I,J) = \begin{cases} 255 & \text{if PIXEL}(I,J) > \text{THRESH} \\ 0 & \text{if PIXEL}(I,J) < \text{THRESH} \end{cases} \qquad (3.3)$$

where THRESH is the deciding threshold. It is the means of determining this threshold value that decides the effectiveness and complexity of the binarisation stage of the operation.

The simplest means is to set a global threshold, that is, a threshold that applies over all the image data. This can be done through the use of suitable hardware, such as an XOR logic circuit or look-up tables, as Müller [1979] and Yatagi [1982] show. This has the advantage of being relatively quick when compared to the

same approach performed by software, as used by Cline [1982]. In both cases however the threshold is set either manually, or by using some form of global grey-level average value.

This global thresholding approach begins to give poor results if the background intensity varies over the image. A way to avoid this problem is to divide the image data up into a series of small regions, and for each regions determine a local grey-level average as the threshold value. Nakadate [1981] does this by dividing his image data up into twenty-five discrete segments, and defining the local grey-scale average value as the threshold for each region. Seguchi [1979] adopts a slightly different approach in that he defines a local neighbourhood around each pixel, and sets the threshold value as a percentage of the sum of the grey-scale values in this neighbourhood.

This local area thresholding method also begins to return poor results when varying fringe density is encountered over the fringe field. For instance, one large dark fringe may predominate in the thresholding window, thus setting an artificially low threshold value. Becker [1982], [1985] avoids this problem by using a binarisation procedure based on the hysteresis technique detailed in 3.1.3.4. to produce a step-like threshold function, the intensity value of each step being the mean grey-level encountered between adjacent extremes (Fig.(3.6)). The entire image data are transformed in this way by using the method over a series of scan lines.

More complicated binarisation procedures are available, such as that suggested by Lahart [1979] which uses local statistical techniques to binarise noisy image data. However a compromise must be made between added computational time and complexity and the increase in effectiveness of the binarisation technique.

3.1.4.3. Fringe co-ordinate extraction

Having successfully binarised the fringe-field, a number of techniques are available for the relevant feature extracton. Basically two methods are available, the location of fringe edges and the location of fringe centre-lines.

Cline [1982] uses a process known as segmentation to identify individual fringes. Fringes are taken to be sets of connected pixels of the same colour, either black or white. The procedure starts in the top left hand corner of the image data. The first fringe is defined as the set of pixels that are the same colour and are connected to the first pixel. Each pixel in the first fringe is labelled A. To find all the pixels in the first fringe, the first pixel is used as a seed pixel in a full algorithm. This algorithm tests the four neighbours of each pixel connected to the seed pixel. Each neighbour of the same colour is labelled A, and used recursively as a new seed pixel. After the first fringe has been labelled A, the image is scanned to find a pixel that has not been labelled, and this pixel becomes the seed of the second fringe. The second fringe is filled with the letter B. The procedure is repeated until all the fringes have been segmented.

The next step is to detect the edges of the fringes and produce an ordered set of co-ordinates defining each fringe. The image is scanned to find the first change in the pixel label that indicates an edge. The co-ordinates of the mid-point between the two pixels describes the first node of the first contour. The edge is then followed by a boundary fill routine that finds the nodes of connected pixel pairs of the same contour until all the nodes of the first contour are found. This process is repeated until all the edge contours have been extracted. Not all the nodes are necessary to describe the contour shape; nodes that lie on straight line regions of a contour are deleted without loss of information. A schematic diagram of this process is shown in (Fig.(3.7)).

Becker describes his methods for the detection of fringe edges. In the simplest of these [1985] the fringe co-ordinates are determined at the transition from white to black, and vice-versa, thus giving the fringe sides as the equal phase lines. A sequential tracking procedure was then used to trace the fringe positions line by line from the top to the bottom of the image data, and the fringe field was then stored as a polygonal data structure, (Fig.(3.8)).

In his work with Meier and Wegner [1982], Becker used a sequential tracking algorithm similar to a feature extraction technique proposed by Agrawala and Kulkarni [1977] to produce a polygonal representation of the fringe data. The left and right

edge points of the fringes due to a scan line were taken and compared to the left and right edge points derived from the next scan line. Each of the edge points in the current scan line was assigned to a fringe polygon by a simple boundary continuation test, different action being taken depending on the continuation conditions. If two edge points merged to one edge point in the next scan line, the right edge points of the left fringe polygon and the left edge points of the right fringe polygon were connected to form a single polygon. A new couple of polygons were initialised if two edge points had no connection to the previous scan line. The collected points belonging to the same fringe polygon were put into a temporary storage buffer. Fig.(3.9) shows the continuation conditions proposed by Agrawala and Kulkarni.

In both his systems Becker uses a redundancy reduction algorithm to reduce the amount of data storage needed. Each polygonal data structure, as it is completed, is approximated by a subset of vertices of the original polygon within a certain given range of tolerance. This algorithm was based on that proposed by Ramer [1972], but other algorithms exist for such data reduction techniques, notably those proposed by Stone [1961], Bellman [1961] and Gluss [1962a], [1962b].

The most popular method for determining fringe co-ordinate data is the extraction of fringe centres by the use of a thinning algorithm. Having extracted the fringe centres in this way, some

way of grouping the points into specific fringe sets is then necessary. Yatagi [1982] and Müller [1979] both adopt this system in their fringe analysis systems, but give no details as to the algorithms they use. Thinning algorithms are however a standard image processing technique, and much literature exists describing them.

Thinning algorithms work basically by eroding the boundaries of a feature until only a fully connected medial line remains. This can be done in two ways, either through parallel processing or through serial processing. In parallel processing, the value given to a point at the z^{th} iteration depends on the values given to the point and its neighbours in the $(z-1)^{th}$ iteration. Parallel processing is advantageous if special purpose computing structures can be used, such as cellular networks, and thinning algorithms based on this methodology also tend to work better than those based on serial processing techniques. Parallel algorithms for obtaining the skeleton of a binary picture have been described by, amongst others, Philbrick [1961], Triendl [1970], Saraga and Woolons [1968] and Deutsch [1969].

As an example of a typical parallel processing algorithm that proposed by Hilditch [1966] is presented here, in a simplified form.

Let $A(p_1)$ be the number of patterns 01 in the ordered set $p_2, p_3, p_4, \ldots p_8, p_2$ of the neighbours of p_1, Fig.3.10.

Let $B(p_1)$ be the number of non-zero neighbours of p_1. Then a point p_1 is deleted from the figure if:

(i) $2 \leqslant B(p_1) \leqslant 6$

and

(ii) $A(p_1) = 1$

and

(iii) $p_2, p_4, p_8 = 0$ or $A(p_2) \neq 1$

and

(iv) $p_2, p_4, p_6 = 0$ or $A(p_4) \neq 1$

This algorithm yields corrected skeletons which are not sensitive to contour noise.

In serial processing, one point at a time is processed; the result of processing a point at the z^{th} iteration depends on a set of points for some of which the results of the z^{th} iteration is already known. Serial processing algorithms have been presented by Montanari [1968], Pfaltz and Rosenfeld [1967] and Hilditch [1969]. Serial processing can be more efficient than parallel processing when it is implemented on a general purpose computer, but this type of algorithm tends not to work as well as parallel processing algorithms.

A typical serial processing thinning algorithm, due to Rosenfeld and Pfaltz [1966], will now be described.

In this algorithm pixels are assigned an increasing order with an increasing distance from the background set. If we consider a data set of m rows and n columns, where:

$$1 \leqslant i \leqslant m \qquad \text{and} \qquad 1 \leqslant j \leqslant n$$

and the data is binarised to a value of 1 and 0,
then two functions are applied to this data set. These are:

i) $f_1 (a_{ij}) = 0 \qquad \text{if } a_{ij} = 0$

$$= \min (a_{i-1,j+1} + 1,\ a_{ij-1} + 1) \text{ if } (i,j) \neq (1,1)$$

$$\text{and } (a_{ij}) = 1$$

$$= m + n \qquad \text{if } (i,j) = (1,1) \text{ and } a_{i,j} = 1$$

This can be described simply if we consider (Fig.(3.10)). Then this function is simply:

If $p_1 = 0$, then the new value of $p_1 = 0$

If $p_1 = 1$, but $i \neq 1$ and $j \neq 1$, the p_1 is assigned the minimum value of p_2+1 and $p_\theta + 1$.

If $p_1 = 1$ and $i = 1$ and $j = 1$, then $p_1 = m + n$.

ii) $f_2(a_{i,j}) = \min(a_{i,j},\ a_{i+1,j} + 1,\ a_{i,j+1} + 1)$

i.e. p_1 is assigned the minimum value of the points p_1, p_6+1, p_4+1.

From these ordered data sets, skeletons defining the maximal orders may be obtained by performing the two following operations.

$g_1(a_{i,j}) = \max(a_{i,j}, a_{i,j-1} - 1,\ a_{i-1,j} - 1)$ in a forward raster sequence

and

$g_2(a_{i,j}) = \max(a_{i,j}, a_{i,j-1} - 1,\ a_{i+1,j} - 1)$ in a backward raster sequence

Seguchi [1979] uses a parallel processing thinning algorithm to extract fringe contours from binarised fringe data. To group the thinned data into fringe sets he then applies a "follow-up" or contour tracing method. The image is scanned from top left to bottom right and when a fringe contour is located it is traced using a simple neighbourhood search scheme, assuming total connectivity of the contour and also the fact that the thinned contour is only one pixel in width. When a bifurcation is encountered it is located in the memory, and the branch last located is traced until the end. The search then backs up to the bifurcation point and traces the other branch or branches, and in this way the complete set of fringes can be located.

Nakadate [1981] proposes a novel, if somewhat cumbersome, technique, for extracting fringe centre co-ordinates from a binary image. In this case the fringe pattern is windowed into many small regions, the windows being square in form with sides a little larger than the width of the dark fringes. A decision about the direction in which this window is to be scanned, horizontally or vertically, is made by determining along which side most zero-valued points lie. The fringe centre is then simply located as the mid-point in the dark region traversed by the scan line, (Fig.(3.11)). This procedure is repeated for the whole fringe system.

3.1.4.4. Fringe Ordering Schemes

In by far the majority of cases, fringe ordering is performed by a manual interactive system. This is because automatic fringe ordering systems tend to be inflexible and not very robust, often breaking down or wrongly ordering fringes. Also the amount of *a priori* knowledge needed to correctly order the fringe fields often precludes the use of an automatic ordering system. However, two methods for automatically ordering a fringe field have been advanced by Becker [1982].

If no discontinuities exist in the fringe field a fairly simple numbering scheme is applicable. The fringe field is divided into regions containing similarly behaved lines, such as a series of straight parallel fringes or a concentric ring system, (Fig.(3.12)).

Then either the inner area of a closed loop system or the inner region of a fringe loop system closed by the image boundary is connected to one similar adjacent region by a straight line. The fringes are then numbered sequentially as they intersect the connecting lines, the starting point being the line system containing the greatest fringe density. If two consecutive points of intersection belong to the same fringe, the fringe counting is inverted. To obtain the absolute fringe order some *a priori* knowledge must be used to determine a relative off-set to correct the fringe orders assigned.

However, in many cases there may be discontinuities in the fringe system for a variety of reasons, usually poor binarisation. In this case, the fringe system is windowed into, typically, 64 x 64 pixel regions (assuming a 512 x 512 pixel spatial resolution). The fringes are then numbered window by window, starting with the window which has a maximum number of fringes with a minimum number of inversion points, ideally a window containing a number of parallel fringes. An adjacent window is then searched for which has at least two consecutive already numbered fringes at the common grid line and which also conforms to the initial criteria. In this way, meshes containing discontinuities are processed last, when a good deal of information about the fringe orders in the system is already known.

The starting point for the series of fringe ordering steps may be defined in several ways, but probably some form of "a priori" knowledge is required.

3.1.5. Summary

The infinite fringe system analysis techniques detailed in this first part of the literature survey may be summarised by the following flow chart:

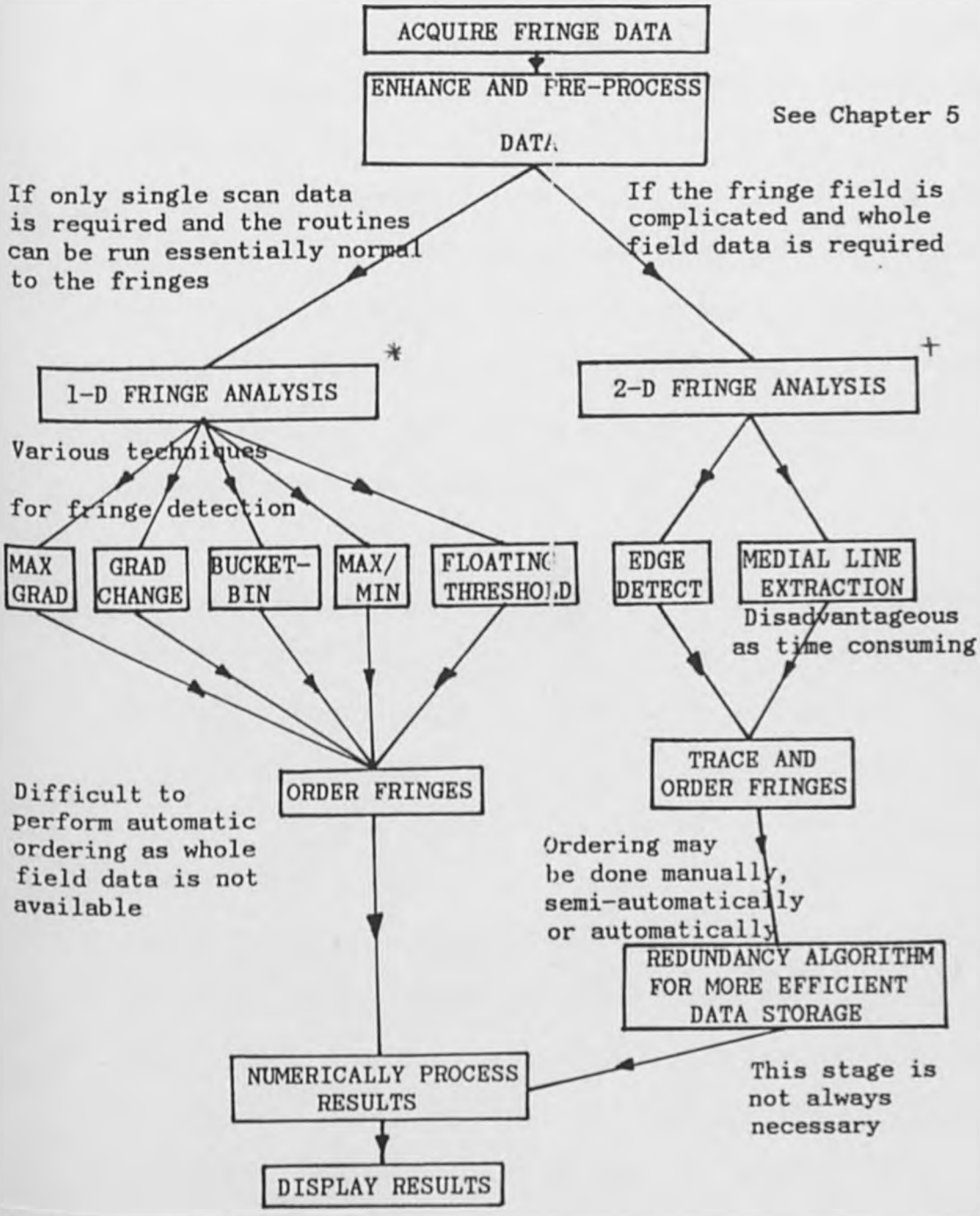

* Discussed in Chapter 6

† Discussed in Chapter 7.

3.2. DIRECT PHASE MEASURING TECHNIQUES

3.2.1. Introduction

As optical frequencies are too high for detectors to follow phase differences are often converted to time-independent irradiance variations, interferograms. It is possible however to produce a signal of low frequency whose phase can be measured electronically, by the use of synchronous phase detection techniques. This is a well known method for determining the phase and amplitude of a sinusoidal signal, and involves multiplying an unknown signal with a sinusoidal reference signal and integrating to filter out the low frequency component of the product. This is a heterodyne technique, and it is usually applied when great accuracy is desired in the measurement of the phase, accuracies of $\lambda/1000$ being possible.

It is also possible to use quasi-heterodyne techniques to obtain a direct measure of the phase. These are not true heterodyne techniques in that they do not rely on the synthesis of a low frequency signal from the addition of two high frequency signals. Instead the phase of one of the interfering waves is controlled to produce either a spatially variable or a temporally variable signal that can be analysed to determine the phase at any point. Such techniques are not as accurate as the heterodyne methods, but they are much easier to use and are more tractable to analysis. Thus they are much more widely used than true heterodyne techniques. Accuracies of up to $\lambda/1000$ are still possible using these quasi-heterodyne techniques and this is sufficient for most applications.

3.2.2. Heterodyne Techniques

The use of heterodyne interferometry was really pioneered by Dändliker et al. from the early seventies with the use of a dual-reference beam holographic interferometer, [1973], [1976], [1982], [1985]. The optical layout used is as that for classical holographic interferometry, except that two angularly separated reference beams are used, (Fig.(3.13)). The first object state O_1 is recorded by reference R_1 and the second object state O_2 by reference R_2. On recording these two reference beams have the same frequency as the object beam. On reconstruction the optical frequencies of the two reference beams are altered so that they differ by some small amount. This can be done in a number of ways, techniques commonly used being a rotating diffraction grating placed in one of the reference beams, or two acoustic-optic modulators, one in each reference beam, operating at slightly different frequencies. This small frequency difference causes the relative phase of the reconstructed wavefield to increase linearly in time, making the observed intensity at a point vary sinusoidally with time at a unique frequency, the beat frequency. The time dependent nature of this signal can be clearly seen from equation (2.21).

The modulation of this beat signal can be separated by a filter whose passband is centred on the beat frequency, $\Delta\omega$, and its phase can be measured electronically with respect to a reference signal derived from a secondary, fixed, detector whilst a primary detector is moved incrementally across the fringe field.

This allows the relative phase over the fringe field to be determined very accurately, and hence the phase difference between the two interfering object waves.

The major advantages of using such heterodyne techniques are that the possible sign ambiguity associated with phase changes in classical interferometry is removed, and also that great accuracy is possible in the measurement of the phase. Accuracies of a thousandth of a wavelength are possible, with spatial resolutions of greater than 10^6 resolvable points Dändliker [1985]

There are however some severe disadvantages to this method. The fringe field must be scanned mechanically by a photodetector, and thus information extraction is a slow process, about one second per point being needed. Also the control required of the frequency difference between the two interfering object beams can be problematical. The use of a dual reference beam in the holographic interferometer introduces problems due to the multiplicity of the reconstructed images and the influence of misalignment of the hologram with respect to the reference beams Dändliker [1976] The sensitivity to angular misalignment of such holograms can however be reduced by using two reference sources close together, a misalignment of 10' as opposed to 0.01' being tolerable in this case,

These problems, coupled with the fact that measurement accuracies of one thousandth of a wavelength are often not suitable or necessary for many applications, means that the use of heterodyne interferometry has been severely limited to applications such as aspherical lens measurement Perrin [1979]

3.2.3. Temporal Quasi-Heterodyne Techniques

With the temporal quasi-heterodyne method, a well-defined discrete phase step is introduced between the two interfering object waves, and the standing interference pattern that arises is scanned electronically, either with an array of photodiodes (C.C.Ds), or with a television camera. This procedure is repeated a minimum of three times, with the total phase shift introduced being less than 2π. Thus we have a system of at least three equations of interferometry such as that given by equation (2.17) but each one having some additional introduced phase shift.

$$I_1(\bar{v}) = a_1^2 + a_2^2 + 2a_1a_2 \cos(\Delta\psi(\bar{v}) + \Phi_1) \qquad (3.4a)$$

$$I_2(\bar{v}) = a_1^2 + a_2^2 + 2a_1a_2 \cos(\Delta\psi(\bar{v}) + \Phi_2) \qquad (3.4b)$$

$$I_3(\bar{v}) = a_1^2 + a_2^2 + 2a_1a_2 \cos(\Delta\psi(\bar{v}) + \Phi_3) \qquad (3.4c)$$

With each phase shift known, and the corresponding intensity distribution observable, it is possible to solve this set of simultaneous equations on a point by point basis to obtain the amplitudes of the interfering waves and their phase differences. It is usual for the electronically sampled fringe fields to be fed into a computer of some sort, so that the phase analysis may be automated.

A pioneer of this technique was Brunning [1974] who utilised a modified Twyman-Green interferometer, with a piezo-electric mirror

translator in the reference beam to allow the introduction of the relevant phase shifts. The reference phase was shifted linearly in time, and the phase at each point was determined from the algorithm:

$$m_1 = \frac{2}{np} \sum_{i=1}^{np} I(x,y,t_i) \cos \Psi_i \qquad (3.5a)$$

$$m_2 = \frac{2}{np} \sum_{i=1}^{np} I(x,y,t_i) \sin \Psi_i \qquad (3.5b)$$

where p is the integer number of fringe periods and n is the number of steps per period. The phase is then determined from the expression:

$$\Phi(x,y) = \frac{1}{2\pi} \tan^{-1} \frac{m_1}{m_2} \qquad (3.6)$$

Dändliker [1973],[1976], made use of his dual-reference beam holographic interferometer for this quasi-heterodyne technique. In this case the fringe field was cycled by altering the relative phase of the reconstructing reference beams, (Fig.(3.14)), using a mirror on a piezo-electric mount located in one of the reference arms. A micro-processor was used to control the phase sampling and perform the necessary computations. This particular approach does suffer from the common problems of dual-reference beam holographic interferometers, that is the over-lapping of the multiple reconstructions and the sensitivity to plate mis-alignment on reconstruction.

Wyant [1975] describes an algorithm in which he integrates over four successive quarter period intervals of a sinusoidal signal, and then computes the phase using algorithms similar to those of Brunning [1974]. The advantage to this method is that the reference phase addition may be ramped rather than shifted in discrete steps.

Sommargen [1977] describes a quasi-heterodyne system which utilises two unique optical components, a reference wave generator that produces two common-path, orthogonally polarised diffuse reference waves, and an optical phase shifter which allows the relative phase of the reconstructed object wave to be shifted by small equi-valued increments. The interference fringe field is scanned using a two-dimensional photodiode array, and an algorithm similar to that proposed by Brunning [1974] is used to determine the relative phase at each point of the interferogram.

A technique very similar to that used by Brunning [1974] is described by Frantz [1979], a modified Twyman-Green interferometer being used. In this case the phase and amplitude data are obtained using a method similar to that adopted by Dändliker [1982], except that in this case the reference beam undergoes discrete phase retardation steps instead of phase advancement. Frantz does make the point that the value for the phase derived in this way is ambiguous in that the quadrant of the complex plane in which the phase is located is not specified. He then goes on to present a method whereby this shortcoming

may be resolved. In this case four intensity measurements are taken, as opposed to the minimal amount of three. These are, the intensity with no phase retardation, the intensity with a phase retardation of $\pi/2$, and the intensity of the object beam alone and the reference beam alone. Using these four intensity values we may determine the relative phase at the point (x,y) from the algorithm.

$$\tan \Phi(x,y) = \frac{I(\pi/2) - I_{object} - I_{reference}}{I(0) - I_{object} - I_{reference}} \qquad (3.7)$$

This allows us to determine the quadrant in which the phase lies simply by inspection of the signs of the denominator and the numerator, and it is also possible to determine the amplitude of the object beam directly,

$$|a_{object}| = \langle I_{object} \rangle^{\frac{1}{2}} \qquad (3.8)$$

A variation on the temporal quasi-heterodyne technique was proposed by Srinivasan [1974], in which the phase distribution of a projected sinusoidal grating, deformed by a surface, is measured. The deformed grating images are detected with an array camera, and processed by a micro-computer. A shearing interferometer, incorporating a phase modulator, was used, the sinusoidal intensity distribution created by the projection of the sinusoidal grating onto the desired surface being controlled by the use of this

modulator. The phase at each point of the surface was then determined using a numerical scheme based on that by Brunning [1974], allowing a surface profile measurement of greater than 10 μm resolution. It should be noted that this is not an adaptation of the heterodyne technique proposed by Perrin [1979], as the deformed grating itself is analysed without the use of a reference grating of any kind.

A generalised algorithm for use with such digital quasi-heterodyne or fringe-scanning interferometers has been offered by Grievenkamp [1984], and is based on a least-squares fit method. The required phase steps may be chosen with unequal spacing and they may extend over a range greater than 2π.

3.2.4. Spatial Quasi-Heterodyne Techniques

Synchronous phase detection may be performed in the spatial domain as well as the temporal domain, a large tilt between the reference and object wavefronts substituting for the piston-type reference phase shifts of the temporal methods. This tilt introduces a heterodyne carrier frequency into the resulting interferogram, basically an additional phase of increasing magnitude across the interference pattern is introduced. This can be clearly seen from equation (2.18), the magnitude of the phase addition depending on the position in the interference field being considered. If there is no change in phase between the two interfering beams except that introduced artificially by a mirror

tilt, then the equation of interferometry is that given by equation (2.18). This means that the interferogram consists of a modulated background intensity, the fringes produced being equi-spaced and orientated in the same direction. If some phase change has occurred between the two interfering object waves in addition to that artificially introduced, then the equation of interferometry takes the form given by equation (2.14).

$$I_1(\overline{v}) = a_1^2 + a_2^2 + 2a_1a_2 \cos[k\overline{\theta v} + \Delta\psi(\overline{v})]$$

The pattern of straight parallel fringes that would thus normally occur on reconstruction is modified by this additional phase element, and analysis of the 'carrier' fringe distortions allows a phase map to be constructed from the fringe-field.*

The analysis of this distorted fringe-field may be performed in a number of ways. Takeda [1982] proposed an analytical method that utilises a Fast Fourier Transform and this method has also been taken up by Macy [1983] and Womack [1984]. An earlier version of this method was presented by Ichioka [1972] in which the properties of the transformed spatial pattern in the frequency domain were used advantageously. The basis of this analysis is as follows:

$$I(x,y) = a_1^2 + a_2^2 + 2a_1a_2 \cos[2\pi f_o x + \Delta\psi(x,y)] \qquad (3.9)$$

* The addition of such a carrier frequency removes the ambiguity of knowing whether the phase is increasing or decreasing at a point, as long as the direction of mirror tilt is known.

where f_o is the introduced carrier frequency which varies rapidly compared to the other modulation terms. This equation may in turn be re-written in the form:

$$I(x,y) = A(x,y) + C(x,y)e^{i2\pi f_o x} + C^*(x,y)e^{-i2\pi f_o x} \qquad (3.10)$$

where $A(x,y) = a_1^2 + a_2^2$, $C(x,y) = a_1 a_2 e^{i\Delta\psi(x,y)}$ and C^* is the complex conjugate of C. This equation may then be transformed with respect to x with the use of a Fast Fourier Transform algorithm (FFT) to give:

$$\underline{G}(f,y) = \underline{A}(f,y) + \underline{C}(f - f_o,y) + \underline{C}^*(f + f_o,y) \qquad (3.11)$$

where the underscored letters denote the Fourier spectra, and f is the spatial frequency in the x-direction. As the spatial variations of the other modulation constants are slow compared to the spatial frequency, f_o, of the carrier frequency, the Fourier spectra takes on the form shown in (Fig.(3.15)). One spectral sideband is selected and shifted by f_o along the frequency axis towards the origin, and its inverse Fourier transform is then computed using an FFT algorithm to obtain C(x,y) in equation (3.10). The complex logarithm of C(x,y) is then computed and the discontinuous phase distribution $\Delta\psi(x,y)$ is obtained from the imaginary part. This procedure is covered fully by Takeda [1982].

The use of this Fourier transform technique is however time-consuming, and may be avoided by adopting a sinusoid

fitting method, as detailed by Metz [1983] and Macy [1983]. This is essentialy a simplified approximation of the Fourier transform technique, and relies on an assumption that the carrier frequency, f_o, is known. If, for instance, the average carrier fringe width is three pixels then three adjacent samples are concerned, A, B and C, and the complex convolution is:

$$z = Ae^{-i2\pi/3} + Be^{io} + Ce^{i2\pi/3} \qquad (3.12)$$

The n-phase, or real part, is:

$$I = (-\tfrac{1}{2})A + B + (-\tfrac{1}{2})C \qquad (3.13)$$

and the quadratic or imaginary part is:

$$Q = (-\tfrac{\sqrt{3}}{2})A + (\tfrac{\sqrt{3}}{2})C \qquad (3.14)$$

The phase is now available directly as the arc-tangent (Q/I). Successive applications of the equations advances the derived phase by 120° per step, i.e. A is replaced by B, B by C, and C by the next pixel along. Subtraction of this nominal advance will effectively shift the carrier frequency down to the origin, or zero spatial frequency, i.e. will remove the effects of the reference tilt.

3.2.5. Intensity Subtraction Techniques

The technique known as image intensity subtraction may also be used for the determination of the relative phase between the interfering object beams. This method has been employed by Schlüter [1980a], [1980b] and Macovski [1971], and it is in fact a real-time version of the dual-reference beam holographic interferometry used by Dändliker (3.13). The advantage of this is that it allows tangential deformation information to be obtained as opposed to single object beam holographic interferometry which is essentially sensitive to normal displacements only.

The principle of the technique is the subtraction of two intensity patterns relating to the same object deformation, with a 180° phase shift between them. This is advantageous in that it allows the separation of the desired interference terms from the undesired image and reference terms by cancellation rather than high frequency filtering as used by Womack [1984]. Macovski utilises the heterodyne interferometry approach of Dändliker, whereas Schlüter adopts the temporal quasi-heterodyne technique, with a piezo-electrically mounted mirror in one of the reference arms to supply the appropriate phase shifts. In both cases two scans are made, with the reference wave phase shifted by 180° inbetween. One signal is subtracted from the other, resulting in the cancellation of the undesired terms and the addition of the interference terms. In Macovski's case the resultant high frequency signal is square-law detected to provide an output signal given by:

$$I_{out} = 4a^2 \, [1 + \cos(\Delta\Psi)] \qquad (3.15)$$

Thus we have an output which is four times the original image intensity, a^2, fully modulated by a set of interference fringes from which it is possible to derive the phase change that has occurred in deformation of the object. It is apparent that this method really loses the increased accuracy of the heterodyne technique, each fringe being indicative of an axial deformation of one-half of a wavelength.

The method adopted by Schlüter however retains the advantages of the quasi-heterodyne technique. In this case the intensity distribution on subtraction is given by:

$$I_{output} = 4|A|^2 \cos[\Delta\Psi + \theta] \qquad (3.16)$$

where $\Delta\Psi$ is the required phase change, and θ is the incremental phase addition due to a mirror shift in one of the reference arms. The zero intensity points of this subtraction interferogram are the new fringe loci, and they exhibit, as previously, a periodicity of π. Varying the added phase term θ allows the interference pattern to be shifted across the object field allowing the accurate determination of the object deformation for any desired object point.

3.3. THE ANALYSIS OF SPECKLE FRINGE PATTERNS

3.3.1. Introduction

Laser speckle is a phenomenon inherent with the use of a highly coherent light source, and as such has been extensively studied, Françon [1979]. The physical origin of such laser speckle may be readily appreciated. Because of its high coherence, laser light scattered by one object point will interfere with that scattered from another object point. This most obviously occurs when laser light impinges on a rough surface (rough, in this case, meaning that the surface has random, microscopic height variations of a scale greater than the wavelength of the light), and is reflected. A detector, such as film or the retina, when placed in the optical field, will observe a random pattern of interference fringes, and this effect is termed 'speckle'.

These speckle patterns may be utilised in two ways for the determination of quantitative data about an object. These are speckle photography and speckle interferometry, and they are both dealt with in the following text. In both cases the analysis of speckled fringe patterns is required for the extraction of quantitative data, and so a brief review of the methods used to pre-process speckle fringes will first be presented.

3.3.2. Speckle Fringe Pre-processing

Speckle fringe systems may be subjected to the same standard pre-processing techniques as other fringe systems for image data enhancement and pre-automatic analysis preparation (see Chapter 5). Such techniques as contrast-enhancement, image binarisation, high and low-pass filtering, may all be used, but their utilisation must involve some degree of local averaging for the results to be useful. Basically, it can be said that the larger the speckle size and the sparser the speckle distribution, the less effectively do these standard routines work. However work has been done on pre-processing techniques that deal specifically with speckled images. Chaubless [1979] describes a digital method which allows an extensive reduction of noise components from data records obtained by the point-by-point interrogation of double-exposure speckle photographs (see 3.3.3). The digital filter developed enhances the data resulting from scanning lines crossing a series of Young's fringes, and removes much of the optical noise associated with laser speckle. This allows an increased accuracy in the determination of the Young's fringe spacing.

A general investigation into the pre-processing of speckle fringe images was carried out by Varman and Wykes [1981]. They specifically described ways of digitally smoothing such images to reduce the noise content using standard techniques such as low-pass filtering, averaging and contrast enhancement, and polynomial smoothing.

3.3.3. Speckle Photography

This technique is used for making moderate-sensitivity measurements of in-plane translation, strain, rotation and vibration, and also out-of-plane rotation (tilt).

Barker and Fourney [1971], Dudderer and Simpkins [1977] and Lallemert et al. [1977], have also cited recent application to the measurement of flow velocities in fluids seeded with tracer particles.

The basis of the technique may be described as follows. Consider a bright object point imaged onto a recording plate, Fig.(3.16). This bright point may either be a speckle from a rough surface, or the illuminated surface of a seed particle in a fluid flow. If we assume the imaging ratio to be 1 : 1, then if the object point is displaced by a small distance, ds, so too is the image point. In a photographic double exposure, the first taken before and the second after the displacement, the object point appears twice, separated by ds, as shown in Fig.(3.17). After development of the photographic recording medium these two object points will appear as two bright spots on a dark background. This information may then be used directly or indirectly.

A direct use of the information is the measurement of the separation of the image pair, ds. In the case of deformation

measurements, the distance ds is inversely proportional to the magnitude of the in-plane displacement. In the fluid flow application, ds = w.dt, where w is the flow velocity and dt is the time interval separating the two exposures.

Indirect use of the information provided by this image pair comes about when the two points are illuminated from behind with a thin laser beam, known as the interrogation beam, Fig.(3.16). The illuminated object points act as two separated point light sources, producing a series of parallel, equally spaced, interference fringes, or Young's fringes. The fringe orientation is normal to the in-plane translation, be it velocity direction or direction of surface translation in a solid object. The fringes are separated by a spacing Δ, where:

$$\Delta = \frac{f_i \lambda}{ds} \qquad (3.17)$$

f_i being the focal length of the imaging lens, λ the wavelength of the interrogating beam, and ds the object point displacement. Thus the magnitude and direction of small, in-plane displacements may be ascertained.

There are however limitations to this technique. We have a lower limit set by the fact that the in-plane displacement vector, ds, must be greater than the object point diameter, dp. We also have an upper limit when the fringe spacing, Δ, becomes too small to be resolvable; a rule of thumb value for this limit of ds is 20 x dp.

Also, under normal circumstances, the illuminated object plane contains many object particles which translate between the two exposures, and so several pairs of image points may be reconstructed by the laser beam. If all these points have experienced the same translation vector, the Young's fringe system will be the same as that if a single image pair had been illuminated. However as small deviations occur between the translation vectors of the image points under interrogation the fringe pattern becomes decorrelated as several different Young's fringe systems overlap. This is apparent as a loss in fringe contrast, and the amount of this decorrelation that is tolerable provides another limiting factor to the method. A certain amount of decorrelation is normally present in practice, and a mean value of displacement is usually attributed to the object points under study.

Full field data can obviously be obtained by scanning the image plane with the interrogating beam a point at a time, and analysing the resulting set of Young's fringes at each point. This limits the speed at which the information may be extracted as the scanning must obviously be done mechanically, and to provide a reasonable through-put the fringe systems obtained must be analysed automatically. As explained earlier, an automatic analysis routine must be able to determine the orientation and separation of the fringes to extract the data, and this really provides two separate problems.

3.3.3.1. Determination of fringe spacing of Young's fringe system

Use may be made of the properties of the Fourier transform to determine the frequency of the fringe separation. The whole fringe field may undergo a two-dimensional Fourier transformation, or some averaged function may be obtained from the image data which then undergoes a one-dimensional transformation.

The discrete two-dimensional Fourier transform of an array is defined as:

$$F(u,v) = \frac{1}{N} \sum_{j=0}^{N-1} \sum_{k=0}^{N-1} f(j,k) e^{-\frac{2\pi i(uj + vk)}{N}} \qquad (3.18)$$

and the discrete inverse transform is thus simply given by:

$$f(j,k) = \frac{1}{N} \sum_{u=0}^{N-1} \sum_{v=0}^{N-1} F(u,v) e^{\frac{2\pi i(uj + vk)}{N}} \qquad (3.19)$$

To provide the necessary computational efficiency this form of the equation must be altered to that of a two-dimensional discrete Fast Fourier Transform, as outlined by Brigham [1974]. After transforming the fringe pattern in this way a simple search for the diffraction peaks occurring in the spectral function gives the fringe frequency, and hence directly the displacement vector. This technique does suffer from the drawback, as indicated by

Robinson [1983],[1985], that to achieve the desired speed of analysis with an array size providing a suitable spatial resolution, typically 512 x 512 pixels, a special purpose hardware FFT transformer or a general purpose array processor is required.

This problem of speed may be alleviated to some extent by applying a one-dimensional FFT to an averaged function, a procedure used both in solid mechanics, Kreitlow [1980], Kauffmann [1980], and speckle velocimetry, Meynart [1982].

If I(x,y) is the digitised intensity, and α is the angle of the fringes along the y-axis, and if we assume a digitised spatial resolution of 512 x 512 pixels, with the co-ordinates (255, 255) being the centre of the picture, then a periodic signal, f(m) may be obtained by averaging over the columns of the picture.

$$f(x) = \sum_{y=0}^{511} I[x - (y-255)\tan\alpha, y] \quad 0 \leqslant x \leqslant 511 \qquad (3.20)$$

Fourier processing of this periodic signal produces the frequency of the function density, and hence the displacement vector.

The main advantage of this one-dimensional averaging technique is its rapidity, but it does possess a secondary advantage in the possibility of obtaining an evaluation of the frequency in the case of very low fringe densities by spectral analysis of log f(m).

It is also possible to determine the fringe spacing directly using spatial techniques. The most widely applied of these methods is the averaged auto-correlation technique, as detailed by Ineichen [1980], Meynart [1982],[1983] and Moraitis [1986]. This technique overcomes the main problem of the FFT one-dimensional technique which is that the averaging procedure has to be performed in a direction essentially perpendicular to that of the fringes. Because each line of the picture may be considered as a noisy periodic signal with a variable phase, the automatic determination of the displacement vector can be performed only by averaging over a quantity independent of the phase. The auto-correlation of each line, or its counterpart the power spectrum, satisfies this requirement.

The auto-correlation function is basically a normalised covariance function, and it may be written as:

$$C_{vv}(x'-x) = \frac{\frac{1}{X}\int_{o}^{X} u(x).\ U(x')\ dx}{\sigma_u^2} \qquad (3.21)$$

where X is the number of samples, u(x) and U(x′) are the quantity of interest measured at two discrete places, separated by a distance Δx, and σ_u is the normal distribution of the quantity under consideration. Actually a discrete form of the auto-correlation function is used in digital processing, as one might expect, and this tends to vary slightly depending on the application.

Ineichen [1980] uses the form of the function that is common in strain and other solid deformation applications. In this case the fringe field is averaged perpendicular to and parallel to the fringe direction, and a function defined such that:

$$f(n) = f(\text{perpendicular})_{av} - f(\text{parallel})_{av} \qquad (3.22)$$

This effectively removes any background intensity variations from the required periodic function. The auto-correlation function is then defined as:

$$A(k) = \frac{1}{M} \sum_{n=o}^{M} f(n)\ f(n+k) \qquad (3.23)$$

where M = n=k. A typical auto-correlation function produced in this manner is shown in Fig.(3.17). The fringe separation, g, is then determined directly from A(k) by looking for the last maximum within the first half of the function A(k), and dividing its position kg by the number of maxima between. Hence the displacement vector can be determined.

Meynart [1983] and Moraitis [1986] both use similar forms of the auto-correlation function, and it is applied to the determination of velocity vectors from speckle velocimetry data. The x-velocity component may be computed from:

$$g(u) = \sum_{y=0}^{1,27} \left\{ \frac{\sum_{x} I(x,y).I(x+u,y)}{\sum_{x} I(x,y)^2} \right\} \quad -127 \leqslant u \leqslant 127 \qquad (3.24)$$

In this case the periodicity of the function is determined by utilising a one-dimensional FFT on the function, (although the procedure following by Ineichen [1980] would still be valid in this case). In this way the x-velocity component may be determined. The y-velocity component may be evaluated by computing the averaged auto-correlation of the columns of I(x,y). (In this case x- and y-velocity components are obtained as the auto-correlation function has not necessarily been obtained in a direction perpendicular to the Young's fringes).

Another very simple method for determining the fringe spacing of a series of Young's fringes is detailed by Robinson [1983a] [1983b]. In this case the image data are averaged along a direction parallel to the fringes, producing an averaged one-dimensinal periodic signal. The intensity extrema of this function are then located by determining regions in which intensity gradient changes occur, as detailed in section [3.1.5]. By determining the average distance between extrema the fringe spacing, and hence vector displacement of the system being considered, may be determined.

3.3.3.2. Determination of fringe orientation of Young's fringe system

It is necessary to determine the fringe orientation so that the direction of the translation that has occurred may be determined, this direction being normal to the fringe direction. The fringe orientation may be arrived at directly when using the auto-correlation technique in which the components of the displacement vector are determined. In other methods a separate means of determining this orientation automatically must be devised.

It is possible to measure the fringe orientation physically, as Ineichen [1980] does. In this case the fringe system imaged onto some imaging plane undergoes a rotation by some means, such as a Dove prism, until the fringes are lying normal to one of the image plane axes. The angle of rotation may then be measured directly to give the fringe orientation.

An automatic analysis approach is given by Robinson [1983a] [1983b]. In this case the intensity values along a series of radial vectors passing through the image centre are summed. The vector angle is then varied in small increments over a range of 180°, and the vector giving the greatest summed value is taken as being representative of the fringe orientation. The procedure is repeated iteratively using a smaller angular increment, a smaller angle range and a longer vector, until the best fitting vector is determined to within a limit of ±1°.

3.3.4. Speckle Interferometry

Speckle interferometry is a technique that involves the coherent addition (interference) of a speckle field and a plane reference wave or another speckle field. This technique has a sensitivity comparable to that of holographic interferometry, and it is discussed fully by Vest [1979] and Butler [1976]. Speckle interferometry is used, in the main, for the analysis of vibration modes and surface displacements, although it is also applicable to such studies as mass transfer, Law [1984].

In the analysis of vibration modes the method usually employed is that in which a varying object speckle field is combined with an unvarying reference wave, and this is usually known as conventional Electronic Speckle Pattern Interferometry, or ESPI, Ennos [1969]. As the object under study moves a small distance the relative phase of the two fields changes, thus the irradiance of the speckle pattern varies periodically as the object vibrates axially. If the object undergoes only a slow axial translation the speckle pattern appears to twinkle. This means that the stationary or nodal regions of the surface form a distinct, stationary speckle pattern in the observation plane. The speckle irradiance at other image points however averages out to a relatively uniform value if it is observed visually or recorded photographically with an exposure time greater than the vibrational period. This allows an observer to detect the nodal regions due to their high speckle contrast, the vibrating regions having a low

speckle contrast. In fact it is possible in some cases to observe some fluctuation in speckle contrast over the vibrating region of the surface, and Ek and Molir [1971] have shown that these bands of constant speckle contrast are contours of vibrational amplitude. The major difficulty here is that this contrast modulation is small, and in practice it is dificult to detect more than two consecutive amplitude contours. A better way to detect regions of varying amplitude and phase of vibration is that proposed by Hurden [1981]. This allows the amplitude and relative phase across the surface of a vibrating object to be determined by the use of a modulated reference beam. The reference beam is reflected from a vibrating mirror and the zero-order fringe appears when the phase and the amplitude of vibration of the mirror matches that of a point (x,y) on the surface. The zero-order fringe is about six times brighter than the first-order fringe, and may be shifted over the object surface by an alteration to the vibration mode of the mirror, allowing the amplitude and relative phase of any point on the surface to be determined.

A technique commonly applied for the measurement of normal surface deformations and tilt is that of double exposure speckle interferometry. In this case the interference speckle pattern of the deformed surface is compared with an initial pattern corresponding to the object prior to deformation. If these two patterns are subtracted, regions which have not changed or have moved by some multiple of the wavelength and have thus retained the same speckle intensity give a zero difference signal, and

therefore appear as dark fringes. Regions where the speckle intensity has changed appear as speckle-modulated bright fringes. Thus the dark fringes are contours of constant normal deformation, the relative phase change between the dark fringes being 2π. Full details of this particular technique may be obtained from Nakadate [1980],[1983] and Denby [1976].

The requirements for the automatic analysis of speckle interferograms are very similar to those of classical interferograms, as outlined in section 3.1.5. These are namely, the accurate location of fringe positions by their relative intensity, and when required the accurate assignation of fringe orders. The major difference comes in the fact that due to the speckled nature of the fringes, fringe detection algorithms must work on the basis of local neighbourhood averages, rather than on a purely pixel by pixel approach. Automatic analysis procedures designed specifically for the processing of speckle fringes have been produced by Nakadate [1980] [1983], Hurden [1982] and Button [1985].

The nature of double exposure ESPI makes it particularly suited to analysis by a T.V. based system, the two speckle patterns being subtracted electronically. Such a system is described by Nakadate [1980]. This system gives provision for such non-linear post-processing as level slicing, that is simply the binarisation of the image using an operator defined threshold, and level windowing. In this case a threshold intensity range is defined, and everything outside this range is set to black,

everything inside is set to white. In an improvement on this system, Nakadate [1985], fringe data are accrued with the use of a light pen to make a simple high-speed processor for speckle fringe data.

A typical semi-automatic system for speckle fringe analysis is described by Nakadate [1985] and Hurden [1982]. Standard pre-processing techniques are used to improve the quality of the speckle fringes, such as local average smoothing, binarisation using local threshold techniques, binary shrink/expand operations and median interpolation. An interactive system is then entered, the operator input side taking the form of a light pen, to trace the fringes and assign the relevant fringe order to them.

Two techniques for automatically identifying fringe positions in speckle patterns are set out by Button [1985]. In the first the fringe is located and tracked by a directional averaging algorithm, while in the second thresholding and smoothing operations are performed to produce a line of uniform intensity in the fringes which can then be tracked.

Automatic methods for determining fringe orders in ESPI are covered in some depth by Jones and Wykes [1983]. These methods are very similar to those covered in section [3.1.5].

CHAPTER 4

4. HOLOGRAPHIC INTERFEROMETRY

4.1. INTRODUCTION

Holography is a technique for recording and reconstructing light waves, the wave to be recorded being known as the object wave. To reproduce this object wave it is only necessary to reproduce its complex amplitude, U_O, at one plane in space. Once this has been reproduced the light wave propagating away will be identical to the original object wave.

In 1949 Gabor proposed that a diffraction pattern could be formed, and recorded, on a photographic plate by the addition of a coherent reference wave to the object wave. When the photographic plate is developed and appropriately illuminated it diffracts light in a manner such that the complex amplitude, U_O, is reproduced at the plane of the plate. The object wave is reconstructed by re-illuminating the diffraction pattern formed on the plate with a suitable coherent uniform plane wave, known as the reconstruction wave. This reconstruction wave must be of a form similar to that of the original reference beam. The theory behind this is given in Appendix [A].

The reconstruction procedure gives rise to three separate wave components. A percentage of the reconstruction wave is transmitted through the holographic plate without being affected

by the diffraction pattern. Two other waves are formed by the diffraction of a proportion of the reconstruction wave, that is the original object wave and a complex conjugate "twin-wave" that is observed in the foreground when the image is viewed.

Gabor used an "in-line" holographic technique in which all the elements of the optical system are in-line. This set-up was a constraint introduced by the poor coherence properties of the light sources available to Gabor. It meant that on reconstruction wave forms were visible in line to the observer, leading to low-contrast, noisy images, (Fig.(4.1)).

In 1962 Leith and Upatnieks improved greatly on Gabor's in-line technique, by introducing a spatial carrier frequency by using a separate reference wave which was incident on the photographic plate at an appreciable angle with respect to the object wave. Such a hologram, when illuminated with the original reference beam, produced a pair of images which were separated by a large enough angle from the directly transmitted beam and from each other to ensure that they did not overlap, (Fig.(4.2)).

This off-axis system, along with the recently developed laser which provided a powerful coherent light source for the first time, led to an upsurge of interest in holography. Thus it was only a matter of time before it was realised that if two object waves were recorded on the same plate with the same reference beam, re-illumination of this plate would produce a wave form

corresponding to the superposition of the two recorded object waves. (The theory of superposition is discussed in Chapter 2). If some slight change is introduced between two object waves they will interfere with each other, thus producing a holographic interferogram. This discovery was made almost simultaneously in 1965 by several groups all working independently (Brooks, Heflinger and Wuerker; Burch; Collier Doherty and Pennington; Haines and Hildebrand; Powell and Stetson).

A complete history of the development of holography and holographic interferometry is given by Lockett [1987] and Vest [1979].

4.2. HOLOGRAPHIC INTERFEROMETRY OF PHASE OBJECTS

As can be seen from the theory in Chapter 2, interferometry records the phase difference between two interfering coherent light beams. In the case of the 'infinite fringe background' method, used in the experimental investigations associated with this project, the resulting interferometric fringe pattern is a map of the phase difference between the two interfering beams. This means that each fringe denotes a constant phase difference (see equation (2.17)).

The holographic interferometric technique may be used to investigate transparent test objects because the phase shifts which give rise to an interference pattern may arise due to variations in

the speed of light within the medium, as opposed to a physical change in the pathlength of the light rays. The speed of light through a transparent medium is dependent on the refractive index of the medium, a simple relationship given by:

$$C = \frac{C_o}{n} \qquad (4.1)$$

where C is the speed of light, n is the refractive index of the medium and C_o is the speed of light in vacuo, 2.99776 x 10^8 ms^{-1}. Now the refractive index n, and thus the speed of light, is dependent on the density of the medium, a relationship given by the Gladstone-Dale equation:

$$n - 1 = G\rho \qquad (4.2)$$

where ρ is the gas density and G is the Gladstone-Dale constant which is a property of the gas.

So variations in density of the transparent medium are directly measureable as phase changes between a homogeneous volume of the medium and one in which the density changes. Holographic interferometry produces such a phase change map by comparing two object beams, one which has passed through an undistorted volume of the medium, and one which passes through the same volume of the medium after some density change has taken place. The two methods used to effect this in the present investigation are known as double-exposure and real-time holographic interferometry.

* The image plane technique is disadvantageous in that the angle over which the image can be viewed is limited by the angular aperture of the imaging lens.

4.2.1. Double-exposure holographic interferometry

As the name implies a photographic plate is subjected to two exposures, the state of the test volume being altered between the two exposures. The plate is then processed prior to reconstruction. The optical arrangement used was the conventional one proposed by Horman [1965] but with the addition of an imaging system prior to the holographic plate, thus forming an image-plane interferometer, (Fig.(4.3)). The image-plane holographic interferometer has two major advantages over the conventional type of holographic interferometer. The reduction in image size, with the corresponding increase in the relative light intensity, allows for shorter exposure times. Also the interferograms thus formed may be reconstructed in white light, removing the speckle problems inherent with coherent light reconstructions. This is especially important when automatic processing is to be considered, as the lack of such speckle noise greatly improves the signal-to-noise ratio. *

4.2.2. Real-time holographic interferometry

In this case a single reference exposure is taken, and the holographic plate is then processed and replaced. This replacement is critical, as the plate must be returned to its original position to within one wavelength of the laser light. This is to avoid the introduction of spurious fringes not produced by a phase change in the test medium. This replacement requirement necessitates the use of a kinematic plate holder.

Having replaced the processed plate the test medium is altered, and a series of 'live' fringes then appear on the holographic plate, as the new, ever-changing, object wave interferes with the reference object wave being reconstructed by the reference beam. These fringe systems may then be captured using some dynamic recording medium. Methods used to date have been high-speed film, video and a motor drive single lens reflex camera.

4.2.3. Application of the holographic interferometry technique

Holographic interferograms from two distinct experimental investigations have been considered in this project.

The first of these was the study of forced turbulent convective heat transfer from a series of smooth and distorted geometries. In this case the flow being considered was incompressible, and the density changes occurring in the flow came about due to the air being heated. The ideal gas equation gives the relationship between the temperature and the density at a particular point, that is:

$$P = \rho RT \qquad (4.3)$$

where P is the pressure, assumed constant at ambient pressure, R is the Universal gas constant, and T is the temperature.

In the study of the heat transfer phenomenon both double-exposure and real-time methods were used to investigate

the temperature fields existing above the surfaces. Sample real-time and double-exposure interferograms are shown in (Fig.(4.4)). Real-time interferograms of the temperature field were used for comparison with results obtained from a Large Eddy Simulation, and this aspect is discussed in Chapter 6.

The second experimental investigation concerned a study of the influence of blade incidence upon the flow within low pressure transonic steam turbine blading. In this case the fact that the gas flow, the gas in this case being air, becomes compressible as it is a transonic flow is used to produce a gas density map by holographic interferometry. A double-exposure technique was used to produce the interferograms, an object wave of the cascade containing still air, and one of the cascade section running, being compared.

In regions away from the shocks that occurred when supersonic flows encountered areas of subsonic flow it was possible to assume isentropic flow conditions. From this it was possible to produce both a pressure map, once again using the perfect gas equation, but this time assuming the gas temperature remains at ambient, and a Mach number map by the expression:

$$M = \sqrt{\frac{2}{\gamma-1}} \left(\left(1 - \frac{N\lambda}{\rho_o LC}\right)^{-(\gamma-1)} - 1 \right) \qquad (4.4)$$

A sample interferogram of this sort is given in Fig.(4.5). The results obtained were compared with those obtained using a

two-dimensional viscous compressible flow code known as TURBINS, and this is discussed further in Chapter 7.

4.3. OPTICAL REQUIREMENTS

4.3.1. Optical elements in holographic interferometry

This section details the kind of optical equipment necessary for successful holographic interferometry, the optical layouts used in both the heat transfer and compressible flow investigations being shown in (Figs.(4.3) and (4.6)).

(i) Optical Table: there is a stability requirement of a quarter of a wavelength of the laser light source being used for a successful holographic exposure. Hence the optical components must be mounted on an optical table that consists of a large mass supported on some form of vibration dampers. This arrangement prevents any structure-borne vibrations from the floor affecting the optical layout over the exposure time.

(ii) Optical component bases: these are either massive, magnetic or possessed of a screw-thread compatible with a series of tapped holes in the surface of the optical table. These bases allow for a rigid fixing of the optical components, preventing vibration of the components.

(iii) **Laser:** for the heat transfer investigation a 3-Watt spectra physics 2020 Argon-Ion laser was used, providing a wavelength of 514.5 nm, and a 20 m coherence length in a single mode.

In the compressible flow investigation a double-pulsed ruby laser was used, supplying a wavelength of 694.3 nm.

(iv) **Beam splitter:** a beam splitter is used to provide a reference beam and an object beam from the single laser beam. An object to reference beam intensity ratio of approximately 6 : 1 is used to form a holographic interferogram.

(v) **Half-wave plates:** these allow control of the polarisation of the light beam. This allows a matching of the polarisation planes at the holographic plate.

(vi) **Spatial filters:** these are used to expand the laser beams, and consist of a microscope objective followed by a pin-hole. The microscope objective expands the light beam, and the pin-hole then cleans it up, by removing unwanted diffraction effects introduced by dust particles and poor quality mirrors.

(vii) **Front-surfaced mirrors:** these are used to steer the laser beams, and in the heat transfer study a Schlieren mirror was used to provide the collimated beam that passed through the test volume. The mirrors are front surfaced to avoid the possible formation of diffraction patterns caused by the light beam reflecting through an initial layer of glass.

(viii) **Plateholder:** a kinematic plateholder is used to hold the photographic plate. Such a plateholder contains four points that touch the plate, thus allowing the plane of the plate to be defined exactly. This is particularly necessary for real-time holographic interferometry.

(ix) **Holographic plates:** glass flats with a standard halide in gelatin photographic emulsion on one side are used. The plate side with the emulsion on it is faced towards the oncoming object beam during the exposure times.

(x) **Shutter:** in the thermal study the exposure times for the double exposure work were controlled by means of a manually operated shutter. The compressible flow study made use of a double-pulsed ruby laser to provide the exposure control.

One of the big advantages with holographic interferometry is that because the two object waves traverse the same optical path, aberrations due to poor optical quality of the optical components are cancelled out. Thus the requirements for optical quality are very much less stringent than with other interferometric techniques.

4.3.2. Processing procedure for the holographic plate

The holographic plate is processed using a standard photographic procedure. Silver halide photographic emulsion

plates are used, the plates being sensitised to a certain frequency bandwidth. Thus the type of plate used is dependent on the wavelength of the laser being used. Also the emulsion must be capable of resolving fringe frequencies comensurate with those forming the diffraction pattern produced at the plane of the plate by the interference of the reference and the object beams. This frequency is dependent upon the offset angle of the reference beam, θ, and is determined by:

$$n = \frac{\sin\theta}{\lambda} \qquad (4.5)$$

where n is the number of lines per mm and λ is the laser wavelength. A typical holographic plate resolution (Agfa 8E56) is in excess of 5000 lines per mm and easily meets this requirement.

A typical processing routine, used for developing the heat transfer holographic interferograms, is as follows:

(i) the plate is developed in a suitable developer (Ilford autophen) for four minutes.
(ii) the plate is washed in running water for five minutes.
(iii) the plate is then fixed with a suitable fixer (Agfa Gevaert GP43l) for three minutes.
(iv) the plate is then washed in running water for fifteen minutes.

The final stage of this process is to bleach the plate, using a dilute bleach such as ferric nitrate. The plate is bleached until

it becomes clear, and then for an extra minute. By bleaching the hologram, amplitude, or intensity, information is lost, and a phase hologram is formed. The advantage of this is that the diffraction efficiency is increased from around 4% to as high as 75%. This greatly increases the ease with which white light reconstructions may be made, and increases the signal-to-noise ratio of the reconstruction.

After bleaching there is a final wash in a solution containing a surface-tension reducing agent. The plate is then air-dried.

4.3.3. Reconstruction of the holographic interferograms

It was possible to reconstruct the image-plane double exposure interferograms using a point white-light source. The major requirement for this white-light source is that the beam incident on the holographic plate strikes at the same angle as the original reference beam. A typical reconstruction geometry is shown in (Fig. 4.7)).

Two methods of acquiring the reconstructed fringe-fields were then used. In the case of the compressible flow investigation and for the rib distorted geometries in the heat transfer study, the fringe-fields were acquired directly from the holographic plate. This is the preferable method removing the need for an intermediate stage of photography that is likely to introduce errors of some kind. It also allows use of the very good

resolution of the holographic interferograms for magnified views, which were necessary in most cases. The image acquisition was by means of a two-dimensional charge-couple device camera (C.C.D.-camera).

For the early work in the heat transfer study, investigating the undistorted surface, a 2-D C.C.D. camera was not available. In this case the interferogram was reconstructed and then photographed. For magnified views of the boundary layer the holographic plate was reconstructed on a Vickers projection microscope. This avoided the problem of granularity obtained when blowing up a portion of a photograph. The photographs obtained were then scanned photo-mechanically by a one-dimensional C.C.D.-array camera for the purposes of digital image analysis, as described in Chapter 6.

For the real-time work it was necessary to view the holographic plate in situ, and to record the fringe systems using some dynamic recording medium. The fringe fields obtained were projected onto a screen, and either a single lens reflex camera taking a series of 35 mm stills, a video camera or a high-speed film used to record the fringe systems.

4.4. EXPERIMENTAL ANALYSIS

4.4.1. Heat Transfer study

A schematic diagram of the wind-tunnel can be seen in (Fig.(1.1)). The air flow was supplied by a Fischbach centrifugal

fan, type D770, regulated by a variable resistor controlling the power to the fan motor. The fan discharges into a large plenum, or settling box, via a diffuser. Air then enters the settling section of the tunnel from the plenum by means of a shaped inlet section, and then passed through a honeycomb situated at the start of the settling section to remove any 'swirl'. This seemingly contorted system of supplying air to the wind-tunnel was found to be necessary to provide symmetrical velocity profiles in the horizontal and vertical planes of the wind-tunnel.

The tunnel itself has a rectangular cross-section of hydraulic diameter 0.12 m, and aspect ratio 4 : 1. An aspect ratio of 4 : 1 was chosen for the tunnel as previous studies (Beavers, Sparrow and Lloyd [1971]) indicated that this was close to the limit for the two-dimensional flow assumption. The tunnel had to be as narrow (spanwise) as possible to minimise refraction errors (section [4.5.2]), whilst maintaining this two-dimensionality. The initial settling section is 20 hydraulic diameters in length to allow for a reasonably full development of the hydrodynamic boundary layer. The working section is 4 hydraulic diameters in length, and has float glass sides and upper walls. The lower wall is made up of the stainless steel heated plate under test. The plate is heated by electrical resistance heaters, and thermocouples are set ½ mm from the flat surface of the plate to provide an estimate of the surface temperature.

An exit section 3.9 hydraulic diameters long ends the tunnel. It was possible to obtain flow regimes extending from transitional to fully turbulent. Four rib-roughened base-plate geometries were studied, and these are shown in Fig.(1.3). Initially a flat stainless steel base-plate was used for proving tests, much data existing for this particular geometry. Having successfully proved both the tunnel and the holographic interferometry technique, the four rib-roughened geometries were then studied.

Firstly 7.95 mm square ribs, (Fig.(4.9a)) were attached along the entire length of the tunnel, at a pitch to height ratio of 7.2 : 1. Mild steel ribs were used for the development and exit sections, whilst stainless steel ribs were employed through the working section. The ribs on the heated base plate were attached using a thermocouple cement to ensure a good thermal contact between the ribs and the base plate. The other ribs were attached using a cyanoacrylate adhesive.

Secondly, rounded ribs were studied, (Fig.(4.9b)), the old heated base being replaced by a similar one with rounded ribs machined onto it. These ribs represented an eroded version of the original square ribs.

Lastly, a casting rubber compound was used to simulate a deposition on both the square-rib geometry, (Fig.(4.9c)), and the rounded rib geometry, (Fig.(4.9d)). This deposition simulated that found on some A.G.R. fuel pins, Mantle [1986].

Sample double-exposure interferograms of all the surfaces studied may be found in (Figs.(4.4) and (4.5)).

Full details of the experimental investigation may be found from Lockett [1987].

4.4.2. Compressible flow study

The experimental investigation in the compressible flow study was carried out at Marchwood Engineering Laboratories on an incidence cascade rig designed specifically for the investigation of off-design incidence effects on low pressure final stage tip section blading.

The cascade comprises seven blades, (Fig.(4.10)), at a stagger angle of 62.6 degrees; the span and chord being 0.095 m and 0.04 m respectively. The blade sections are thin and of low camber, with a thickness to chord ratio of approximately $^1/_{16}$ and a camber angle of 13 degrees. The end walls of the cascade are manufactured in optical quality glass to facilitate optical measurements within the blade passages. The central blade passes through flexible seals in the end wall windows and is then attached at each end to Kistler load cells, which measure the aerodynamic forces on the blade. Extending approximately 20 chords upstream of the blade row, the cascade inlet has moveable side walls, hinged at their downstream ends, to allow the approach flow angle to be adjusted to give blade metal incidence angles

continuously variable over the range ±25 degrees. Variable-area suction slots are installed in the side walls immediately upstream of the blade row to remove the side wall boundary layer. The inlet entrance is flared and is open to the atmosphere. Downstream of the blade row, the tailboard is of the porous type in order to minimise shock reflections. The cascade is connected via a fast acting flap valve to a vacuum vessel with a volume of approximately 45 m^3, which may be evacuated to an initial pressure of 0.25 atmospheres.

On opening the flap valve a stable flow is established through the cascade within 0.5 seconds, and is maintained for approximately 5 seconds, the exact duration being a function of inlet incidence. The blade approach flow is subsonic and passage Mach numbers typically rise to 1.3 ahead of the suction side trailing edge shock.

It should be noted that in the double-exposure holographic interferograms taken, (Fig.(4.5)), the blade profiles are not themselves visible. This is due to the shadow cast by the blade mounts on each wall, which for the upper and lower three blades take the form of a long rectangle with rounded ends. The large central shadow is due to the flexible end seals and Kistler load cells attached to the ends of the central blade. These shadows meant that observations could not be made around the surface of the blades, but as this area would suffer from diffraction effects this loss of information was deemed negligible.

4.5. ANALYSIS OF HOLOGRAPHIC INTERFEROGRAMS

4.5.1. General Analysis

In the analysis of infinite fringe holographic interferograms the quantity of primary interest is the optical pathlength, Φ, of a ray through the medium. This is defined as:

$$\Phi = \int n ds \tag{4.6}$$

which is the path integral of the refracting index, n, along the ray path, s. When refraction is negligible, rays remain straight lines and the path integral becomes a line integral. If the ray is parallel to the z-axis ds is replaced by dz, and so:

$$\Phi(x,y) = \int n(x,y,z)dz \tag{4.7}$$

In this refractionless limit the effect of passing through the medium is a change of phase relative to that of a light ray traversing the same straight path in a homogeneous medium, thus:

$$\Delta\Phi(x,y) = \int[n_{ref} - n(x,y,z)]dz \tag{4.8}$$

where n_{ref} is the refractive index of the homogeneous or reference medium state, and n(x,y,z) is the refractive index of the changed medium. It can be seen that $\Delta\Phi$ is the phase difference given in equation (2.17) for infinite fringe interferometry,

$$I(\bar{v}) = a_1^2 + a_2^2 + 2a_1a_2 \cos(\Psi_2(\bar{v}) - \Psi_1(\bar{v}))$$

The equation of a bright fringe is given by:

$$\Delta\Phi(x,y) = \int[n_{ref} - n(x,y,z)]dz = N\lambda \qquad (4.9)$$

where N is an integer. The evaluation of an interferogram consists of determining $\Delta\Phi$ from the fringe pattern and then inverting equation (4.9) to calculate $[n_{ref} - n(x,y,z)]$. This quantity may then be related to other physical properties for various applications.

It is possible to measure $\Delta\Phi$ directly in units of wavelength λ by assigning order numbers to the fringes. The number N = 0 is assigned to the bright fringe occupying the undisturbed region of the medium. The centres of all subsequent bright fringes are assigned the numbers 1,2,3...consecutively. The centres of all dark fringes are assigned numbers N = 0.5, 1.5, 2.5..... There is a sign ambiguity in fringe order numbers which arises because $+\Delta\Phi$ and $-\Delta\Phi$ yield identical fringe patterns. This necessitates *a priori* knowledge of the likely refractive index distribution for correct fringe ordering.

Once $\Delta\Phi$ has been evaluated for an interferogram, equation (4.9) must be inverted to obtain $[n_{ref} - n(x,y,z)]$. The ease with which this inversion can be accomplished depends, in increasing order of difficulty, on whether:

(i) a two-dimensional phase object is being studied, that is an object with no variation of refractive index along one axis.

(ii) a radially symmetric phase object is being studied.

(iii) an asymmetric phase object is being studied.

The test sections used in both the heat transfer study and the compressible flow study are so designed that the transparent medium may be considered a two-dimensional phase object, with no variation of refractive index in the spanwise, or z, direction. This assumption is not strictly accurate because end effects cause some variation in the refractive index distribution at both sides of the test section. The effect of these end effects is to cause a blurring of the observed fringes, due to spanwise averaging across the test section. This problem of spanwise averaging was much more apparent in the heat transfer interferograms than in the compressible flow interferograms, but in both cases is essentially negligible. An estimate of the error introduced by such end-effects is given in Appendix [B].

With a consideration of a two-dimensional phase object, the change of refractive index is a function of x and y only, so equation (4.9) becomes:

$$N\Lambda = \int_0^L [n_{ref} - n(x,y)]dz \qquad (4.10)$$

So,

$$N\lambda = [n_{ref} - n(x,y)]L \qquad (4.11)$$

where L is the width of the test section.

Now the refractive index of the medium is related to its density by the Gladstone-Dale equation given in (4.2).

Substituting this into equation (4.11) and re-arranging:

$$\rho_{ref} - \rho(x,y) = N(x,y)\lambda/GL \qquad (4.12)$$

This equation is the starting point for the various quantitative applications for holographic interferometry of phase objects.

4.5.2. Quantitative analysis of heat transfer interferograms

In the heat transfer investigation the air flow may be considered incompressible, and the perfect gas equation may be used to relate density and temperature at a constant pressure. The perfect gas equation is given by:

$$P = \rho RT \qquad (4.13)$$

where the symbols have their standard meaning.

Thus:

$$\rho_{ref} = \frac{P_{ref}}{RT_{ref}} \qquad (4.14)$$

and

$$\rho(x,y) = \frac{P_{ref}}{RT(x,y)} \tag{4.15}$$

Substituting equation (4.14) and (4.15) into equation (4.12) and re-arranging, the expression obtained is:

$$T(x,y) = T_{ref}\left[1 - \frac{N\lambda}{\rho_{ref}GL}\right]^{-1} \tag{4.16}$$

This is very similar to the equation of interferometry given by Hauf and Grigull [1970] for an incompressible two-dimensional boundary layer:

$$T(x,y) = T_{ref}\left[1 - \frac{N\lambda C\ell_i}{G\rho_{ref}L}\right]^{-1} \tag{4.17}$$

The extra term here, $C\ell_i$, is a correction factor for refraction errors; that is additional phase changes introduced by the deviation of the measured ray path from the ideal one parallel to the heated surface due to refraction.

These refraction errors may be determined, up to the limit after which ray crossing occurs, by using an iterative ray-tracing technique due to Walklate [1981].

The correction factor $C\ell_i$ is determined from the equation:

$$C\ell_i = L\left[T(x,y)_{z=0} \int \frac{d\Phi}{T(x,y)}\right]^{-1}\Bigg|_{i-1} \tag{4.18}$$

with i-1 denoting the position in the iterative procedure that the estimate has been made.

The actual ray path, $\Phi(x,y)$, can be traced by utilising standard refraction theory:

$$\left.\frac{d^2y}{dz^2}\right|_{z,y} = \frac{1}{n}\left.\frac{dn}{dy}\right|_{z,y} = \left[\frac{-G\rho_{ref}}{(T/T_{ref}+G\rho_{ref})T}\right]\left.\frac{dT}{dy}\right|_{z,y} \qquad (4.19)$$

The following Taylor series expansions are used to perform the integration, assuming that Δz is small when compared to the plate width L:

$$\left.\frac{dy}{dz}\right|_{z+\Delta z} = \left.\frac{dy}{dz}\right|_{z} + \Delta z \left.\frac{d^2y}{dz^2}\right|_{z} \qquad (4.20)$$

$$\left.y\right|_{z+\Delta z} = \left.y\right|_{z} + \Delta z \left.\frac{dy}{dz}\right|_{z} + \frac{\Delta z^2}{z}\left.\frac{d^2y}{dz^2}\right|_{z} \qquad (4.21)$$

Initially $C\ell_i$ is set to unity, and the values used are:

$$\left.\frac{dy}{dz}\right|_{z=o} = 0 \qquad (4.22)$$

$$\left.y\right|_{z=o} = \text{measured displacement of the fringe from the wall} \qquad (4.23)$$

Consecutive iterations are then performed until the values obtained for $C\ell_i$ converge to a correct value.

Hence the temperature field existing above the plate may be determined. Wall temperatures may then be estimated by fitting a curve to the line temperature distributions above the plate, and the near wall temperature gradient may be determined. The heat flux in the near wall region may then be determined by assuming that the laminar sublayer heat transfer takes place by conduction only. Heat transfer coefficients and local Nusselt numbers may then be determined using the standard relationship:

$$Nu = \frac{h_c De}{k} = \frac{q_{wall} De}{(T_{wall} - T_{ref})k} \qquad (4.24)$$

where h_c is the heat transfer coefficient, k is the thermal conductivity of the air, and q_{wall} is the local heat flux at the wall. De is the hydraulic diameter of the wind-tunnel.

4.5.3. Quantitative analysis of compressible flow interferograms

The fringe interpretation presented here is that put forward by Bryanston-Cross [1980], who in turn used the theory presented by Sinclair [1978].

From equation (4.12) it is possible to determine the existing density distribution due to compressible flow effects:

$$\rho(x,y) = \rho_t - N(x,y)\lambda/GL \qquad (4.25)$$

where ρ_t is the stagnation density.

This equation is only applicable to regions of the flow that may be considered isentropic, that is regions away from shock waves.

Having determined the density field it is possible to determine the local Mach number distribution from the equation:

$$\rho = \rho_t \left[1 - \frac{\gamma-1}{2} M^2\right]^{-\frac{1}{\gamma-1}} \qquad (4.26)$$

where M is the Mach number, and γ is the ratio of specific heats.

If, as in this case, the experimental fluid is air, $\gamma = 1.4$, and the Mach number becomes:

$$M = \sqrt{5\left(1 - \frac{N}{102.8}\right)^{-0.4} - 1} \qquad (4.27)$$

CHAPTER 5

5. DATA PREPARATION AND IMAGE ENHANCEMENT

5.1. INTRODUCTION

Before a fringe system may be analysed automatically a certain amount of data pre-processing is usually needed. This pre-processing may conveniently be divided into two categories.

The first of these is data preparation, in which the fringe field data are formatted to allow the use of the fringe analysis routines. This data preparation stage includes such things as masking off physical objects appearing in the fringe field; defining the boundaries of the fringe field if necessary; and defining common points for location and scaling purposes if for any reason a magnified portion of the fringe field has to be analysed separately and then merged into the fringe data.

The second category is that of image enhancement. This stage is necessary because the conversion of an image from one form to another, such as by digitisation, often leads to a loss in quality of the output image when compared to the input image. Image enhancement techniques attempt to improve the quality of this output image and make it more amenable to automatic analysis. It should be noted that with image enhancement processes the aim is not necessarily to improve the fidelity of the image with regard to some ideal form of the image. No attempt is made to estimate any degradation effect and use this estimate to correct the image data, such techniques coming under the provenance of image

restoration methods. Certain general properties of picture degradation are taken into account however in the pursuit of enhancement techniques. Contrast enhancement techniques are used as degradation usually distorts the picture signal: edge sharpening is reasonable as degradation usually blurs an image and finally smoothing is necessary as degradation usually introduces noise, and the original image may be assumed to have been smooth.

Finally it should be said that there is no general unifying theory of image enhancement at present because there is no general standard of image quality that can serve as a design criterion for an image enhancement processor. Thus in practical situations it is necessary to experiment extensively to find an effective enhancement technique, and very often this has to be a "tunable" method whose parameters may vary from place to place in the image data.

The image enhancement techniques used to try to improve the quality of the fringe field data prior to quantitative analysis are all based on standard enhancement techniques, and so a relevant bibliography is included to cover both the unreferenced section of this chapter, and to allow the reader to explore techniques not used by the author.

5.2. DATA PREPARATION

5.2.1. Masking techniques

In most fringe field analysis situations it is necessary to define the extremities of the fringe field so that the fringe analysis routines may recognise the boundaries within which they must operate. It may also be necessary to mask off physical objects obtruding in the flow field, so that the fringe analysis routines may ignore them.

In the thermal field studies a means of masking off the rib-roughened geometries was required, allowing the plate surface position to be defined by the following routines.

With the compressible flow studies it was necessary to mask off the cascade section edges, thus defining the extent of the fringe field, and also to mask off the blade sections that occurred in the image under study.

In both cases several means of doing this presented themselves. The first was a segmentation technique, the regions to be masked being detected purely by their grey-level. Such a method was inapplicable in this case, as the regions to be masked off did not occupy a distinct grey-level range.

Secondly, some form of boundary tracing algorithm was considered, which having been positioned at one boundary point of

the region to be masked would define the necessary boundary automatically. Many such boundary tracking algorithms exist, Pratt [1978] p.543, Castleman [1979], p.311, and they usually work on some maximal gradient principle. However, they are very sensitive to noise, and even a small amount of noise can send the tracking temporarily or hopelessly off the boundary. Even though noise effects can be reduced before implementation of the tracking routine, closed boundaries cannot be guaranteed, and there is still a possibility of the tracking algorithm getting lost and running off the border of the image. The final prognosis is that gradient tracking bugs are usually useful only in extremely low-noise images or where some form of operator intervention is possible to correct possible derailments. They also suffer from being computationally expensive to implement.

A template matching scheme was also considered, a replica of the object to be masked being compared with all the objects in the image field. This method was also inapplicable as it necessitates the segmentation of the whole image field. Also the objects present in the image field are not consistent. For instance, in the compressible flow study a whole blade section might have been visible, or any portion of this blade, and so a blade template wouldn't necessarily match up with the blade portions visible.

The masking solution adopted for both the heat transfer study and the compressible flow study was as follows.

Initially the image data were purged of all the grey-level values consistent with that which was to be assigned as the unique masking value. All further routines were designed so as to ignore this value, and in the case of the enhancement routines to prevent this unique value recurring.

An edges routine was then implemented. This routine was used to mask off any portions of the fringe field boundaries that could be defined by straight lines, such as the cascade section limits in the compressible flow study case. An operator controlled cursor was used to define the start and end points of the straight-line section, and the direction to be masked off was then specified. A whole series of such straight-line sections could be specified before masking commenced, the unique masking grey-level value being assigned everywhere between the straight-line sections and the image boundaries.

The next stage was to mask off the more complicated shapes appearing in the fringe field. In the compressible flow study this necessitated the masking off of the blades and parts of blades in the flow field. In the heat transfer study it was the rib-roughened geometries that had to be masked off. A similar procedure was followed in both cases. The basic geometry of the shape was written into a file, along with a separate list of the basic geometric descriptors, that is, separate easily definable points in the geometry. On the image data itself a cursor was used to locate the geometric descriptor points necessary, and by

comparing this with those in the data file it was possible to get the scale, orientation and position of the region to be masked. Masking was then performed in a region defined by the basic geometry stored in the data file, the grey-level values in this region being changed to the unique grey-level.

For instance, with the blade shape in the compressible flow study, the basic geometry was a rectangle with a semi-circle positioned at each end. The geometric descriptors were the length, width and angular orientation of the blade. The cursor defined points necessary on the image data for the first blade were two on the upper surface to describe the angular orientation, one on the lower surface which combined with one of the upper surface points gave the blade thickness, and one point at one end of the blade end points to describe the blade position. Subsequent blades needed only one cursor point on the blade end to describe the blade position, the previously obtained data being used for a complete description.

A similar procedure was used to describe the ribs in the heat transfer study. Examples of typically masked images may be seen in (Fig.(5.1)) and flow charts describing the masking procedures in (Fig.(5.2)).

5.2.2. Common point description for resolution considerations

This is often a necessary procedure in fringe field analysis, as common points are needed to merge separate image data together,

or to merge into a set of image data the results from a magnified sub-set of the data. In the compressible flow study it was found necessary on occasion to merge four sets of frame data together to obtain the necessary image resolution to successfuly analyse one complete blade passage, a criterion taken as the minimum necessary for useful quantitative data to be extracted. In the heat transfer study it was found necessary to merge magnified portions of the near wall region into the full field image set, as the resolution of the system did not allow for the successful digitisation of all the fringes in a full field shot. The selection of common points for the successful application of the merging techniques is a data pre-processing aspect, and so is included here. Different methods were used in the compressible flow and heat transfer studies, and they will be detailed separately.

5.2.2.1. Compressible flow study

There was a minimum resolution requirement of two pixels per fringe for the automatic analysis to be performed successfully. This criterion excluded regions of shock where the spacing could be ignored, the fringe frequency naturally being much higher in these regions. This criterion had to be balanced against the fact that a minimum of one blade passage had to be analysed to provide meaningful data, and on occasion these two requirements proved to be mutually exclusive. This necessitated the development of an expanded picture-store in the hard disk of the computer.

Basically four quarters of one blown-up blade passage could be grabbed independently by the frame-grabber, and then merged together to form one 1024 x 1024 x 8 bit data file. The separate image data was written to this file as a series of 1-byte strings, and the absolute co-ordinates necessary for a successful merging were supplied by the introduction of an array of fiducial marks before each image was grabbed. Each one of the images to be merged contained at least one fiducial mark common to the other three.

An example of an image with an overlaid series of fiducial marks can be seen in (Fig.(5.3)). The fiducial marks had to be removed and replaced between grabbing images, but it was found possible to replace them very accurately by using a kinematic plate holder to hold the plate on which the fiducial marks were drawn.

With the use of suitable subroutines it was possible to make the extended picture file act very much like a framestore, although the time taken to perform operations was increased due to the fact that the data were accessed from a hard disk.

It is readily apparent that the amount of data viewable on the monitor was still limited to a 512 x 512 x 8 bit image, but a windowing routine was written that allowed the operator to select a window from any part of the image file for viewing purposes.

5.2.2.2. Heat transfer study

In the heat transfer study it was found that when a full-field image was digitised the high frequency near wall fringes could not always be resolved. This meant that the near wall regions had to be digitised separately at a higher magnification, analysed and then merged back into the full-field data.

To do this a pair of common points is selected from a full-field image and a magnified image by means of a cursor. To define the pair of points in each image an easily recognisable feature must be used, typically some portion of one of the rib geometries. Using these common point pairs, it is then possible to determine the relevant scale and position of the magnified image data with respect to the full-field image data. This allows the successful merging of the analysed data.

5.3. IMAGE ENHANCEMENT

After the image data has been masked, it is often necessary to apply certain image enhancement techniques to try to make the fringe data more tractable to the image analysis routines. To do this image enhancement menus were incorporated into both the heat transfer and compressible flow systems. In both cases the menu elements were common, but the heat transfer menu was much more comprehensive than that used in the compressible flow system. This was because there was less control over the

digitisation step of the image acquisition process due to the equipment available, and also the holographic inteferograms were of poorer quality than the compressible flow interferograms. Thus a greater degree of enhancement was required for the heat transfer fringe systems.

The menus available in both cases were:

Compressible flow system	Heat transfer system
(i) Contrast enhancement by linear histogram stretch [G]	(i) Low-pass filtering (smoothing) [G/L]
(ii) Low-pass filtering (smoothing)	(ii) High-pass filtering (edge crispening) [G/L]
(iii) High-pass filtering (edge crispening [G/L]	(iii) Histogram stretch |contrast (iv) Histogram equalise |enhance- | ment (v) Histogram split | [G]
	(vi) Intensity equalise [G]
	(vii) Median filter, cross neighbourhood [G/L]
	(viii) Laplacian edge-detection [G]
	(ix) Sobel edge-detection [G]

The letters after the enhancement routine name indicate whether the routine is applicable only globally [G] or globally and locally [G/L]. Local operations take place within an operator defined window, a cursor specifying the top-left and bottom-right corners of the window. Only the data occurring within the window is then operated on by the enhancement routine. Global operations obviously affect all the image data.

All the enhancement routines are written so that they will ignore the masked regions, and so that they will not allow the unique grey-level defining the masked regions of the fringe field to reappear in the fringe-field data itself.

A description of the image enhancement algorithms, and the problems that they are designed to overcome, is now given.

5.3.1. Contrast Enhancement of the Grey-levels

The digital imaging systems used are capable of resolving to 8 bits, or 255 separate grey-levels. It should be noted that this is the spectral resolution, as opposed to the spatial resolution mentioned in the section on defining common points. Black is set as the 0 grey-level and white as the 255 grey-level, and the rest of the grey-levels are linearly distributed between these two extremes.

Although most modern imaging systems are capable of automatic adjustment so that the image being digitised occupies the full dynamic range, the presence of high and low intensity noise often means that the actual grey-levels carrying image information form a sub-set of the digitised grey-levels. Contrast enhancement techniques attempt to redistribute these grey-levels over the whole dynamic range, and thereby increase the image quality. This is usually done by manipulating the grey-level histogram, which provides a record of the grey-level distribution over the dynamic range. Three forms of histogram manipulation have been used.

(i) Linear histogram stretch

The image histogram is studied and the limiting values defining the grey-scale range of interest, b_{Hi} and b_{Lo}, are determined. These values are defined by the operator, who specifies that a certain percentage of the pixels must be set to black, and a certain percentage of pixels to white. The remaining grey-scale levels are then linearly scaled to cover the complete grey-scale range from 0 to 255. The results of such an operation are shown in (Fig.(5.4)).

(ii) Histogram equalisation

It is possible to force the histogram to some desired form to achieve the desired rescaling of the image grey-levels. More effective use of the available grey-scale can be made by equalising the histogram, Andrews [1972] and Hall [1971], [1974], where:

$$F(i) = \text{Min}(255, \left[\sum_{j \leqslant i} H(j) :: \frac{256}{N}\right]) \qquad (5.1)$$

N is the total number of pixels in the image, the square brackets stand for the operation of taking the largest integer less than or equal to the enclosed expression, and a 256 level grey scale is assumed (0→255).

The effect of equalisation is to flatten the histogram in the sense of making the cumulative histogram:

$$C(i) = \sum_{j \leqslant i} H(i) \qquad (5.2)$$

as close as possible to the line, C(i) = i x N/255. It is also possible to force the histogram to adopt an exponential or hyperbolic form. Such a procedure was first suggested by Frei [1977] as a means of accounting for the eye's logarithmic intensity response, but the complications involved make this technique undesirable.

An example of histogram equalisation is shown in (Fig.(5.5)).

(iii) Histogram split

It was noticed that the grey-level histogram often took on a bimodular, or double peaked, form. From this observation a technique was developed that split these two peaks in the middle, the peaks then being redistributed to either end of the grey-scale range. A typical example of such an operation is shown in (Fig.(5.6)).

Although these techniques for contrast enhancement can prove very beneficial as increasing the contrast between the fringes maximum and minimum grey-level values greatly aids the fringe detection algorithms, care should be taken with their usage. This is because artificial contouring may be introduced into the fringe field data by sudden grey-level discontinuities. For this reason the image data should be checked by taking intensity distribution plots across the fringe-field, and thereby ensuring that the magnitude of such introduced contouring is small compared to the sinusoidal variation of the fringes.

5.3.2. Noise cleaning

Noise, that is contributions to the image which do not convey information about the scene in front of the imaging system, can greatly affect the quality of the digitised data.

Two categories of noise can be defined: fixed and random, or stochastic, noise. Fixed noise is due, typically, to imperfections in the image sensing device. In the use of charge couple device cameras (C.C.D.-cameras) this takes the form of an uneven response from the individual charge couple device in the array. It is possible to correct such imperfections by acquiring an image of a scene of constant luminance intensity, and using any variations obtained across the digitised image as correction factors for following images obtained by the same camera. However such an error can usually be ignored. For a two-dimensional C.C.D. camera of dimensions 320 x 512 a local sensitivity variation of less than 5% (Müller et al. [1979]) is expected, and the necessary correction may be made at the image enhancment stage.

The most important causes of random noise are:

i) Electrical noise due to power supply variations and electro-magnetic induction in the cables. The distribution of this noise depends on the environment. It can be modelled as a Poisson process with mean varying across the picture due to shielding from the camera enclosure and inhomogeneity in the ambient radiation field.

(ii) The output of a photoelectric sensor exhibits fluctuations due to the quantum nature of light and the discrete character of charge conduction (short noise and generation-recombination noise). At low light levels the detected intensity has a Poisson distribution and at higher intensities this is nearly Gaussian with equal mean and variance.

(iii) Quantisation noise, this is the error involved in approximating a continuous quantity, image luminance, by its sampled values on a discrete lattice and in representing the sampled values by a finite set of grey-levels.

(iv) Grain noise, this can be a problem if magnified portions of a fringe field photograph are digitised, the granular nature of the exposed emulsion producing a multiplicative form of noise. To a large extent this possible source can be ignored in this study, as the majority of the image data is taken directly from the holographic plate.

(v) Speckle noise, the use of a coherent reconstruction beam necessarily leads to problems with speckle noise. Such laser speckle is caused by underlying secondary interference effects, and gives a 'pepper-and-salt' appearance to the image data. The use of an image-plane interferometric set-up allows a white light

reconstruction beam to be used in the case of double-exposure interferograms, thus avoiding the speckle problem. However there is no avoiding it in the real-time case.

(vi) Processing noise, this is noise introduced onto the holographic plate during the processing stage, and includes such things as finger-prints, scratches and water stains. Such additional noise can be avoided by careful treatment of the plate, both during processing and storage.

Such stochastic noise may usually be modelled as the addition to the picture signal of a random component with finite variance, Hill et al. [1977]. This noise may be interpreted as high-frequency components of the image frequency spectrum due to the rapid local variations in contrast that it represents, i.e. due to its spatial decorrelatedness. This property of the noise component is used by techniques that attempt to relieve or ameliorate the effect of the noise component.

A measure of the noise content in an image is the signal-to-noise ratio, SNR, defined as,

$$\text{SNR} = \frac{\text{RMS fluctuations in the signal}}{\text{RMS fluctuations of the noise}} \qquad (5.3)$$

where RMS stands for Root Mean Square value.

It is the task of the noise smoothing techniques to produce as large an SNR as possible.

(i) Spatial Filtering

Low-pass spatial filtering may be used to reduce the noise content in an image, making use of the fact that this noise component, as mentioned previously, is found in the high frequency end of the image frequency spectrum.

The technique used was based on the formulation of a linear system like a convolution equation,

$$F_2(m_1,m_2) = \sum_{n_1} \sum_{n_2} F_1(n_1,n_2)\ H(m_1-n_1+1, m_2-n_2+1) \qquad (5.4)$$

where F_2 is an output array formed by the discrete convolution of the input array F_1 with the convolution operator H. $H(m_1-n_1+1,m_2-n_2+1)$ is defined as the kernel of the convolution operator, and it possesses constant values, the coefficients of the kernel being characterised by the weighting that it is desired to give to the averaging process. The kernel is normalised to unit weighting so that the noise-clearing operation does not introduce a brightness bias in the processed image.

Typical kernel forms that have been used are shown in (Fig.(5.7)), along with their results on an intensity distribution plot across a typical fringe field.

It should be noted here that if the required kernel becomes large in order to achieve adequate noise clearing, it may be computationally more efficient to perform the convolution operation indirectly using the Fourier techniques put forward in Appendix [C]. The advantage of this is that a spatial convolution is transposed to a product in the frequency domain. The effect of noise smoothing is then realised by the attenuation of high frequencies, corresponding to an integration in the spatial domain.

(ii) Median Filtering

The low-pass filtering methods work by attenuating the high frequency components in the image frequency spectrum. Unfortunately these same high frequency components contain useful information such as edge and surface texture information which is also characterised by rapid changes in luminance value. Thus the result of these techniques is to blur the image, in fact a slightly defocussed image can be said to have undergone an optical low-pass filtering. This effect is often unacceptable, and attempts to develop algorithms which smooth noise whilst preserving edge data have been made. The simplest of these is median filtering, developed by Tukey [1971], in which a point is replaced by the median intensity value in a designated surrounding neighbourhood, instead of some mean value, (Fig.(5.8)). In one dimension this process removes isolated spikes without distorting edges or gradual intensity variations, (Fig.(5.9)). In two dimensions the effect of the median filter on the image data is very dependent on the shape of the local neighbourhood being inspected. A square

neighbourhood preserves edges but rounds off corners and removes thin lines. A cross-neighbourhood, which was used, leaves horizontal and vertical lines and similarly orientated corners untouched, but destroys diagonal lines, (Fig.(5.10)).

This median filtering technique is about as effective as low-pass filtering for noise removal, but it also maintains picture detail.

5.3.3. Edge Enhancement

Edge enhancement techniques have a limited applicability in fringe analysis systems. They are useful when the fringe detection routine is trying to locate fringe edges or regions of maximum grey-level gradient, as it is these regions that they tend to enhance. However their use can often be a double-edged sword. By their very nature edge enhancement procedures must enhance the high frequency components of the image frequency spectrum, this corresponding spatially to regions of rapid transition in luminance value, the hallmark of the edge. However, as described in setion 5.2., this is exactly where the majority of the noise components might be expected to occur, thus leading to the possibility of noise enhancement as well as edge enhancement.

Also because the edge enhancement is performed locally, the resulting edge structure is somewhat different to that of the original edge, (Fig.(5.11)). This can adversely affect regions

containing many closely spaced lines. The locality of the edge enhancement techniques means too that detected edges are not necessarily continuous, but may well be fragmented. This can offer problems both to the visual observer and to automatic analysis routines.

(i) Spatial Filtering

High-pass filtering may be implemented in a way identical to that of the previously mentioned low-pass spatial filtering. Typical convolution operators are shown in (Fig.(5.12)). The rotational symmetry of such masks is necessary to avoid directionality in the output. The degree of enhancement may be altered by charging the magnitude of the central coefficient, the large the coefficient the nearer the result will be to the original. Of course the normalising factor must in each case be adjusted to take this into account.

(ii) Non-linear methods

Such methods use non-linear combinations of pixels as a means of edge enhancement. These usually take the form of weighted masks acting over a small neighbourhood, usually 2 x 2 or 3 x 3 pixels in extent. Of the forms possible a Sobel operator is offered, (Duda et al.[1973]), as shown in (Fig.(5.13)). The Sobel filter is a non-linear combination of the output of two linear filters. The edge enhancement plane is defined as:

$$G(j,k) = \sqrt{x^2 + y^2} \qquad (5.5)$$

where

$$x = (I_2 + 2I_3 + I_4) - (I_0 + 2I_7 + I_6) \qquad (5.6)$$

and

$$y = (I_0 + 2I_1 + I_2) = (I_6 + 2I_5 + I_4) \qquad (5.7)$$

(iii) Linear methods

A linear filter, working on the discrete differentiation principle, is offered with the Laplacian edge-detection routine. This allows edge sharpening without directionality, and the relevant mask is shown in (Fig.(5.14)).

5.3.4. Background Intensity Equalisation

It is often the case that the background intensity function is found to vary across the digitised image, and not remain constant as would be expected. This may be due to several factors, such as an uneven response over the C.C.D.-array but in the case of holographic interferometry the main culprit is the Gaussian beam distribution of the reconstruction beam.

Because the background function is modulated by the fringe function, it is not possible to model the Gaussian distribution for correction purposes, and so an alternative method must be found. A method similar to that proposed by Becker [1985] was used in the heat transfer analysis case. The digitised image was divided into a number of small square regions, typically 1024. The

average grey-level was determined over each small square (excluding contributions from masked regions), and these values used to form a coarse grid of node points. An average (grey-level intensity) surface was then fitted over this grid using the bilinear interpolation technique, shown in (Fig.7.9), and the surface then used to provide a relative correction factor as each point. A typically corrected image may be seen in (Fig.5.15).

In the compressible flow study case the background equalisation technique was incorporated in the binarisation stage, and this is described fully in Chapter 7.

CHAPTER 6

AUTOMATIC ANALYSIS OF HEAT TRANSFER INTERFEROGRAMS

6.1. INTRODUCTION

Examples of the heat transfer holographic interferograms produced by Lockett [1987] are shown in (Fig.(4.4)). The quantitative information required from such interferograms was:

(i) point temperature profiles

(ii) streamwise averaged temperature profiles

(iii) local Nusselt numbers

(iv) full-field temperature contours

Lockett identified an error of 4.7% in manually locating the fringes in an image field for the extraction of quantitative data. The major aims of the automatic processing system are to increase this accuracy of location, and to increase the speed with which quantitative data may be extracted from the images.

The quantitative results wanted, specifically the temperature profiles and the local Nusselt numbers, required that data are available for individual scan lines perpendicular to the plate surface. This criterion led to the adoption of a one-dimensional analysis system, as discussed in section [3.1.3]. The fringe data

were analysed along a series of vertical lines, the sampling rate of these vertical lines being determined by the operator. All the desired information could then be extracted from these scan lines, and a full-field isothermal contour plot obtained by interpolation between the scan line data.

The rate at which vertical scan lines were taken across the image data was really dependent on the Nyquist rate, that is the frequency of vertical scanning should be twice the frequency of any specific object in the flow field about which information was required. In practice there was no restriction to doing a vertical scan at every pixel station except processing time. However, as in most cases the fringe data varied consistently across the image field, a fairly coarse series of vertical scan lines sufficed to extract the relevant quantitative results.

When a series of one-dimensional analysis routines was being used, the grey-level data was utilised. The initial stage of the analysis procedure was to mask and enhance the image data where necessary, and to determine relevant common points if merging was required between a full-field image and a magnified boundary layer region. This aspect of the system has been covered in Chapter 5. Therefore the rest of this chapter will be a description of the actual image analysis routines tested and implemented, and the attendant numerical analysis routines.

6.2. HARDWARE AND DATA ACQUISITION

Throughout the heat transfer interferogram analysis part of this project the host computer was a Prime mini-computer. The analysis routines have been run on the Prime, and its attendant peripherals used to display the results.

It was possible to display the image data in analog form either by using a Sigma display generator type 5664 with a Sigma colour display monitor No.C-3412 or on a Sigma T5670 black and white display terminal. Hard copies of these displays could be obtained from a Tektronix 4631 hard copy unit. Standard peripherals such as a Benson flat bed plotter, magnetic tape drive and hard disc drives were also available.

The means of acquiring a digital image from the holographic plates changed, for the better, during the course of the project.

Initially photographs were taken of the reconstructed holographic plate, both full-field and magnified boundary layer portions. These photographs were then digitised using an electro-mechanical scanning system, that is one dimension is scanned mechanically and one electronically. The digitising system consisted of a motor-driven moveable bed, with a one-dimensional C.C.D. (Charge Couple Device) camera suspended above the bed.

The bed was built in-house, and consisted of a perspex base mounted horizontally in a metal frame which could be moved backwards or forwards by means of a pulley system driven by a small stepper-motor. This motor could be controlled manually with a hand control, to allow for easy positioning of the target photograph. To aid in this positioning an oscilloscope was used, the oscilloscope being connected to the camera output and responding to intensity changes. When the target photograph was correctly positioned, the stepper-motor was controlled automatically via a PDP11 mini-computer. This caused the stepper-motor to move the bed in steps of 50 microns.

The camera scanned the image one line at a time in a direction normal to the movement of the bed. The C.C.D.s are an array of photo-detectors, each sensor accumulating a charge proportional to the incoming light. This charge is shifted as a "packet" down a series of internal capacitors until it reaches an external terminal, and an output signal is produced. This signal determines the grey-scale level assigned to that particular pixel, the range normally being between 0 and 255. The digitised image array thus obtained was written onto magnetic tape, and transferred via this medium to the Prime mini-computer.

An array 512 x 512 pixels square, with a grey-level range of 255, was obtainable with this digitising system, shown in a schematic form in (Fig.(6.1)). However, there was very little control of the quality of the digitised image, due to the lack of a

display device during the digitising process. This necessitated a large image enhancement section in the digitial analysis system. The situation was improved by the later digitising system to be used.

The second digitising system consisted of a Pip-4000 image processor hosted onto an IBM-PC-AT micro-computer. The image was digitised directly from a re-illuminated holographic plate by the use of a two-dimensional array C.C.D.-camera, 560 x 480 pixels in size. A frame 512 x 512 pixels square was grabbed from this camera by the Pip-4000 image processor, and stored in one of the eight available frame-stores. This digitised image could then be displayed, and various features such as a gain adjustment and an offset adjustment for the input signal made. Thus a certain amount of image pre-processing was available at this digitisation stage.

The digitised image was then stored on a floppy disc, and transferred via a Gould mini-computer to magnetic tape, from where it was transferred to the host Prime computer. A schematic diagram of this processing system is available in (Fig.(6.1)).

6.3. FRINGE CO-ORDINATE EXTRACTION

Having enhanced and masked the image data, the next step is to extract the co-ordinates of the fringe along the vertical scan lines chosen. As has been stated in section [3.1.3] five major

ways of utilising the grey-scale data to extract such co-ordinates exist. All five possible methods were tested using computer-generated fringe data in which the true locations of the fringe maxima and minima were known, as well as the fringe edge locations. This computer-generated data gave the operator the ability to alter the fringe visibility, defined by Michelson as:

$$v = \frac{(I_{max} - I_{min})}{(I_{max} + I_{min})} \qquad (6.1)$$

where I_{max} is the maximum irradiance occurring in the bright fringe nearest the point under consideration, and I_{min} is the minimum irradiance occurring in the nearest dark fringe.

Also it was possible to alter the signal-to-noise ratio experienced when scanning the fringe data, the noise being modelled as simple stochastic additive noise. The definition used for the signal-to-noise ratio, or SNR was:

$$SNR = \frac{\text{RMS variation due to the signal}}{\text{RMS fluctuations due to the noise components}} \qquad (6.2)$$

The fringe detection routines now described were all tested against both a varying fringe visibility, and a varying signal-to-noise ratio.

6.3.1. Fringe detection by maximum and minimum grey-level intensities

This fringe detection routine located regions of maximum and minimum grey-level intensity as the fringe co-ordinates. The routine looked for a maximum intensity, then a minimum, then a maximum, and so on. An extra criteria was introduced in that the located maximum had to be higher than a certain threshold, I_{Hi}, and the located minimum lower than a similar threshold, I_{Lo}. I_{Hi} was set at 80% of the grey-level histogram distribution value, and I_{Lo} at 20% of the same.

6.3.2. Fringe detection by locating regions of gradient change

A single scan line was studied using a series of short vectors. At every pixel point two vectors were looked at, the vector being known as the gradient length. Initially tests were carried out using a gradient length of three pixels, that is tests to determine the effects of a varying fringe visibility and signal-to-noise ratio on the effectiveness of this method.

One of the gradient lengths was known as the previous gradient length, and was defined as:

$$P_{GRAD} = I(i,j) - I(i,j-2) \qquad (6.3)$$

the other was the current gradient length, defined by:

$$I_{GRAD} = I(i,j) - I(i,j+2) \qquad (6.4)$$

If both P_{GRAD} and I_{GRAD} had positive values, and as an additional criteria the point under consideration I(i,j) had an intensity greater than a threshold I_{Hi}, then a fringe maximum was located. Before another maximum could be located, a fringe minimum then had to be found. A fringe minimum was detected if both P_{GRAD} and I_{GRAD} were negative, and the point I(i,j) was less than a threshold value I_{Lo}.

The two threshold values, I_{Hi} and I_{Lo}, were set at 90% and 10% of the grey-level distribution respectively.

The next stage was to ascertain the effect of gradient length on the performance of the gradient change detection algorithm. By a simple inspection of the problem two points become apparent. These are:

(i) if the gradient length is small, for instance, two pixels in length, then noise effects will have a greater influence on the operation of the algorithm.

(ii) if the gradient length becomes too long, by this it is meant greater than three-quarters of the local sinusoidal wavelength, then sensitivity is progressively lost. This means that true regions of gradient change, that is either a fringe maximum and minimum, may not be detected.

A noise-free, constant fringe visibility fringe field was generated, and the gradient change algorithm tested with various gradient lengths on varying fringe thicknesses. This procedure was adopted to try to prove the previous supposition that, for an effective algorithm

$$2 < \text{gradient length} < 1\tfrac{1}{2} \times \text{local sinusoidal wavelength} \qquad (6.5)$$

6.3.3. Fringe detection using regions of maximum gradient

This algorithm relied on the detection of fringe edges, that is regions of maximum grey-level gradient, to determine the fringe co-ordinates. A trio of gradient lengths were inspected, each three pixels in length and adjoining each other. Fringe co-ordinates were detected when the magnitude of the central gradient length was greater than either of the two adjoining gradient lengths.

6.3.4. Fringe detection using a floating threshold

A floating threshold of the same form as that described in section [3.1.3.4] was used in this algorithm. In this case the constant, Δ, used was 0.3.

The algorithm worked in this way. Assuming a start point on a white fringe, then the maximum value encountered along the scan line was set at a value MAX, until the grey-level dropped below a value defined by MAX–THR. The location of this point was set as point 1. The algorithm then searched for the minimum value encountered along the scan line, this value being written into MIN. When the grey-level value rose above an intensity defined by MIN+THR, this point was set as point 2, and the search continued for a new value of MAX. The fringe location was then defined as:

$$\text{FLOC} = \frac{\text{Point 1} + \text{Point 2}}{2} + \text{Point 1} \qquad (6.6)$$

and in this case this corresponded to a fringe minimum. The procedure then repeated, searching for maxima and minima in this way, the only extra criterion being that a fringe maximum must succeed a minimum, and vice-versa.

6.3.5. Fringe detection using a bucket-bin technique

Two slightly different techniques were included under this algorithim.

The initial procedure was to locate the zero crossing points between a pre-set threshold value and the grey-level function.

Two threshold values were determined, one connected with the fringe maxima known as I_{Hi}, and set at 60% of the grey-level distribution, and one with the fringe minima called I_{LO}, and set at 40% of the grey-level distribution, as shown in (Fig.(6.2)).

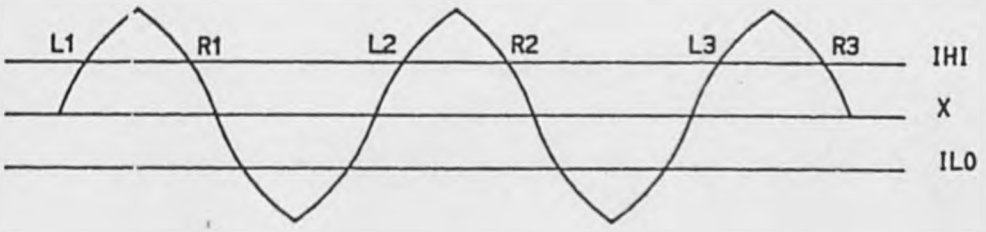

Fig.(6.2). Determination of zero crossing points.

The fringe maximum and minima were then treated separately, although in the same way. The procedure to determine the location of the fringe maxima will now be described.

The points where the threshold I_{Hi} intersected the grey-level distribution function, known as the zero crossing points, were located and written into an array as a series of pairs, signifying the left hand side and right hand side of a particular fringe

maximum (i.e. L1 and R1 in Fig.(6.2)). Each pair of points was then taken, and the grey-level distribution between them inspected.

To determine the position of the fringe maximum from this set of grey-level points, two methods were tested:

(i) Centre of gravity

The centre of gravity of the region enclosed between the points designated by the left hand side and right hand side points was determined using the standard relationship:

$$C \text{ of } G_x = \Sigma \frac{(\text{Grey-level intensity} \times x)}{\Sigma \text{ Grey-level values}} \qquad (6.7)$$

where x is the distance of each pixel from the left hand zero crossing point. This equation gave the distance of the centre of gravity from the left hand zero crossing point, and this point was used as the position of the fringe maximum.

(ii) Curve fitting

In this case a curve was fitted to the points lying between the left and right zero crossing points, using a polynomial regression method (Gaussian elimination was the technique used). The curve fitting routine supplied coefficients for a suitable cubic polynomial, which was then differentiated so that the point of zero gradient along this curve could be determined, and set as the position of the fringe maximum.

A similar set of procedures was followed for the determination of the fringe minima positions.

6.3.6. Results of fringe detection tests

The results obtained using the previous described fringe detection routines are now discussed.

6.3.6.1. Effects of a varying fringe visibility

The effects of a varying fringe visibility are shown graphically in (Fig.(6.3)) for each of the algorithms tested. As might be expected a varying fringe visibility had little effect on the accuracy of the fringe detection algorithms, a slight decrease in the accuracy of location being noted as the fringe visibility decreased. The test runs ended with a fringe visibility of 0.25, but the general trends observed indicated that a slight decrease in accuracy would continue to occur until the fringe visibility became of the order of zero, when a very rapid drop would occur.

The tests were conducted on a noise-free image. The effect of noise with a decreased fringe visibility is to decrease the signal-to-noise ratio (SNR), and this aspect is discussed in the next section.

6.3.6.2. Effect of a varying SNR

The general trend is, as would be expected, a decrease in the accuracy of fringe location with a decreasing signal-to-noise

ratio. The results obtained are displayed graphically in (Fig.(6.4)).

For the maximum gradient detection method this general trend is true, but it should be noted that the introduction of any noise into the image data brings an immediate decrease in the accuracy of location (compare the results in (Figs.(6.3) and (6.4)), from an RMS error of between 0.4 and 0.1 with no noise, and a varying fringe visibility, to an RMS error of between 2.4 and 3.4 with a decreasing SNR.

The gradient change detection algorithm showed a good accuracy throughout, an RMS error of between 0.05 and 0.36 being found with a decreasing SNR. The accuracy of location was found to decrease only marginally until an SNR of about 20 was reached, when it began to decrease fairly rapidly.

The maxima/minima detection algorithm showed a good accuracy of location until an SNR of about 24 was reached, when the accuracy become very poor, and RMS error of 60 being reached at the lower SNR. This is as expected, it can be seen intuitively that this technique would be very noise sensitive.

Both bucket and bin algorithms, that is using a centre of gravity and a curve fit to locate the fringe positions, operated effectively throughout, very low RMS errors being found. An almost parabolic form was adopted by the test results, an initial

slow decrease in the accuracy of location down to an SNR of about 16 being following by a more rapid decrease in accuracy.

The floating threshold detection algorithm appeared little perturbed by a decreasing SNR, an almost constant RMS error of 2.00 being observed.

6.3.6.3. Effect of a varying gradient length on the gradient change detection routine.

The effect of a varying gradient length on the accuracy of the gradient change fringe detection algorithm was investigated on noise-free data, with a fringe visibility of 1 and varying fringe thickness. The results are shown in (Fig.(6.5)).

From the results it can be seen that for broad fringes a longer gradient length is needed, and this would also be the case for noisy fringe data. Also, for all fringe thicknesses, if the gradient length increases over about 0.75 x fringe width, inaccuracies begin to increase at a rapid rate, and the algorithm becomes invalid.

6.3.6.4. Conclusions

From the results obtained in the previously described tests, it became apparent that the most effective one-dimensional fringe analysis routines available were either the bucket-bin routines, or the gradient change routine. These two methods were then adopted for the fringe co-ordinate extraction part of the heat transfer analysis system, on an either/or basis.

6.4. IMAGE ANALYSIS SYSTEM

The actual image analysis system used for the analysis of the heat transfer holographic interferograms was based on a menu system, shown in (Fig.(6.6)), and a description of the system will now be given based on the order in which the menus were used.

Before the main menu was displayed, the operator was asked if a full-field fringe system only was to be analysed, or if a magnified boundary layer was to be incorporated into the full-field data as well. If the latter case was true, the operator was asked to define a series of common points on both the full-field and boundary layer data, to allow the necessary scaling to occur for successful merging of the fringe fields. This aspect is discussed in section [5.2.2].

The results were displayed on the terminal in one of two spaces, a space on the left being reserved for image data display, and a workspace on the right being reserved for such procedures as intensity profiles and histograms.

6.4.1. Main Menu

Twelve options were presented to the operator by the main menu, selection being by input of the desired choice number.

Option 0 simply allowed the operator to quit the programme.

Options 1 to 4 were image acquisition and display options, and were written by Dr.G. West specifically for the Prime mini-computer, and kindly lent to the author.

Option 1 acquired an image from the data file.

Option 2 allowed a grey-scale image to be displayed on the Sigma colour monitor. In this case it was necessary to specify the number of bit shifts required to scale the data for display, usually 4, and the minimum grey-level to be displayed, always 0. The scaling was necessary as the data had a possible dynamic range of 256 grey-scales whereas the colour monitor was only able to display with a dynamic range of 32 grey-levels.

Option 3 allowed a binary image to be displayed on either the Sigma colour monitor or the Tektronix black and white monitor. The operator was required simply to input the required binary threshold. It should be noted here that this binary display did not affect the image data itself, which remained as grey-scale data but only the displayed image.

Option 4 calculated and displayed a histogram showing the grey-level distribution of the pixels in the image. This was drawn to the side of the image (in the reserved workspace) - a typical example is shown in (Fig.(6.7)), and was extremely useful in certain image enhancement procedures, (section [5.3.1]).

Option 5 allowed the image enhancement menu to be displayed [6.4.2].

Option 6 accessed the image analysis menu, [6.4.3].

Option 7 displayed the results display menu, [6.4.4].

Option 8 was the refresh display option. When option 8 was selected a small menu was displayed, giving the following options:

(i) 0 Black - this option removes the whole display by re-initialising the appropriate terminal.

(ii) 1 Histogram - this option overwrites the histogram on the terminal, leaving the workspace blank.

(iii) 2 Intensity Plot - this option overwrites the intensity plot on the terminal (described later), leaving the workspace blank.

Option 9 was the option required for masking off the edges of the image data, and the plate profiles (i.e. the ribs) where necessary. This procedure is described fully in section [5.2.1].

Option 10 was invoked to combine the fringe detection results obtained from both a full-field and a magnified boundary layer, the combined data then being written into a separate data file ready for further processing.

Option 11 automatically ordered the fringe data, assuming a linearly increasing order towards the heated plate. After all the ordering had been done, it was possible for the operator to intervene and re-order any wrongly ordered fringes. The field temperature distribution was then determined and written into the results file.

6.4.2. Image Enhancement Menu

Six options were available from this menu, again selection being by inputting the required option number.

Option 50 returned the operator to the main menu.

Option 51 provided a Laplacian edge-detection routine as described in section [5.3].

Option 52 provided a Sobel edge-detection routine, as described in section [5.3].

Option 53 gave a plot of the intensity profile along an operator selected column of data, the plot being written into the workspace

provided beside the image display workspace. Such an intensity plot was scaled so that the maxmium intensity amplitude experienced along the column of data chosen filled the breadth of the workspace. A typical example is shown in (Fig.(6.7)), along with the attendant image. Such an intensity profile was useful for ascertaining the effect of the various image enhancement routines, and for checking the effectiveness of the fringe analysis routines.

Option 54 called up a menu which gave the grey-level enhancement options available. This menu provided the operator with 9 possible options, and these were as follows:

(i)	0	-	quite this menu and return to the image enhancement menu	
(ii)	1	-	low pass filter	the details
(iii)	2	-	high pass filter	of these
(iv)	3	-	median filter	enhancement
(v)	4	-	histogram split	routines are
(vi)	5	-	histogram linear stretch	described fully
(vii)	6	-	histogram equalisation	section [5.3]
(viii)	7	-	intensity equalisation	
(ix)	8	-	this was a display image option, and allowed the operator to display either a grey-scale or a binary image to allow an estimation of the effect of the enhancement routines used.	

Option 55 presented the display refreshing menu already discussed in section [6.4.1].

6.4.3. Image Analysis Menu

This menu really presented the heart of this system, that is the fringe detection schemes. The options displayed by this menu were as follows:

Option 60 was the return to main menu option.

Option 61 was a plot of the intensity data down a column of image data, as described previously.

Option 62 was a gradient change fringe detection option which will also be described more fully in section [6.4.5].

Option 63 was a bucket-bin/curve fit type fringe detection option, described more fully in section [6.4.5].

Option 64 was the previously detailed refresh display option.

Option 65 was an image inversion option, which basically reconstructed the grey-scale image data to produce a 'negative' of the image data. Thus an image data point of grey-scale value 255 was assigned a grey-scale value of 0, an image point of grey-scale value 254 was assigned a grey-scale value of 1, and so on. This procedure had to be implemented if hard copies of the image were required from the Tektronix 4631 hard copy unit, as the images produced by this are inverses of the image appearing on the display unit.

Option 66 was a refraction error correction option. This option is described more fully in section [6.4.6].

Option 67 was a Nusselt number calculation option, and this is described more fully in section [4.5.2].

6.4.4. Results Display Menu

This menu listed the options available for displaying the results obtained from the image analysis menu.

Option 70 was the return to main menu option.

Option 71 plotted the temperature profiles obtained for every column of data analysed over the image.

Option 72 was a plot option for a streamwise averaged temperature plot. This plot was useful in the comparison with the Large Eddy Simulation programme (LES) discussed at the end of the chapter. The temperature profile plotted was that obtained from averaging the point temperature profiles obtained across the image.

Option 73 was a temperature contour plot. Temperature contours were obtained by interpolation between the equal ordered fringes in each of the sampled columns.

Option 74 was a Nusselt number plot, the local Nusselt number distribution being plotted for each column of data sampled, and the average Nusselt number calculated.

Option 75 was the refresh display option, described previously.

6.4.5. Fringe Detection Routines

Options 62 and 63, that is the gradient change fringe detection and the bucket-bin fringe detection techniques, were the important stage in the fringe analysis system. The basic algorithms have been described respectively in sections [6.3.2] and [6.3.5] but the algorithms actually used on the experimental data varied somewhat from these basic algorithms.

6.4.5.1. Bucket-bin fringe detection.

The algorithm used in this case was very similar to that described in section [6.3.5]. However, only one threshold value for the determination of zero crossing points was used, and this was set at the average grey-level value encountered down the scan line (excepting masked regions). The zero-crossing points thus defined were used for the determination of both the maxima and the minima of the fringe signal.

If the separation between zero-crossing points was less than ten pixels, the centre-of-gravity technique was used to find the extremum, otherwise the curve fitting technique was used.

An interactive validating procedure was incorporated into this routine, and this is described in section [6.4.5.3].

6.4.5.2. Gradient change fringe detection

Again the algorithm used was very similar to that described in section [6.3.2], but only a single threshold was defined, corresponding to the average grey-level value encountered down the scan line. The fringe maxima then located had to lie above this value, and the fringe minima below it. A further criterion was added in that the value of the gradient had to be greater than a pre-determined value for it to be counted as significant (lower values were attributed to noise).

An interacting validating system was also incorporated into this fringe detection system, and it is described below.

6.4.5.3. Interactive validating routines

These occurred at two points in the fringe detection algorithms. When the average grey-level value was determined, a plot of the intensity distribution obtained down the column of interest was displayed in the workspace, and a line corresponding to the grey-level value superimposed on this. This allowed the operator to check that the threshold value set was reasonable, i.e. cut across all the fringes present somewhere between the maximum and minimum value of that fringe, (Fig.(6.8)).

After the fringe maxima and minima had been located along a particular scan line, symbols representing the detected locations were plotted alongside an intensity distribution plot for the column in the workspace. If a detected fringe location was wrongly placed, a fringe had been missed, or an extra fringe included due to noise or a spurious artefact, the operator could intervene at this stage and alter the data using a cursor, (Fig.(6.9)).

This procedure was followed for every scan line taken across the data.

6.4.6. Refraction Error Correction

The factor for the correction of errors due to refraction is discussed in section [4.5.2], and the equations for the determination of this correction factor given by equations (4.18) to (4.23).

A programme was written that determined the correction factor in the manner described, the major change being that equation (4.18) was altered to the following format, for the purposes of digital computation:

$$C\ell_i = L \left[T(x,y)_{z=0} \cdot \sum_{z=0}^{L} \frac{\Delta z}{T(x,y)_z} \right]^{-1} \qquad (6.8)$$

The programme utilised the temperature distribution determined along each scan line, and a correction factor was determined for each fringe until the correction factor approached unity, when

the procedure was halted. It can be seen from equation (4.19) that the steeper the temperature gradient, the greater the refraction error. Thus the greatest refraction errors would be expected near to the heated plate, and if the near wall fringe evinces a negligible refraction error, such errors can be ignored.

This refraction error correction programme became redundant towards the end of the project, as all the interferograms to be analysed were taken with the aid of a focussing lens, Lockett [1987]. If Fig.(6.10) is studied, it can be clearly seen that the error due to refraction will increase evermore rapidly across the width of the test section, as the gradient of the optical path increases (assuming a two-dimensional temperature field).

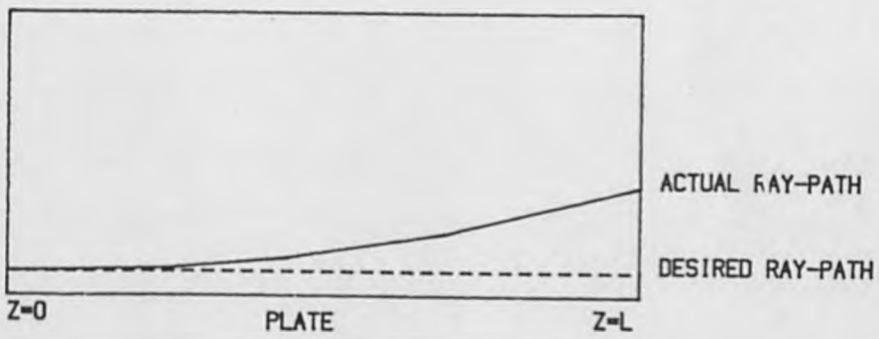

Fig.(6.10) Showing the deviation of a light ray across the test section due to refraction errors.

The positioning of a focussing lens between the test section and the holographic plate allows a plane from somewhere inside the test section to be focussed on the holographic plate. Correct focussing helps to minimise the effect of refraction errors, Beach, Muller and Tobias [1973], and they can be assumed negligible; that is the additional phase change introduced due to an increased pathlength is negligible compared to the change in phase produced by the passage of the light through the field of varying refractive index.

6.5. RESULTS AND DISCUSSION

6.5.1. Fringe Analysis Considerations

As far as the automatic fringe analysis of the heat transfer holographic interferograms are concerned four distinct regions within the fringe field may be identified, and these are indicated in (Fig.(6.11)).

The first of these is a region next to the plate, and around the ribs if they are present, that extends some way into the flow, and in which no fringes are visible, region A. This is the diffraction, ray crossing (due to refraction) region, and it is recognisable as a grey amorphous region separating the first resolvable fringe from the plate position proper. Such a region is unavoidable with the use of holographic interferometry, diffraction always occurring around the surface of any solid object

traversed by a light beam. Such an effect can however be reduced by the correct positioning of a focussing lens just prior to the holographic plate.

At high heat transfer rates there is the possibility of refraction errors occurring, as discussed in section [4.5.2]. The severity of such refraction errors is determined by the magnitude of the temperature gradients extant in the region under consideration, and so the worst refraction errors tend to occur in the very near wall regions. In the most extreme cases ray crossing may occur, a near wall ray being so refracted that it crosses the ray above. Such a phenomenum prevents a refraction error correction being determined, as no fringes are resolvable.

These ray crossing occurrences may again be minimised by the correct positioning of a focussing lens. However, a lens position that minimises refraction error effects maximises diffraction effects, and vice-versa, leading to the need for compromise.

Thus some unresolvable near wall region nearly always exists, and this necessitates an extrapolation of the temperature profile from the resolvable fringes to the plate so that the temperature gradient at the plate, as well as the wall temperature, may be determined. This allows the calculation of the local heat transfer and hence the local Nusselt number, as at the plate, in the laminar sub-layer of the wall velocity boundary layer, the air is static, and so heat transfer due to conduction only may be assumed.

Directly above this unresolvable region there comes a series of evenly spaced uniform fringes, representing a laminar sub-layer in the thermal boundary layer, region B. These are useful as they provide a springboard for extrapolation into the unresolvable region, but they are not always present. This is especially true with the square rib geometry, the square ribs being very effective turbulence promoters, breaking up the thermal boundary layer and preventing the formation of a laminar sub--layer. With the rounded and deposited rib geometries such a region of fine, evenly spaced, fringes is nearly always apparent. This would indicate that such ribs, being more streamlined, allow an earlier reattachment of the flow, and thus a laminar sub-layer may have time to build up.

Region B produces problems in the automatic analysis only in that all the fringes in this region are not always resolvable. This means that a magnified view of this region is often needed to allow all the fringes to be resolved, and hence a complete solution to be determined. This magnified section must then be merged into the full-field data, and this aspect is detailed in section [5.2.2.2].

The third region, region C, usually consists of two or three broader fringes. These fringes are well defined, and give no problems to the automatic analysis system. Real time studies indicate that the position of the fringes in this region are, to a limited extent, time dependent. This would seem to indicate that the fringes in this outer wall region are found in the turbulent transition and fully turbulent portions of the thermal boundary

layer. Thus some of the fringe broadening may be due to a certain amount of spanwise averaging of turbulent activity, but the "sharpness" of the fringes seems to indicate that such a contribution is negligible.

Region D is the main flow region, and is characterised by very broad, diffuse fringes. Real time considerations, illustrated by the time sequence shown in (Fig.(6.12)), indicate that this region is extremely time dependent, with time dependent "structures" such as closed fringe systems appearing in the flow. An inspection of a typical intensity profile across some of these broad fringes shows that they are very ill-defined compared to the other fringes that appear in the fringe field, (Fig.(6.13)).

This diffuseness is due to several points. The fringes are broad here due to the low temperature gradients that exist. The two-dimensional assumption also breaks down, due to the turbulent activity in this region, heat transfer being mainly by advection. This leads to a large amount of spanwise averaging, which is exacerbated by the fact that end effects become more important in this region due to the low temperature gradients that exist. This leads to broad diffuse fringes.

Such fringes present two main problems to the automatic fringe analysis system. The first is that the signal-to-noise ratio is low across such fringes, and it is necessary for the routines to avoid detecting false fringes due to the noise, but just to isolate

the main fringes. This can be done by ignoring anything that purports to be a thin fringe in such a region, and by locally smoothing the signal several times by low-pass filtering or median filtering, section [5.3]. The second problem is to determine the fringe maximum or minimum in such regions. This can be done using the curve-fitting fringe location routine detailed in section [6.4.5.1], but a degree of uncertainty is still apparent as to whether these found extremums represent the true extremums, or if they are misplaced due to the spanwise averaging.

The accuracy to which the fringes can be located in each region is detailed in Appendix B.

Typical temperature contours and temperature profiles are shown in (Fig.(6.14)) for all the types of rib geometry, as well as the flat plate, (Fig.(6.21) and Fig.(6.23)).

6.5.2. Real Time Considerations

Fig.(6.12) shows a typical real time sequence obtained using a 35 mm single lens reflex camera. In this sequence, and in other sequences obtained by Lockett [1987] using a high speed camera framing at 600 frames per second, or the single lens reflex camera framing at ten frames per second, "structures" in the main flow region are apparent. The question raises itself, are these structures significant or are they just indicative of the advective nature of the heat transfer.

The literature seems to suggest that such structures are not in themselves indicative of large eddies in the main flow. Cantwell [1981] in his review of boundary layer flows suggests that the size of the typical large eddy in the main flow region is somewhere in the range $h/2 \rightarrow h \times h/4 \rightarrow h/2$, where h is the channel height. Such an eddy has a spanwise depth of $0.25h \rightarrow 0.5h$ and eddy centres are typically spaced $h \rightarrow 3h/2$ apart in the spanwise direction. The test section used has a width of 4 h and so it may be surmised that spanwise averaging would reduce the effect of any single eddy to invisibility compared to the surrounding thermal field.

The visible structures may, however, be the result of spanwise averaging over a number of large eddies which are distributed across the test section. Such a case is difficult to make for the flat plate results, but stands up pretty well in the rib-roughened case. If the ribs are considered as two-dimensional turbulence promoters, as they are in this case, then it would seem reasonable to expect a string of large eddies to form simultaneously across the span of the test section. Due to the two-dimensional nature of the flow these eddies would then propagate downstream at the same rate, giving rise to the apparent "structure" that is visible and that rolls downstream.

As has been mentioned before, this case is harder to make for the flat plate results, as there is no reason for a spanwise string of eddies to be promoted 'at the same instant' across any one

spanwise station. However, measurements taken from Lockett's high speed films indicate that the visible structures have a size of typically 0.48h x 0.29h, and that they move with a speed that is 90% of the bulk velocity. This agreement with the dimensions put forward by Cantwell would seem to indicate that these visible structures are connected with large eddies in some way. It is hoped that a better insight to this phenomenum may be gained by comparison of an experimental flat plate heat transfer with a Large Eddy Simulation, a numerical solution to this heat transfer geometry. Such a comparison and its results are discussed in section [6.6.].

6.5.3. Discussion of the Heat Transfer Results

6.5.3.1. Flat Plate Heat Transfer Results

The flat plate results were taken by Lockett [1987] to prove the wind-tunnel and the technique for heat transfer visualisation used, that is holographic interferometry.

The average Nusselt numbers obtained for a range of Reynolds numbers are shown in (Fig.(1.2)), and compared with results obtained by Walklate [1981] and the empirical relationship for heat transfer in a duct:

$$Nu = 0.023\ Re^{0.8} Pr^{0.4} \qquad (6.9)$$

Good agreement is obtained throughout with Walklate's results.

With the empirical relationship good agreement is obtained for most Reynolds numbers, but some deviation is apparent especially at the higher Reynolds numbers.

In fact a straight line fit to the available points indicates a slightly different power law to that given in equation (6.9), and this is:

$$Nu = 0.0475\ Re^{0.7} \qquad (6.10)$$

or

$$Nu = 0.0545\ Re^{0.7}Pr^{0.4} \qquad (6.11)$$

The fact that the experimentally derived empirical relationship differs from that proposed in equation (6.9) is not really too surprising, as equation (6.9) really refers to a smooth duct with all four walls heated. The newly proposed 0.7 power law corresponds to an 0.7 power law describing the growth of the thermal boundary layer found both experimentally and in a Large Eddy Simulation. Thus the 0.7 power law would seem a more accurate empirical relationship for forced convective heat transfer in a low aspect ratio duct with only one wall heated, as is the case with our experiments.

6.5.3.2. Rib-Roughened Geometry Heat Transfer Results

The Reynolds number range for which the heat transfer from the ribbed geometries could be visualised was limited, at the lower end by the wind-tunnel geometry and the fan to above an Re,

based on the hydraulic diameter, of 7000, and at the upper end by the refraction errors. With the square-ribbed geometries no corrective focussing was used, and so a maximum Re of 30,000 could be visualised before refraction errors seriously thwarted analysis due to ray crossing. With the other ribbed geometries focussing was attempted, the correct focus position being assigned to the rib tops, the area where the maximum refraction error may be expected as this is where the highest temperature gradients occur. This focussing allowed Reynolds numbers of up to 54,000 to be studied before ray-crossing presented a serious problem.

The heat transfer coefficient data is presented as a dimensionalised quanity $Nu_{local}/Nu_{average}$ plotted against a quantity x/e, where x is the distance moved downstream from the chosen leading rib edge, and e is the rib height. Such a presentation scheme has been used for two reasons. The first is that it allows a comparison of the heat transfer data for the various rib geometries. The second is that a dimensionalised Nusselt number reduces possible errors, as an extrapolation through the near wall unresolvable region to determine the local wall temperature can be avoided. The dimensionalised Nusselt number approximates simply to the ratio of the local temperature gradient with an average temperature gradient.

An absolute Nusselt number plot has been produced for the square rib geometry, (Fig.(6.15)), using momentum field data from Martin [1987] to ensure a correct extrapolation through the

unresolvable near wall region, to determine correct wall temperatures. This shows that the effect of increasing the Reynolds number is an increase in the local Nusselt numbers, an expected result. From this plot we can also see that for the square rib the Nusselt number profile is independent of the Reynolds number, indicating that the heat transfer distribution in the case of a square rib is dictated purely by the rib, and not the flow conditions.

Plots of dimensionalised Nusselt number versus dimensionalised distance in the downstream direction of the flow channel are given in (Figs.(6.16),(6.17),(6.18), (6.19)) for all the rib geometries. As the overall shape of the heat transfer profiles are the same, a general explanation of the Nusselt number distribution will now be given.

Peak heat transfer occurs at the leading edge of the rib, and this is due to the thermal boundary layer being separated from the surface by the rib at this point. This separation leads to a small recirculation region just forward of the rib, and an increase in the advective heat transfer (eddying). The heat transfer then drops off rapidly behind the rib, in the rib wake region. This wake region contains a small recirculation region that effectively reduces the heat transfer to a minimum for about a rib height downstream of the rear of the rib.

The heat transfer then beings to increase as the flow moves downstream, until it peaks at about four rib heights from the rear

of the forward rib. This peak in heat transfer is thought to coincide with the reattachment of the separated flow to the plate, and this supposition is supported by Edwards [1962].

After reattachment the thermal boundary layer begins to grow again, causing a reduction in the heat transfer. A second heat transfer minimum is thus reached at a position approximately one rib height upstream from the downstream following rib. An increase in heat transfer is then experienced as the flow again separates just prior to this rib, and a secondary recirculation region is formed just upstream of the rib.

The square rib geometry shows two anomalies to this general heat transfer distribution. The first is a secondary peak in heat transfer that occurs towards the rear of the rib, and which is due to the formation of a small recirculation region just after the leading edge of the tip. Such a region is confirmed by Williams [1970] who proposes the mechanism suggested in (Fig.(6.20)) to explain the heat transfer distribution over a square rib.

The second anomaly is a peak in the heat transfer just prior to the rib, and it is thought that such a peak is due to secondary recirculation causing reattachment of the boundary layer.

The major contribution to the heat transfer comes from the central, or inter-rib region, where the heat transfer peak is lower than that at the leading edge of the rib, but much broader. The

whole heat transfer distribution across the ribbed surfaces agrees with the commonly accepted flow theory of flow separation just prior to the ribs, reattachment at some point between the ribs and eddies in the rib corners, Wilkie [1966].

The rounded and deposited rib geometries, being more streamlined than the square-rib geometry, introduce a certain Reynolds number dependence into the Nu distribution. Because of the streamlining the reattachment of the flow over the ribs is affected by the flow conditions, and the size of the recirculating regions at the rib roots is reduced. Also the secondary recirculating region found at the rib tip in the square rib geometry is removed. Thus the two extra peaks in heat transfer found with the square rib geometry are missing in this case.

6.5.4. Suggested Improvements to the Automatic Analysis Procedures

A major improvement could be made to the bucket-bin one-dimensional fringe detection technique used in this study, and this is the use of a floating threshold to define the zero crossing points of the signal, as opposed to a fixed threshold which in this case was defined to be the average grey-level experienced over the scan line. Such a change would allow the fringe detection routine to cope with scan lines across which the background intensity and modulation of the fringe system changes. At present such difficulties are overcome by using a background equalisation

pre-processing technique, (Chapter 5). However, a greater efficiency in the fringe processing time could be realised if such a change were made. The floating threshold envisaged is that as described in section [3.1.3.4], the positions along the scan lines where the algorithm detects a maximum and starts looking for a minimum, and vice-versa, being used as the zero-crossing points.

6.6. COMPARISON OF EXPERIMENTAL FLAT PLATE HEAT TRANSFER DATA WITH A LARGE EDDY SIMULATION (L.E.S.)

6.6.1. Large Eddy Simulation

Fluid flow generally has three space co-ordinates and time dependency. Laminar and turbulent flows are essentially the same phenomenon, there being no physical difference between fluids in turbulent and laminar flows. A common description is possible by equations expressing the conservation of mass and momentum using simple pressure, viscosity and advective transfer concepts. The difficulty is in solving the non-linear equations in the general case.

For many years the only practical approach to turbulence problems was through time-averaged equations, time-averaging reducing the dimensionality of the problem and producing stable, static solutions. The turbulent motions are averaged out of the linear terms, their only influence on the equations being through the Reynolds stresses that arise from the non-linear terms; the

solution of the equations is then analogous to the laminar solution, modified by the Reynolds stresses. Such Reynolds stresses have to be put into the equation from the outside, and they may be modelled directly, such a model being known as a closure model. However, these closure models have been subject to criticism, Reynolds [1976], [1978], on the grounds that they model high order statistical quantities in terms of lower order ones that respond to changing conditions on a similar or shorter time scale.

Such criticisms have led to the rejection of time averaging in favour of the direct digital simulation of flows in the three spatial co-ordinates and with time. This has given rise to the development of large-eddy simulations in which the temporal evolution of the large scale structures in the flow are directly simulated numerically.

A typical turbulent flow has a characteristic spectral dynamic behaviour. The gross mean flow, whose energy arises from imposed shear, pressure gradients, buoyancy or other body forces constrained by boundary conditions, is treated as the largest 'eddy'. This mean flow loses energy through vortex formation or other mechanisms to eddies of the next smaller size; these are the largest true turbulent eddies. They in turn lose energy to smaller structures through vortex stretching or tilting. This process is known as an energy cascade, and it peters out eventually because the smaller eddies evince higher strain rates and vorticities than the larger eddies. The velocities involved

are lower, but the velocity gradients higher. Because of this molecular viscosity plays an increasingly important role, until eventually an eddy scale is reached where all the energy extracted from the larger eddies is dissipated by friction, thus ending the downward flow of energy.

With a low Reynolds number flow ($Re_\lambda < 50$) it is possible to simulate directly all the relevant scales since the large eddies produced by the imposed flow are dissipated by molecular viscosity before they can break up into smaller eddies, Orszag et al. [1972], Schuman, et al. [1978].

With a higher Reynolds number the size of the dissipating eddies decreases rapidly. At a Reynolds number of 10^4 for instance, Voke and Collins [1982], the range of eddy sizes involved covers some three orders of magnitude. To simulate such a flow directly, roughly 10^9 mesh points would be needed in a finite-difference computation, or a corresponding number of degrees of freedom in other methods. Each decrease in the dissipation scale by one order of magnitude requires 10^3 times more computer storage and 10^4 times as much computational time due to the four-dimensional nature of the simulation. Thus the direct simulation of medium and high intensity Reynolds numbers is impractical, if not impossible, and coarse meshes must be used that resolve only the large scale eddies. Unresolved turbulence is taken into account through a subgrid scale (SGS) model, (Voke and Collins [1982] section 5). The advantage of the LES method -

spatial smoothing rather than time-averaging - is that models of the small scale or high wavenumber structures of turbulence are potentially far more universal than models of time-mean correlations involving all scales (closure models). The large eddies contain most of the energy, perform most of the turbulent transport, and interact most with the overall mean rate of strain of the flow. The small eddies are more isotropic, random and dissipate most energy. Thus many of the important practical properties of the flow are determined by the large eddies, while the small ones play a more passive role of removing kinetic energy from the large scales and dissipating it.

6.6.2. Aspects of the Comparison

The growth of a homogeneous passive thermal boundary layer within a low Reynolds number turbulent channel flow was simulated by the previously described spectral methods, i.e. a large eddy simulation. Starting from a fully developed isothermal channel flow simulation, the temperature along one wall was suddenly increased to a non-zero value, and the subsequent growth of the thermal boundary layer within the channel turbulence was followed. The thermal layer growth closely followed a 0.8 power law with time. The spectral simulation code used has been described in more detail by Hunter et al.[1986], Voke and Collins [1984] and Voke [1983].

The experimental study of the thermal fields due to forced convection above a flat plate, under similar Reynolds number conditions to those included in the simulation (that is an Re of 9800 based on hydraulic diameter) was run in parallel. A real-time technique was used (detailed in Chapter 4), a 35 mm motor-driven camera being used to obtain photographs of the fringes at two stations, 204 mm and 418 mm from the upstream end of the heated plate, henceforth referred to as the upstream and downstream positions. A typical interferogram, with temperature contours determined by automatic analysis of the fringe system, is shown in (Fig.(6.21)).

6.6.3. Results and Discussion of Comparison

The major obstacle to the comparison rested on the fact that in the simulation thermal boundary layer growth was temporal, whereas experimentally it was, of course, spatial. Thus a relationship between the experimental spatial growth and the theoretical temporal growth was required for a successful comparison.

Antonia, Dahn and Prabhu [1977] have studied the growth of a thermal layer internal to a boundary layer that was itself growing. The thermal layer was produced by a sudden step in the temperature of the wall. They found that the growth of the thermal layer, measured by the ratio of the layer thickness δ_T to the thickness of the boundary layer δ_0 at the sudden step in

temperature, to be related to the downstream distance x in the simple way:

$$\delta_T/\delta_o = 0.08(x/\delta_o)^{0.8} \qquad (6.12)$$

The simulation showed a temporal growth rate that obeyed a similar law. In this case δ_T is defined as the distance from the lower wall at which the planar average temperature is 1% of the wall temperature step, and we non-dimensionalise with respect of h, the half-channel height. The behaviour of this quantity is shown in (Fig.(6.22) as a function of tU_T/h, the solid line representing the relationship:

$$\delta_T/h = 0.74(tU_T/h)^{0.8} \qquad (6.13)$$

This result seems to indicate that there is a close relationship between the temporal growth rate in a simulation and the spatial growth rate of experimental layers, giving confidence in any comparison attempted. (Such confidence is further increased by the work of Kim [1983] who discussed the modification of a variable interval time averaging technique (VITA), used for isolating coherent phenomena from LES turbulent flow predictions. The VITA technique was modified to a variable interval spatial averaging technique (VISA), to allow a comparison with the spatial structures produced by flow visualisation experiments).

From equations (6.12) and (6.13) a constant convective velocity, x/t, can be postulated that relates the simulation time to the distance the layer is convected downstream experimentally.

The experimental study did not, however, yield a power law comparable with that shown in equation (6.12), a lower power actually being obtained. It is thought that this was due chiefly to the under-estimation of the thermal boundary layer thickness, δ_T, in the downstream profile. The definition of the thickness measure, that is the position at which the planar average temperature is 1% of the wall temperature, means that the thermal boundary layer thickness is located in the outer wall region of the flow. Due to the low temperature gradients and spanwise averaging encountered in this region of the flow the interferomeric fringes tend to be very broad and diffuse here. For this reason it is notoriously difficult to accurately locate fringes in this region, see section [6.5.1]. A close inspection of the temperature contours extracted from the holographic interferogram (Fig.(6.2)), shows that in fact the outer wall fringe has been located automatically in a position slightly different from where it would have been if located by hand, being somewhat lower, thus leading to the under-estimation of the thermal boundary layer thickness, δ_1.

Other effects due to three dimensionality, such as an enhanced heat transfer near the side walls, may also have contributed to a lower power law being obtained in the experiment.

To avoid the problems encountered when working in the outer wall flow region with experimental data, a new thickness measure was defined, at which the planar average temperature was 20% rather than 1% of the wall temperature step. In this case it was found that both the Large Eddy Simulation and the experimental data gave power laws close to 0.7.:

$$\delta_{20}/h = 0.053(x/h)^{0.7} \quad \text{(experimental)} \qquad (6.14)$$

$$\delta_{20}/h = 0.17(tU_T/h)^{0.7} \quad \text{(simulation)} \qquad (6.15)$$

A good agreement between experimental and theoretical temperature profiles was obtained, (Figs.(6.23), (6.24)), experimental point temperature profiles being compared with simulation temperature profiles at the relevant time step. This agreement was good despite the fact that equations (6.14) and (6.15) imply a convective velocity of $5.3U_T$, a very low figure when compared to the mean velocity of the flow, which is $15.4U_T$ (approximately 30%).

An experimental streamwise averaged temperature profile was also determined, and compared with a time-averaged simulation temperature profile, (Fig.(6.25)). Again good agreement was found.

Having established a correspondence between the spatially dependent experimental results and the temporally dependent simulation results, simulated holograms, or pseudo-holograms were constructed from the simulation data. To simulate the spanwise averaging encountered experimentally, the simulation data were

also spanwise averaged and the resulting data plotted as a series of isotherms, (Fig.(6.26)).

Due to the random, chaotic, nature of turbulence it is obviously impossible to try and identify detailed structures occurring in both the experimentally obtained temperature contours and those derived from the simulation. However, a broad similarity can be observed between the two plots put forward. Of course, with the simulation data the possibility exists of producing temperature contours at particular spanwise stations, (Fig.(6.27)). This is particularly useful as it can reveal the details of the thermal eddies that are smeared out by spanwise averaging, and give a clue as to what sort of structures in the spanwise averaged contours correspond to these eddies.

CHAPTER 7

AUTOMATIC ANALYSIS OF COMPRESSIBLE FLOW INTERFEROGRAMS

7.1. INTRODUCTION

An investigation into the influence of blade incidence upon the flow within low pressure steam turbine blading was initiated at the C.E.G.B's Marchwood Engineering Laboratories. This took the form of an experimental investigation and a companion computer simulation; holographic interferometry being used to obtain spanwise averaged density contours for a range of blade incidence angles, and a two-dimensional Navier-Stokes solver, TURBINS, being used to obtain predictions of the density field at zero blade incidence. The results obtained from both methods were then compared, the experimental results acting as a validating source for the computer code as well as providing intrinsically useful data.

The experimental side of this investigation has been dealt with thoroughly in Chapter 4, typically obtained holographic interferograms of the cascade section being presented, (Fig.(4.5)), and a complete description of the experimental equipment also being detailed. This Chapter will very briefly describe the computer simulation, and then move on to cover in more detail the automatic fringe analysis techniques used to extract quantitative data from the holographic interferograms.

7.2. COMPUTER SIMULATION

A two-dimensional flow prediction program "TURBINS" (Dawes et al. [1978]), was used to predict the flow field within the M.E.L. Incidence Cascade, specifically for the zero incidence case. TURBINS was designed to predict turbomachinery blade passage flows, and it solves a system of equations describing steady, compressible, viscous, isentropic flow in two dimensions, using a time-marching finite volume methodology and a quasi-orthogonal mesh. Turbulence is included in the form of an eddy viscosity which is described by a simple two-layer mixing-length model. The inflow and outflow boundaries of the computational mesh are parallel to the stagger line. The boundary conditions require constant stagnation pressure and flow angle at inflow and constant isentropic Mach number, i.e. constant static pressure, at outflow.

An example of the computer simulation output is shown in (Fig.(7.1)). If this figure is compared with the extracted quantitative experimental data, (Fig.(7.4) and (7.22)) it can be seen that many of the flow features are correctly predicted, and a reasonable density field extracted. A greater insight into this aspect of the project may be obtained from Dawes et al. [1978] and Ball et al. [1987].

7.3. HARDWARE AND DATA ACQUISITION

Each holographic plate contained a view of the complete cascade section, comprising some seven blade passages. The

resolution of the system required that a maximum of one blade passage at a time be studied, if all the relevant fringes were to be detectable (section 5.2.2), and it was thus found necessary to construct an angled framework on which a two-dimensional array Charge Couple Device (C.C.D.) camera could be mounted. This allowed the camera to be rigidly traversed the length of the cascade section, allowing one blade passage to be acquired and digitised at a time. The holographic plate was reconstructed using a point white-light source, removing the problem of laser speckle.

The output from the C.C.D. camera was then digitised by a Matrox VAF-512 8-bit video digitiser, and the subsequent digital image stored in two Matrox RGBGRAPH video framestore boards, providing effectively a 512 x 512 x 8 bit image store which allowed for an assignation of 255 grey levels to the digitised image.

The host computer was an Intel iSBC86/14 Single board computer, with a CPU 8086 running at 8 MHz. A 768 Mbyte RAM was available on the multibus in the form of a 512 kbyte board and a 256 kbyte board. It can be seen that this would effectively only allow a 64 x 64 x 8 bit region of the image to be buffered at any one time. For this reason the general course was to access the framestore direct, either grabbing individual pixels or a horizontal or vertical string of pixels. This procedure greatly improved the image access time, with benefits for the subsequent analysis routines.

A complete rundown of the hardware and standard software used can be obtained from Appendix [D]. A schematic diagram of the image processing system can be seen in (Fig.(7.2)), and a photograph of the reconstruction and data acquisition set-up in (Fig.(7.3)).

7.4. IMAGE ANALYSIS

The major objective of the automatic analysis system was to produce an iso-density contour map, similar to that obtained by hand, (Fig.(7.4)), but very much faster and more accurately. This would have the advantage that all fringe data would be stored in a form that was both easily retrievable and easily manipulable for future processing.

Typically hand analysis of a blade passage took about an hour.

From the complexity of the fringe field and the necessity for a complete field analysis, it was apparent that a two-dimensional form of image analysis system was required (section 3.1.4). This involves binarising the digitised fringe data, extracting the fringe coordinates, and then ordering these extracted fringes.

The initial requirements were for the suitable preparation and enhancement of the digitised fringe-field data, so that the subsequent fringe analysis routines could operate effectively and consistently. This aspect of the work is covered thoroughly in Chapter 5. We shall therefore commence this section assuming suitably masked and enhanced image data.

7.4.1. Image Binarisation

The masked, enhanced grey-level fringe data was now converted to a two tone image with the use of a binarisation technique. This stage was very important as the fringe field had to be segmented consistently over its whole extent, to allow an accurate extraction of the fringe coordinates by the following routines.

This desire for accurate segmentation had to be balanced against the computational expense of the process used. Statistical methods for binary segmentation, such as that proposed by Lahart [1979] were considered and then rejected on the grounds that the increased algorithm complexity and computer expense were not justified by the expected accuracy of segmentation. Several algorithms were tested for effectiveness, and these are described below.

Fig.(7.5) shows a fringe field that has undergone a simple thresholding process, the thresholds being set at (a) 120 and (b) 150. This type of procedure takes no account of possible variations in the background luminance intensity over the image data. Because of this some regions of the image are poorly segmented, fringe data being lost in these areas.

A technique for correcting this variation in the background intensity, such as that described in (5.3.4), could be used to remove many of the difficulties experienced with straight binary

thresholding. However, it was decided that a more efficient algorithm could be produced by including such a correction factor in the binarisation algorithm itself.

A new thresholding technique was then tried, this time the image being divided into small regions and the local average grey-level being used as the threshold for the local region. Typically regions 32 pixels square were used. A typical result may be seen in (Fig.(7.6)).

Although this method did correct for uneven background illumination, it was found that discontinuities arose at the region boundaries, destroying its usefulness for further analysis routines.

Binarisation by a floating threshold technique, as used by Becker [1982, 1985], was then tried. In this case if the grey-level value rises above a value of:

$$MIN + \Delta(A_L + A_T)/2 \qquad (7.1)$$

the following pixels are set to a grey-level of 255, and the grey-level value drops below a threshold defined by:

$$MAX - \Delta(A_L + A_T)/2 \qquad (7.2)$$

the following pixels then being set to a grey-level of 0. This process is then repeated until the whole scan line has been

binarised, and is then repeated for all the scan lines over the image data, a typical threshold function being shown in Fig.(7.6).

In the equations MIN and MAX stand for respectively the minimum grey-level and the maximum grey-level encountered since the last change. A_L is the average grey-level over some local region, usually a 32 pixel square region, and A_T is the average grey-level over the whole flow field. Both averages are used to prevent the threshold value becoming too small in predominantly dark regions, and too large in mainly white regions. Δ is a constant used for fine-tuning the algorithm, and it should lie somewhere between 0.2 and 0.3. Deciding on the best value for Δ is purely an empirical thing, and (Fig.(7.7)) shows some typical results obtained for a Δ of (a) 0.2, (b) 0.25, and (c) 0.3. It was found that best results were obtained using a Δ of 0.25.

It was also noted that the direction in which the image is scanned affects the results of this binarisation procedure, and (Fig.(7.8)) shows the differences resulting from horizontal and vertical scanning, a Δ of 0.25 being used in both cases.

Such floating threshold routines were found to operate effectively in regions of broad diffuse fringes, but less so in areas of narrow, closely spaced fringes. This was due to the threshold not tripping at the appropriate moment, due to some influence of noise or poor contrast, and so producing an extended arm of white or black pixels along the scan line. Such arms can be clearly seen in (Fig.(7.8)). The application of a binary smoothing algorithm

section (7.4.2) was found to greatly reduce the effect of such false extensions, but problems were still experienced with false fringe corrections in regions of thin, closely spaced fringes.

A binary segmentation technique that made use of bilinear interpolation was also tested, the algorithm used being very similar to that used for the correction of a varying background intensity. The image was divided up into a number of small regions, and the local average grey-level for each region was used as the node on a grid of such values. The average grey-level value for any point in the image was then obtained by bilinear interpolation between the four adjacent node points, (Fig.(7.9)). This grey-level was then used as the threshold for the image pixel at the point. Two techniques were tried, one in which the nodes on the mesh consisted of mean local grey-scale values, the other in which the nodes consisted of median local grey-scale values. Typical results are shown in (Fig.(7.10)).

It can be seen that both the mean and median approaches work consistently, with some problems arising in regions of broad diffuse fringes. This problem is due to the nature of the algorithm. Because the fringes are broad the threshold value will vary slowly between node points. However the presence of noise, even after smoothing, can cause fluctuations about the threshold value, especially in the fringe edge regions, where the grey-level slowly changes from a low to a high value. A small contribution from spanwise averaging exacerbates this problem. The net result

is regions of poor segmentation around the edges of the broad fringes, a problem that can be improved by binary smoothing, but not removed completely.

Overall it was found that the mean method was the most effective procedure,the median method leading to other areas of poor segmentation, such as around the blade tip region at the stagnation end of the blade.

The final segmentation routine that was used combined a background mean bilinear interpolation routine with operator defined regions of horizontal and vertical floating threshold segmentation to deal with the broad fringe regions. A typical example of an image binarised using this routine is shown in (Fig.(7.11)).

7.4.2. Binary Image Enhancement Routines

Having binarised the fringe field data, it was often found necessary to apply some binary image enhancement techniques to clear up regions of poor segmentation that may have arisen. Two facilities were available:

(i) Binary smoothing

This worked by looking at a nine-pixel neighbourhood and determining how many of the eight pixels surrounding the central pixel have the same value as the central pixel. If there are less

than a certain limit, in this case three, the value of the central pixel is reversed so that it coincides with the majority of the surrounding pixels.

Such a routine is useful for removing 'pepper and salt' type noise, i.e. localised spots of wrongly segmented pixels. It is particularly useful for removing the extended 'arms' that occur with the floating threshold binarisation process, as these are usually a single pixel in width.

(ii) **Binary shrink/expansion**

This routine was applied locally over an operator defined window, and was used to remove poorly segmented regions that were too large for the binary smoothing routine to handle. These regions typically occurred on the edges of broad fringes.

The routine searched a pre-set window, and located regions of segmentation that were completely enclosed by a different region, such as a small black region appearing inside a white fringe. The option was then given to either shrink or expand this region, and if desired the region could be made to disappear completely.

Care had to be taken when using this routine as once connectivity of regions had been lost, it wasn't possible to regain it.

Variable Size Windowing

Windowing the fringe field into regions of varying size, dependent on the local fringe frequency, is a very useful technique both for local thresholding, and for checking the validity of detected fringes (a certain fringe frequency being expected in a particular area). However, a problem arises as a knowledge of the fringe density is needed to accurately determine the correct window size over a local area, but the fringe frequency is best determined by using local windows of varying size.

7.4.3. Fringe coordinate definition

At this stage the image data had been suitably masked and binarised. The next step was to somehow define the position of each fringe from this data.

7.4.3.1. Fringe thinning for coordinate definition

This was the first method considered for defining the fringe locations. The idea was to thin the white fringes and to use the remaining centre line as the fringe definition.

Fringe thinning is a standard image processing technique, and thus much literature exists concerning its implementation. This has been discussed to a certain extent in (section 3.1.4.3) and from this discussion it becomes apparent that two distinct forms of fringe thinning routine are available. That is serial process thinning and parallel process thinning. However, it has been found, Saraga [1974], that parallel thinning algorithms are more suitable than sequential ones when practical applications are involved.

Several thinning algorithms were tested for effectiveness. These were the sequential method suggested by Rosenfeld and Pfaltz [1966], and parallel thinning algorithms suggested by West [1986], Arcelli [1975] and Hilditch [1966].

7.4.3.1.1. Sequential Thinning Algorithms.

The serial process thinning algorithm suggested by Rosenfeld and Pfaltz, and described in (section 3.1.4.3) was tested on typical fringe data. The procedure assigns an order to elements that increases with an increasing distance from some background set. The data may then be reviewed to pick out maximally valued pixels, these then representing the skeleton of the object.

The procedure was very quick in operation, taking only 1¼ minutes to process the test data. However the results obtained were very unsatisfactory. An increasing order was assigned to pixels as their distance increased from some background set of pixels. However this background set was only definable for one side of the fringes, i.e. if the image was scanned from left to right, top to bottom, only the zero or black regions to the left or above a white fringe were definable as the background set. This led to an increasing pixel order over the white range, with a sudden discontinuity when the next black fringe was reached.

Typically assigned numerical orders are shown in (Fig.(7.17)) for a portion of the fringe field. The result of skeletonising such a fringe-field is shown in (Fig.(7.13)). The problem here is that the extracted skeleton cannot be said to represent the medial lines of the white fringes, and so the data is effectively worthless.

7.4.3.1.2. Parallel thinning algorithm

Three algorithms were tested. These were due to Hilditch described in section (3.1.4.3), and Arcelli and West.

The algorithm due to Arcelli was very simple. The following masks were applied to the data in the order shown (the choice of application order was not trivial), the central element lying in each configuration being erased.

0	0	.	0	0	0	.	0	0	1	.	0			
0	1	1	.	1	.	1	1	0	1	1	0			
.	1	.	1	1	.	.	1	.	.	.	0			
	(1)			(2)			(3)			(4)				
.	1	.	.	1	1	.	1	.	0	.	.			
1	1	0	.	1	.	0	1	1	0	1	1			
.	0	0	0	0	0	0	0	.	0	.	1			
	(5)			(6)			(7)			(8)				

The algorithm due to West was slightly more complicated. The data was searched four times, locating four elements corresponding to the configurations:

.	.	.	.	0	.	.	.	.	.	.	.
0	1	.	.	1	.	.	1	0	.	1	.
.	.	.	.	.	.	.	.	.	.	0	.
	(1)			(2)			(3)			(4)	

When an element was found that corresponded to the relevant mask, a check to see if the element was a skeleton point or not was performed using the following masks, the element being assigned as a skeleton point if it fulfilled the mask criteria:

x	x	x				x	0	y									
0	1	0				x	1	y		where $\Sigma x \neq 0$							
y	y	y				x	0	y		and $\Sigma y \neq 0$							
	(i)						(ii)										
+	+	+		2	0	+		+	0	2		+	+	+			
0	1	+		0	1	+		+	1	0		+	1	0			
2	0	+		+	+	+		+	+	+		+	0	2			
	(iii)				(iv)				(v)				(vi)				

where $\Sigma + \neq 0$ and the element 2 represents a previously found skeleton point.

Elements not satisfying the skeleton point criteria were deleted.

The parallel thinning routines tested worked effectively, but were found to take an excessive time to complete, typically more than 10 minutes. Typical examples obtained from test fringe patterns are shown in (Fig.(7.14)).

Although the parallel fringe thinning algorithms were found to work reasonably well in certain areas of the fringe field, several disadvantages quickly became apparent. These were:

(i) the thinning algorithms are computationally expensive, taking a long time to run due to their iterative nature.

(ii) the thinning algorithms tend to produce false features such as small sections of false median lines that branch out from the true median lines. As branching may be expected to occur in certain regions in actual fact, it is very difficult to separate the false branches from the true branches.

(iii) It is necessary to anchor the ends of the medial line defined by the algorithm to the fringe field boundaries, to prevent a slight contraction of these points. This may be done by defining extra criteria for the points adjoining masked border sections.

(iv) Perhaps most importantly if a region has been poorly segmented it is often the case that the extracted set of medial lines bears very little resemblance to the actual fringe structure in that area, leading to erroneous fringe information.

For these reasons an alternative method for extracting the fringe coordinates was considered, that is using the fringe edges.

It should be noted that in some cases fringe edges might not necessarily be correctly located.

7.4.3.2. Edge Detection for Coordinate Definition

Using the fringe edges to define the fringe coordinates had several advantages. These were as follows:

(i) It was possible to obtain the location of the fringe edges very quickly, the algorithm used being the equivalent of a single complete pass of the iterative parallel thinning techniques.

(ii) The fringe definition was more accurate as two sets of ordinates defined a fringe position, as opposed to a single medial line.

(iii) For each fringe edge it was possible to assume that no branching should occur, as the fringe edges only defined complete contours. Thus any points where branching was found to occur could be studied with a view to determining which branch was a false structure.

(iv) As the fringe data itself was not altered, it was possible to correct, in part at least, edge data for regions which had been wrongly segmented.

These points led to an edge point coordinate scheme being adopted.

The fringe edges themselves were located using a simple edge detection routine based on four neighbour connectivity. A supplementary criterion that at least three of the other pixels in a nine-pixel neighbourhood had to conform to the relevant grey-level was also adopted, to make the routine less susceptible to false edge-points created by noise. The mask used for this algorithm is shown in (Fig.(7.15)).

Located edge-points were assigned a unique grey-level value. Thus at this stage the image field was segmented into four distinct grey-level regions, representing the physical objects in the flow field, the binary fringe data, and the edge points.

7.4.4. Fringe Tracking

The detected edge points had now to be traced and written to the hard disc as separate fringe structures.

The image data was scanned from left to right and top to bottom. Each time the unique grey-level signifying an edge-point was detected, the fringe tracking routine commenced. As each fringe was tracked it was assigned an alternative grey-scale value, so as to avoid redetection. After the fringe in question had been traced to a conclusion, the routine returned to the scan point last reached when the fringe was detected, and the scanning re-commenced.

The tracking procedure itself was reasonably robust. The first edge pixel located was investigated to see what sort of start point it was. If a physical boundary was one of the eight surrounding neighbours, it was labelled as a proper start point. If not, and it had more than one edge point neighbour, it was regarded as potentially the mid-point of a fringe, or part of a closed fringe. If only one neighbour was an edge point and there were no physical boundary neighbours, the fringe was assumed to have a poor start point, i.e. the likelihood was that this region had been poorly segmented. The assumption made here was that all fringes should either end on a physical boundary, or be closed fringes. Any deviation from these criteria was then supposed to occur in a region of poor segmentation.

Having located the initial edge pixel, tracking was then implemented by assuming simple eight-neighbour connectivity, i.e. the eight neighbours surrounding a located edge pixel were searched for other edge pixels.

Three possibilities existed at this stage, they were:

(i) no edge point neighbours
(ii) one edge point neighbour
(iii) more than one edge point neighbour.

To improve the search technique a bias system was introduced.

The last direction moved between edge pixels was set as the bias direction, and the next step started looking in this direction, and then worked back, (Fig.(7.16)).

If criterion (ii) was observed, that is, only one connected edge-pixel, the algorithm obviously proceeded on to this pixel, using it as the start point for the next search.

If criterion (iii) was observed, that is, more than one edge-point neighbour, then a branch point was detected. Now as fringe edges were being traced, a branch point could be assumed to be a false artefact. This reasoning is explained in (Fig.(7.17)). The problem is to trace the true fringe, and neglect the extraneous branches. This decision was made on two criteria. The first was the aforementioned bias criterion. The second was a prefer criterion, (Fig.(7.16)). The type of edge that was being traced was recorded, i.e. whether the edge points were left, right, top or bottom edges, and a prefer value assigned accordingly. Fringe tracking then continues with the fringe pixel that best satisfies both the bias and the prefer criteria.

However, a note was made of the point at which the branch point was located. If the advance direction chosen then turned out to be false, that is, the fringe being tracked ended in a false end point within a defined distance from the branch point, the algorithm then backed up to the branch point and tried one of the other possible branches.

If criterion (i) was observed, that is, no neighbouring edge-points, then a fringe end-point was assumed. As with the fringe start points, three possibilities existed. These were a true end-point ending on a boundary, a closed fringe, or a false end-point due to poor segmentation

If the fringe start point now indicated that the fringe being tracked had initially been located somewhere along its length, and not at the start, the tracking routine returns to the initially located point, and then tracks the fringe to a start point.

The tracked fringe data then underwent a re-assessment. If the tracked fringe was shorter than a certain threshold, in this case twenty pixels, it was discarded, as the likelihood was that it was due to some spurious artefact introduced by poor binary segmentation.

Retained fringe data was then inspected for cut-points. These were regions in which the fringe data should be separated, as the tracked fringe represents two separate edges, spuriously joined because of poor segmentation. A typical example is shown in (Fig.(7.18)), and it can be seen that these cut-points are characterised by a rapid reversal of both the fringe direction and the edge orientation.

To isolate a cut-point from the fringe data the bias and prefer criteria were looked at over a local region of the fringe. A

position was being looked for in which the prefer criteria altered from being, for instance, a left hand edge, to being a right hand edge, in conjunction with a change in the bias criteria of at least 135°, over a short range of fringe data, typically a ten pixel length.

Fig.(7.19) shows a series of tracked fringes with the cut-points defined by crosses. Some regions look as if they should have been cut but no cross appears. This is because the previous checks have already correctly identified a seemingly connected fringe as in fact being two separate fringes wrongly segmented.

Having located all the cut-points, the fringe data is then re-ordered into separate fringe strings, each component being defined by the cut-points.

The traced fringe data was then written into a file as a string of two-byte words, with an initial two-byte word reserved at the top of the string for the fringe order. Initially this reserved space was filled with a value of 255.

Having completed the scanning of the image field all the fringes have been located and traced, and stored on file. A flow diagram of the fringe tracking procedure is given in (Fig.(7.20)).

7.4.5. Fringe Display

A fringe display routine was written that allowed the fringe data in the file to be displayed on the monitor. The intensity with which each fringe was displayed depended directly on the fringe order of the fringe. Thus at this stage all the grey-levels were displayed with a grey-level of 255. After ordering the fringes will be displayed with a grey-level commensurate with their order, greatly facilitating further data processing.

7.4.6. Fringe Ordering

Having located all the fringe coordinates the final stage is to order the fringe system.

Initially a fully automatic fringe ordering system was designed. This utilised the points defined for masking the blade section to trace around the blade, ordering the fringes encountered. The start position, that is, the position of the zeroth order fringe at the stagnation point, had to be located by the operator, as its position was dependent on the blade incidence angle.

Having ordered the fringes surrounding the blade the other fringes were ordered from these ordered positions, working from the blade position out to the edges of the image.

This fully automatic ordering system was found to run into a lot of trouble, and it proved to be very unrobust. Two major

difficulties were found. The first was that the shock regions, which could not be segmented properly and which should not be ordered, were in fact ordered. This led to the false ordering of fringes in the surrounding regions. The second was that regions of closed fringe systems exhibited the usual problem of indeterminancy, that is, should the fringe order increase or decrease as the centre of the loop system was approached. The only way to actually determine this was by using *a priori* knowledge about the flow system, something which proved to be difficult to write into an automatic analysis routine.

The conclusion drawn from this was that some form of semi-manual ordering system was required. This had the advantage of being flexible, adaptable to other fringe analysis situations, and of allowing the use of *a priori* knowledge.

The form of the semi-manual ordering system was as follows: The operator defined a start point and an end point with a cursor, and whether the fringe order between these two points was increasing or decreasing. The location of every fringe point located across this line was then written into a work array. The points in this array were then compared, one at a time, with the fringe data on file. The fringe containing such an edge point was then assigned the correct order, the order being written into the previously mentioned reserved two-byte word at the start of every fringe data string.

Due to time limitations the automatic analysis system devised was not as complex as those proposed by Becker, which have a more general applicability.

Having worked through this initial array of points, the operator was then given the choice to specify another line using the last end point as a start point, or to start at another point in the fringe field. A typical series of operator cursor moves needed to order a complete fringe field is shown in (Fig.(7.21)).

At the end of this operation all the fringes have been assigned a correct order in the fringe data structure, and the fringes can be displayed with a grey-level equivalent to the fringe order. Typical examples of ordered fringe fields are given in (Fig.(7.22)).

7.5. DISCUSSION

7.5.1. Fluid Flow Considerations

The flow under study is a transonic compressible flow. The flow enters each blade passage subsonically, is accelerated by the blades to a supersonic speed, and is then reduced to a subsonic velocity after the tail-end of the blade. The compressibility of the flow leads to the changes in the refractive index of the flow field that are measured by the holographic interferometry technique, as explained in Chapter 4.

Each blade passage in the cascade section exhibits a very similar flow pattern, a typical example being shown in (Fig.(7.23)). The lettered regions are discussed here.

Region (a): this is the stagnation point, the incident flow being brought to rest at this point on the blade. The stagnation point is dependent on the angle of incidence, and is important in that the properties throughout the blade passage are determined relative to those at this point.

Region (b): this region of narrow, closely spaced, fringes indicates that the flow is accelerating rapidly over the top of the blade.

Region (c): this region of broad fringes indicates that the flow is accelerating only slowly over the underside of the blade, as would be expected.

Region (d): these are non-isentropic trailing shock regions, caused by the supersonic flow suddenly decelerating to a subsonic flow. The lower shock is very much weaker than the upper shock, and close inspection indicates that it is possible to order fringes through this region, the discontinuities experienced here being slight.

Region (e): this indicates a weak reflected shock, or Mach wave.

Region (f): this is the wake region, formed by the blade boundary layers separating from the blade at the trailing edge. This region is of very little interest in the analysis procedure.

7.5.2. Problem regions for the automatic analysis routine

Several of the flow regions create problems for the analysis routines.

Region (d), specifically the strong upper shock, and region (f) the wake region, create problems in that they are difficult to binary segment effectively. This is because both regions contain fringes whose spacing is outside that of the system resolution, as well as complicated structures. Both such regions may be ignored in the analysis as they play no useful part, but they do tend to interfere with automatic fringe ordering routines. The solution to this problem would be either to mask out the shock and wake regions, or adopt a semi-automatic ordering scheme as suggested.

The region of accelerating flow at the tip of the blade, region (b), also causes segmentation problems. Towards the blade itself the fringe spacing becomes very narrow, and the fringe contrast can suffer. It is possible to alleviate this problem by adopting the procedures outlined in Chapter 5 to increase the system resolution. However it was still found that problems arose with one fringe edge incorrectly being joined to another, and the detection of possible cut-points was initiated specifically for these regions.

7.5.3. Fringe Ordering

It should be noted that the fringe edges, and not the fringe centres, were traced with this analysis routine. The centres of white fringes take integer values, that is, 0, 1, 2, 3.....N, and the centres of black fringes take half integer values, that is 0.5, 1.5, 2.5,....N.5.

Thus the traced fringe edges should take the values, 0.75, 1.25, 1.75, 2.25.....N.25. However the ordered fringe traces are shown numbered with integer values. The reason for this is purely practical. The computer system used during this part of the project had no facility for writing to the screen. Thus each number to appear on the screen had to be made up from scratch by changing the relevant pixels in the framestore to a grey-level of 255, so approximating the figure. This process meant that a minimum figure size was necessary for the numbers to be decipherable. This space constraint, added to the difficulty of producing decimal point figures, led to the use of integer values to give a visual display of the relative fringe orders. Thus the automatically analysed fringe traces are not directly comparable with the TURBINS plot or the hand analysed trace, but they give a very good idea of the kind of results expected. It is of course a trivial exercise to correctly reorder the fringes in the data file.

7.5.4. Processing time

The major advantage of the automatic analysis system is that it allows an unskilled operator to produce an accurate iso-density map of the fringe field in a short time compared with that necessary for a manual analysis, and the results are in a form that is amenable to further computer processing.

A definitive processing time for the system is not available, as this depends very much on the amount of pre-processing needed, that is image enhancement and possibly image merging routines, as well as the complexity of the particular fringe field under study. However, it can be said, from experience gained by processing many of these holographic interferograms, that a complete density map of the flow field in a single blade passage may be obtained in between ten and fifteen minutes.

7.5.5. Possible Improvements to the System

A flow diagram for the complete automatic analysis system is given in (Fig.(7.24)). Several improvements and modifications may be suggested to improve the performance of this system as it stands now. These are:

(i) the bilinear interpolation of mean grey-levels to produce thresholds for binarisation could be improved by making the node points a function of the local mean value and a

global mean value, instead of just a local mean value. This would prevent poor thresholding over local regions in which a broad fringe predominates.

(ii) after the binarised fringe edges have been detected and assigned a unique grey-level, a thinning routine should be run that is sensitive to the unique grey-level denoting these edges. This would ensure that the fringe edge data is a connected string only one pixel in width, thus aiding the tracking procedure. The time needed to run such a thinning procedure would of course be small as the detected edge data should be very near the thinned version already.

(iii) some means of reducing the amount of data storage necessary by the implementation of a redundancy algorithm should be available. At present this is not a problem, but with a large number of complex interferograms it could become so. The most attractive method for such a redundancy algorithm is to represent each fringe as a subset of vertices, a procedure proposed by Ramer [1972].

CHAPTER 8

MULTI-DIRECTIONAL HOLOGRAPHIC INTERFEROMETRY AND THREE-DIMENSIONAL TOMOGRAPHY

8.1. PROPOSED FURTHER WORK

Due to the optical geometry used in the discussed investigations of both heat transfer and compressible fluid flow, specifically the use of a collimated object beam passing through the test volume, the holographic interferograms studied have been two-dimensional in nature. That is the reconstructed holographic interferograms have only given refractive index distribution details in a two-dimensional plane normal to the propagation direction of the plane waves composing the collimated object beam. However holographic interferometry does have the potential for three-dimensional whole field fringe data, and it is proposed to use this capability in future investigations.

The use of diffuse illuminated and/or multi-directional holographic interferometry allows a series of two-dimensional interferometric fringe systems to be obtained. Using suitable techniques the pathlength data obtainable from these interferograms may be inverted to produce an estimation of the refractive index, and hence density field extant in the test volume.

Such a process is known as tomography, and a number of reconstruction procedures are available.

Using such optical and reconstruction methods the investigation of three convective heat transfer systems is proposed. The first two are nominally symmetrical well-documented thermal cases, and they are proposed to allow the testing of the optical techniques, and the development of a suitable tomographic reconstruction technique. They are:

a) a (natural convection) thermal plume,

and

b) a (forced convection) jet mixing study.

The simple test rig proposed for these studies is shown in (Fig.(8.1)). The geometry allows for data gathering over an angle of 180°, the importance of this being discussed in section [8.3]. This rig will be used to investigate the effect of a reduced angle of view on the reconstruction procedures developed, and the double source allows the refinement of asymmetry to be introduced.

Having gained experience both with the optical procedures involved and in the development of an optical reconstruction method, the technique may then be applied to a study of the natural convection roll instabilities in a rectangular box, without and with horizontal forced flow. The existing wind-tunnel,

(Fig.(1.1)), could be adapted for this work, and the experimental results compared with those developed by Oertel [ ], and the theoretical predictions of Professor P.G. Daniels (T.C.U. Mathematics Department). For the refinement of additional forced flow, Professor Daniels intends to provide corresponding analytical data.

8.2. THREE-DIMENSIONAL HOLOGRAPHIC INTERFEROMETRY

The possibility of applying optical holography for the provision of diffuse illumination interferograms was first reported by Heflinger et al. [1966] for aerodynamic studies.

In order to measure three-dimensional asymmetric temperature fields it is necessary to make multi-directional measurements of optical pathlength through the medium under study. Such measurements are obtainable by the insertion of a diffuser just prior to the test section in an off-axis holographic interferometer, (Fig.(8.2)). This diffuser acts as a multiple series of point light sources, scattering light in all directions through the test section. On reconstruction of the holographic plate, the fringe field may be viewed from any direction in which a source point from the diffuser has passed both through the test section and the holographic plate. This effect gives three-dimensionality to the interferometric fringe-field.

8.2.1. Diffuser Considerations

If one holographic plate is considered, the limiting factor to the angle of view, or angular range, over which pathlength data may be obtained is the effectiveness of the diffuser, that is the efficiency with which light is scattered by the diffusing plate.

Two types of diffuser are available, surface diffusers, such as ground or frosted glass, and volume diffusers such as opal glass. The volume type diffuser consists of a three-dimensional collection of very small scattering centres, and gives a much better angular distribution of irradiance of light, as is indicated in (Fig.(8.3)). However a surface diffuser affects only the optical pathlength of the transmitted light, whereas the volume diffuser affects both the amplitude and the phase of the transmitted light. The light is randomly polarised by the multiple scattering in the volume diffuser, George et al. [1975], and this depolarising effect is important with regard to interference with the reference wave, as explained in Chapter 2. Although the depolarisation effect can be compensated by the positioning of a polariser in front of the hologram during recordings, Heflinger et al. [1966], the added complication can be undesirable.

8.2.2. Multi-directional interferometry

Tomographic reconstruction techniques often require pathlength data over an angular viewing range of 180° for a

complete solution. Although this problem has been tackled with a view to reducing the angular requirement, details are given in section [8.3], it is desirable to have an angular view as large as the geometry of the test section will allow. It is then found that a single diffuser, even if a volume diffuser, will not allow angular views of a range greater than about 45° before an unacceptable drop in the irradiance occurs. This factor necessitates the use of multi-directional interferometric techniques, basically the use of more than one object/reference beam pair through the test section.

The physical design and extent of such a multi-directional layout is obviously dependent on the test section and optical table geometry, but a typical example, as used by Mewes and Ostendorf [1986], is given in (Fig.(8.4)).

8.2.3. Fringe localisation and reconstruction techniques

Although three-dimensional interferograms are pleasing to view, an attempt to photograph the fringe system or resolve fine fringes will prove to be unsatisfactory. This is due to the fringe localisation effect, Vest [1979], Vest and Sweeney [1970], depth of field problems and image intensity variations.

When the hologram is viewed, the fringes apear to be localised in some surface in the vicinity of the test object. As the viewing direction is varied, both the fringe pattern and the surface of fringe localisation are observed to change. In the general case of

a large, unsymmetrical refractive index field, the surface of apparent fringe localisation may be quite complicated. This leads to depth of focus problems when trying to photograph the fringe systems. Two methods for solving this problem exist.

The first is to use a small aperture when photographing the fringe system, thus obtaining the necessary depth of focus.

The second is to reconstruct the object wave using a thin laser beam technique, the plate being reconstructed a point at a time, Chau and Zucker [1973]. This increases the depth of field tremendously, the fringe image being in focus almost everywhere along the direction of the projecting image.

Both techniques run into one major problem. The use of a small aperture or a thin reconstructing beam cuts off the high frequency content of the object illumination, causing the appearance of laser speckle (it should be remembered that three-dimensional holograms must be reconstructed using a coherent light source) and hence decreasing the signal-to-noise ratio. As the visibility of the interferometric fringes rapidly decreases as the fringe frequency becomes of the order of the characteristic speckle frequency, this can be a serious problem. Tanner [1967] has shown, for example, that for a typical object having an axial dimension of 10 cm, sufficient fringe clarity would be obtained only for optical path changes not exceeding about 1 fringe per mm.

There are two possible solutions to this problem. One is to maximise the aperture or reconstructing beam size to allow for maximum signal-to-noise ratio while still keeping the minimum required depth of focus. The other is to replace the diffuser with some method for providing a number of discrete viewing angles. Although this solution would now allow the viewing of the interferograms from a series of completely arbitrary directions, this should present no problems. This is because the numerical solution of the tomographic reconstruction techniques by computer will obviously require discrete data anyway, which is what will be obtained. The problem will be to design a grating that will present enough discrete pathlength data to effect a solution.

8.3. TOMOGRAPHIC RECONSTRUCTION TECHNIQUES

All tomographic measurement techniques share the common feature that the object volume is traversed by beams from several directions. The measured values for each beam direction are obtained as projections of a particular cross-sectional plane, and are evaluated separately for each plane. A typical measurement volume is shown schematically in (Fig.(8.5a)), individual cross-sectional planes being indicated by z_1 to z_3; the recorded measured values for any one plane z_k being shown in (Fig.(8.5b)) in the form of the image functions, $\Phi_i(\rho,\theta_i,z_k)$ for the four directions of irradiation.

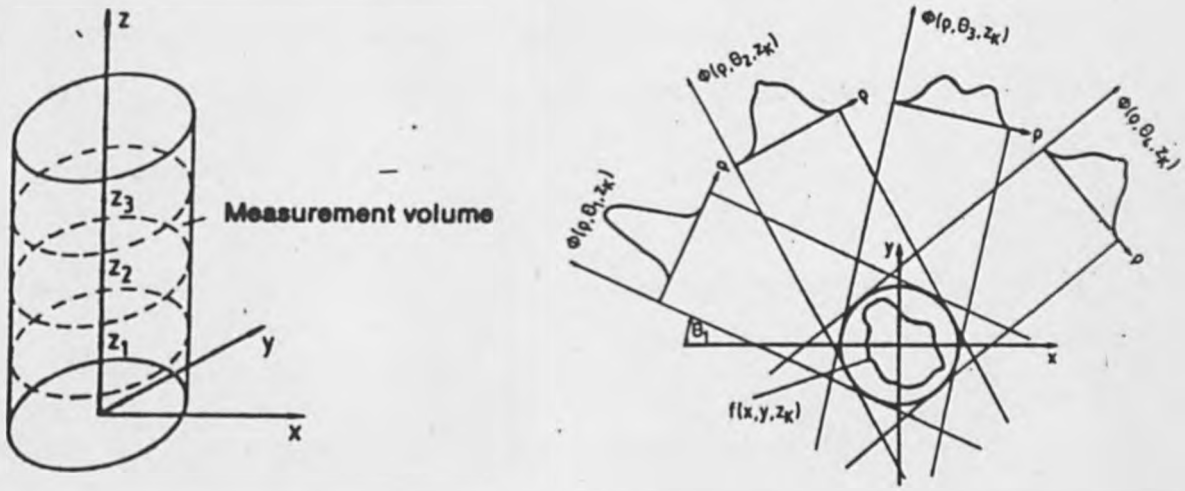

Fig.8.5.

(a) A typical measurement volume (b) Pathlength data gathering.

The relationship between the field function f and its projection in the direction θ_i is given by the pathlength function Φ_i:

$$\int_{Si} f(x,y,z_k)\ ds = \Phi_i(\rho, \theta_i, z_k) \qquad (8.1)$$

As one cross-sectional plane is being considered at a time, this equation reduces to:

$$\int_{Si} f(x,y)\ ds = \Phi_i(\rho, \theta_i) \qquad (8.2)$$

We have previously established, in Chapter 4, that the field function f is the refractive index distribution in the test volume for such an application to holographic interferometry of phase objects. So:

$$\int_{Si} f(x,y)\ ds = \int [n_{ref} - n(x,y)]\ ds = \Phi_i(\rho, \theta_i) \qquad (8.3)$$

It can be seen that for the tomographic treatment the integral in equation (8.3) must be evaluated along straight lines, that is no z component can enter. Such a requirement is implicit in all tomographic reconstruction techniques, and necessitates the experimental investigator working in the refractionless limit. That is, ray curvature across the test volume due to refraction must be insignficant. This criterion obviously puts limitations on the test conditions.

In fact Snyder and Hesslink [1984] have proposed a tomographic technique that can deal with refraction errors, based on an iterative ray tracing technique as detailed in Chapter 4. This is computationally very expensive, and so of limited use.

The range of θ over which the data is actually collected is known as the angle of view, and equation (8.2) includes all possible beams included in the range $-90^{\circ} < \theta \leqslant 90^{\circ}$.

The problem to be considered is the inversion of the pathlength function, Φ, given in equation (8.2) to extract the distribution of the field function, f.

The first consideration of image reconstruction from projections was by Abel in 1826, who proposed an inversion scheme by which objects with circular symmetry might be reconstructed, Winckler [1948], Herlitz [1963]. Such a scheme is obviously very limited and the first really significant contribution to the general theory of reconstruction from a series of projects was that of Radon. Radon solved the integral equations relating two-dimensional non-symmetric objects to the projections, and the Radon inversion formula is the basis for many modern developments, both theoretical and practical, Radon [1917].

The first real solution of equation (8.2) was in the field of radio-astromony, Bracewell [1956], Bracewell and Riddle [1967], and involved a Fourier synthesis technique. The pathlength data for each direction of view may be used to generate a single radial line through the origin in the Fourier transform plane of f(x,y). The Fourier transform is then built up one line at a time until the entire frequency plane is filled. Then f(x,y) can be obtained by taking the inverse transform of the Fourier plane F(fx,fy). This approach suffers from the fact that it is computationally intensive, and needs several co-ordinate transforms. Also certain format problems arise in the treatment of the frequency plane, leading to the possibility of numerical instabilities.

To avoid this formatting problem a direct inversion technique was developed independently by Berry and Gibbs [1970], Alwang et al.[1970] and Junginger and van Haeringer [1972]. Such a

technique is in fact very similar to the convolution algorithms used for transverse section reconstructions implemented in Fourier space, as proposed by Ramachandran and Lakshminarayanan [1971]. This technique is alternatively known as convolution back-projection, or Fourier convolution.

Back-projection itself is a very simple method for reconstructing the field function, the measured values obtained along each line being projected back along the same line, the measured value being assigned at each point in the line. Pure back-projection gives only a crude reconstruction, high frequency components being smeared out leading to a blurring of the field function. To improve this a filtered back-projection algorithm may be used, otherwise known as rho-filtered layergram. This name comes from the fact that the radial co-ordinate of Fourier space was designated by ρ in the derivation by Bates and Peters [1971] and Smith et al.[1973]. The procedure is as follows: the projection data is back projected, a two-dimensional Fourier transform of the back-projection image is taken, and then multiplied by a filter function, and the field function is then obtained by an inverse two-dimensional Fourier transform.

This method is disadvantageous in that it is computationally intensive, two two-dimensional fast Fourier transforms being required. Once again a means of circumventing this problem exists, in which a back-projection and filtering method can be used in which only one-dimensional Fourier transforms are needed.

This technique is known as convolution back-projection, see Ramachandran et al, and the procedure takes the following form.

The projection data is Fourier transformed using a one-dimensional Fast Fourier Transform, and then the complex values of the Fourier coefficient are convolved with a suitable filter. Then an inverse Fourier transform is applied and the modified projection data are then back-projected.

Typical filters utilised in both the convolution back-projection and the filtered back-projection technique are the Butterworth, Hann, Hamming and Pazen filters. The filters and convolution functions are very application dependent.

The convolution back-projection procedure is computationally very attractive, and this is perhaps the most widely used reconstruction algorithm, Snyder and Hesslink [1984], [1985], Budinger (1979].

The algorithms detailed so far all have the major problem that an angle of view, θ, of 180° is needed for a solution. Such an angle of view is not always practicable with holographic interferometry techniques, and Sweeney and Vest [1973] have investigated some reconstruction algorithms that need a smaller angular range.

The most important of these is that of reconstruction using series expansions. These techniques all use a series expansion of the form:

$$\bar{f}(x,y) = \sum_{M=0}^{M-1} \sum_{N=0}^{N-1} a_{Mn} H_{Mn}(x,y) \qquad (8.4)$$

to represent f(x,y). $H_{Mn}(x,y)$ are the generating functions and a_{Mn} their coefficients. As only a finite number of terms are employed in the expansion, the series is in general only an approximation $\bar{f}(x,y)$ to f(x,y). Early work by Maldonado and Olsen [1966] was used by Matulka and Collins [1971] in their inversion scheme using series expansion, and an independent solution was arrived at by Cormack [1963]. These schemes however rely on the fact that the coefficients of the expansion are determined by substitution into the integral equation and subsequent orthogonalizing the result equations. Thus in the absence of symmetry a 180° range-of-viewing angle is still necessary. Alternative series expansions are presented by Sweeney and Vest [1973],[1974] that do not require orthogonalisation for the determination of the expansion coefficients.

A potential problem with this method is that of poor convergence.

Iterative techniques are the last category of reconstruction methods to be considered. These rely solely on the ability to adjust the parameters (reconstructed pixel values) such that when these values are projected the resulting projections are as close as possible to the measured data.

The best known of these iterative schemes is ART, algebraic reconstruction technique, and is given in its additive form as:

$$f_{ij}^{q+1} = f_{ij}^{q} + \frac{\rho_j - \sum_{1}^{N} f_{ij}^{q}}{N} \qquad (8.5)$$

where q is the iteration value, and in its multiplicative form by:

$$f_{ij}^{q+1} = \frac{\rho_j}{\sum_{i=1}^{N} f_{ij}^{q}} \cdot f_{ij}^{q} \qquad (8.6)$$

Initially all values of f_{ij} are assumed zero, and the known data are the projection data. An iterative procedure then ensues, with the solution becoming increasingly accurate as more projection data is involved.

ART is discussed by Gordon and Herman [1974] and a general survey of iterative reconstruction techniques is given by Herman and Lent [1976]. Specific applications of the technique are given by Chau and Zucker [1973], Oertel [ ] and Gordon, Bender and Herman [1970].

A comparison of many of the techniques detailed here is given by Sweeney and Vest [1973], and the results for a test object consisting of a double Gaussian function,

$$T(x,y) = T_o + 8' e^{[8(x-0.5)^2-25(y-0.28)^2]} + 10e^{[-8(x-0.5)^2-25(y-0.72)^2} \quad (8.7)$$

are given in the following table.

Method	No.of Views	Rays per View	Angle of view (deg.)	Average error (%)	Maximum error (%)	Computer time	Comments
Fourier synthesis	16	19	180	1.63	4.32	3.4	
Direct Inversion	16	19	180	0.67	1.45	2.5	
Sample Method	16	19	180	0.30	1.06	16.7	M=7,N=7
			90	0.87	3.15	10.3	M=5,N=7
			45	5.44	12.33	2.8	M=3,N=5
Grid Method	16	19	180	1.43	5.21	11.0	M=7,N=7
			90	2.10	10.39	6.5	M=5,N=7
			45	2.61	8.73	1.4	M=3,N=5
Frequency plane restoration	16	19	180	0.66	1.82	16.1	M=7,N=7
			90	1.09	2.69	10.5	M=5,N=7
			45	0.70	1.86	3.2	M=3,N=5
Iterative reconstruction	16	19	180	1.24	3.29	15.4	M=9,N=9
			90	2.99	12.82	12.2	M=6,N=9
			45	4.70	14.92	7.0	M=4,N=6

Fig.8.6.

8.4. CONCLUSIONS

The experimental aspects of optical tomography of phase objects are well documented and should be relatively easy to implement in practice. In fact an initial feasibility study has already been carried out, using the optical layout shown in (Fig.(8.2)). The diffuser used was a coarse-ground glass screen,

and its goniometric properties are shown in (Fig.(8.3)). Typical interferometric results, taken with a small apertured camera, are shown in (Fig.(8.6)). Experiments were also carried out with a variety of other diffusers, including opaled plastic, but unsatisfactory results were obtained. This was probably due to the lack of a polariser prior to the diffusing screen.

From the tomographic reconstruction viewpoint, two methods recommend themselves from the survey performed. If an angle of view of 180° is possible, a convoluted back-projection with some form of filtering is indicated. For an angle of view of less than 180°, a series expansion method is indicated, the exact nature of which will depend on the test geometry being studied. Obviously further investigation is indicated for a final decision.

Much confidence is evinced for the possibility of success in the undertaking of such a tomographic study of heat transfer.

CHAPTER 9

9. CONCLUSIONS

Holographic interferometry has been shown to be a useful technique for the investigation of phase objects, the engineering applications studied being forced convective heat transfer and compressible flow. Such a technique produces full-field data of the object being studied, in the form of a fringe field. With the infinite fringe background method used in this study each fringe represents an iso-density contour, corresponding either to a constant Mach number or a constant temperature. These fringe fields give an extremely useful qualitative appraisal of the region of interest, but the wealth of qualitative data available necessitates the use of an automatic analysis system for effective, efficient, data extraction and utilisation.

Two main approaches to the problem of the automatic analysis of infinite fringe holographic interferograms have been identified, these are, one-dimensional analysis methods and two-dimensional analysis methods.

With all the fringe systems studied, however, one common area to the analysis techniques used is that of image pre-processing and data preparation.

The major obstacles to be faced with automatic fringe analysis are the spatial resolution of all the significant fringes, determination of the extent of the fringe field, and increasing the signal-to-noise ratio over the whole fringe field to allow for accurate fringe location.

The spatial resolution problem has been alleviated by merging magnified portions of the fringe field either together, or into the whole field data, thus allowing all the significant fringes to be detected. The lower limit on the spatial sampling rate is that defined by the Nyquist rate for any fringe of significance.

Definition of the area of analysis, that is, the exclusion of the fringe field boundaries and of any physical objects obtruding into the flow field, has been performed using a masking technique. Geometric models stored in the computer are used, along with manual scaling and location routines driven by a cursor, to mask off such regions with a unique grey-level, allowing the fringe analysis routines to ignore such regions.

Standard image pre-processing techniques are used to try to increase the signal-to-noise ratio of the fringes, the area identified as that most inimical to automatic fringe analysis. Such methods either reduce the effect of the noise through smoothing, or increase the signal strength by contrast enhancement and high-pass filtering techniques.

A successful one-dimensional analysis system has been developed for the automatic analysis of forced convective heat transfer interferograms. After initial stages of pre-processing and data preparation two fringe detection methods are offered, working on a gradient change and a bucket-bin fringe detection principle. The accuracy of fringe location has been changed from the 4.7% identified by Lockett [1987] (for manual positioning) to between ± 5.1% and 5.2% depending on where in the temperature field the fringe is located.
However, Lockett's estimate of 4.7% is low.

A refractive error correction factor has been built into the system, and a complete two-dimensional analysis of the fringe field is possible, with the combining of several one-dimensional scan lines, in between 10 and 15 minutes, depending on the amount of pre-processing required.

The heat transfer from a flat plate has been studied as a proving exercise for the holographic visualisation and analysis techniques, and a comparison performed with a Large Eddy Simulation modelling such a geometry. Good agreement has been found between the simulation and experimental data, and a new power law relationship for the forced convective heat transfer in a duct with one wall heated has been proposed.

The heat transfer from a variety of ribbed geometries has also been studied and a mechanism to account for the relative heat transfer distributions encountered has been postulated.

mainly

A two-dimensional automatic analysis system has also been developed for the more highly convoluted fringe systems produced in a compressible flow study at Marchwood Engineering Laboratories. The system developed was reasonably robust, and was able to produce an iso-density map of a single blade passage in a cascade section in under fifteen minutes, with an accuracy of up to ±4%.

The format identified for such two-dimensidonal analysis systems is:

i) image pre-processing and data preparation

ii) image binarisation, followed by some binary enhancement

iii) fringe edge detection

iv) fringe tracing

v) fringe ordering.

The most important stage in such a procedure is the image binarisation: it is the effectiveness and accuracy of this step that really determines the effectiveness of the system. With the system developed, edges were detected with an accuracy of between ±4% and ±11%, depending on whether the fringe was broad and diffuse, or sharp and well defined.

Fringe edge detection, rather than fringe thinning followed by medial line tracing, was used for three major reasons. These were:

i) no sacrifice in the resolution requirements were necessary.

ii) an extra processing step which was potentially lengthy as well as introducing extra inaccuracies was avoided.

iii) a reduction in the amount of inter-fringe interpolation for a full analysis was achieved.

A cursory comparison with a computer simulation of such a flow, TURBINS, was carried out, as a validation exercise for the code used. The essential flow features were found to agree quite well between the experimental data and the simulation data.

An investigation into the use of holographic interferometry and automatic fringe processing to resolve the third dimension available from such holographic interferometry techniques has been carried out, and a short survey of tomographic reconstruction techniques is included in the thesis. In real engineering situations, where a limited angle of data collection might be anticipated, a series expansion method is proposed as the best means of tomographic reconstruction.

A new approach to the problem of automatic fringe analysis has been adopted, that of considering as two categories one-dimensional and two-dimensional fringe analysis techniques. A set of programs have been developed for each case, and although not as complex as the work presented by Becker [1982], [1985], each system works well, giving a significant reduction in processing time over manual techniques.

REFERENCES AND BIBLIOGRAPHY

ABEL, N. [1826]
J. Reine. Angew. Math., 1, pp.153-157.

AGRAWALA, A. and KULKARNI, A. [1977]
"A sequential approach to the extraction of shape features"
Computer Graphics and Image Processing, 6, pp.538-557.

ALWANG, W. et al. [1970]
"Item 1, Final Report, Pratt and Whitney, PWA-3942 (NAVAIR LAIR-602) contract.

ANDREWS, H.C., TESCHER, A.G. and KRUGER, R.P. [1972]
"Image Processing by Digital Computer"
IEEE Spectrum, 9, 7, pp.20-32.

ANTONIA, R.A., DANH, H.Q. and PRABHU, A. [1977]
"Response of a turbulent boundary layer to a step change in surface heat flux"
J. Fluid Mech., 80, pp.153-177.

ARCELLI, C., CORDELLA, L. and LEVIALDI, S. [1975]
"Parallel thinning of binary pictures"
Electronics Letters, Vol.11, No.7. p.148.

AUGUSTYN, W., ROSENFELD, A. and ZANONI, C. [1978]
"An automatic interference pattern processor with interactive capability"
SPIE, Vol.153, Advances in Opt. Metrology, pp.146-155.

AUGUSTYN, W. [1979]
"Versatility of a micro-processor based interferometric data reduction system"
SPIE, Vol.192, Interferometry, pp.128-133.

BALL, G.J., GORDON, A.L., HUNTER, J., RICHARDS P.H., THOMPSON, G.J. [1987]
"Application of holographic interferometry for the mapping of gas density in a transonic flow.
"Holographic Systems, Components & Applications" I.E.R.E. Conference, Churchill College, Cambridge, U.K.

BALL, G.J., GORDON, A.L., RICHARDS, P.H., and THOMPSON, G.J. [1987]
"The measurement and prediction of local gas density in low pressure steam turbine blade passages at off design influence"
CEGB Report TPRD/M/1122/M87.

BARKER, D.B. and FOURNEY M.E. [1977]
"Measuring fluid velocities with speckle patterns"
Optics Letters 1, pp.135-137.

BATES, R. and PETERS, T. [1971]
"Towards Improvements in Tomography"
N.Z. J. Sc. I., 14, pp.883-896.

BEAVER, G.S., SPARROW, E.M. and LLOYD, J.R. [1971]
"Low Reynolds number flow in large aspect ratio ducts"
Trans. ASME, J. Basic Eng., 38, p.181.

BECKER, F., MEIER, G. and WEGNER, H. [1982]
"Automatic evaluation of interferograms"
SPIE, 359.

BECKER, F. and YU, Y. [1985]
"Digital Fringe Reduction Techniques applied to the measurement of three-dimensional transonic flow fields"
Opt. Eng., 24, p.429.

BELLMAN, R. [1961]
"On the approximation of curves by line segments using dynamic programming"
Comm.A.C.M., 4, p.284.

BEN-DOR, G., WHITTEN, B. and GLASS, I. [1979]
"Evaluation of perfect and imperfect gas interferograms by computer"
Int. J. Heat and Fluid Flow, 1, 2, p.77.

BEN-DOR, G., and ARZOAN, Y. [1985]
"Fully computerized evaluation of interferograms from fluid flow investigations"
Int. J. Heat and Fluid Flow, 6, p.133.

BERNAL, E. and LOOMIS, J. [1977]
"Interactive video image digitiser - application to interferogram analysis"
SPIE, Vol.126, 'Clever Optics', pp.143-151.

BERRY, M. and GIBBS, D. [1970]
"The Interpretation of optical projections"
Proc. Roy. Soc. London, A.314, p.143.

BIRCH, K. [1976]
"A TV based system for interferogram analysis"
SPIE, 369, p.186.

BRACEWELL, R.N. [1956]
"Strip Integration in Radio Astronomy"
Aust. J. Phys., 9, pp.198-217.

BRACEWELL, R.N. and RIDDLE, A. [1967]
"Inversion of fan-beam scans in Radio Astronomy"
Astrophys. J., 150, p.427.

BRIGHAM, E. [1974]
"The Fast Fourier Transform"
Prentice-Hall Inc., Englewood Cliffs, N.J., U.S.A.

BROOKS, R.E., HEFLINGER, L.O. and WUERKER, R.F. [1965]
"Interferometry with a holographically reconstructed comparison beam"
Appl. Physics Letters, 7, pp.248-249.

BRUNNING,J.H., HERRIOT,D.R., GALLAGHER, J.E., ROSENFELD, D.P., WHITE, A.D. and BRANGACCIO, D.J. [1974]
"Digital wavefront measuring interferometer for testing optical surfaces and lenses"
Appl. Opt., 13, p.2693.

BRYANSTON-CROSS, P.J., LANG, T., OLDFIELD, M.L.G. and NORTON, R.J.G. [1980]
"Interferometric measurements in a turbine cascade using image plane holography"
ASME, Paper No.80-GT-91.

BUDINGER, T.F., GULLBERG, G.T. and HUESMAN, R.H. [1979]
"Topics in Applied Physics 32, Image Reconstruction from Projections" Ed. G.T. Herman
Springer-Verlag, pp.189-200.

BURCH, J.M. [1968]
"The application of lasers in production engineering"
The Production Engineer, 44, pp.431-432.

BUTTERS, J.N. [1976]
"The engineering uses of coherent optics" Ed. E. Robertson.
Cambridge University Press,

BUTTON, B.L., JUTTS, J., DOBBINS, B., MOXON, C. and WYKES, C. [1985]
"The identification of fringe positions in speckle patterns"
Opt. Laser Tech., 17, p.189.

CANTWELL, B.J. [1981]
"Organised Motion in Turbulent Flow"
Ann. Review Fluid Mech., pp.457-515.

CASTLEMAN, K.R. [1979]
"Digital Image Processing"
Prentice-Hall, Inc.

CHAMBLESS, S. and BROADWAY, J. [1979]
"Digital filtering of speckle photography data"
Exp. Mech., 19, p.286.

CHAU, H. and ZUCKER, O. [1973]
"Holographic thin-beam reconstruction technique for the study of 3-dimensional refractive index fields"
Opt. Commun., 8, pp.336-339.

CHIRGWIN, C. [1973]
"Maxwell's equations and their consequences"
Elementary Electromagnetic Theory, Vol.3.

CHOUDRY, A. [1981]
"Digital holographic interferometry of convective heat transport"
Appl. Opt., 20, 7, p.1260.

CLINE, H., HOLIK, A. and LORENSON, W. [1982]
"Computer-aided surface reconstruction of inteference contours"
Appl. Opt., 21, p.4481.

COLLIER, R.J., DOHERTY, E.T. and PENNINGTON, K.S. [1965]
"Application of Moire techniques to holography"
Appl. Physics Letters, 8, pp.44-46.

COLLINS, M.W. and VOKE, P.R. [1983]
"The application of large-eddy simulation to engineering problems"
Calore e Tecnologia, 1, 1, pp.36-55.

CORMACK, A.M. [1963]
"Representation of a function by its line integrals, with some radiological applications"
J. Appl. Phys., 34, 9, pp.2722-2727.

DANDLIKER, R., INEICHEN, B. and MOTTIER, F. [1973]
"High resolution hologram interferometry by electronic phase measurement"
Opt. Comm., 9, pp.412-416.

DANDLIKER, R., MAROM, E. and MOTTIER, F. [1976]
"Two reference beam holographic interferometry"
J. Opt. Soc. Am., 66, p.23.

DANDLIKER, R., THALMANN, R. and WILLEMIN, J. [1982]
"Fringe interpolation by two reference beam holographic interferometry reducing sensitivity to hologram misalignment"
Opt. Eng., 24, p.824.

DAWES, W.N., BERRY, P.E., GRANT, R.J. and RICHARDS, P.H. [1984]
"Computation of the Flow in a Cascade of High Stagger Transonic Tip Sections"
CEGB Report, TPRD/M/1418/N84.

DENBY, D., QUINTANILLA, G.E. and BUTTERS, J.N. [1976]
"The Engineering use of Coherent Optics" Ed. E. Robertson.
Cambridge University Press,

Dändliker, R. and Thalman, R. [1985] "Heterodyne and quasi-heterodyne holographic interferometry" Opt.Eng. 5, 24, pp.824-831.

DEUTSCH, E.S. [1969]
"Comments on a line thinning scheme"
Comput. J., 12, p.412.

DUDA, R.O. and HART, P.G. [1973]
"Pattern Classification and Scene Analysis"
Wiley, N.Y. U.S.A. p.271.

DUDDERER, T.D. and SIMPKINS, P.G. [1977]
"Laser Speckle Photography in a fluid medium"
Nature, 270, p.45-47.

EDWARDS, F.J. [1962]
"The heat transfer and friction characteristics of rough surfaces for forced convection turbulent flow"
Ph.D. Thesis, University of Manchester.

ENNOS, A, ROBINSON, D, and WILLIAMS, D. [1985]
"Automatic fringe analysis in holographic interferometry"
Optica Acta., 32, p.135.

ENNOS, A. et al. [1969]
"Visual observations of surface vibration node patterns"
Nature, 222, p.263.

EK, L. and MOLIN, N. [1971]
"Detection of the nodal lines and the amplitude of vibration by speckle interferometry"
Opt. Commum., 2, p.419.

FRAÇON, M. [1979]
"Laser Speckle and Application in Optics"
Academic Press, New York, U.S.A.

FRANTZ, L., SAWCHUK, A. and OHE, W. [1979]
"Optical phase measurement in real-time"
Appl. Opt., 18, p.3301.

FREI, W. [1977]
"Image Enhancement by Histogram Hyperbolisation"
Comput. Graphics, Image Processing, 6, pp.286-294.

FRESNEL, J. [1819]
Paris Academy of Science

FUNNELL, W.R.J. [1981]
"Image processing applied to the interactive analysis of interferometric fringes"
Appl. Opt., 20, p.3245.

GABOR, D. [1949]
"Microscopy by reconstructed wavefronts"
Procs. Roy. Soc., A197, pp.4540487.

GEORGE, N., JAIN, A. and MELVILLE, R. [1978]
"Speckle, diffusers, and depolarisation"
Appl. Phys., 6, pp.65-70.

GLASSMAN, A. and ORR, C. [1979]
"Automated Inteferogram Reduction"
SPIE, Vol.181, 'Contemporary Optical Systems and Components Specifications" pp. 64-73.

GLUSS, B. [1962]
"Further remarks on line segment curve fitting using dynamic programming"
Comm. ACM, 5, pp.441-443.

GLUSS, B. [1962]
"A line segment curve fitting algorithm related to optical encoding of information"
Information and Control, 5, pp.261-267.

GORDON, R., BENDER, R. and HERMAN, G. [1970]
"Algebraic Reconstruction Techniques (ART) for 3-dimensional Electron Microscopy and X-ray photography"
J. Theor. Biology, 29, 3, pp.483-487.

GORDON, R., and HERMAN, G. [1974]
"Three-dimensional reconstruction from projections: a review of algorithms"
Intern. Rev. Cytol., 38, pp.111-151.

GREEN, W.B. [1983]
"Digital Image Processing - a systems approach"
Van Nostrand Reinhold Co.

GRIEVENKAMP, J. [1984]
Opt. Eng., 23, p.350.

HAINES, K.A. and HILDEBRAND, B.P. [1965]
"Contour generation by wavefront reconstruction"
Appl. Physics Letters, 19, pp.10-11.

HALL, E.L. [1974]
"Almost uniform distribution for computer image enhancement"
IEEE Trans. Computers, C-23, 2, pp.207-208.

HALL, E.L. et al [1971]
"A Survey of Preprocessing and Feature Extraction Techniques for Radiographic Images"
IEEE Trans. Computers, C-20, 9, pp.1032-1044.

HAUF, W. and GRIGULL, W. [1970]
"Optical methods in heat transfer"
Adv. in Heat Transfer, Vol.6, p.133.

HEFLINGER, L., WUERKER, R, and BROOKS, R. [1966]
"Holographic Interferometry
J. Appl. Phys., 37, pp.642-649.

HERLITZ, S.I. [1963]
"A method for computing the emission distribution in cylindrical light sources"
Arkiv. Fysik, 23, p.571.

HERMAN, G. and LENT, A. [1976]
"Iterative Reconstruction Algorithms"
Comput. Biol. Med., 6, pp.273-294.

HILDITCH, C.J. [1969]
"Linear skeletons from square cupboards"
Machine Intelligence IV, Eds. B.Meltzer and D. Michie,
American Elsevier, N.Y., U.S.A. pp.403-420.

HILL, J. et al. [1977]
"Image Processing Techniques"
SPIE, Vol.130.

HORD, R.M. [1982]
"Digital Image Processing of Remotely Sensed Data"
Academic Press.

HORMAN, M. [1965]
"An application of wavefront reconstruction to interferometry"
Appl. Opt., 4, pp.333-336.

HURDEN, A.P.M. [1982]
"Vibration mode analysis using electronic speckle pattern interferometry"
Opt. Laser Tech., 14, p.21.

HUYGENS, O. [1967]
"Traite de la Lumiere"

ICHIOKA, Y. and INUIYA, M. [1972]
"Direct Phase Detecting System"
Appl. Opt., 11, p.1507.

INEICHEN, B, EGLIN, P and DANDLIKER, R. [1980]
"Hybrid optical and electronic image processing for strain measurements by speckle photography"
Appl. Opt., 19, p.2191.

JONES, R. and WYKES, C. [1983]
"Holographic and Speckle Interferometry"
Cambridge University Press, Cambridge.

JUNGINGER, H. and VAN HAERINGER, W. [1972]
"Calculation of three-dimensional refractive index field using phase integrals"
Opt. Comm., 5, pp.1-4.

KAUFMAN, G, ENNOS, A, GALE, B and PUGH, D. [1980]
"An electro-optical read-out system for analysis of speckle photographs"
J. Phys. E., 13, p.579.

KIM, J. [1983]
"On the structure of wall-bounded turbulent flows"
Phys. Fluids., 26 (8).

KREIS, T. and KRIETLOW, H. [1980]
"Quantitative evaluation of holographic interference patterns under image processing aspects"
SPIE, J., 210, 18.

LAHART, M. [1979]
"Local segmentation of Noisy Images"
Opt. Eng., 18, 1.

LALLEMENT, J.P., DESAILLY, R. and FROEHLY, C. [1977]
"Measurement of speed in a liquid by coherent diffusion"
Acta Astronautica, 4, pp.343-356.

LAW, H. and MASLIYAH, J. [1984]
"Coherent optical measurement techniques in profilometric determination of local mass transfer coefficients"
Opt. Lasers Eng., 5, p.211.

LEITH, E.N. and UPATNIEKS, J. [1962]
"Reconstructed wavefronts and communication theory"
J. Opt. Soc. Am., 52, pp.1123-1130.

LOCKETT, J., HUNTER, J., VOKE, P. and COLLINS, M.W.[1985]
"Investigation of convective heat transfer enhancement using real-time holographic inteferometry".
Procs. 6th Int. Conf. on Photon Correlation and Other Optical Techniques in Fluid Mechanics, Cambridge.

LOCKETT, J.F. and COLLINS, M.W. [1986]
"Holographic Interferometry and its application to Turbulent Convective Heat Transfer"
Int. J. Opt. Sensors, 1, pp.191-208.

LOCKETT, J. [1987]
"Heat transfer from Roughened Surfaces using Laser Interferometry"
Ph.D. Thesis, The City University, London.

MACOVSKI, A., RAMSEY, S.D. and SCHAEFER, L.F. [1971]
"Time-lapse interferometry and contouring using television systems"
Appl. Opt., 10, p.2722.

MACY, W. Jr. [1983]
"Two-dimensional fringe pattern analysis"
Appl. Opt., 22, 23, p.3898.

MALDONADO, C. and OLSEN, H. [1966]
"New Method for Obtaining Emission Coefficients from emitted spectral Intensities: Part II Asymmetrical Sources"
J. Opt. Soc. Am., 56, 10, pp.1305-1313.

MANTLE, P, FREEMAN, A.R. and WATTS, J. [1986]
"Conductivity effects of ribbed surface heat transfer"
Int. J. Heat Mass Transfer, 14, p.1825.

MARTIN, S. and DRAIN, L. [1987]
"Investigation of turbulent flow in a ribbed wall flow channel using two component L.D.A."
U.K.A.E.A. Harwell, Report, AERE-R-12080.

MATULKA, R, and COLLINS, D. [1971]
"Determination of three-dimensional density fields from holographic interferograms"
J. Appl. Phys., 42, 3, pp.1109-1119.

MAXWELL, B. [1881]
"A treatise on electricity and magnetism" 2nd Edition.

MERTZ, L. [1983]
"Real-time fringe pattern analysis"
Appl. Opt., 22, p.1535.

MEYNART, R. [1982]
"Digital image processing for speckle flow velocimetry"
Rev. Sci. Instrum., 53(1), p.110.

MEYNART, R. [1983]
"Instantaneous velocity field measurements in unsteady flow by speckle velocimetry"
Appl. Opt., 22, p.535.

MONTANARI, U. [1968]
"A method for obtaining skeletons using a quasi-Euclidean distance"
J.A.C.M., 15, pp.600-624.

MORAITIS, C. et al. [1986]
"Computer processing of fringe patterns for laser speckle velocimetry processing"
U.K.I. Lecture Series, 1986-09.

MULLER, R.K. and SAACKEL, L.R. [1979]
"Complete Automatic Analysis of Photoelastic Fringes"
Expt. Mech., 19, p.245-255

NAKADATE, S., YATAGI, T. and SAITO, H. [1980]
"Electronic Speckle pattern interferometry using digitial image processing techniques"
Appl. Opt., 19, 11, p.1879.

NAKADATE, S., YATAGI, T. and SAITO, H. [1981]
"Computer-aided speckle pattern interferometry"
Appl. Opt., 22, 2, p.237.

NAKADATE, S. [1983]
"Hybrid holographic inteferometer for measuring three dimensional deformations"
Opt. Eng., 20, 2, p.246.

OERTEL, H. Jr.
"Three-dimensional convection within rectangular boxes"
Institut fur stromungslehre und stromungsmaschiner, Universitat Karlsruhe, G.D.R.

ORSZAG, S. and PATTERSON, G. [1972]
"Numerical simulation of 3-dimensional homogeneous isotropic turbulence"
Phys. Rev. Letters, 28, 2, pp.76-79.

PERRIN, J. and THOMAS, A. [1979]
"Electronic processing of Moire fringes: application to Moire topography and comparison with photogrammetry"
Appl. Opt., 18, p.563.

PFALTZ, J. and ROSENFELD, A. [1967]
Communication of the A.C.M. 10, pp.119-125.

PHILBRICK, O. [1968]
"Shape description with the medial axis transformation"
Pictorial Pattern Recognition, Ed.G. Cheng, et al.
Thompson Book Co.

POWELL, R.L. and STETSON, K.A. [1965]
"Interferometric vibration analysis by wavefront reconstruction"
J. Opt. Soc. Am., 55, pp.1593-1598.

PRATT, W.K. [1978]
"Digital Image Processing"
Wiley-Interscience.

RADON, J. [1917]
Ber. Verh. Sachs. Akad. Wiss, Leipzig, Math. Phys. Kl.69, pp.262-277.

RAMACHANDRAN, G. and LAKSHMINARAYAN, A. [1971]
"Three-dimensional Reconstruction from Radiographs and Electron Micrographs: Application of Convolutions instead of Fourier Transforms"
Proc. Nat. Acad. Sci., U.S.A., 68, pp.2236-2240.

RAMER, U. [1972]
"An iterative procedure for the polygonal approximation of plane curves"
Computer Graphics and Image Processing, 1, pp.244-256.

REYNOLDS, W. [1976]
"Computation of Turbulent Flows" Ed.van Dyke, Vincenti, Wehausen.
Ann. Rev. Fluid Mech., 8, pp.183-208.

REYNOLDS, W. and CEBECI, T. [1978]
"Calculation of Turbulent flows" in 'Turbulence". Ed. P. Bradshaw.
Topics in Applied Physics, Vol.12, Springer-Verlag.

ROBINSON, D.W. [1983a]
"Automatic fringe analysis with a computer image processing system"
Appl. Opt., 22, p.2169.

ROBINSON, D.W. [1983b]
"Role for automatic fringe analysis in optical metrology"
SPIE, 376, p.20.

ROSENFELD, A. [1969]
"Picture Processing by Computer"
Academic Press, New York, U.S.A.

ROSENFELD, A. [1976]
"Digital Image Processing and Analysis"
NATO Advanced Study Institute on Digital Image Processing and Analysis.

ROSENFELD, A. and KAK, A. [1976]
"Digital Picture Processing"
Academic Press, New York, U.S.A.

ROSENFELD, A. and PFALTZ, J. [1966]
"Sequential operations in digitial picture processing"
J.A.C.M., 13, 4, pp.471-494.

RUTOINTZ, D. [1966]
"Pattern Recognition"
J. Royal Stat. Soc., 129, pp.504-530.

SARAGA, P. [1974]
"Thinning Operators"
Mullard Research Labs., Technical Note 1294.

SARAGA, P. and WOOLLONS, D.J. [1968]
"The design of operators for pattern processing"
I.E.E. - NPL Conf. on Pattern Recognition, Teddington, Middx.
Conf. Publ. 42, I.E.E. London, pp.106-116.

SCHEMM, J.B. and VEST, C.M. [1983]
"Fringe pattern recognition and interpolation using nonliner regression analysis"
Appl. Opt., 22, 18, p.2850.

SCHLUTER, M. [1980]
"Analysis of holographic interferograms with a TV picture system"
Opt. Laser Techn., 93.

SCHLUTER, M. [1980]
"In-plane deformation measurement by video-electronic hologram interferometry"
Optica Acta., 27, pp.799-808.

SCHUMANN, U. and PATTERSON, G. [1978]
"Numerical study of the return of axisymmetric turbulence to isotropy"
J. Fluid Mech., 88, pp.711-735.

SEGUCHI, Y., TOMITA, Y. and WATANABE, W. [1979]
"Computer-aided fringe pattern analyser - A case of photoelastic fringe"
Expt. Mech., 19, p.362.

SINCLAIR, D.W. and WHITFIELD, D.L. [1978]
"Holographic Interferometry measurements of subsonic turbulent boundary layers"
AIAA, 11th Fluid and Plasma Dynamics Conf., ARO Inc., Arnold, Tenn.

SMITH, P., PETERS, T. and BATES, R. [1973]
"Image Reconstruction from finite numbers of projections"
J. Phys. A. Math. Nucl. Gen., 6, pp.361-382.

SNYDER, R and HESSLINK, L. [1984]
"Optical tomography for flow visualisation of the density field around a revolving helicopter blade"
Appl. Opt., 23, 20, pp.3650-3656.

SNYDER, R. and HESSLINK, L. [1985]
"High speed optical tomography for flow visualisation"
Appl. Opt., 24, 23, pp.4046-4050.

SOMMARGEN, G.E. [1977]
"Double exposure holographic interferometry using common path reference waves"
Appl. Opt., 16, p.1736.

SRINIVASAN, V., LUI, H. and HAHORIA, M. [1984]
"Automated phase measuring profilometer of 3-dimensional diffuse objects"
Appl. Opt., 23, p.3105.

STONE, H. [1961]
"Approximation of curves by line segments"
Math. Comp., 15, pp.40-47.

SWEENEY, D. and VEST, C. [1973]
"Reconstruction of three-dimensional refractive index fields from multi-directional interferometric data"
Appl. Opt., 12, 11, pp.2649-2664.

SWEENEY, D. and VEST, C. [1974]
"Measurement of three-dimensional temperature fields above heated surfaces by holographic interferometry"
Int. J. Heat Mass Transfer, 17, pp.1443-1454.

TAKEDA, M, INA, H. and KOBAYASHI, S. [1982]
"Fourier transform method of fringe pattern analysis for computer based topography and interferometry"
J. Opt. Soc. Am., 72, p.156.

TICHENOR, D.A. and MASDEN, V.P. [1979]
"Computer analysis of holographic interferograms for non-destructive testing"
Opt. Eng., 8, p.469.

TRIENDL, E.E. [1970]
"Skeletonisation of noisy hand-drawn symbols using parallel operations"
Pattern Recognition, 2, pp.221-226.

TUKEY, J.W. [1971]
"Exploratory Data Analysis"
Addison-Wesley, Reading, Mass., U.S.A.

VARMAN, P. and WYKES, C. [1981]
"Smoothing of speckle and Moire fringes by computer processing"
Optics and Lasers in Eng., 3, p.87.

VARMAN, P. [1984]
"A Moire system for producing numerical data of the profile of a turbine blade using a computer and video store"
Optics and Lasers in Eng., 5, pp.41-58.

VEST, C.M. [1979]
"Holographic Interferometry"
Wiley-Interscience.

VOKE, P.R. and COLLINS, M.W. [1982]
"Large Eddy Simulation: Retrospect and Prospect"
U.K.A.E.A. Harwell, Report AERE-R-10716.

VOKE, P.R. and COLLINS, M.W. [1984]
"Large Eddy Simulation of Turbulent Flow in Plain and Distorted Channels"
U.K.A.E.A. Harwell, Report HTFS R5551 (Annual Research Symp., University of Warwick, U.K.) pp.349-358.

WALKLATE, P.J. [1981]
"A Two-wavelength holographic technique for the study of two-dimensional thermal boundary layers"
Int. J. Heat Mass Transfer, Vol.24, No.6, pp.1051-1057.

WALKLATE, P.J. [1983]
"A holographic technique for the study of heat transfer from a rib-roughened surface"
3rd Int. Symp. on Flow Visualisation. University of Michigan, Ann Arbor, U.S.A. pp.438-446.

WEST, G.A.W. [1986]
Private Communication.

WILKIE, D. [1966]
"Forced convection heat transfer from surfaces roughend by transverse ribs"
3rd Int. Heat Transfer Conf., 1, Chicago, U.S.A. p.1.

WILLIAMS, F. and WATTS, J. [1970]
"The development of rough surfaces with improved heat transfer performance and a study of the mechanisms involved"
CEGB Berkeley Nuclear Labs, 4th Int. Conf. on Heat Transfer, Versailles, France.

WOMACK, K.H. [1984]
"Interferometric phase measurement using spatial synchronous detection"
Opt. Eng., 23, p.391.

WYANT, J.C. [1975]
"Use of an a.c. hetrodyne lateral shear interferometer with real-time wavefront correction systems"
Appl. Opt., 14, p.2622.

YATAGI, T. [1982]
"Interactive fringe analysis system: applications to Moire Contourgram and Interferograms"
Opt. Eng., 21, 5, p.901.

YATAGI, T., INABA, S., NAKARO, H. and SUZUKI, M. [1984]
"Automatic flatness tester for very large scale integrated circuit wafers"
Opt. Eng., 23, p.401.

APPENDIX A

HOLOGRAM FORMATION

If we assume that the x-y axes are in the plane of the hologram, then we may describe a typical reference wave in the form:

$$U_{ref} = U_{oref} \cos (\omega t - \Phi_{ref}(x,y)) \qquad (A.1)$$

Similarly, the object wave scattered from the object may be expressed as:

$$U_{obj} = U_{oobj} \cos (\omega t + \Phi_{obj}(x,y)) \qquad (A.2)$$

From equation (2) we know that the resulting irradiance, on the superposition of these two waves is the product:

$$I = \langle |U_{ref} + U_{obj}|^2 \rangle \qquad (A.3)$$

where the triangular brackets denote a time averaged quantity. Thus:

$$I = \langle U_{ref}^2 \rangle + \langle U_{obj}^2 \rangle + \langle 2U_{ref}U_{obj} \rangle \qquad (A.4)$$

The time average of a squared sinusoidal function is simply half the amplitude of the function Thus the first two terms in equation (4) reduce simply to:

$\frac{1}{2}U_{oref}^2$ and $\frac{1}{2}U_{oobj}^2$

Considering the last term in equation (4), then:

$$U_{ref}U_{obj} = U_{oref}U_{oobj} \cos(\omega t - \Phi_{ref}(x,y)) \cos(\omega t - \Phi_{obj}(x,y)) \quad (A.5)$$

$$= U_{oref}U_{oobj} [\cos^2(\omega t)\cos(\Phi_{ref})\cos(\Phi_{obj}) + \cos(\omega t)\sin(\omega t)\cos(\Phi_{ref})\sin(\Phi_{obj}) + \sin^2(\omega t)\sin(\Phi_{ref})\sin(\Phi_{obj}) + \cos(\omega t)\sin(\omega t)\sin(\Phi_{ref})\cos(\Phi_{obj}) \quad (A.6)$$

The following equalities may then be used,

$$\cos(\omega t)\sin(\omega t) = 0 \quad (A.7)$$

and

$$\cos^2(\omega t) = \sin^2(\omega t) = \frac{1}{2} \quad (A.8)$$

to reduce equation (6) to:

$$U_{ref}U_{obj} = \frac{1}{2}U_{oref}U_{oobj} [\cos(\Phi_{ref} - \Phi_{obj})] \quad (A.9)$$

So equation (4) may be written:

$$I = \tfrac{1}{2}U_{oref}^2 + \tfrac{1}{2}U_{oobj}^2 + U_{oref}U_{oobj} \cos (\Phi_{ref}-\Phi_{obj}) \quad (A.10)$$

The diffraction pattern formed on the holographic plate thus consists of an interference pattern with background irradiance:

$$\tfrac{1}{2}U_{oref}^2 + \tfrac{1}{2}U_{oobj}^2$$

modulated by the sinusoidal function,

$$U_{oref}U_{oobj} \cos (\Phi_{ref} - \Phi_{obj})$$

We now consider the reillumination of such a diffraction pattern with a suitable reconstruction wave, U_{rec}, where:

$$U_{rec} = U_{orec} \cos (\omega t + \Phi_{rec}(x,y)) \quad (A.11)$$

If we suppose that this reconstruction wave is travelling in the same direction as the original reference wave, then the wave resulting from the interference of such a reconstruction wave with the established diffraction pattern, U_{res}, is given by:

$$U_{res} = U_{rec} I \quad (A.12)$$

$$= \left\{ \frac{U_{oobj}^2}{2} + \frac{U_{oref}^2}{2} + U_{oobj}\, U_{oref} \cos (\Phi_{ref} - \Phi_{obj}) \right\} U_{orec} \cos (\omega t + \Phi_{rec}) \quad (A.13)$$

This reduces to:

$$U_{res} = \tfrac{1}{2}U_{orec}[U_{oobj}^2 - U_{oref}^2] \cos(\omega t + \Phi_{rec})$$

$$+ \tfrac{1}{2}U_{oobj}U_{oref}U_{orec}[\cos(\omega t + \Phi_{rec} - \Phi_{ref} + \Phi_{obj})$$

$$+ \cos(\omega t + \Phi_{rec} + \Phi_{ref} - \Phi_{obj})] \qquad (A.14)$$

Because the reconstruction beam being considered is exactly the same as the original reference beam, then:

$$\Phi_{ref} = \Phi_{rec}$$

and so,

$$U_{res} = \tfrac{1}{2}U_{orec}(U_{oobj}^2 + U_{oref}^2) \cos(\omega t + \Phi_{ref})$$

$$+ \tfrac{1}{2}U_{orec}U_{oobj}U_{oref} \cos(\omega t + 2\Phi_{ref} - \Phi_{obj})$$

$$+ \tfrac{1}{2}U_{orec}U_{oobj}U_{oref} \cos(\omega t + \Phi_{obj}) \qquad (A.15)$$

These three separate terms describe the wavefronts issuing from the diffraction pattern, or holographic plate, on reconstruction. The first is simply an attenuated reconstruction beam, the zeroth-order undeflected reference beam. It contains no information about the phase of the object, and is of little practical concern.

The remaining two terms represent first order waves being respectively the conjugate and an actual representation of the original object wave with the addition of a multiplicative constant. Hence the object wave has been recorded (by the hologram) and may be reconstructed with the use of a suitable reference beam.

APPENDIX B

—

ESTIMATION OF ERRORS

FRINGE DETECTION ERRORS:-

As far as this project is concerned, the minimisation of such errors is of primary importance.

In the heat transfer study the accuracy with which a particular fringe could be located depended on the nature of the fringe, broad diffuse fringes giving a greater margin of error than narrow, tight fringes. Also, any error in fringe location produced a correspondingly greater error in the low fringe order regions, as small temperature differences exacerbate the error caused by small mis-location of fringe positions.

The initial tests carried out using both the bucket-bin fringe detection and the gradient change fringe detection routines indicated a potential RMS error, in the presence of noise, of between 0.05 and 0.36. These seem to be extremely low values for error, especially with high SNR's, and are probably attributable to the fact that ideal fringes, albeit tainted with noise, were used as the test data.

The experimentally obtained errors might be expected to be somewhat larger, as spanwise averaging moves the fringe data away from the ideal case.

With the narrow near wall fringes, the estimation of the error was relatively straightforward, as a sine curve could be fitted to the individual fringe data, and the maximum/minimum positions from such a fit compared to those obtained experimentally. In such cases the bucket-bin and gradient change fringe detection routines operated with a similar degree of accuracy, the fringe location being detected to within ± one pixel. As these narrow fringes tended to be on average ten pixels in width, this produced a detection error of $\pm \frac{1}{20}$ of a fringe, or ± 5%

The estimation of an error from the broad diffuse fringes was much more difficult. It was found that the gradient change detection routine operated very poorly in such regions, and no consistent error was obtainable. With the bucket-bin curve fit algorithm (as more than ten pixels were involved) an error of ± $\frac{1}{20}$ of a fringe, based again on comparison of experimentally located fringe positions on those obtained with, in this case, an approximate sine curve fit, was estimated. As these broad fringes tend to be in the region of one hundred pixels wide, an error of ± 5% in the fringe detection algorithm was estimated.

In the two-dimensional fringe analysis routines the objective was to binarise the image data, and then to trace the edges of the binarised fringes. Thus the effective error involved occurred in the binarisation process, and the task was to determine how well the binarisation routine picked out the fringe edges from the data.

This was done by isolating typical broad and narrow fringes from the data, and fitting the function:-

$$I = A + B \cos \Phi \qquad (B.1)$$

where I is the perceived intensity, A is the background irradiance, and B cos Φ is the modulation envelope, varying between $\pm B$.

From equation (B.1) it can be seen that:

$$I_{max} = A + B \qquad (B.2)$$

$$I_{min} = A - B \qquad (B.3)$$

and so combining equations (B.2) and (B.3).

$$A = \frac{I_{max} + I_{min}}{2} \qquad (B.4)$$

Thus the grey-level representing the fringe edge is defined by the background irradiance constant A.

Using this criterion to investigate the accuracy to which the fringe edges were detected, it was found that the complete segmentation process used, when applied to the medium and narrow well defined fringes, consistently set a grey-level threshold of ±4% of that defined by A.

For the broader, more diffuse fringes, a threshold that was between ±11% of the desired threshold was set at each point.

Thus the expected error for the two-dimensional analysis ranged between ±4% and ±11%, depending on the nature of the fringe.

BUOYANCY EFFECTS:-

Such effects only have relevance to the heat transfer study. Buoyancy effects may be estimated by evaluation of the Richardson number, given by:

$$Ri = \frac{Ra}{Re^2 Pr} \qquad (B.5)$$

where Ra is the Rayleigh number. For Richardson values below 10^{-3} buoyancy is negligible, Bradshaw [1969].

For the lowest experimentally used flow-rate, Re = 3,000, and a temperature difference, ΔT of 30 K, the Richardson number has a value of 1.5×10^{-2}. This has a small effect on the growth of the boundary layer, giving an estimated error of ±0.3%.

EMULSION SHRINKAGE:-

Swelling, shrinking and distortion of the emulsion occurs during the processing and drying of photographic plates.

With double-exposure interferometry, no effect on the result is encountered as the distortion of the emulsion affects both the reference and the changed object beams.

With real-time holographic interferometry, three main effects are produced by such shrinkage.

(i) a uniform phase shift affecting the background field intensity to some small extent, i.e. the background irradiance constant.

(ii) a loss in diffraction efficiency due to a slight re-orientation of the diffraction pattern on the plate, so that on repositioning the plate the Bragg condition is no longer ideally met.

(iii) the introduction of extraneous fringes due to the non-uniform distortion of the emulsion.

This last effect is by far the most important, and in practice it was found that the appearance of extra fringes could be limited to only one or two in the outer flow regions, by careful repositioning. Accordingly, the effect of emulsion shrinkage is deemed to be negligible for real-time interferometry also.

OBJECT BEAM MISALIGNMENT:-

Misalignment of the object beam on entry to the test section can cause severe errors, Beach et al [1973]. To ensure the beam was correctly aligned in the heat transfer investigation a flat polished mirror was placed on the test section surface. A screen

was then placed at the plane of the hologram, and it was assumed that alignment errors were negligible when no interference pattern was observed on the screen.

In the compressible flow investigation, alignment was less critical, and was performed by studying the shadows cast by the aerofoil sections.

DIFFRACTION ERRORS:-

Diffraction errors were minimised by correct positioning of the focussing lens. They were only notable in the low Reynolds number heat transfer interferograms, where diffraction fringes dominate the unresolvable near wall region. Hence, in the compressible flow situation, and the high Reynolds number heat transfer interferograms, diffraction effects are deemed negligible.

At low Reynolds numbers in the heat transfer study, the banding of the near wall region by such diffraction fringes led to an estimated error of about ±1% in the analysis procedures.

END EFFECTS:-

End effects increase in importance as the Reynolds number decreases, due to a thickening of the side wall boundary layers relative to the tunnel width. Thus for the very high Reynolds number compressible flow study end effects can be counted as negligible.

For the heat transfer study, if we assume a temperature change, ΔT, of 30 K, and a $^1/_7$th power law boundary layer profile on the flat side walls which are at a temperature of 290 K, then the non-dimensional temperature profile is:

$$\frac{T - T_w}{T_f - T_w} = \left\{\frac{y}{\delta}\right\}^{1/7} \qquad (B.6)$$

where T_f is the free-stream static temperature, which in the worst case, near to the heated plate, may be taken as 303 K, y is the perpendicular distance from the heated plate, and δ is the boundary layer thickness.

Assuming constant pressure throughout the boundary layer, the density profile is then given by:

$$\frac{\rho_f}{\rho} = \frac{T}{T_f} = \frac{T_w}{T_f} + \left\{1 - \frac{T_w}{T_f}\right\} \left\{\frac{y}{\delta}\right\}^{1/7} \qquad (B.7)$$

The optical pathlength change introduced by the presence of the boundary layer is then,

$$\Delta L = \frac{1}{\rho f} \int_0^{\delta} \rho dy - \delta$$

$$= \delta \left\{ \int_0^1 \frac{\rho}{\rho f} d\left\{\frac{y}{\delta}\right\} - 1 \right\} \qquad (B.8)$$

or

$$\Delta L = \delta \left\{ \int_0^1 \frac{1}{\left\{\frac{T_w}{T_f} + \left\{1 - \frac{T_w}{T_f}\right\} \left\{\frac{y}{\delta}\right\}\right\}^{1/7}} d\left\{\frac{y}{\delta}\right\} - 1 \right\} \qquad (B.9)$$

For $T_w/T_f = 0.957$, equation (B.9) can be integrated numerically using a double substitution,

$$t = \left\{\frac{y}{\delta}\right\}^{1/7} \qquad \text{and} \quad u = \frac{T_w}{T_f} + \left(1 - \frac{T_w}{T_f}\right) t,$$

to give,

$$\Delta L = 0 \tag{B.10}$$

to eight significant figures.

Thus it is fair to say that in all the experimental cases studied, end effects are negligible.

INCORRECT FOCUSSING:-

The focussing lens was positioned by a trial-and-error technique, a real-time system being used; a screen representing the plane of the holographic plate and the focussing lens being moved until refraction effects on the top of the rib appeared negligible. Hauf and Grigull [1970] estimate the error to be 1% of the thermal field gradient once the focus position has been obtained.

REFRACTION ERRORS:-

In the compressible flow study refraction errors are negligible except in regions of shock at the trailing edge of the blades. As no quantitative data are extracted from such regions, no error analysis will be attempted.

In the heat transfer study refraction errors only play an important part with high Reynolds number flows when the temperature gradients are at their most extreme. As the refraction errors are reduced by correct focussing, and, outside of the ray-crossing regime, may be determined using the suitable correction factor outlined in Chapter 4, the errors involved are equivalent to those experienced with the accuracy of fringe location.

A summary of the errors mentioned is now given.

SOURCE	HEAT TRANSFER STUDY		COMPRESSIBLE FLOW STUDY
	Low Re	High Re	
a) Fringe detection Broad fringe	5 %	5 %	11%
a) Fringe detection Narrow fringe	5 %	5 %	4%
b) Refraction error	-	-	-
c) End effects	-	-	-
d) Buoyancy	0.3%	-	-
e) Emulsion Shrinkage	-	-	-
f) Optics misalignment	-	-	-
g) Diffraction errors	1%	-	-
h) Incorrect focussing	1%	1%	-
Total error	± 5.1%	± 5.2%	±11% to ±4%

APPENDIX C (p. 279-286) has been removed for copyright reasons

C.E.G.B. Internal Reports."Fourier Transforms in Image Processing" J.C. Hunter. Report. TPRD/M/TB1054/M85. October 1985

APPENDIX D

SPECIFICATION OF IMAGE PROCESSING SYSTEM USED IN COMPRESSIBLE FLOW STUDY

Hardware

Intel multibus backplane

Intel iSBC 86/14 single board computer - CPU 8086 running at 8 MHz.

8087 Maths co-processor running at 8 MHz.

Quantum Q2020 20 Mbyte 8" rigid disk drive.

Mitsubishi M2896 1.2 Mbyte 8" floppy disk drive.

SMS FWD 8001 Winchester/floppy disk controller board.

768 Kbyte RAM (1 x 512K and 1 x 256K boards) on the multibus.

Televideo 950 VDU.

Matrox VAF-512, 8 bit video digitiser board.

2 x Matrox RGBGRAPH video framestore boards providing a 512 x 512 x 8 bit image store.

Software

Intel iRMX 86 real time multiuser/multitasking operating system (Version 7.0).

Intel AEDIT programmers editor.

Language compilers for FORTRAN 86 and PLM 86.

ASM 86 Mono assembler.

LINK 86 Object module linker.

LIB 86 Librarian.

Camera

Pulnix 2-D array C.C.D. camera.

APPENDIX E

PUBLISHED PAPERS

"Holographic Interferometry and Digital Fringe Processing"

J.C. Hunter and M.W. Collins.

J. Phys. D.: Appl. Phys. 20, pp.683-691, (1987)†

"Problems in using holographic interferometry to resolve the four dimensional character of turbulence. Part II: Image & Data Processing"

J.C. Hunter and M.W. Collins

Int. J. Opt. Sensors, Vol.1, No.3, pp.227-234 (1986)†

"The Large Eddy Structure in Turbulent Flows"

J.C. Hunter, J.F. Lockett, P.R.Voke and M.W. Collins

Heat and Technology (Calore e tecnologia), Vol.4, No.1. (1986)

"A Comparison of large-eddy simulation predictions of a thermal layer with holographic interferograms"

J.C. Hunter, H.M.Tsai, J.F. Lockett, P.R.Voke, M.W. Collins, and D.C. Leslie.

Procs. 5th Int. Conf. on Numerical Methods for Thermal Problems, Montreal, Canada, (1987)

"Heat Transfer Analysis using Laser Interferometry"

J.C. Hunter, J.F. Lockett, M.W. Collins, and J.R. Croft.

Instrumentation for the 21st Century, Instrument Society of America, IMEKO XI, Houston, U.S.A., Oct.1988 (to be published).

"Application of Holographic Interferometry for the Mapping of Gas Density in a Transonic Flow"

G.J. Ball, A.L. Gordon, J.C. Hunter, P.H. Richards, and G.T. Thompson.

Procs. I.E.R.E. Int. Conf. and Tutorial on Holographic Systems, Components and Applications, Churchill College, Cambridge, Sept.1987*

"Investigation of Convective Heat Transfer Enhancement using Real-Time Holographic Interferometry"

J.C. Lockett, J.C. Hunter, and M.W. Collins

Optical Measurements in Fluid Mechanics (Procs. of 6th Int. Conf. on Photon Correlation and other Optical Techniques in Fluid Mechanics), Institute of Physics Conf. Series 77, Adam Hilger, Bristol, U.K. pp.129-134, 1985.

C.E.G.B. Internal Reports.

"Fourier Transforms in Image Processing†

J.C. Hunter.

Report. TPRD/M/TB1054/M85. October 1985.

"The Automatic Analysis of Compressible Flow Interferograms"

J.C. Hunter.

Report. December 1987.

Presented Papers

"Holographic Interferometry and Digital Fringe Processing.

J.C. Hunter and M.W. Collins

11th Lecture Series - Flow Visualisation and Digital Image Processing, Von Karman Institute for Fluid Dynamics, June 1986.

"Automatic Analysis of Compressible Flow Fringes".

J.C. Hunter and M.W. Collins

Video presentation, FASIG (Fringe Analysis Special Interest Group), November 1987.

† = included in the Appendix.

* = presented by the author at Cambridge.

Appendix E has been removed for copyright reasons

"Holographic Interferometry and Digital Fringe Processing" J.C. Hunter and M.W. Collins. J. Phys. D.: Appl. Phys. 20, pp.683-691, (1987)

"Problems in using holographic interferometry to resolve the four dimensional character of turbulence. Part II: Image & Data Processing" J.C. Hunter and M.W. Collins. Int. J. Opt. Sensors, Vol.l, No.3, pp.227-234 (1986)

APPENDIX F

FIGURES

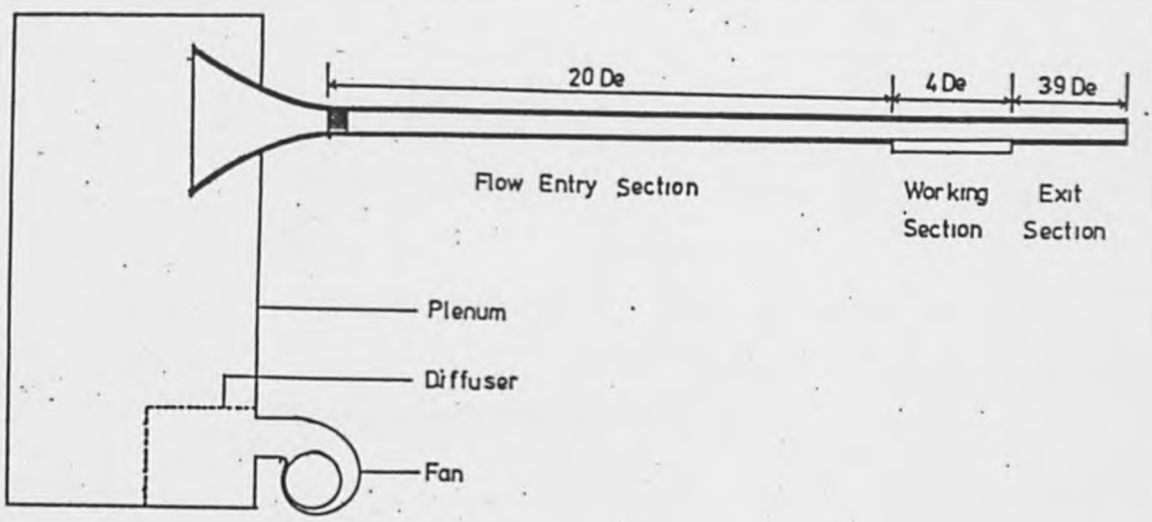

Fig.(1.1). Schematic diagram of experimental wind-tunnel.

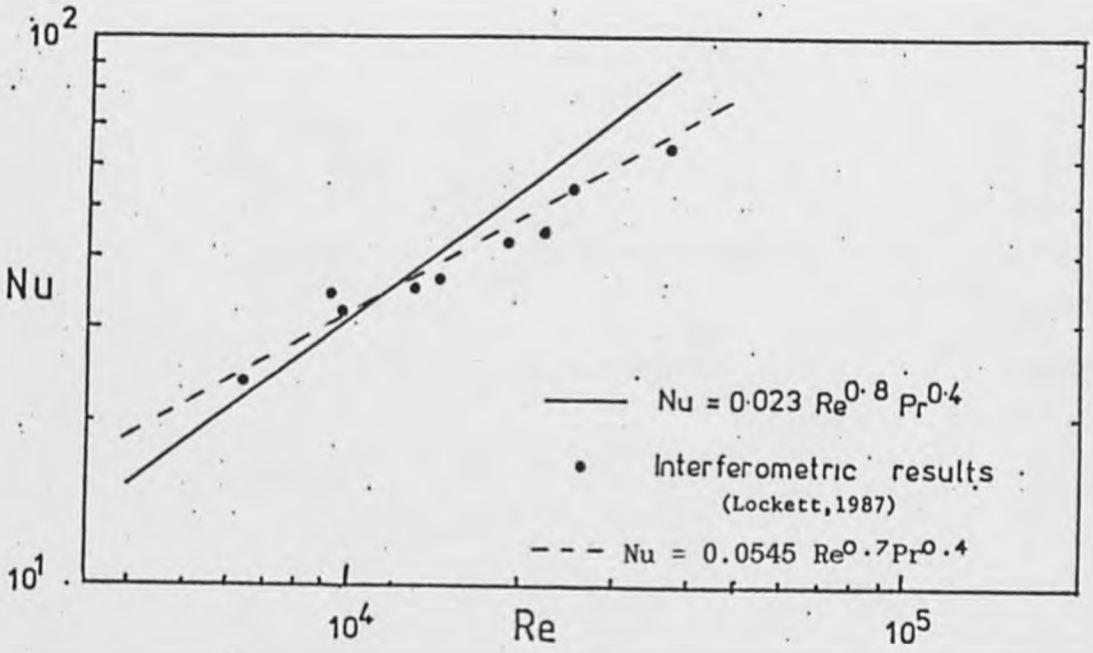

Fig.(1.2). Flat plate heat transfer results

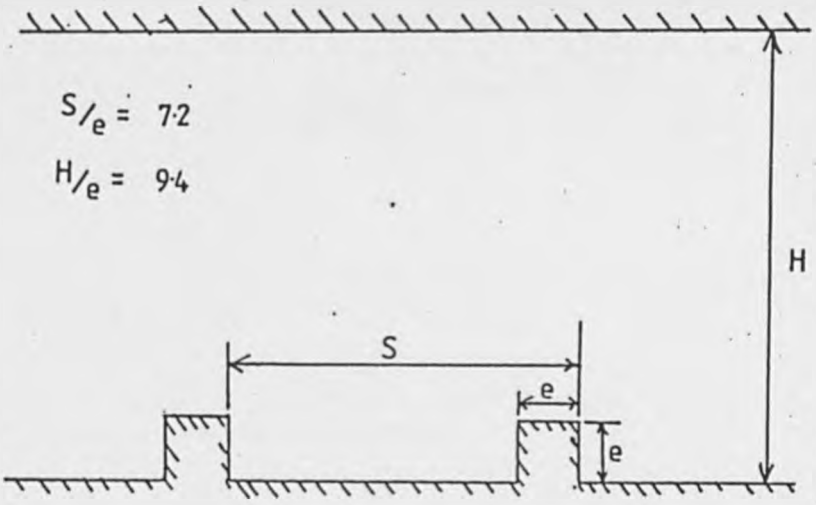

SQUARE RIB GEOMETRY STUDIED

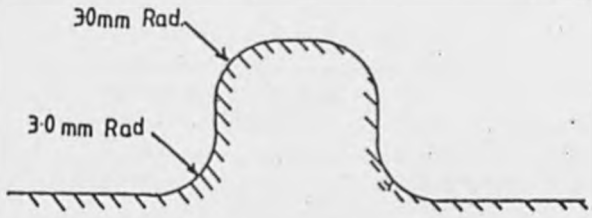

Rounded rib

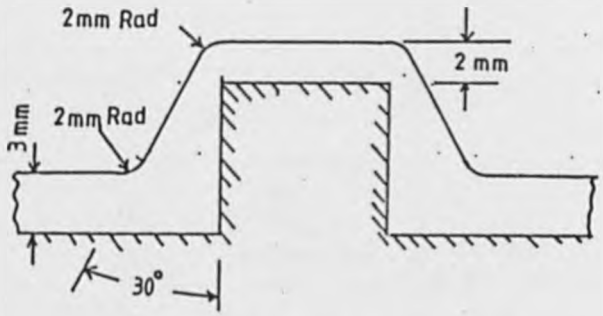

Square rib deposition

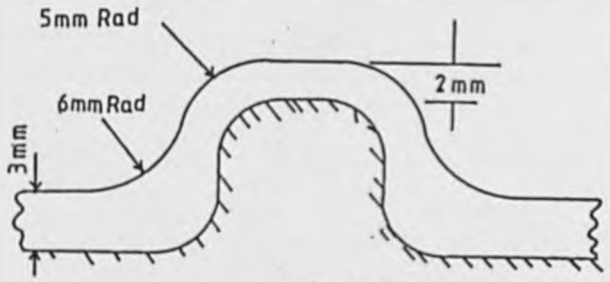

Rounded rib deposition

Fig.(1.3). Rib geometries used in the heat transfer investigation.

FIG (3·1) RIFRAN FLOW DIAGRAM

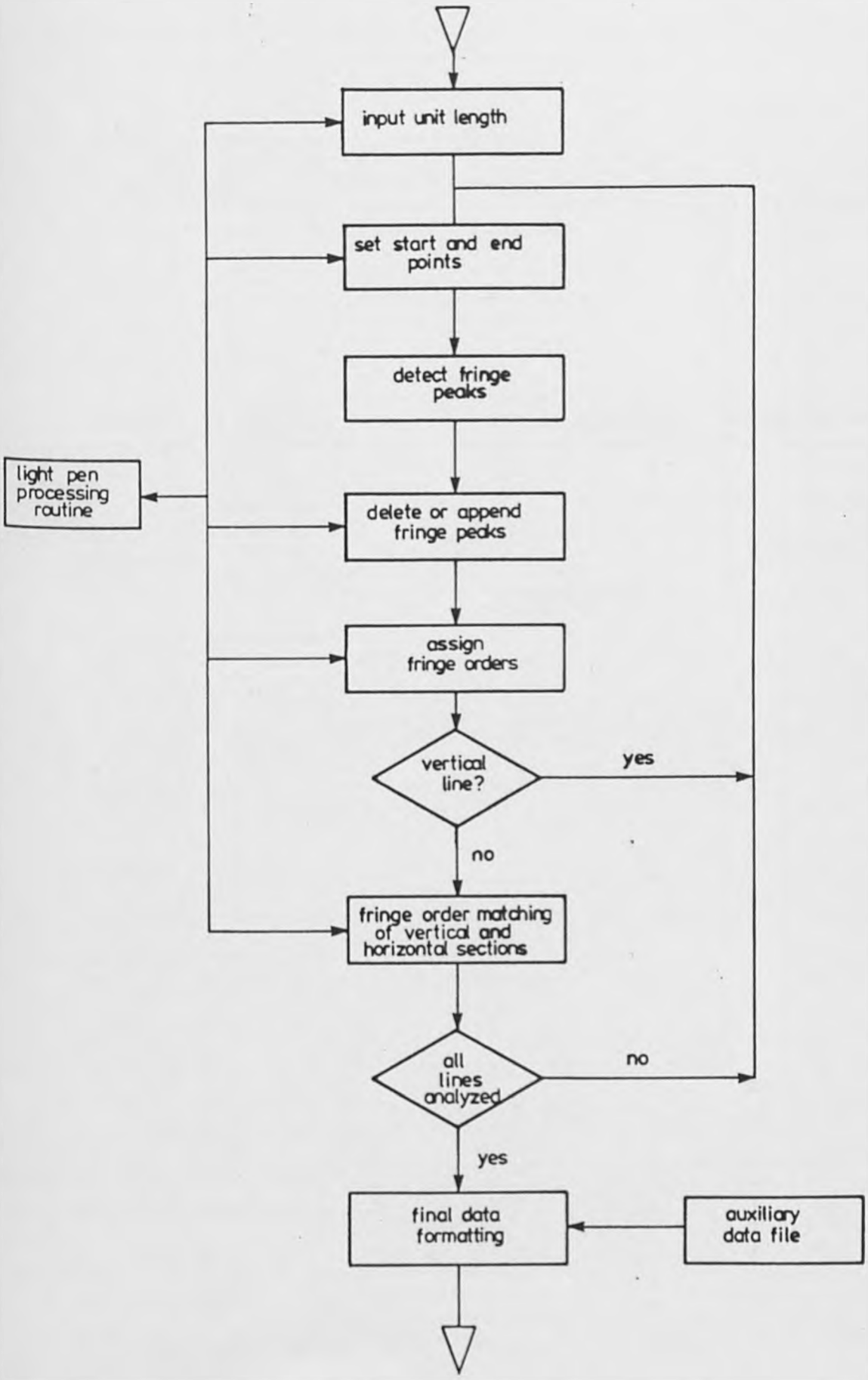

FIG (3·2) CONCEPTUAL CONFIGURATION FOR AN INTERACTIVE FRINGE ANALYSIS SYSTEM

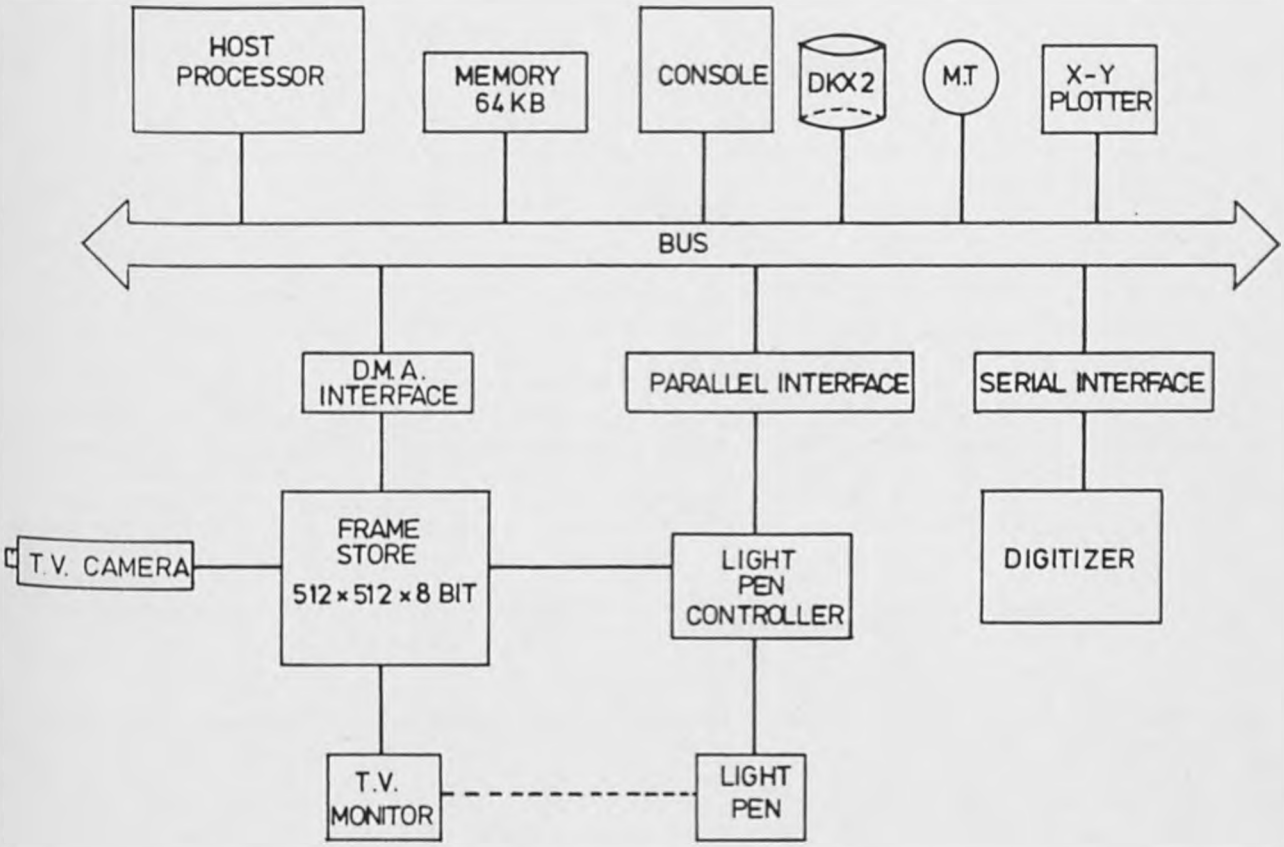

FIG (3·3) THE FIVE MAJOR FRINGE DETECTION TECHNIQUES

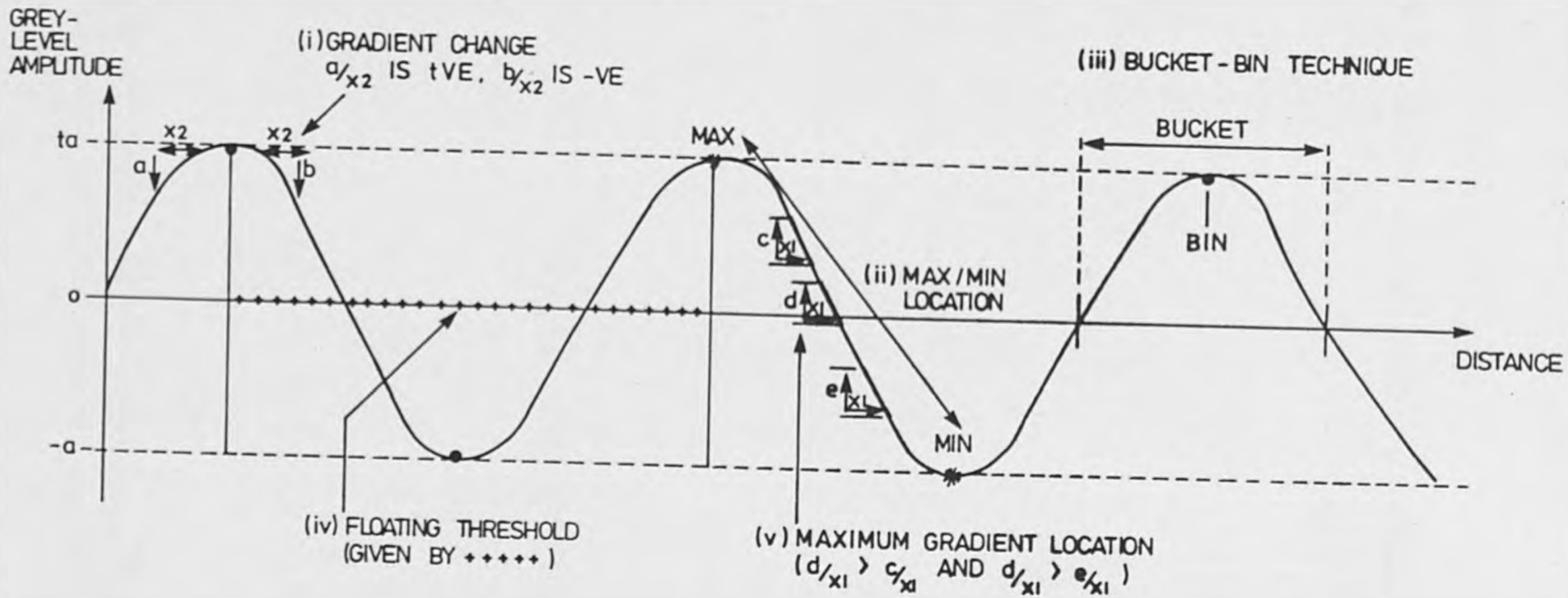

FIG (3·4) FRINGE TRACKING VECTORS

The vectors are all L-pixels long, and separated by θ° (in this case 45°). As a bright fringe is being traced progress is in the maximal intensity direction.

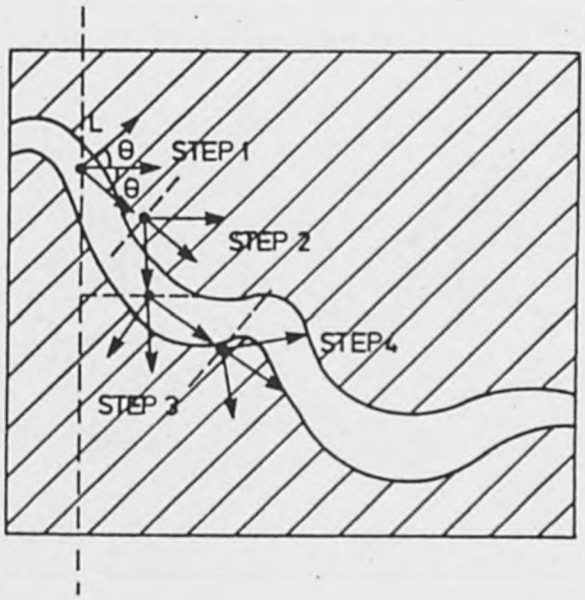

FIG(3·5) BUCKET-BIN FRINGE DETECTION, DUE TO CHOUDRY

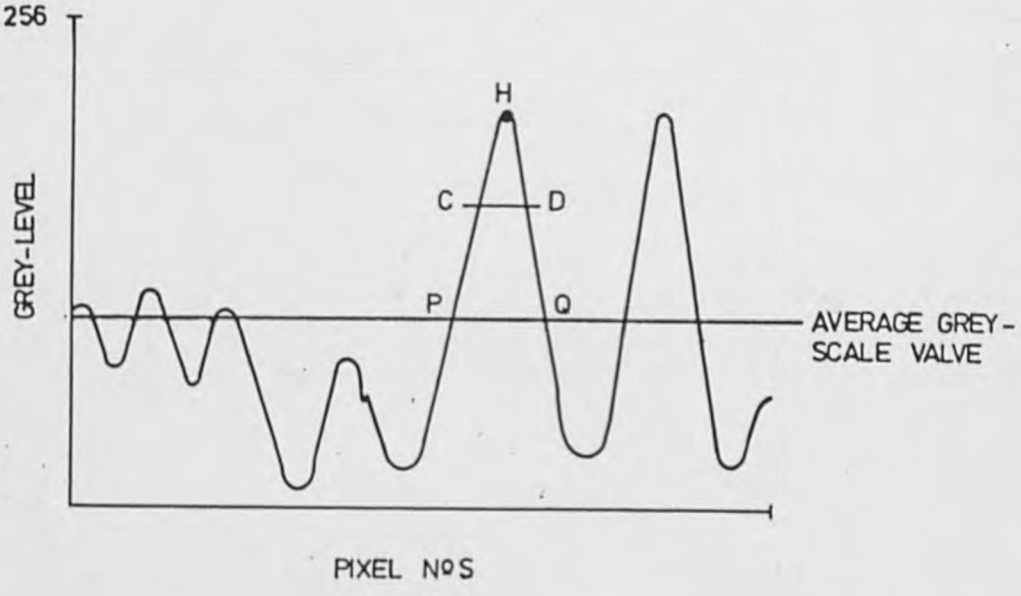

FIG (3·6) BINARISATION USING A FLOATING THRESHOLD

(a) INTENSITY PROFILE

(b) PROFILE AFTER APPLICATION OF THE THRESHOLDING ALGORITHM

FIG (3·7) FRINGE SEGMENTATION PROCESS DUE TO CLINE

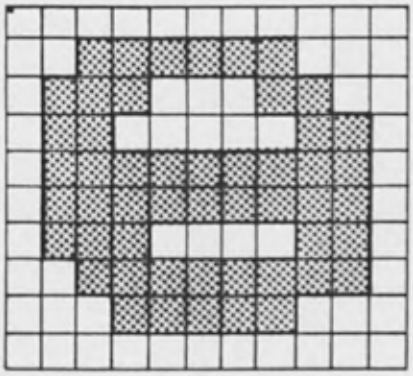

(a) DIGITISATION

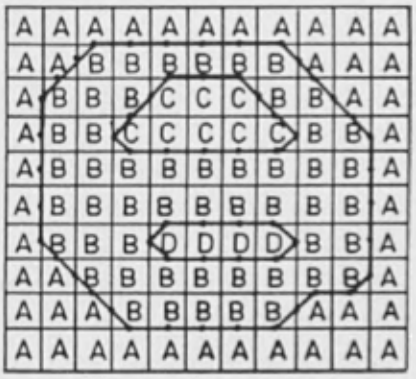

(b) SEGMENTATION

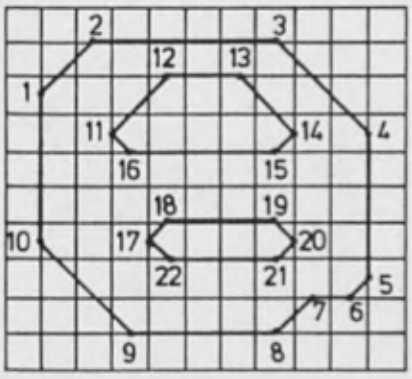

(c) EDGE DETECTION

FIG(3·8) POLYGONAL REPRESENTATION OF INTERFERENCE FRINGES DUE TO BECKER

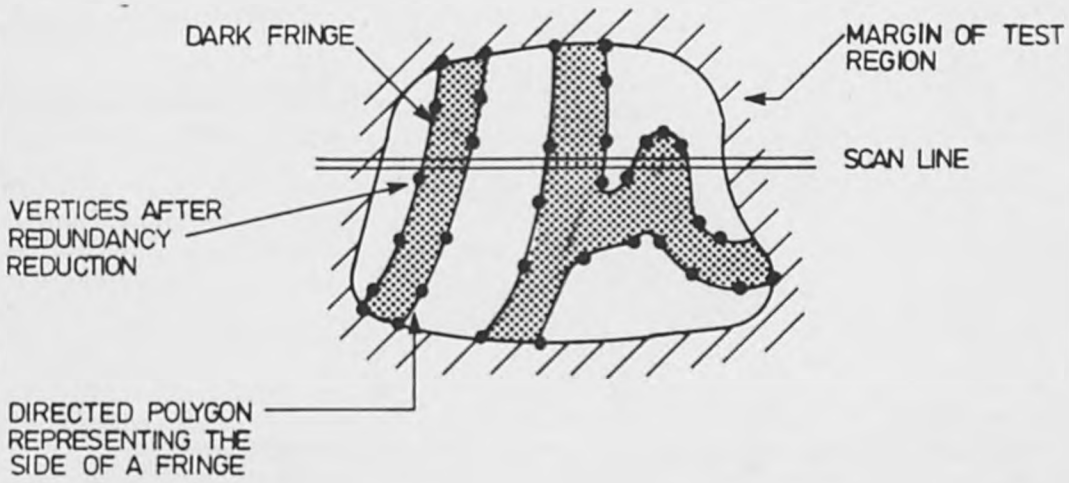

FIG (3·9) EXTRACTION OF SHAPE FEATURES DUE TO AGRAWALA AND KULKARNI

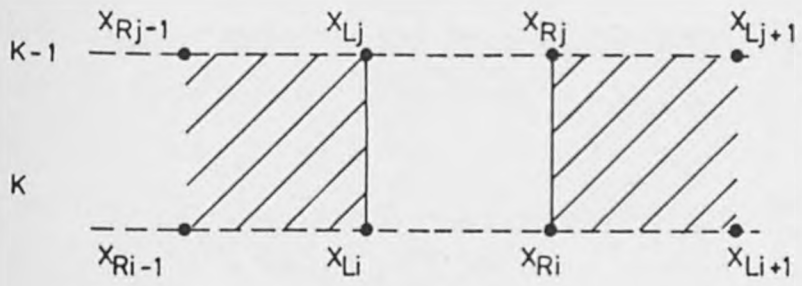

RIGHT BOUNDARY

$X_{L_i}(k) < X_{R_j}(k-1) < X_{L_{i+1}}(k)$

$X_{L_j}(k-1) < X_{R_i}(k) < X_{L_{j+1}}(k-1)$

LEFT BOUNDARY

$X_{R_{i-1}}(k) < X_{L_j}(k-1) < X_{R_i}(k)$

$X_{R_{j-1}}(k-1) < X_{L_i}(k) < X_{R_j}(k-1)$

(i) CONTINUATION CONDITIONS

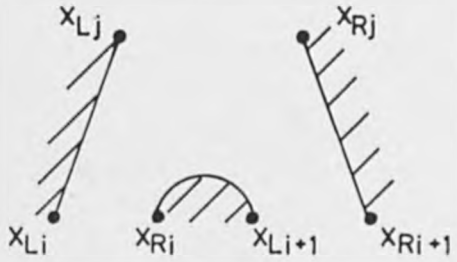

HOLE :- $X_{Li+1}(K) < X_{Rj}(K-1)$

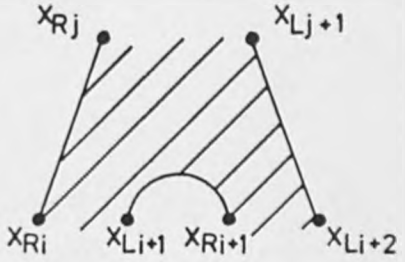

BODY :- $X_{Ri+1}(K) < X_{Lj+1}(K-1)$

(ii) NEW OBJECT CONDITIONS

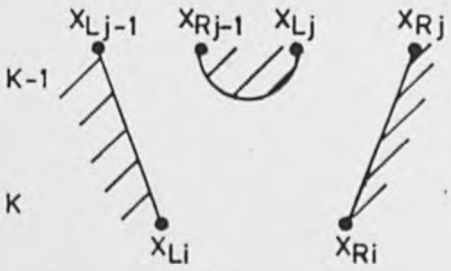

HOLE TERMINATION $X_{Lj} < X_{Ri}$

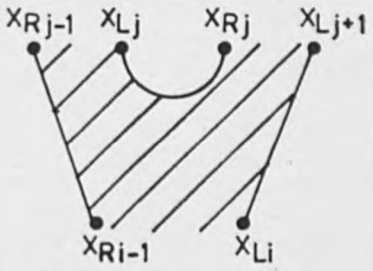

BODY TERMINATION $X_{Rj} < X_{Li}$

(iii) TERMINATION CONDITIONS

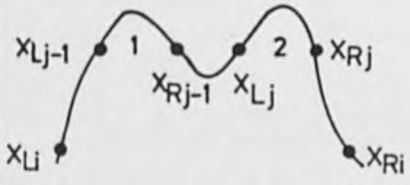

(a) Merging of the same type of objects, both bodies.

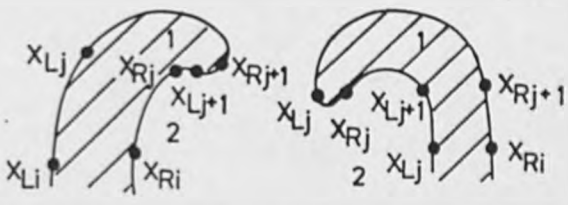

(b) Different object types merging
(i) Left object is parent of right
(ii) Right object is parent of left

(iv) MERGING CONDITIONS For detecting a merge, the edge point conditions are as those for termination, with the proviso of different object numbers for the discontinued boundaries.

FIG (3·10) PIXEL NEIGHBOURHOOD CONSIDERED IN THINNING ALGORITHIMS

FIG (3·11) SCHEMATIC DIAGRAM OF CENTRE-LINE EXTRACTION

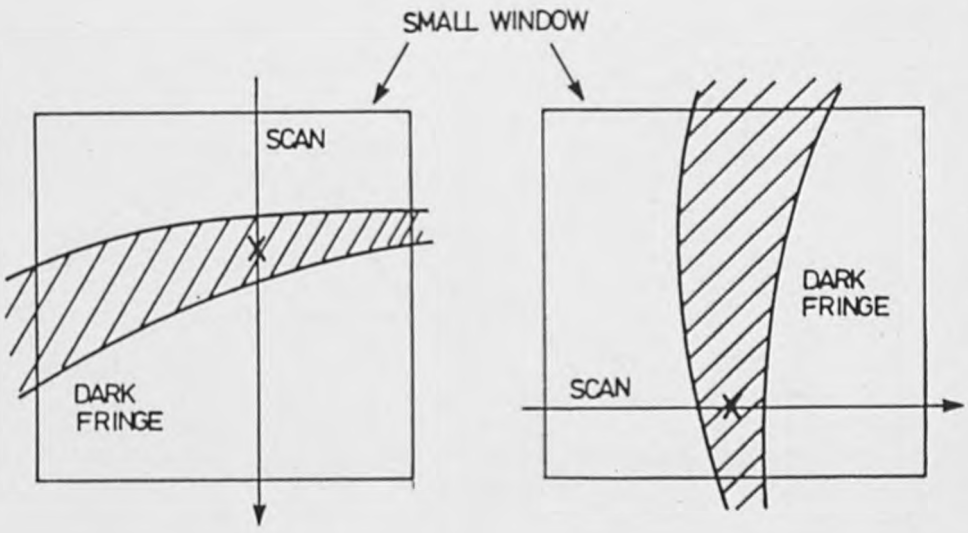

(a) VERTICAL SCANNING

(b) HORIZONTAL SCANNING

FIG (3·12) FRINGE ORDERING SCHEME DUE TO BECKER

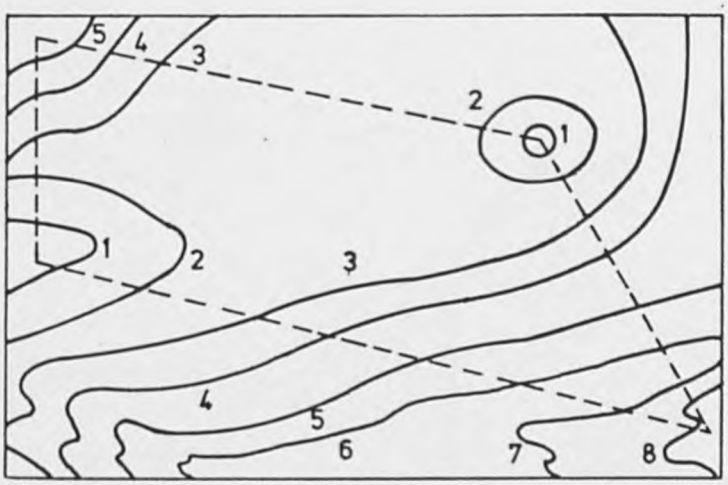

FIG (3·13) DUAL REFERENCE BEAM HETERODYNE HOLOGRAPHY AFTER DÄNDLIKER

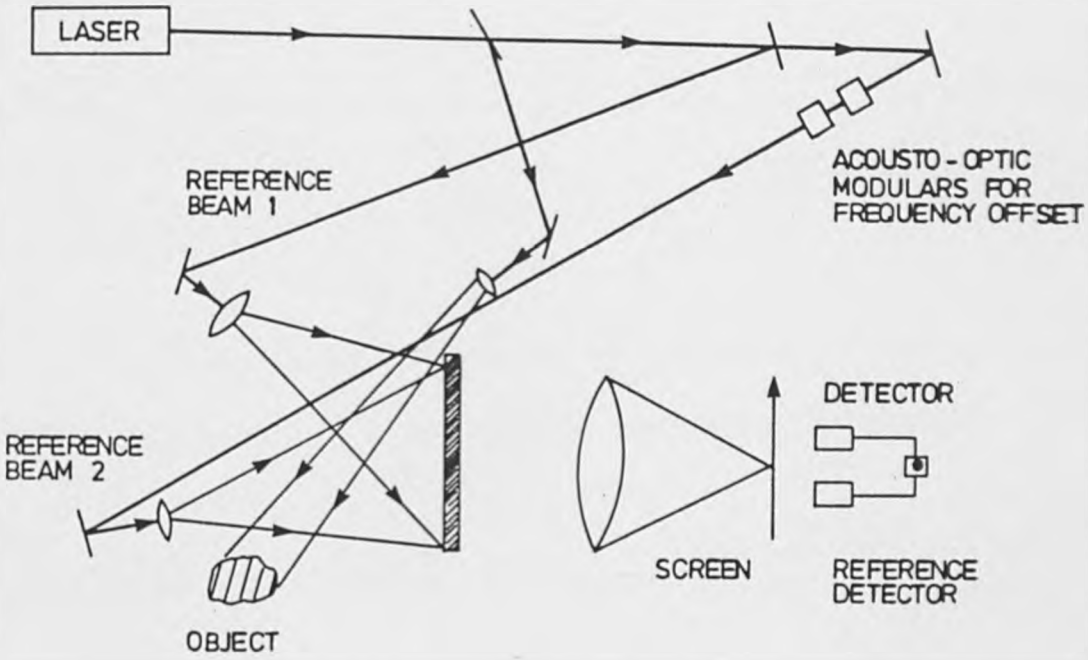

FIG (3·14) DUAL REFERENCE BEAM QUASI-HETERODYNE HOLOGRAPHY AFTER DÄNDLIKER

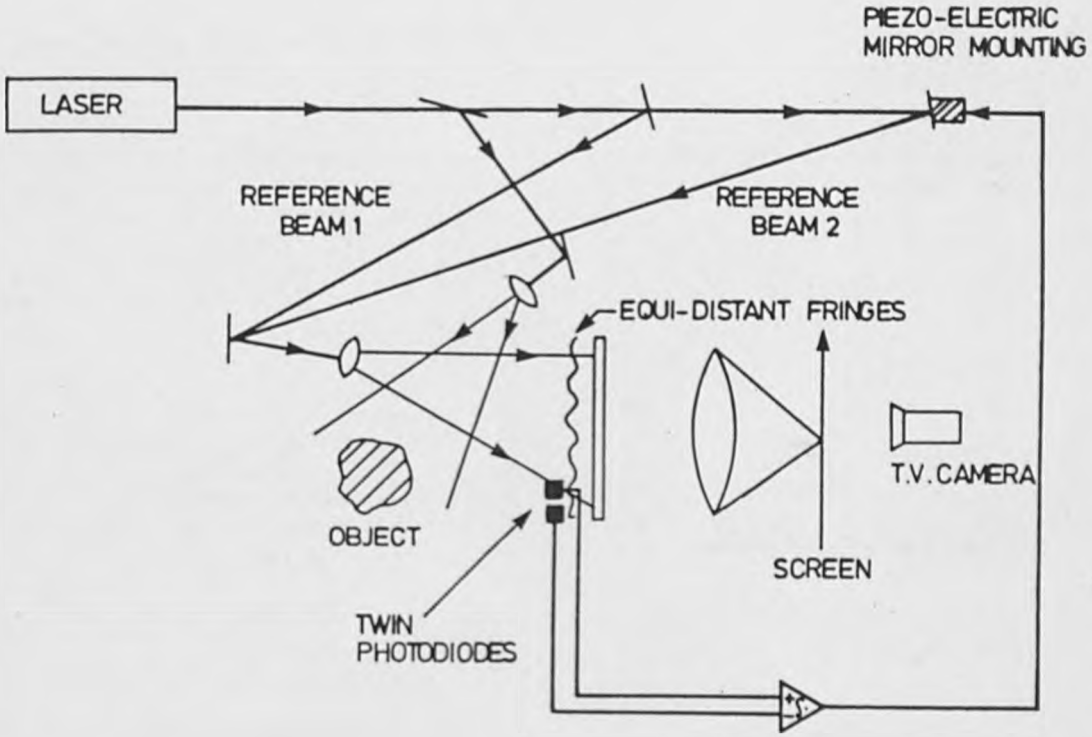

FIG (3·15) FOURIER TRANSFORM ANALYSIS DUE TO ICHIOKA

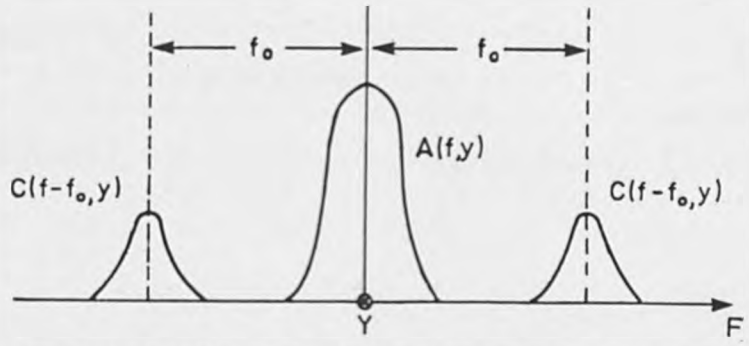

(a) SEPARATED FOURIER SPECTRA OF A NON-CONTOUR TYPE OF FRINGE PATTERN

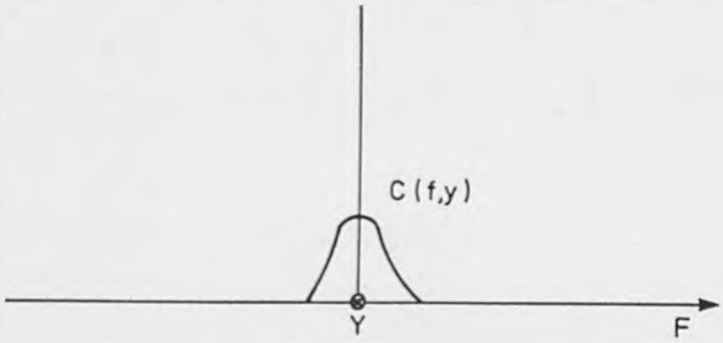

(b) SINGLE SPECTRAL SIDEBAND SELECTED AND SHIFTED TO THE ORIGIN

N.B THE Y-AXIS IS NORMAL TO THE FIGURE

FIG(3·16) THE PRINCIPLE OF SPECKLE PHOTOGRAPHY

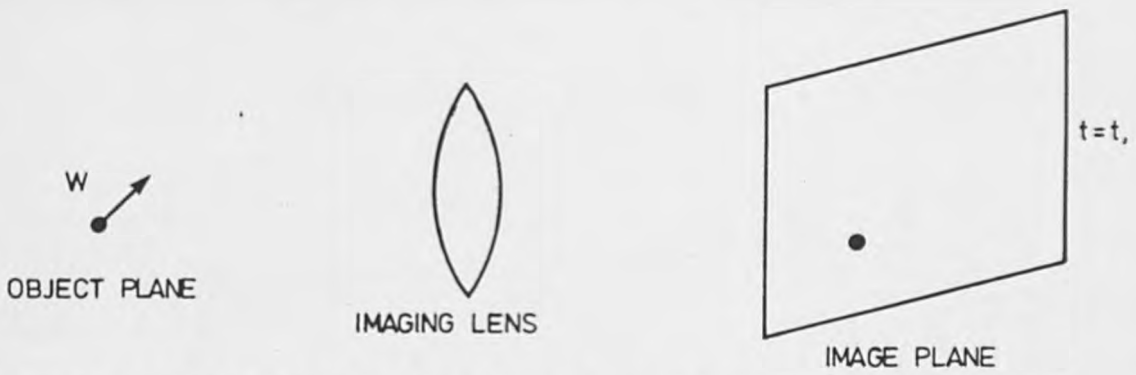

(a) FIRST EXPOSURE OBJECT POINT MOVING AT A VELOCITY W

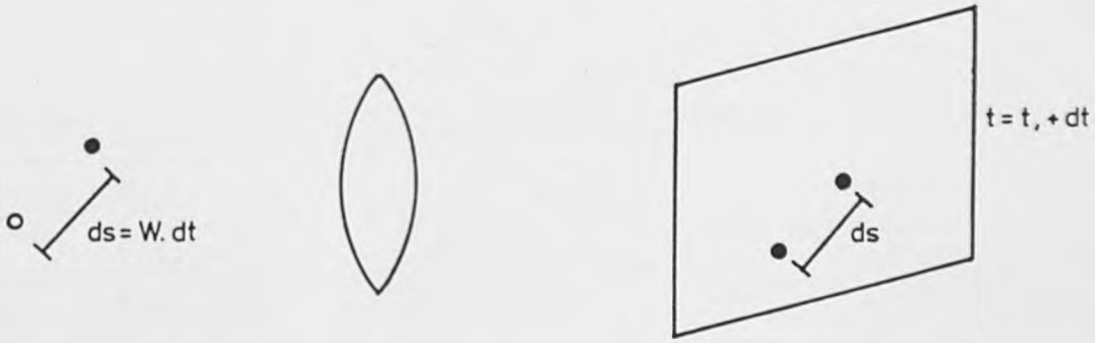

(b) SECOND EXPOSURE OF THE POINT, dT LATER

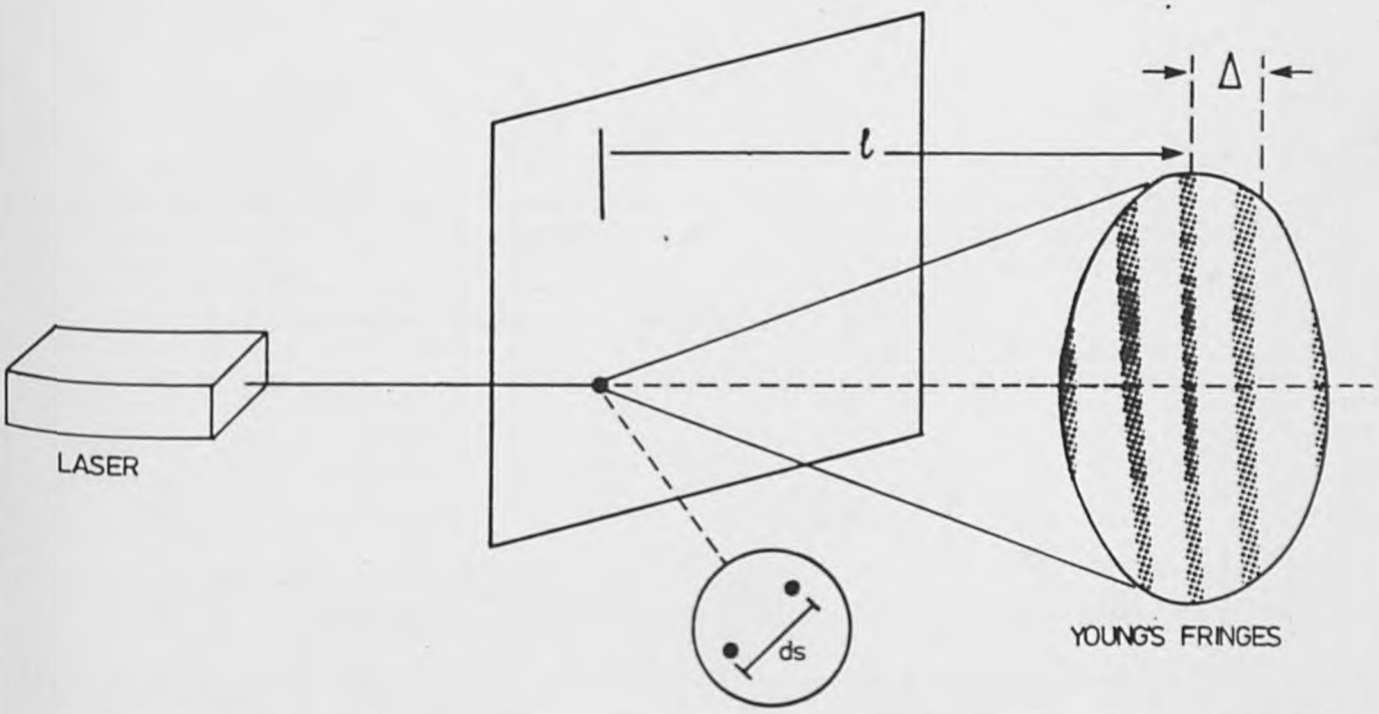

(c) THE LASER ILLUMINATES A SMALL CIRCULAR AREA INCLUDING THE PAIR OF IMAGE POINTS. A SET OF YOUNG'S FRINGES IS FORMED IN A PLANE AT DISTANCE l FROM THE ILLUMINATED PAIR OF POINTS.

FIG (3·17) A TYPICAL AUTOCORRELATION FUNCTION SHAPE

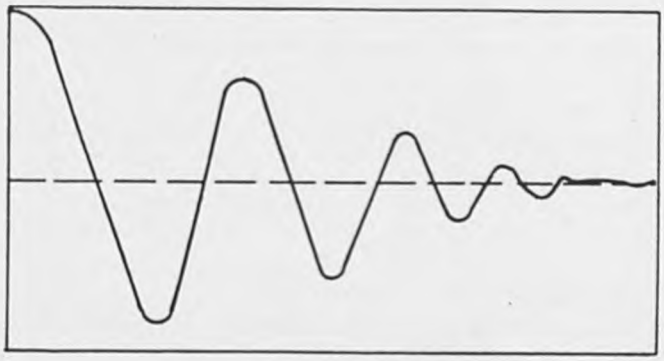

FIG (4·1) GABOR'S IN-LINE HOLOGRAPHIC TECHNIQUE

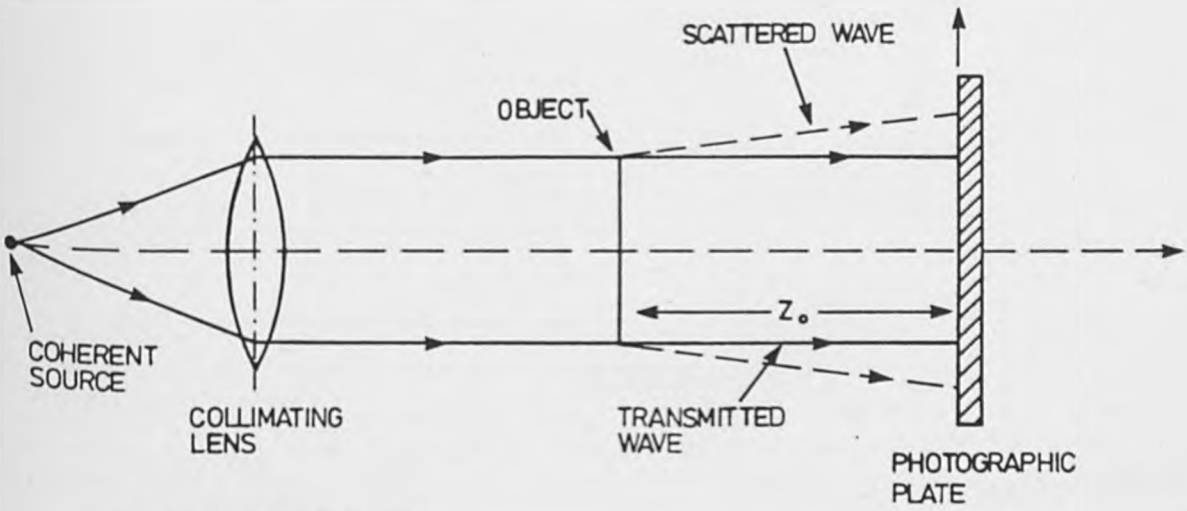

(a) RECORDING GEOMETRY

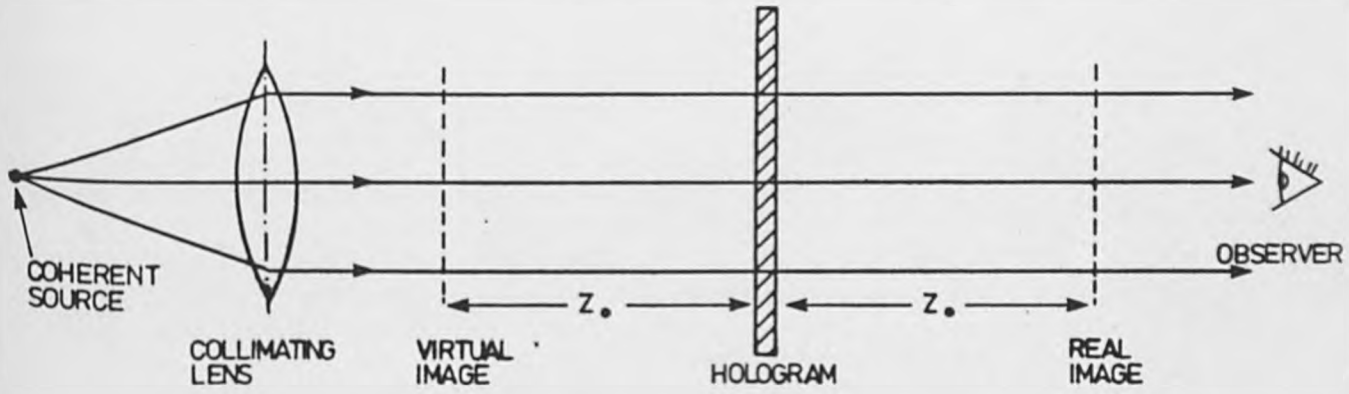

(b) RECONSTRUCTION GEOMETRY

FIG (4·2) THE OFF-AXIS HOLOGRAPHIC TECHNIQUE

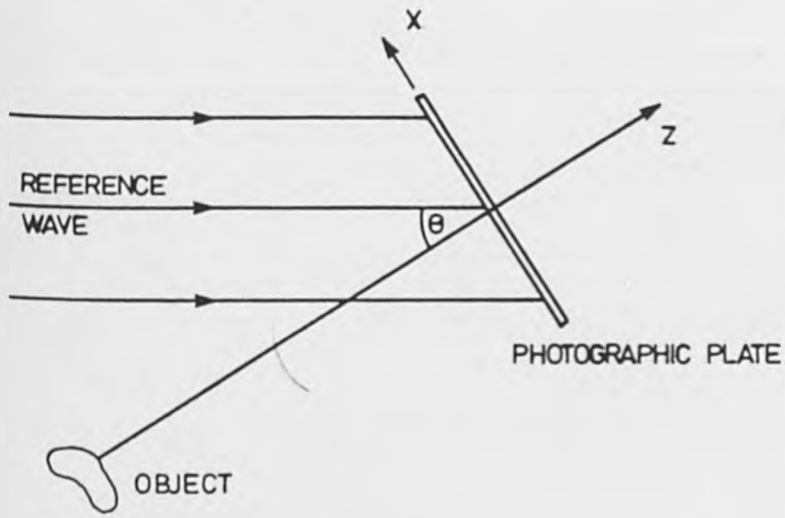

(a) RECORDING GEOMETRY

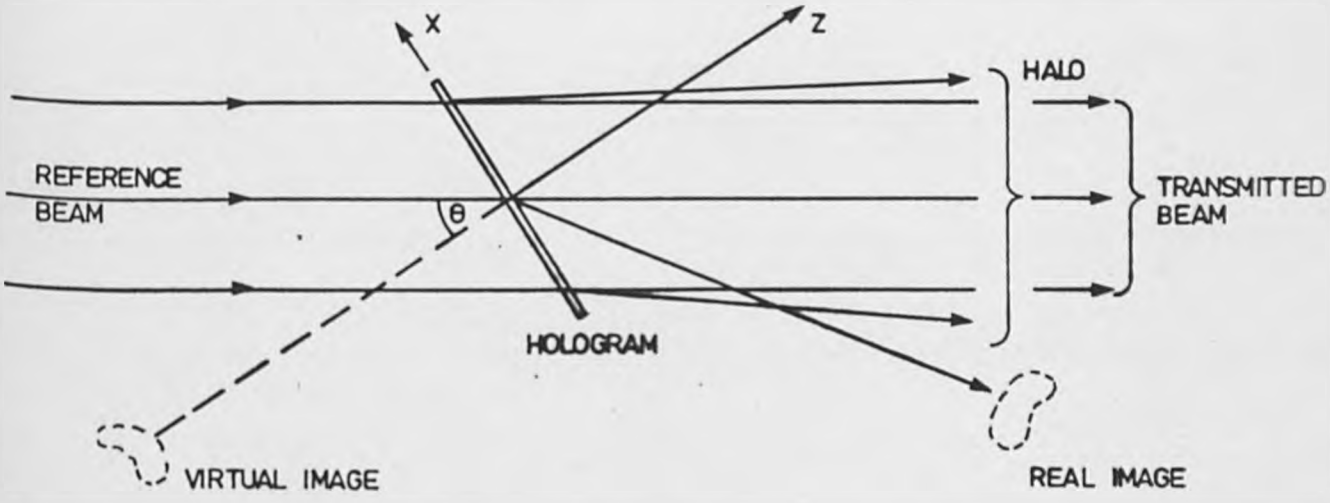

(b) RECONSTRUCTION GEOMETRY

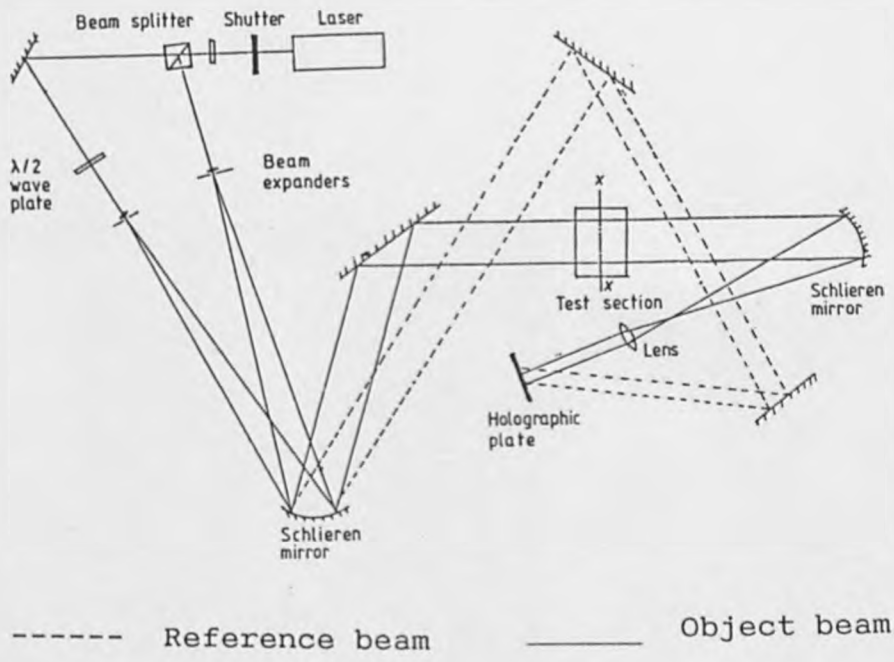

Figure 4.3. Experimentally used Image-Plane Interferometer.

(a) Real-time square rib - Re = 3,540

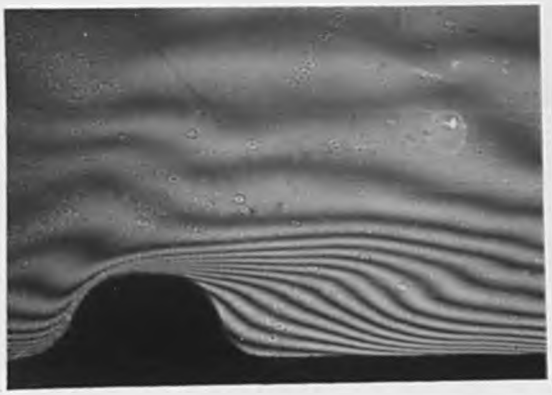

(b) Real-time rounded rib - Re = 3,620

(c) Double exposure square rib - Re = 10,600

(d) Double exposure square deposited rib - Re = 15,000

Figure 4.4. Example Heat Transfer Interferograms.

Figure 4.5. Example Compressible Flow Interferogram

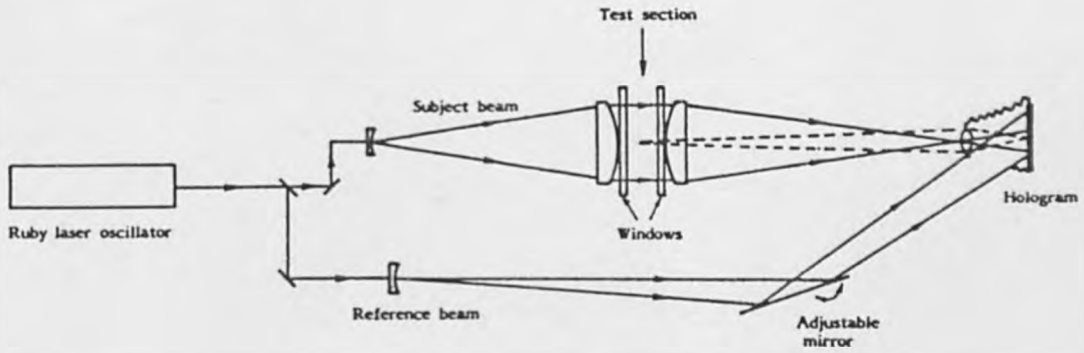

Figure 4.6. Schematic of Holographic Interferometer used in Compressible Flow Study.

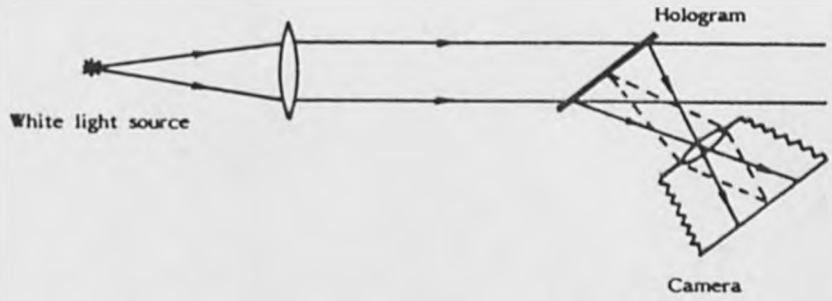

Figure 4.7. A Typical White-light Reconstruction Geometry.

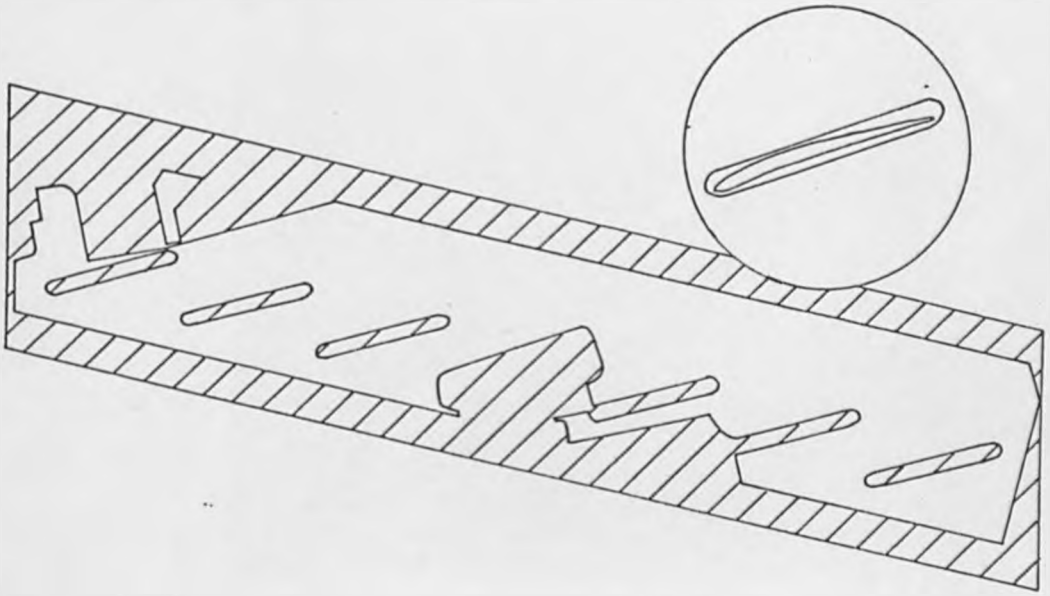

Figure 4.8. Schematic of the Cascade Section, showing Blade Profiles.

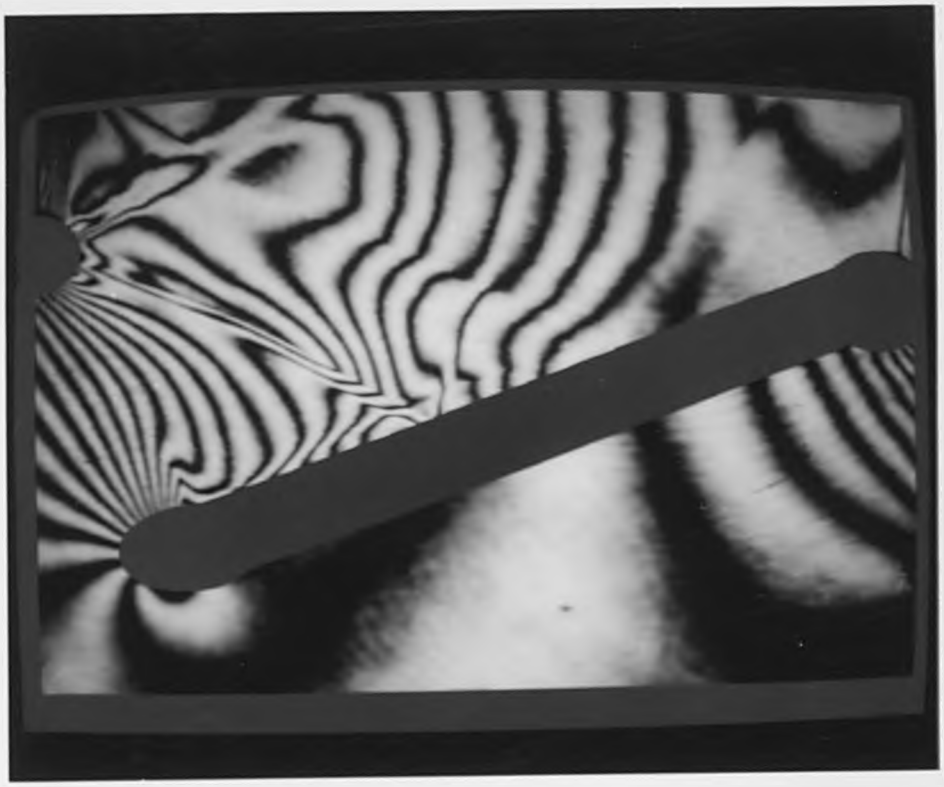

Figure 5.1. Typically Masked Image Data.

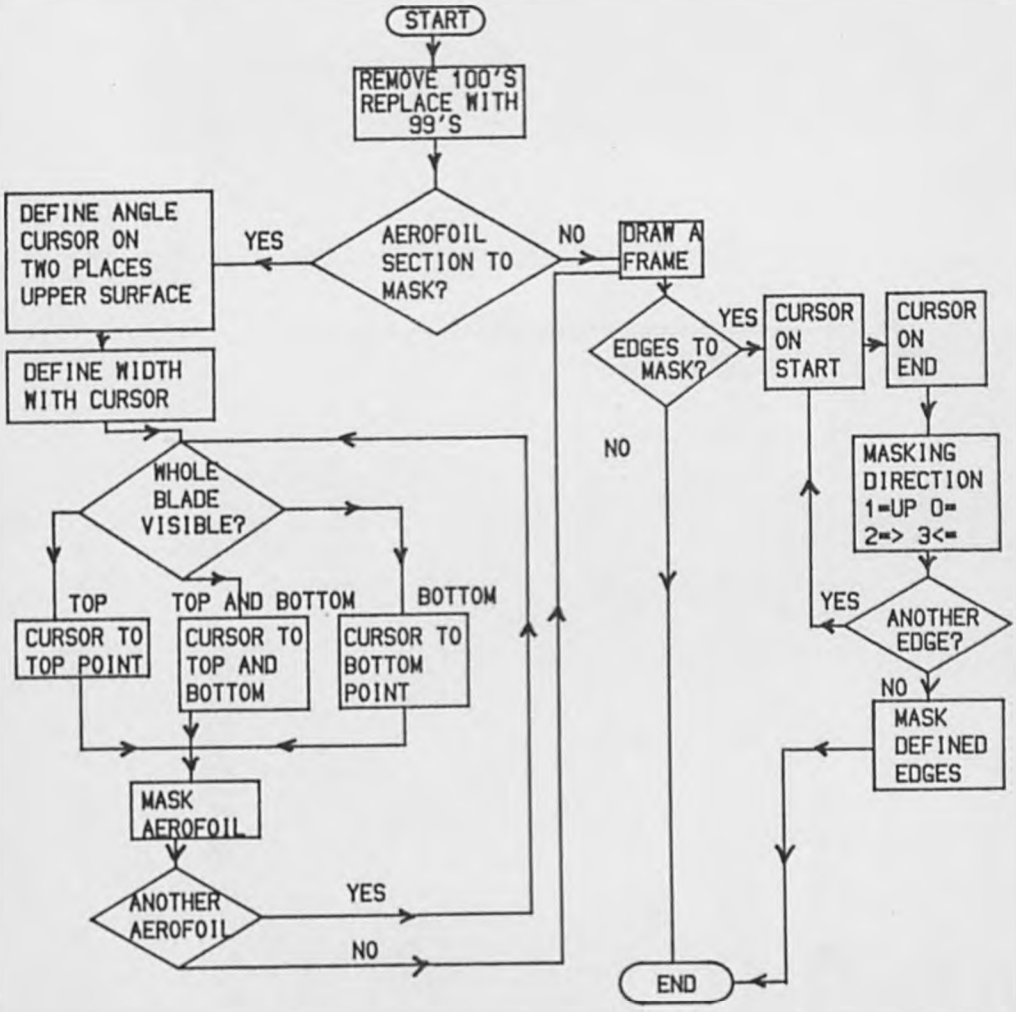

Figure 5.2. Flow Chart for the Masking Procedure.

Figure 5.3. Image Data showing Fiducial Overlays.

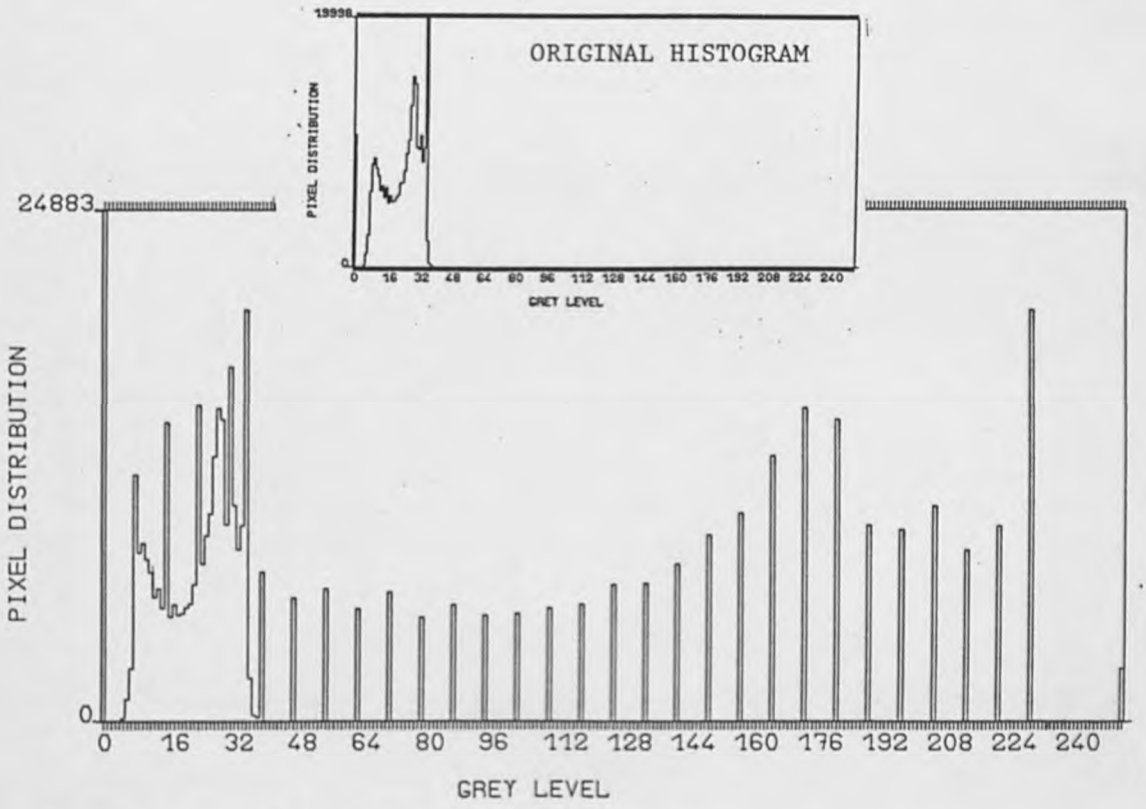

Figure 5.4. Linear Histogram Stretch.

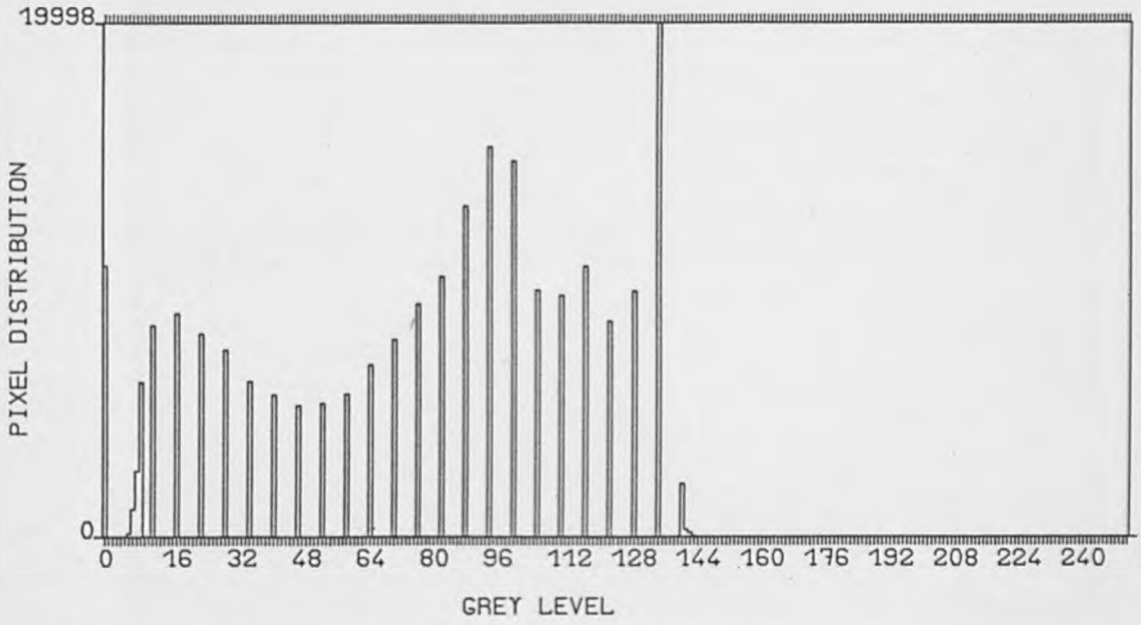

Figure 5.5. Histogram Equalisation.

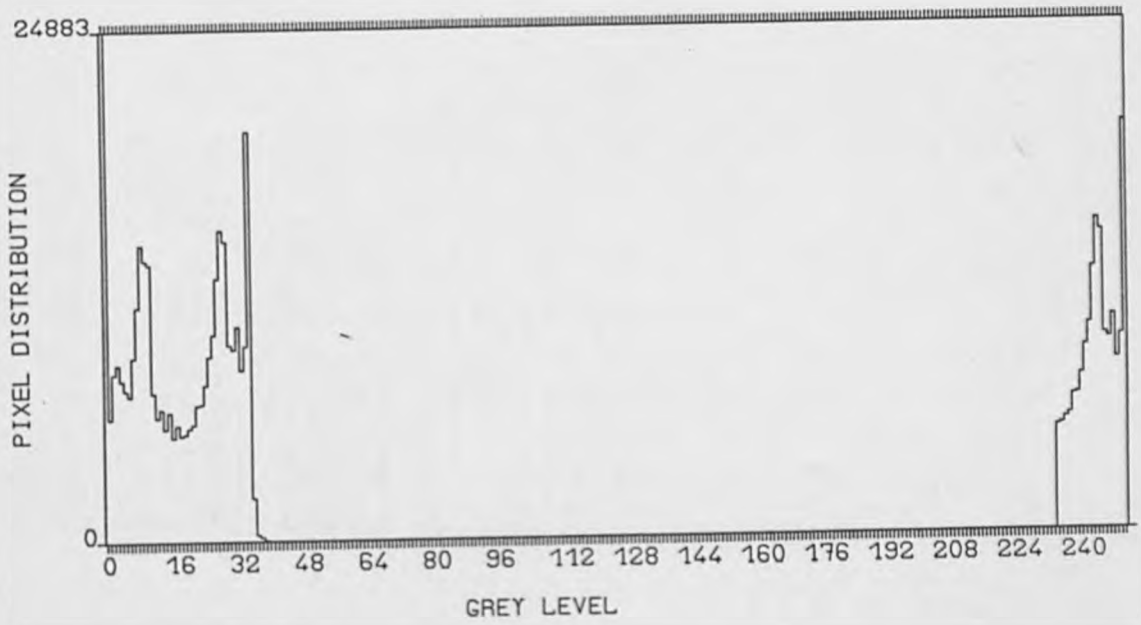

Figure 5.6. Histogram Split.

$$\frac{1}{9}\begin{bmatrix} 1 & 1 & 1 \\ 1 & 1 & 1 \\ 1 & 1 & 1 \end{bmatrix}$$

$$\frac{1}{10}\begin{bmatrix} 1 & 1 & 1 \\ 1 & 2 & 1 \\ 1 & 1 & 1 \end{bmatrix} \qquad \frac{1}{16}\begin{bmatrix} 1 & 2 & 1 \\ 2 & 4 & 2 \\ 1 & 2 & 1 \end{bmatrix}$$

Figure 5.7. Typical Noise Smoothing Masks.

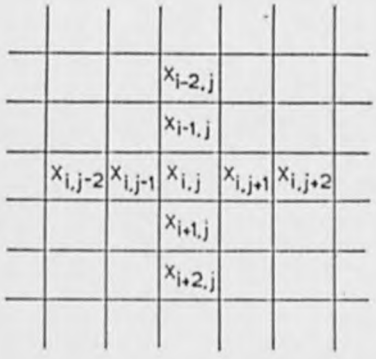

Cross neighbourhood of Xi,j in the original image

$$Y_{i,j} = \text{median of } \{ X_{i,j-2}, X_{i,j-1}, X_{i,j}, X_{i,j+1}, X_{i,j+2}, X_{i-2,j}, X_{i-1,j}, X_{i+1,j}, X_{i+2,j} \}$$

Formation of pixel in location i,j of filtered image

Figure 5.8. A Median Filter, cross-shaped Neighbourhood.

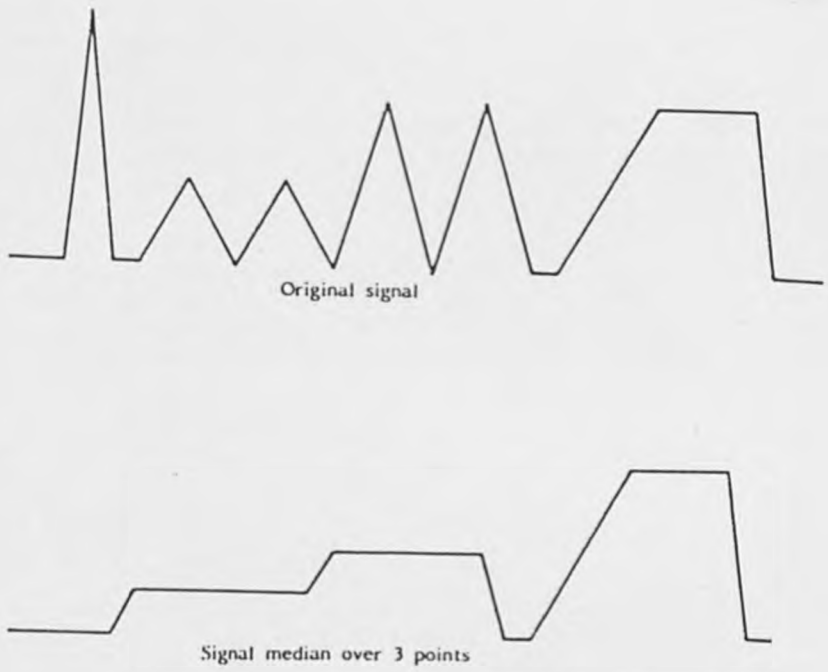

Figure 5.9. Example One-dimensional Median Filtering.

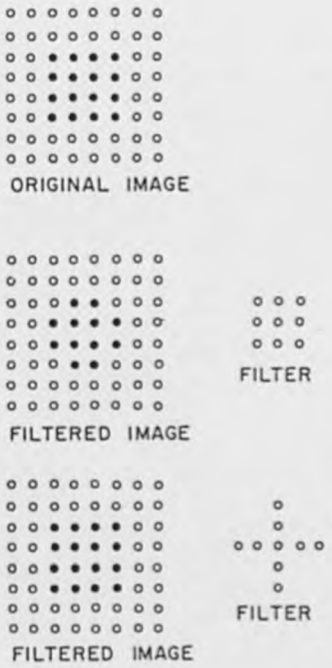

Figure 5.10. Example Two-dimensional Median Filtering.

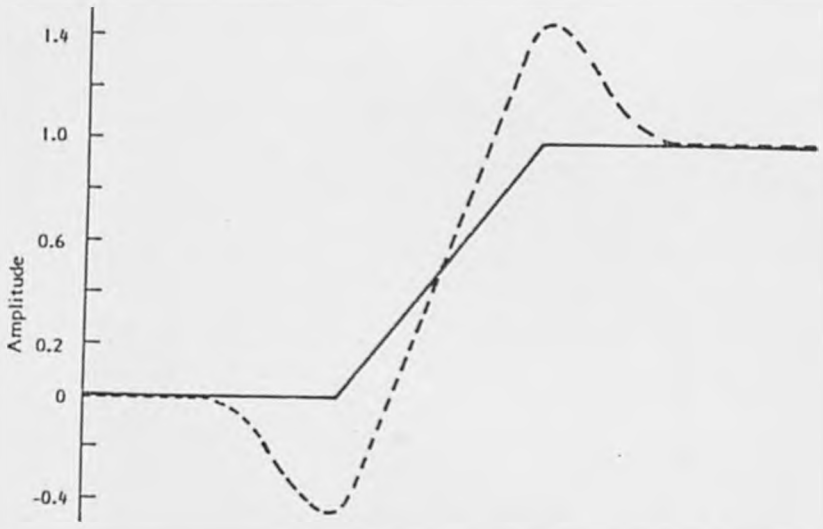

THE ORIGINAL EDGE (——) IS TRANSFORMED INTO THE ENHANCED EDGE (- - - -)

Figure 5.11. Edge Structure after Edge Enhancement.

$$\frac{1}{2}\begin{bmatrix} & -1 & \\ -1 & 6 & -1 \\ & -1 & \end{bmatrix} \qquad \begin{bmatrix} -1 & -1 & -1 \\ -1 & 9 & -1 \\ -1 & -1 & -1 \end{bmatrix}$$

3 x 3

$$\frac{1}{2}\begin{bmatrix} & & -1 & & \\ & -1 & 0 & -1 & \\ -1 & 0 & 10 & 0 & -1 \\ & -1 & 0 & -1 & \\ & & -1 & & \end{bmatrix} \qquad \frac{1}{6}\begin{bmatrix} -1 & -1 & -1 & -1 & -1 \\ -1 & -3 & 0 & -3 & -1 \\ -1 & 0 & 30 & 0 & -1 \\ -1 & -3 & 0 & -3 & -1 \\ -1 & -1 & -1 & -1 & -1 \end{bmatrix}$$

5 x 5

$$\frac{1}{6}\begin{bmatrix} & & -1 & & & & \\ & -1 & -1 & -1 & -1 & -1 & \\ & -1 & 0 & 4 & 0 & -1 & \\ -1 & -1 & 4 & 10 & 4 & -1 & -1 \\ & -1 & 0 & 4 & 0 & -1 & \\ & -1 & -1 & -1 & -1 & -1 & \\ & & -1 & & & & \end{bmatrix} \qquad \frac{1}{9}\begin{bmatrix} & & -1 & -1 & -1 & & \\ & -1 & -2 & -2 & -2 & -1 & \\ -1 & -2 & 1 & 5 & 1 & -2 & -1 \\ -1 & -2 & 5 & 25 & 5 & -2 & -1 \\ -1 & -2 & 1 & 5 & 1 & -2 & -1 \\ & -1 & -2 & -2 & -2 & -1 & \\ & & -1 & -1 & -1 & & \end{bmatrix}$$

7x7

Figure 5.12. Typical Edge Sharpening Masks.

1	2	1
0	0	0
-1	-2	-1

1	0	-1
2	0	-2
1	0	-1

SOBEL EDGE ENHANCEMENT : THE VALUE OF THE ENHANCEMENT IMAGE IS FOUND BY ADDING TO THE ORIGINAL THE ABSOLUTE VALUES OF THE RESULTS OF APPLYING THE ABOVE TWO MASKS

Figure 5.13. The Sobel Operator.

$$\begin{bmatrix} 0 & -1 & 0 \\ -1 & 4 & -1 \\ 0 & -1 & 0 \end{bmatrix}$$

Figure 5.14. The Laplacian Operator.

Fig.(5.15) An example of an enhanced raw image.

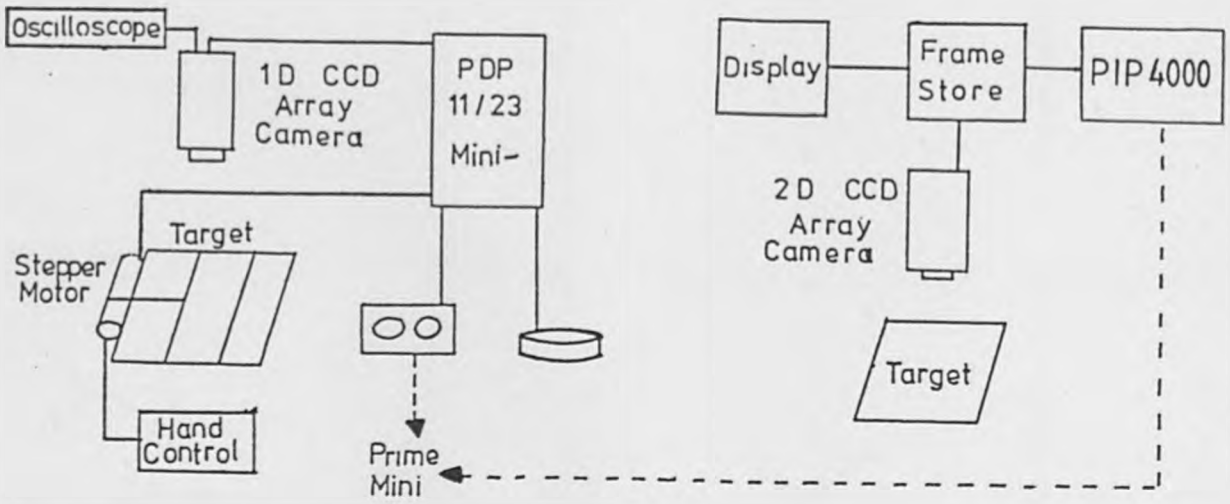

Figure 6.1. Schematic lay-out of Image Processing systems.

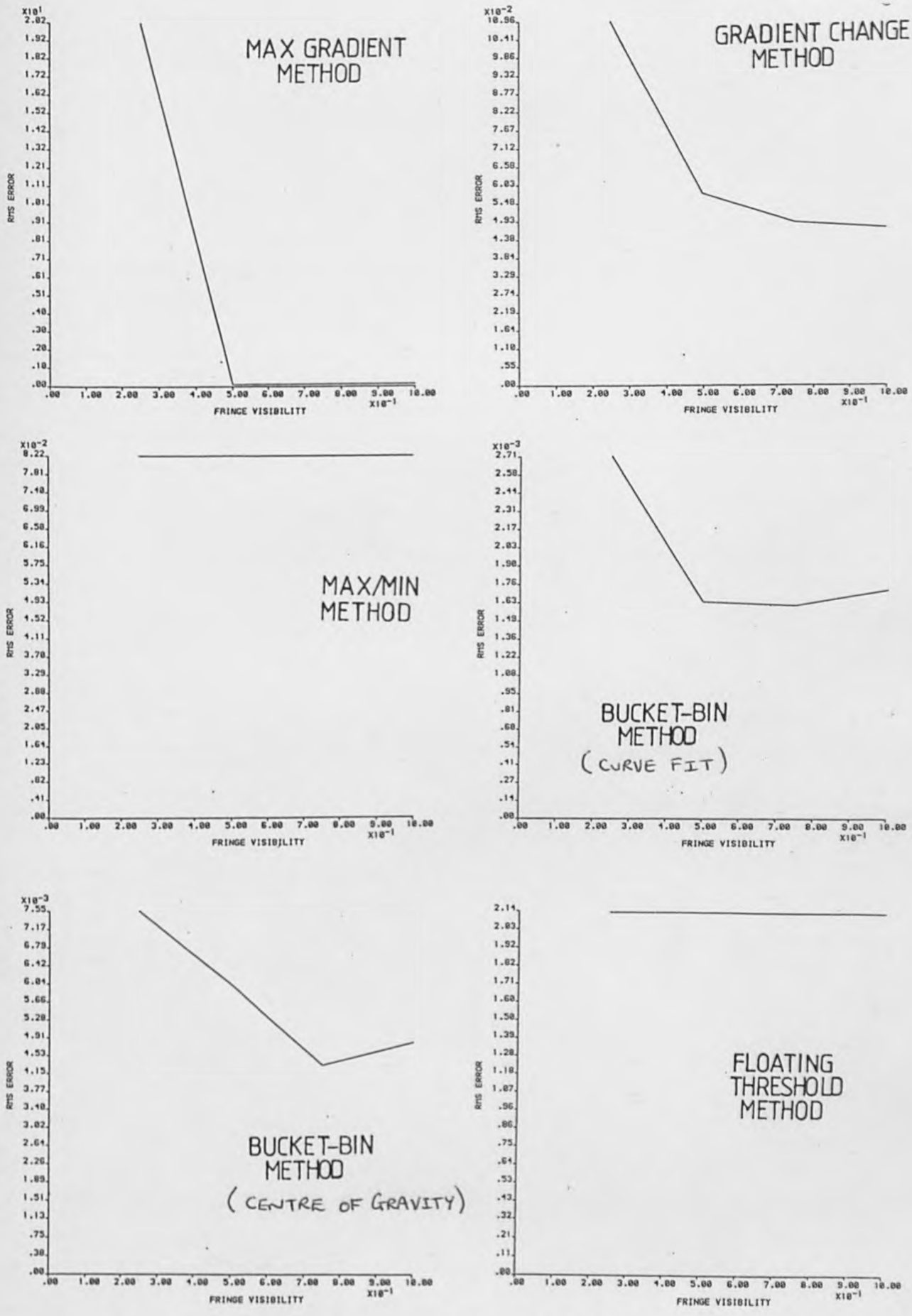

Figure 6.3. Effect of varying fringe visibility on One-dimensional Fringe Detection routines.

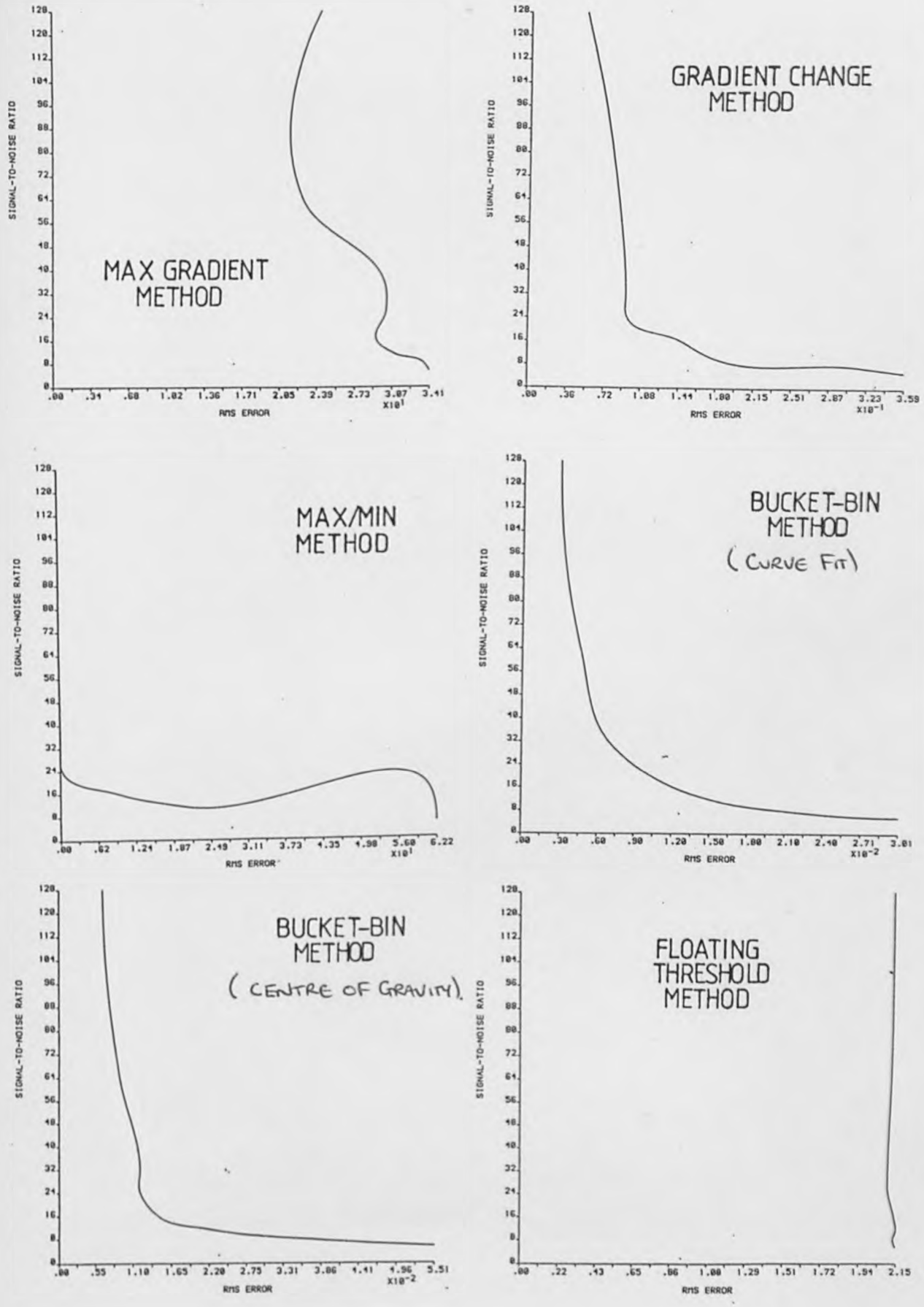

Figure 6.4. Effect of varying signal-to-noise ratio on One-dimensional Fringe Detection routines.

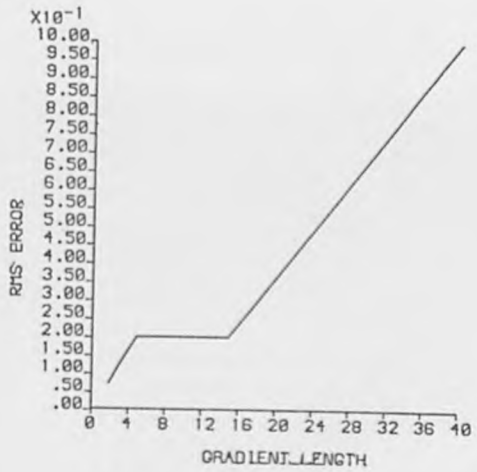

GRADIENT LENGTH=10

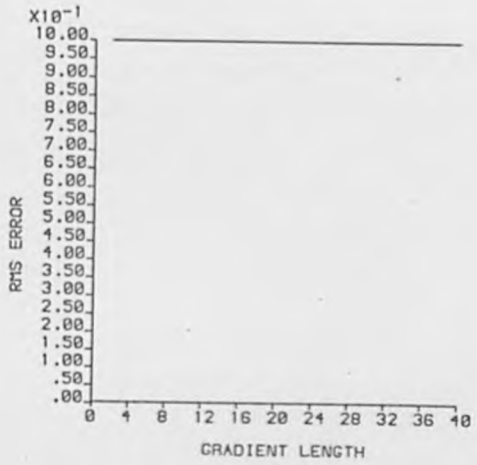

GRADIENT LENGTH=20

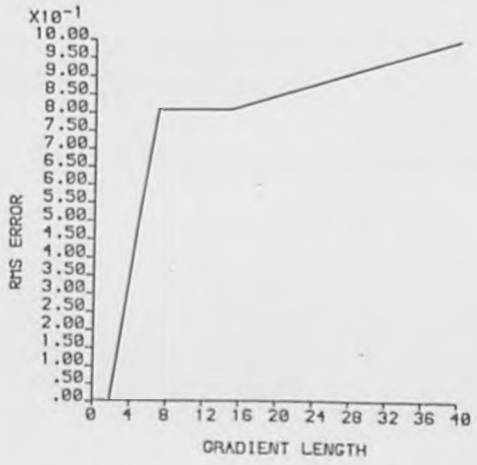

GRADIENT LENGTH=40

Figure 6.5. Effect of varying gradient length on the gradient change Fringe Detection routine.

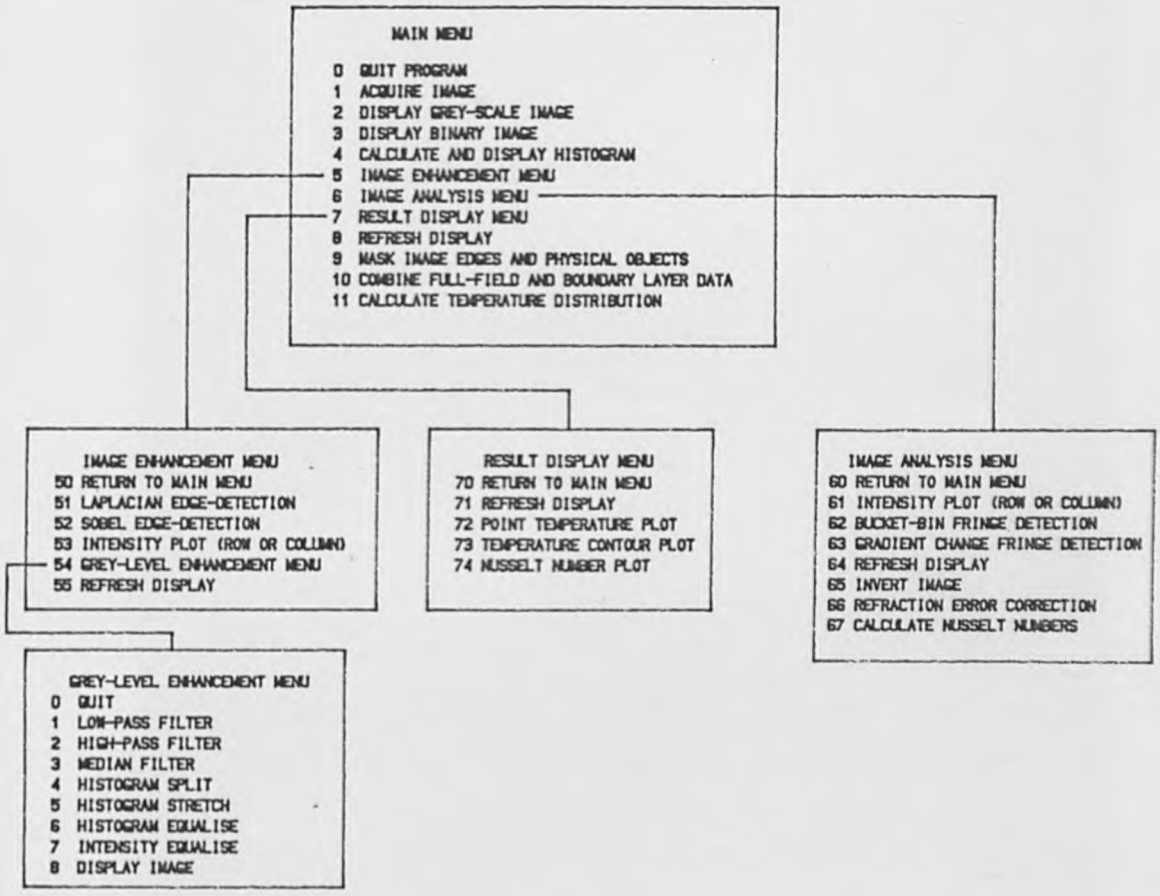

Figure 6.6. Menu system for the Fringe Analysis system.

Figure 6.7. Typical image/workspace distribution, showing an intensity plot.

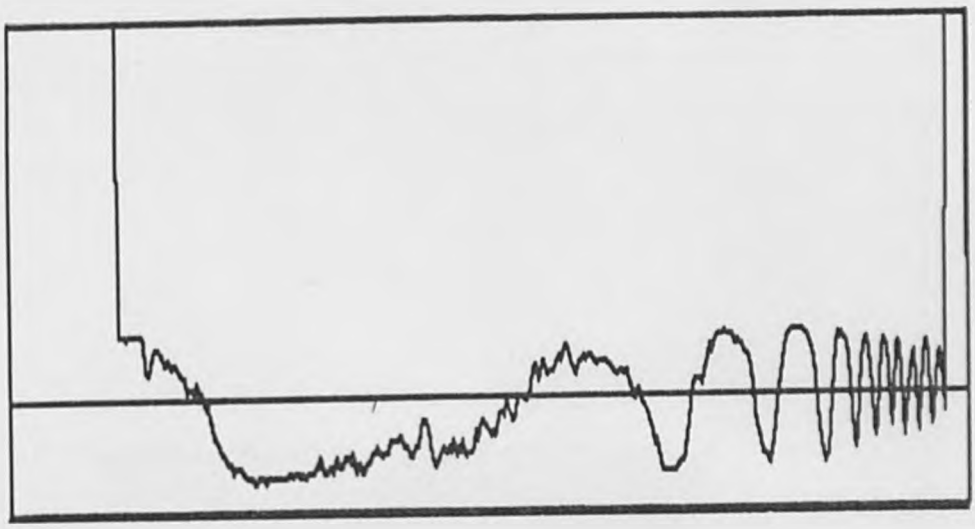

Figure 6.8. Validation of the average grey-level value determined along a scanline.

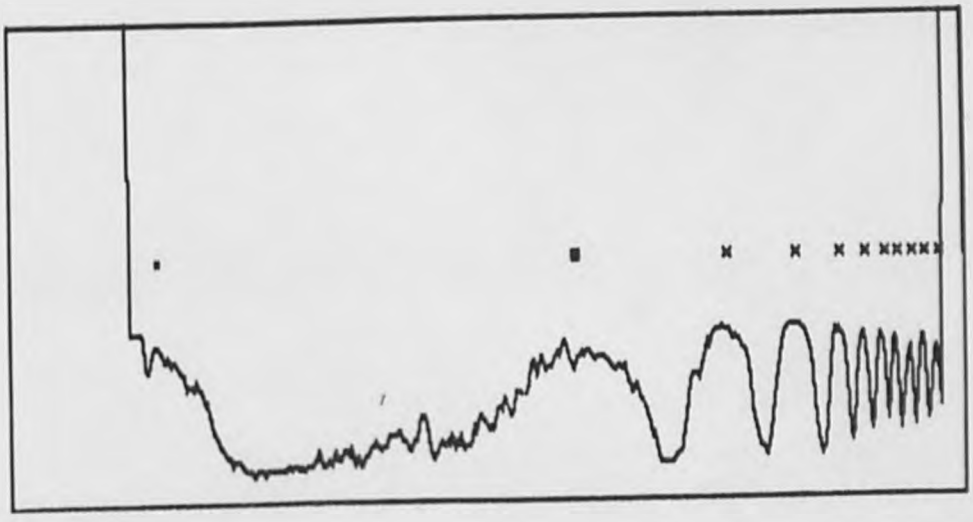

Figure 6.9. Validation of the Fringe location routines.

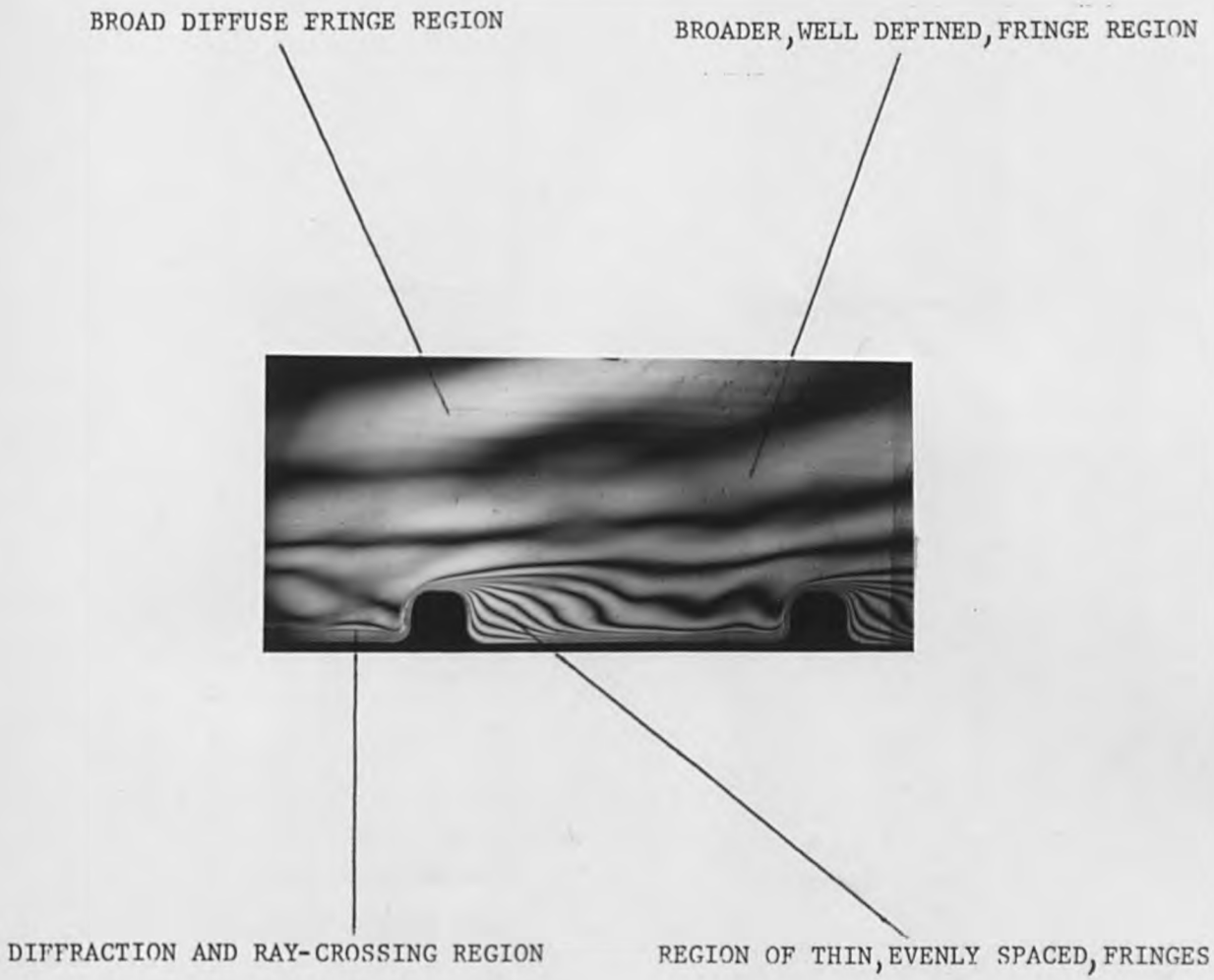

Figure 6.11. Distinct regions identifiable in Heat Transfer Interferograms.

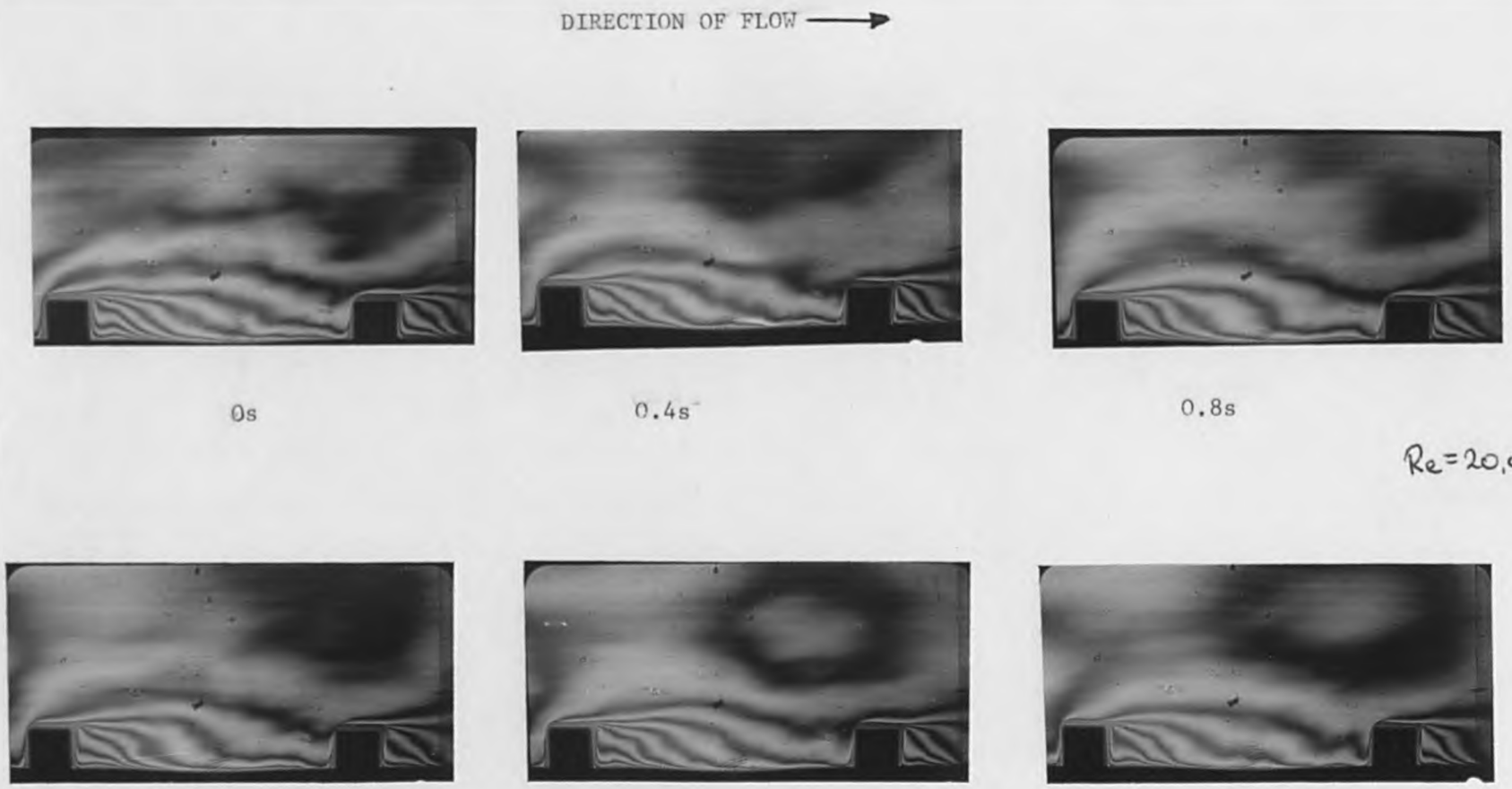

Figure 6.12. An example Real-time Heat Transfer sequence.

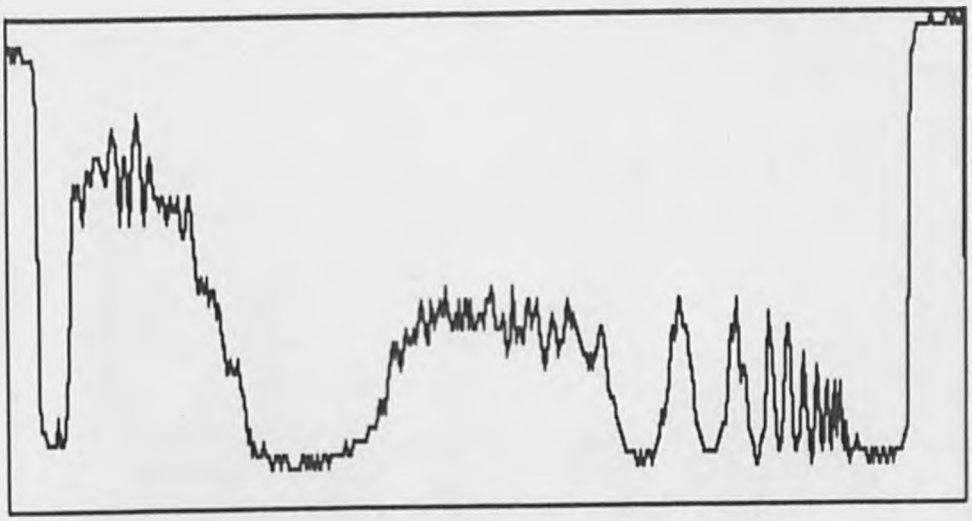

Figure 6.13. A Typical intensity profile, showing the problems caused by the broad fringes.

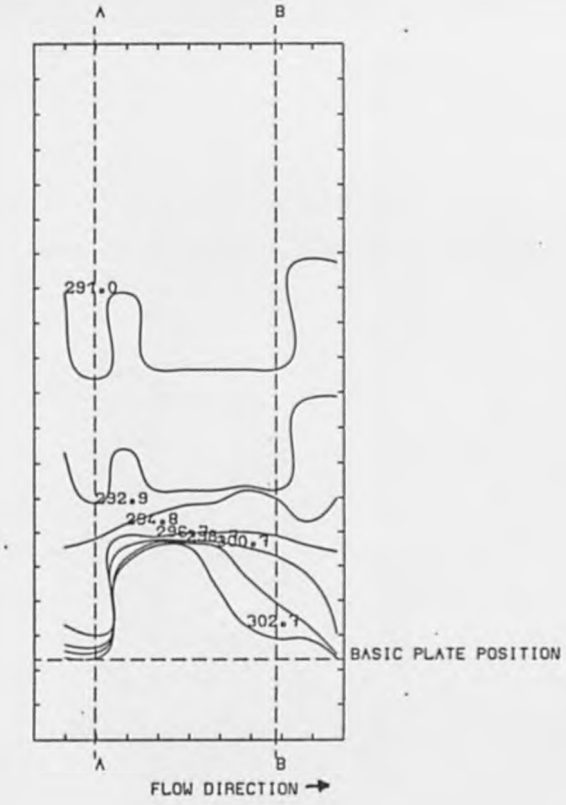

(a) SOUARE RIB,Re-10600

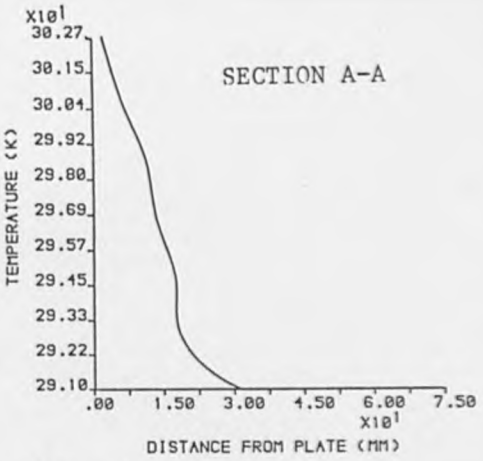

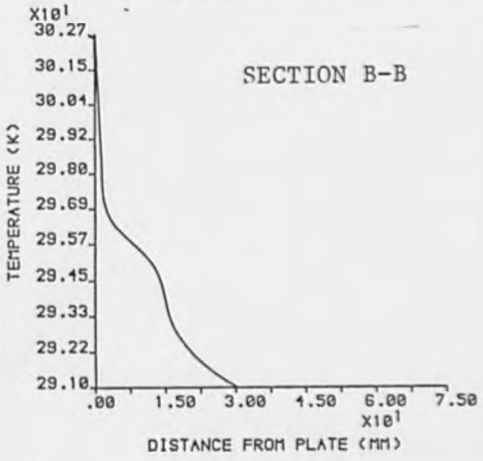

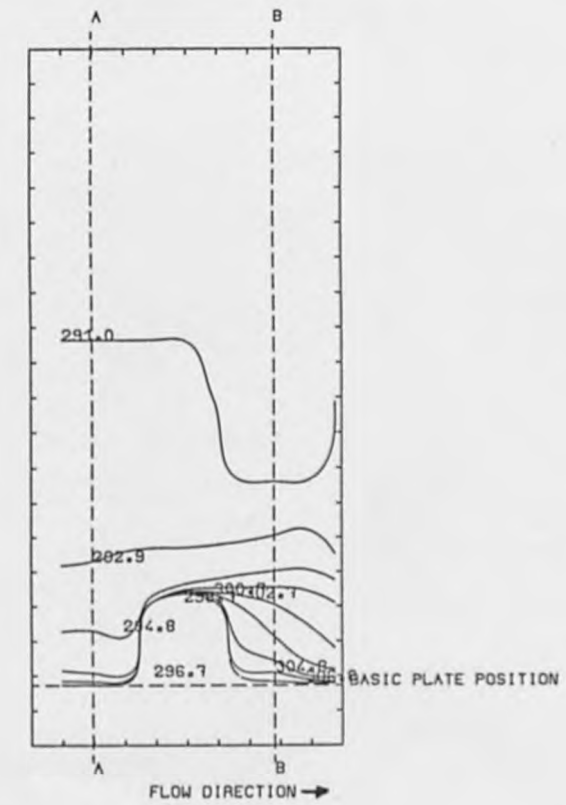

(b) ROUND RIB,Re-53860

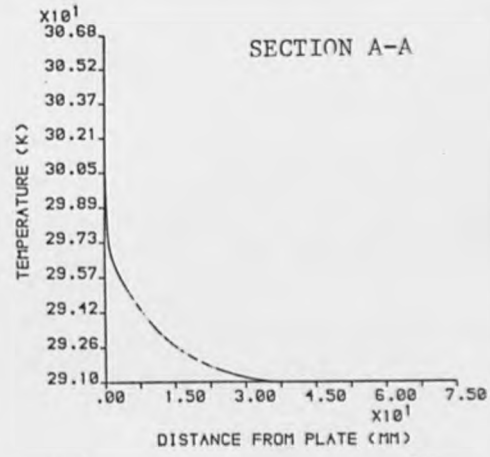

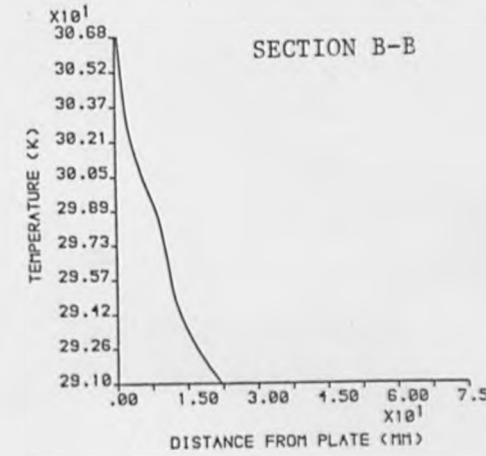

Figure 6.14. Automatically extracted temperature contours and temperature profiles.

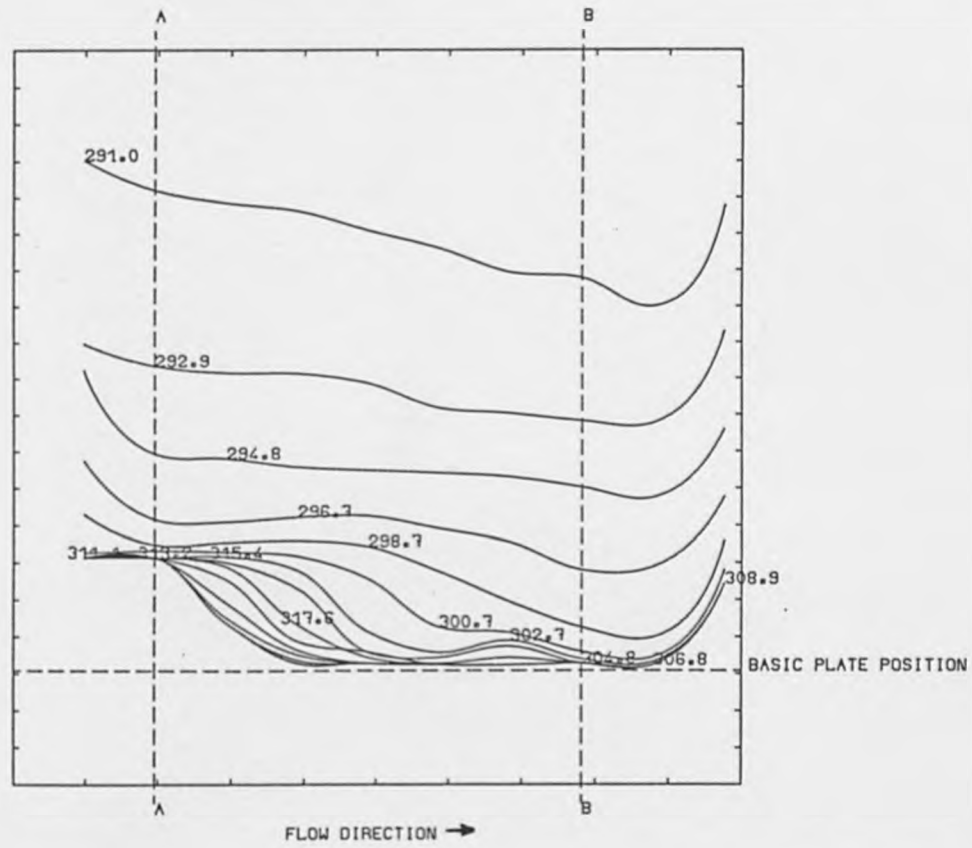

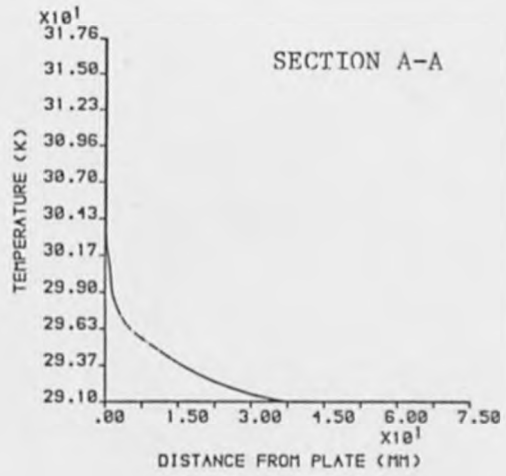

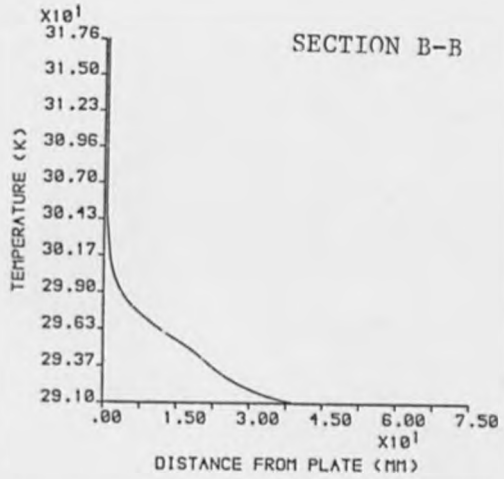

(c) SQUARE DEPOSITED RIB, Re-29000

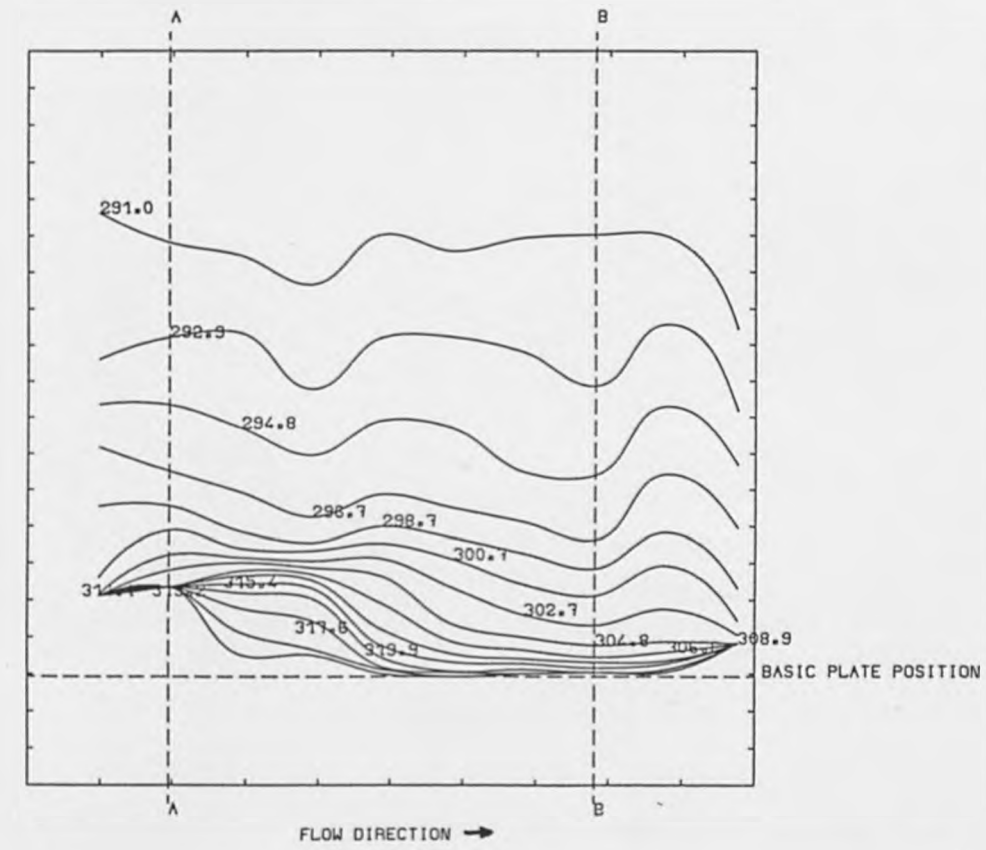

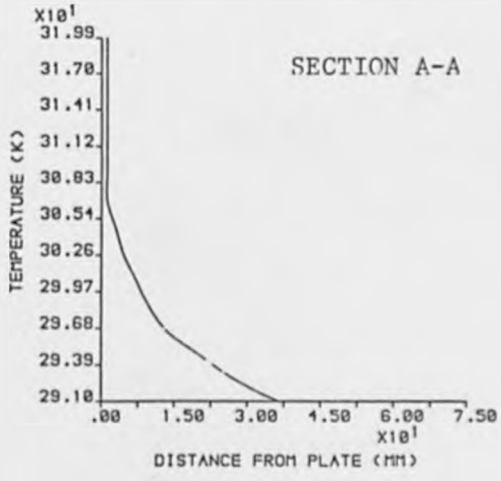

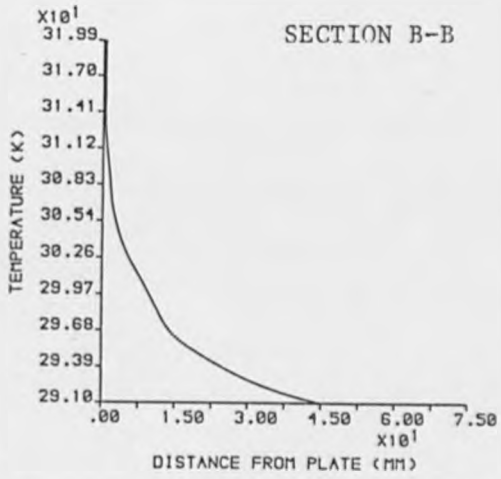

(d) POUND DEPOSITED RIB, Re-3620

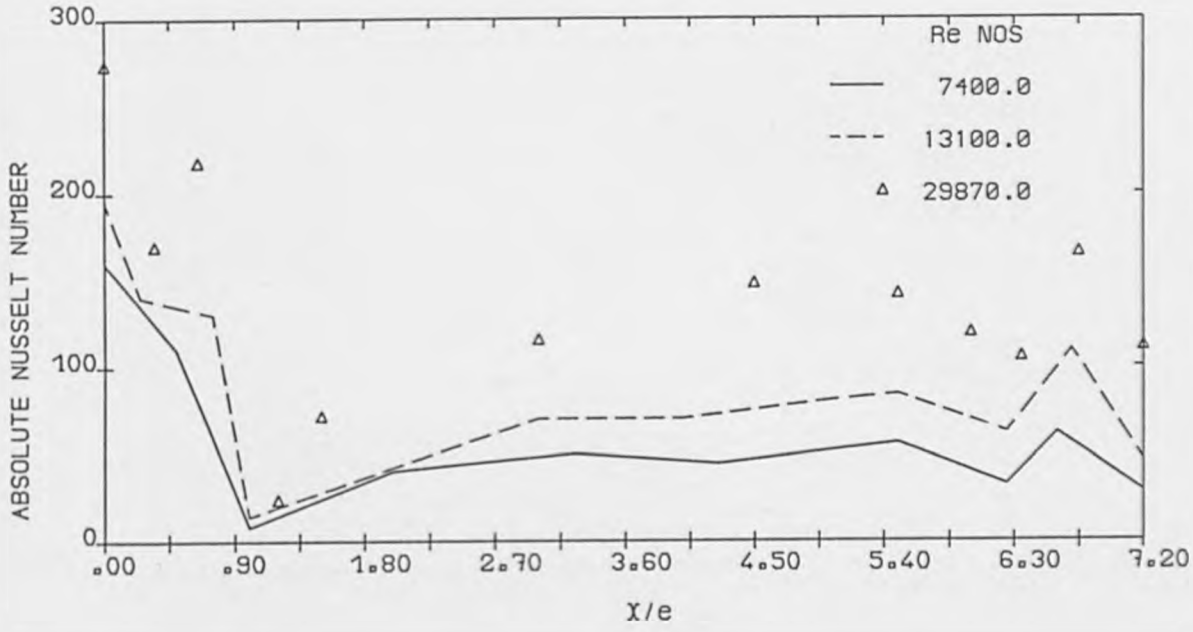

Figure 6.15. Absolute Nusselt number plot, square rib geometry.

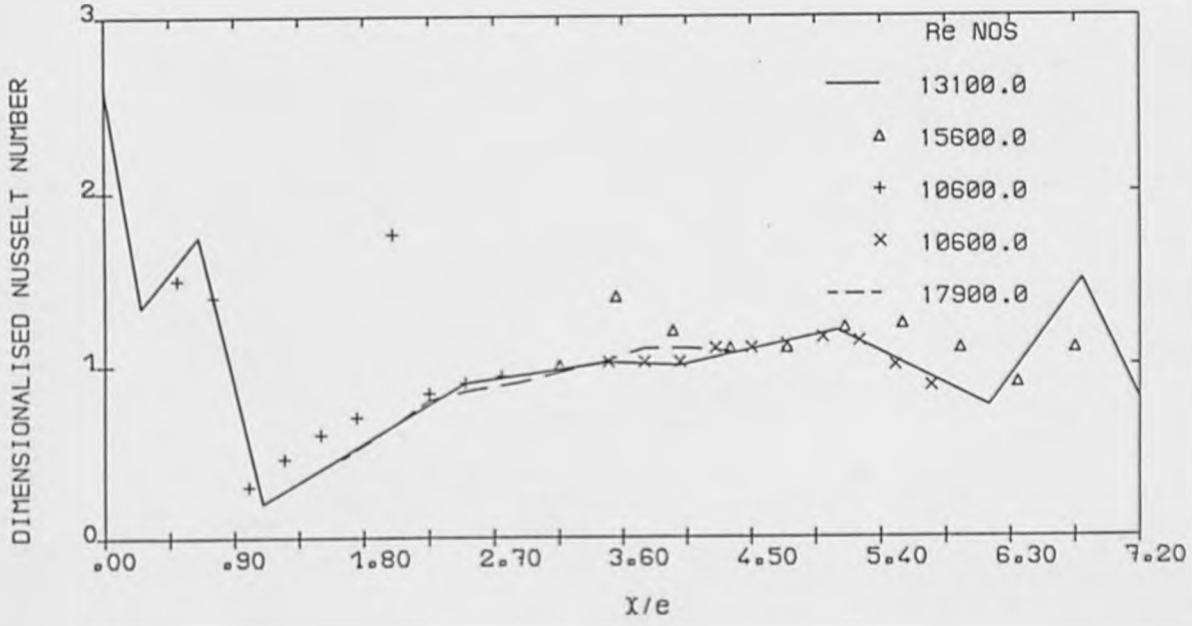

Figure 6.16. Dimensionalised Heat Transfer plot, square rib geometry.

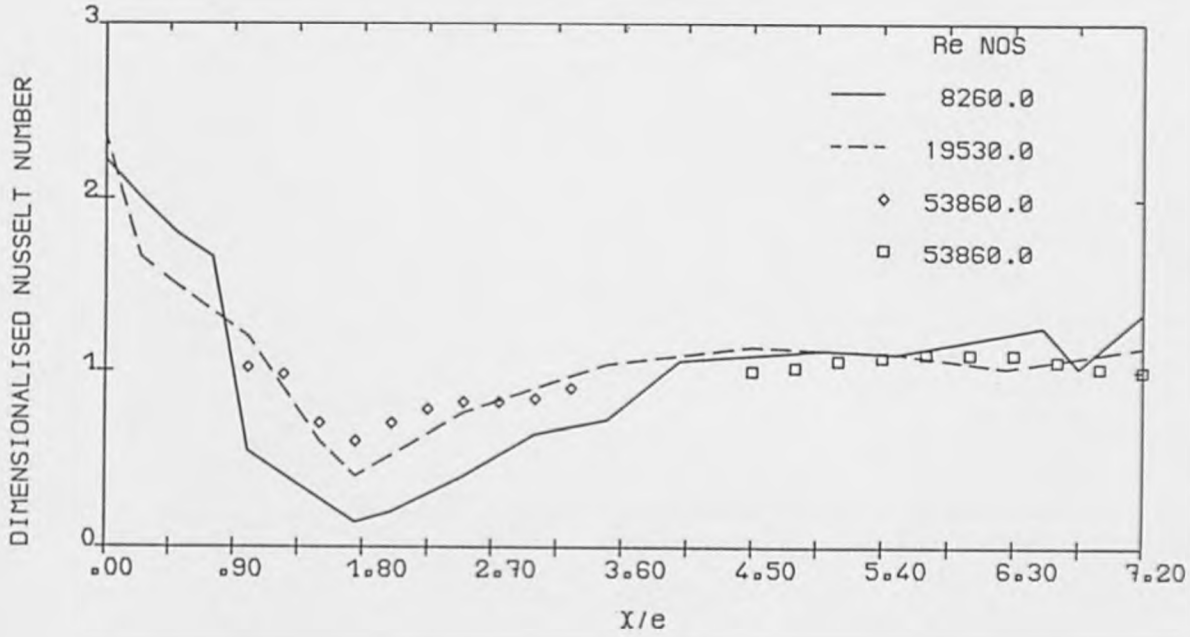

Figure 6.17. Dimensionalised Heat Transfer plot, rounded rib geometry.

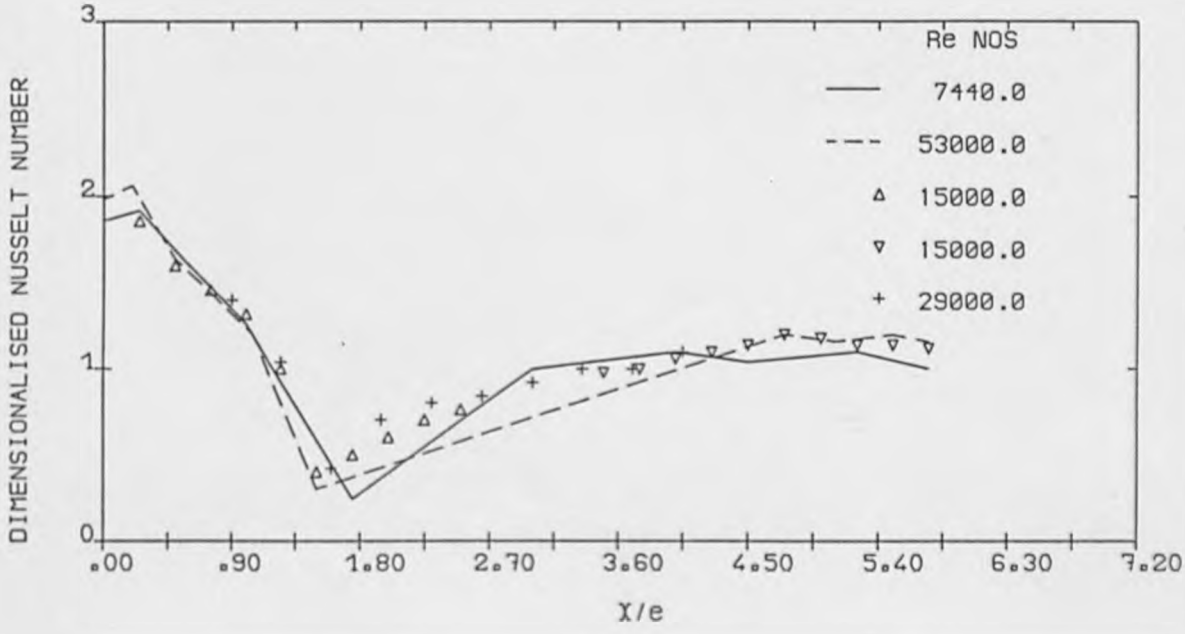

Figure 6.18. Dimensionalised Heat Transfer plot, deposited square rib geometry.

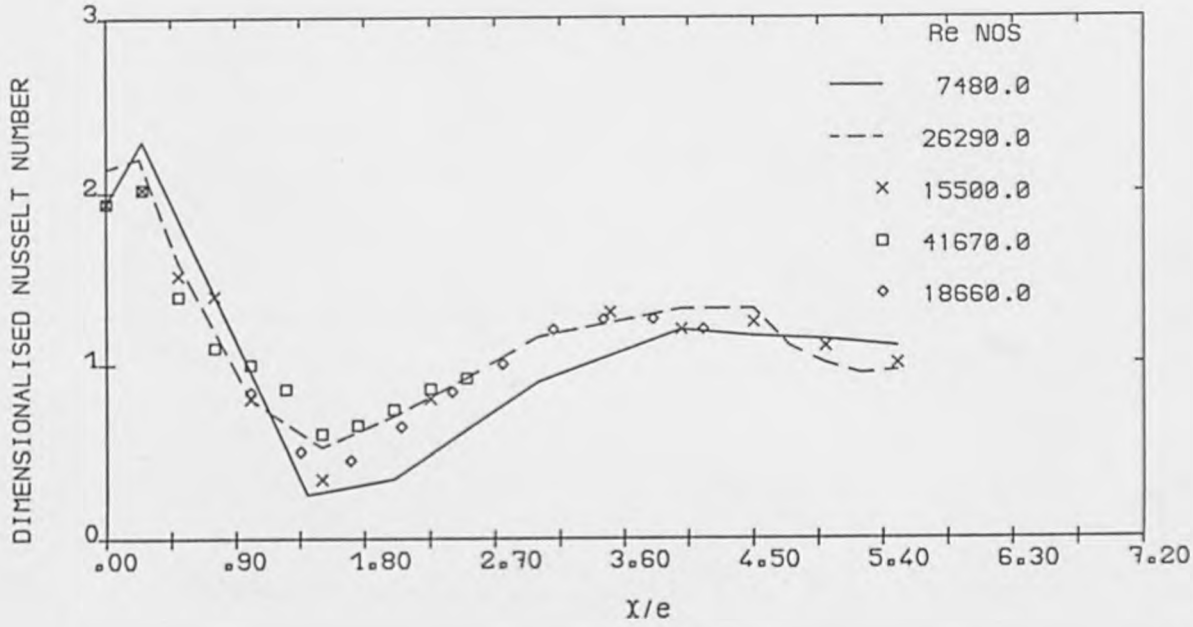

Figure 6.19. Dimensionalised Heat Transfer plot, deposited rounded rib geometry.

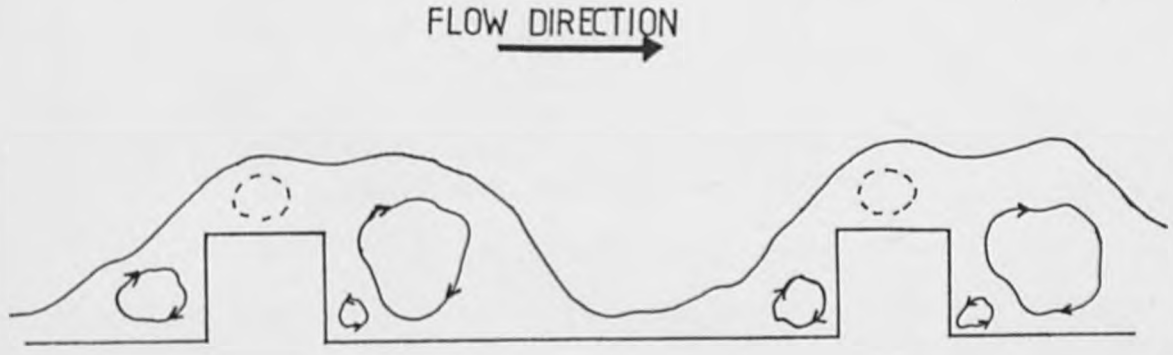

Figure 6.20. Square rib Heat Transfer mechanism.

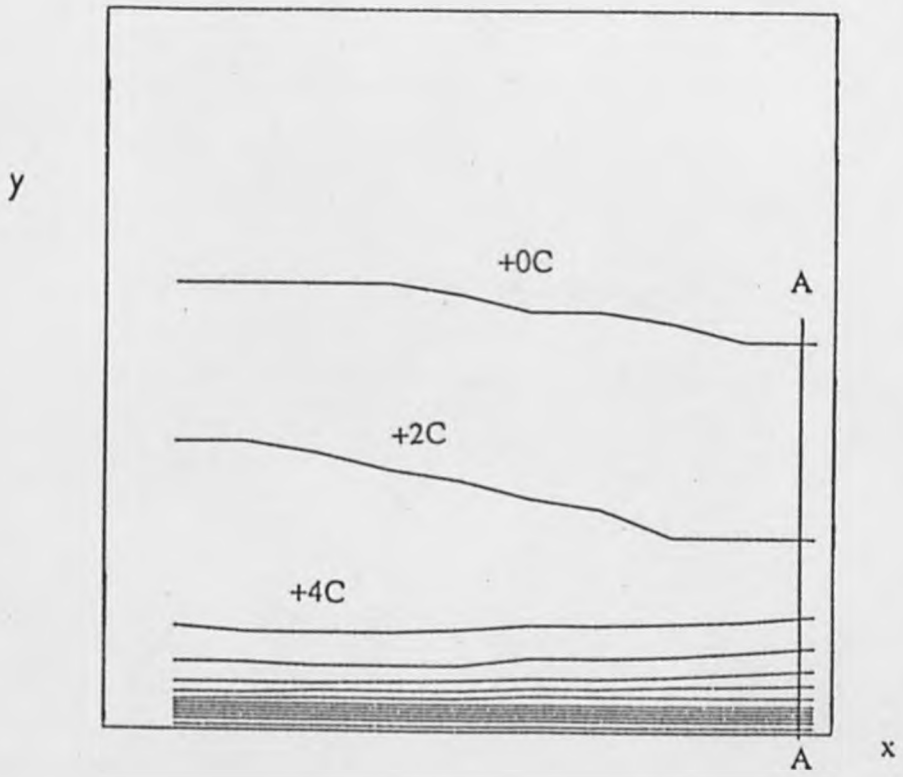

Figure 6.21. Experimental flat plate temperature contours for comparison with the L.E.S. Simulation.

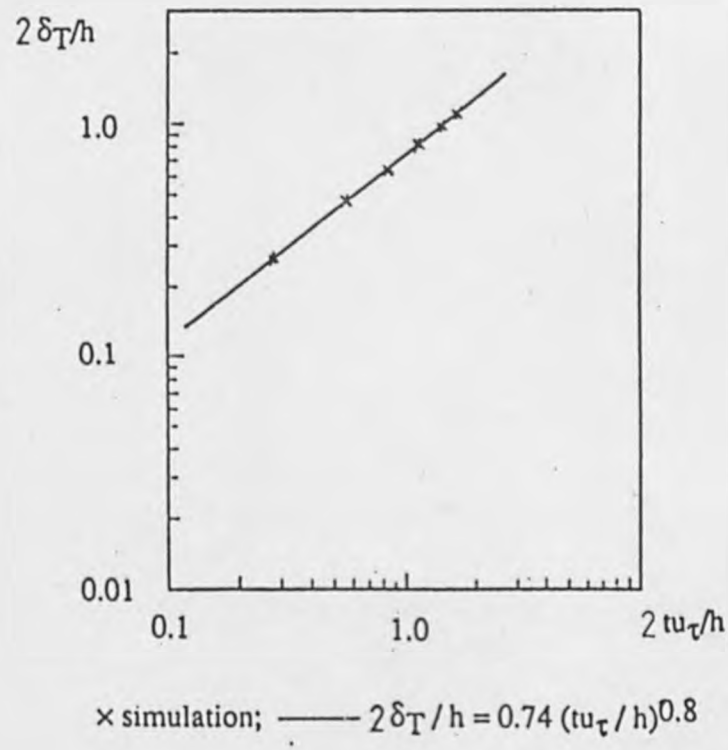

Figure 6.22. Variation of Layer Thickness with Time.

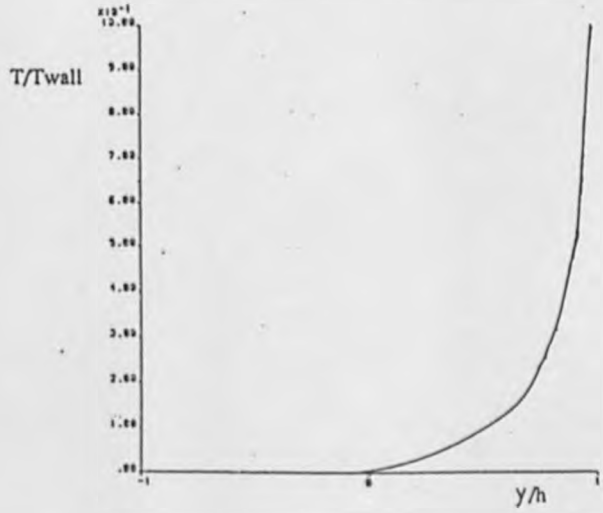

Figure 6.23. Experimentally obtained temperature profile.

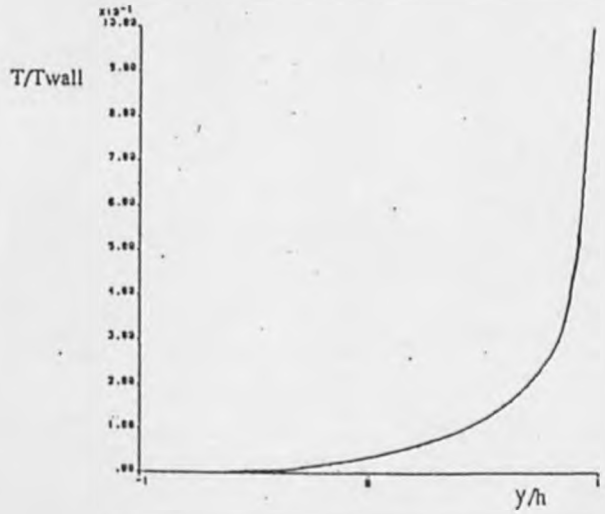

Figure 6.24. Simulation temperature profile.

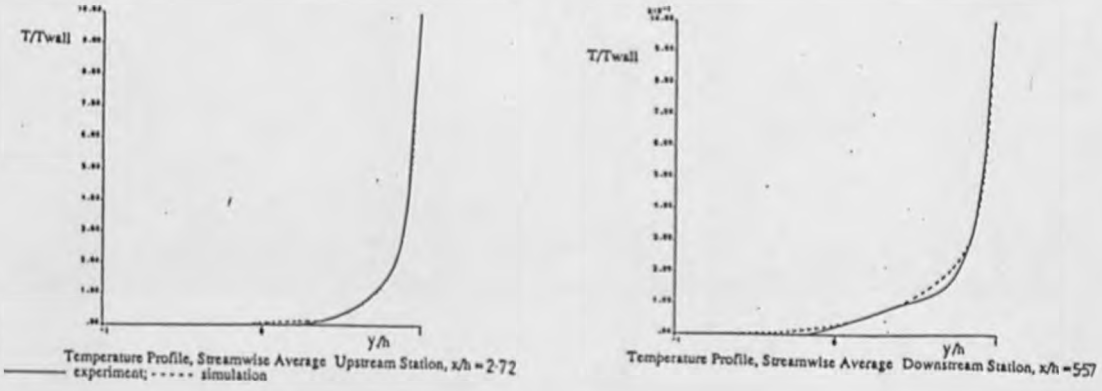

Figure 6.25. Streamwise averaged temperature profiles.

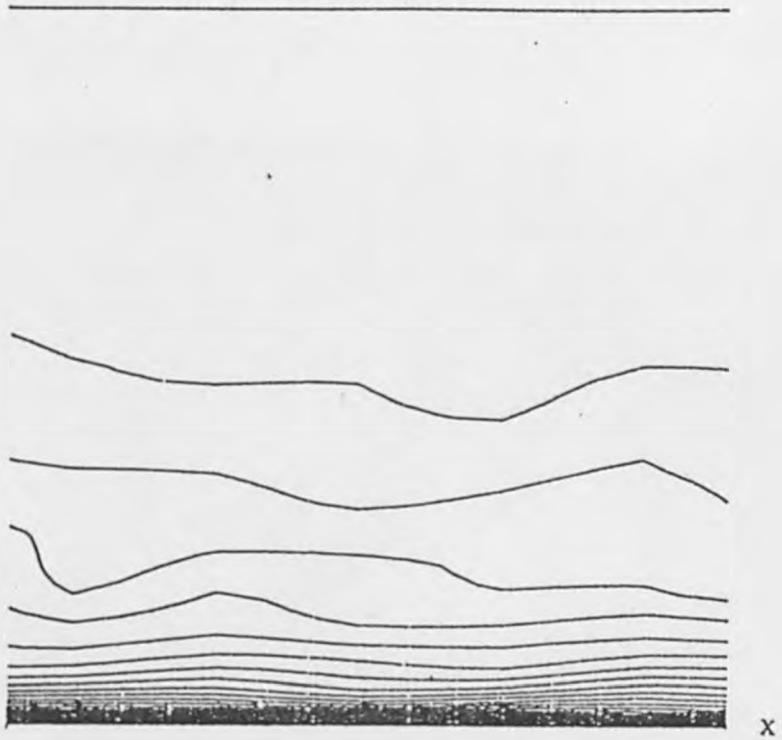

Downstream Station, $tu_\tau / h = 1.05$

Figure 6.26. Spanwise averaged simulation isotherms.

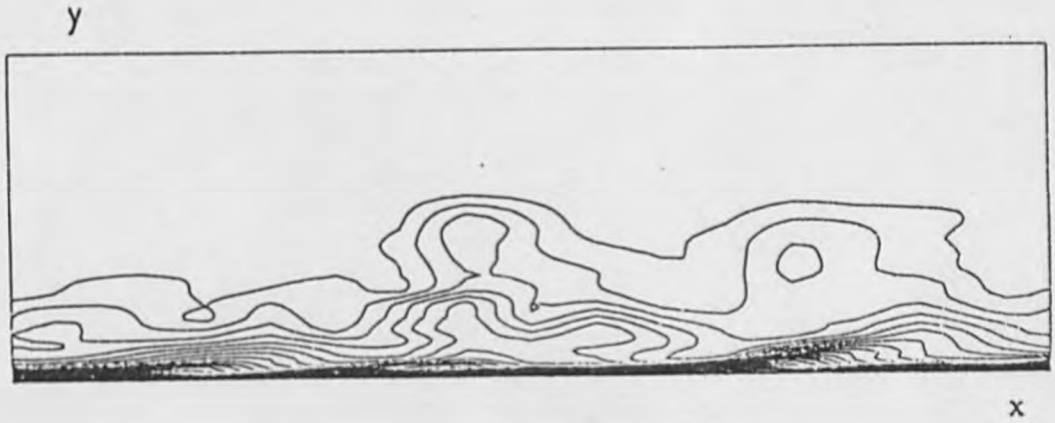

simulation, $tu_\tau / h = 1.05$

Figure 6.27. Simulation isotherms taken at one particular spanwise station.

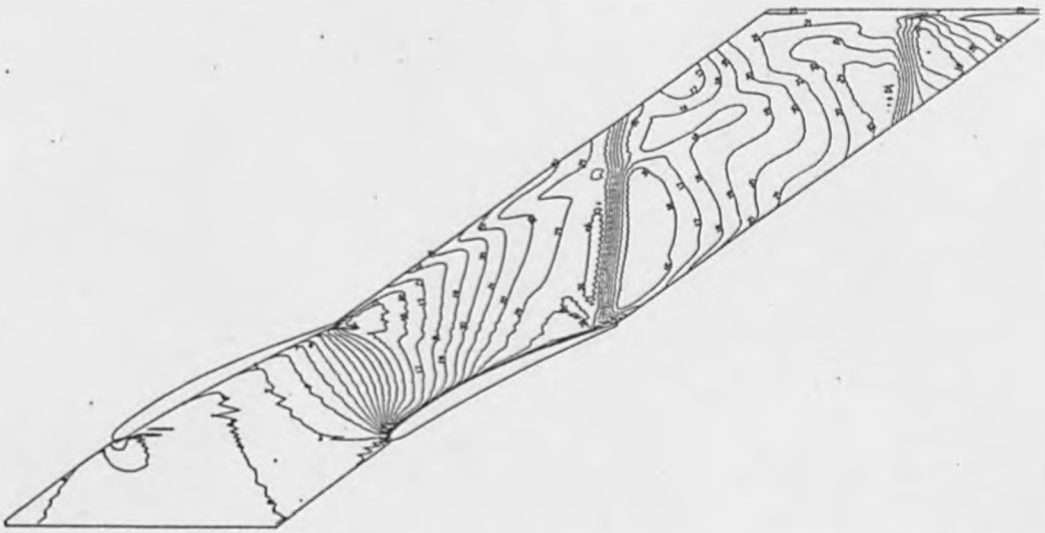

Figure 7.1. TURBINS output.

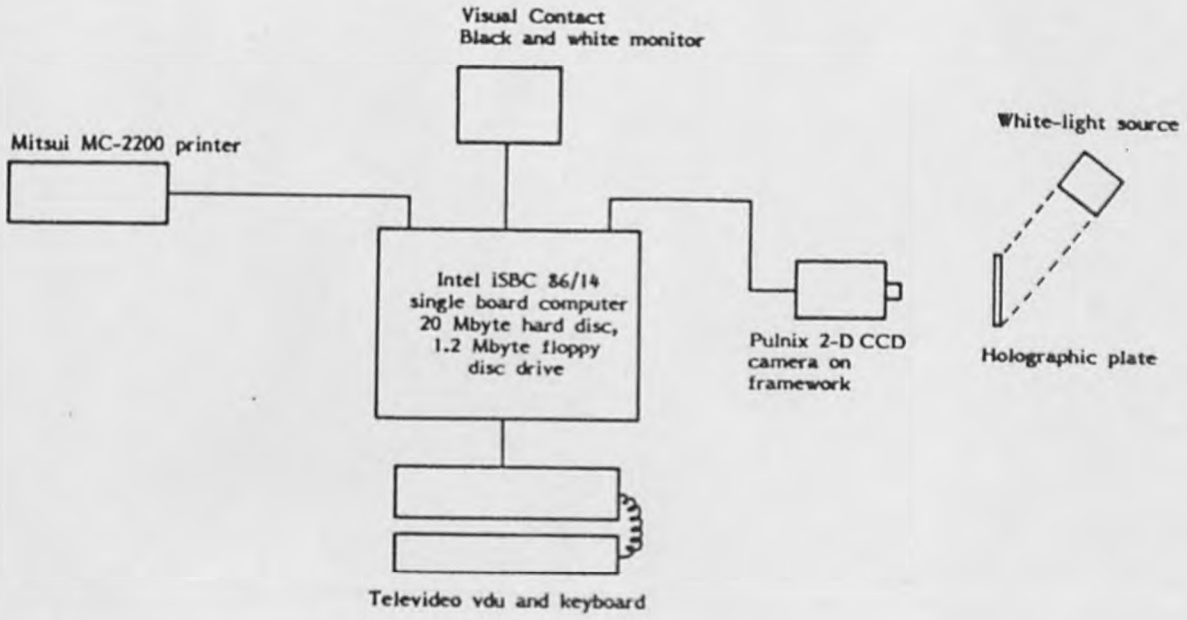

Figure 7.2. Schematic lay-out of Image Processing system.

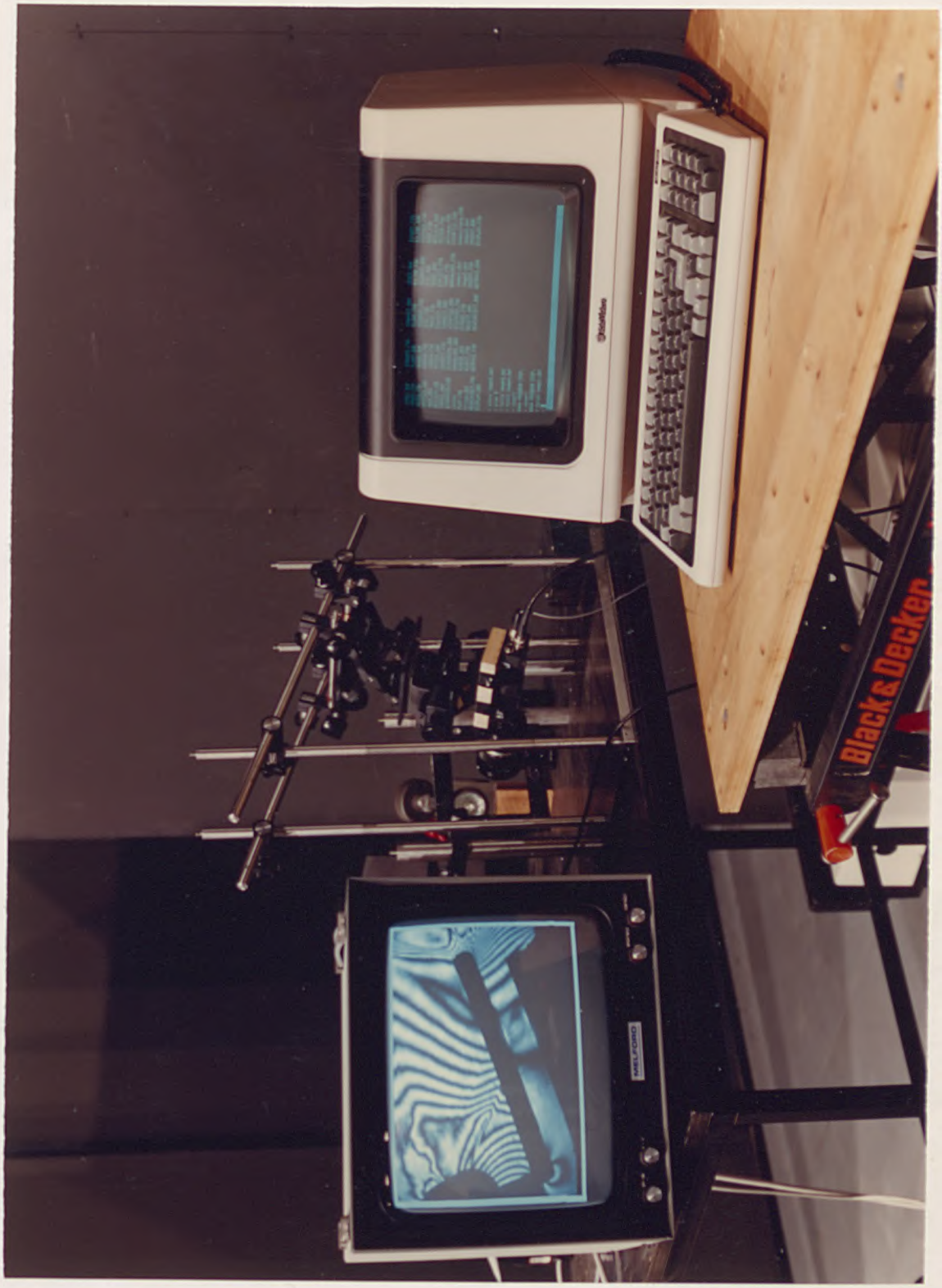

Figure 7.3. Reconstruction rig and computing system.

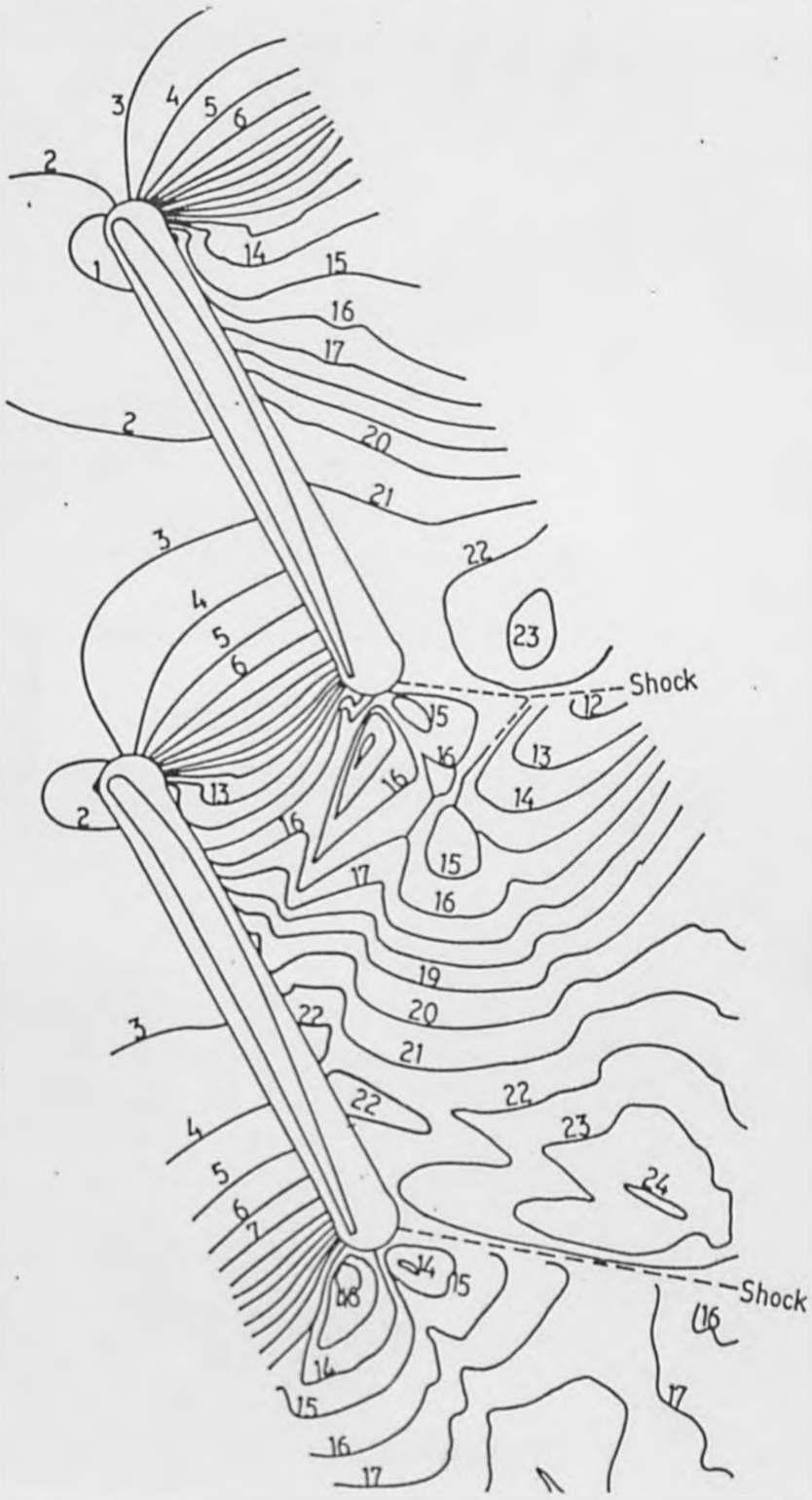

Figure 7.4. Hand analysis of a typical blade passage.

(a) Grey-level threshold of 120

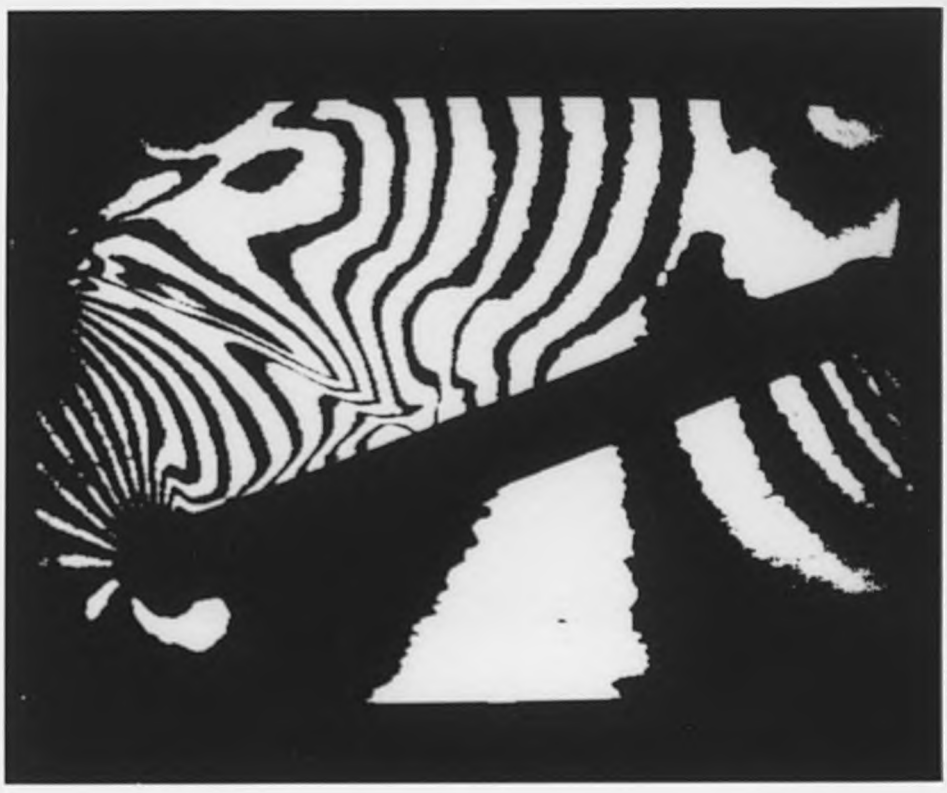

(b) Grey-level threshold of 180

Figure 7.5. Effect of simple binary thresholding.

Figure 7.6. Effect of local binary thresholding.

(a) Constant, Δ, of 0.2

Figure 7.7. Example of a floating binary threshold, with a varying Δ.

(b) Constant, Δ, of 0.25

(c) Constant, Δ, of 0.3

(a) Horizontal floating threshold, $\Delta = 0.25$

(b) Vertical floating threshold, $\Delta = 0.25$

Figure 7.8. Example of a floating binary threshold, varying scan directions.

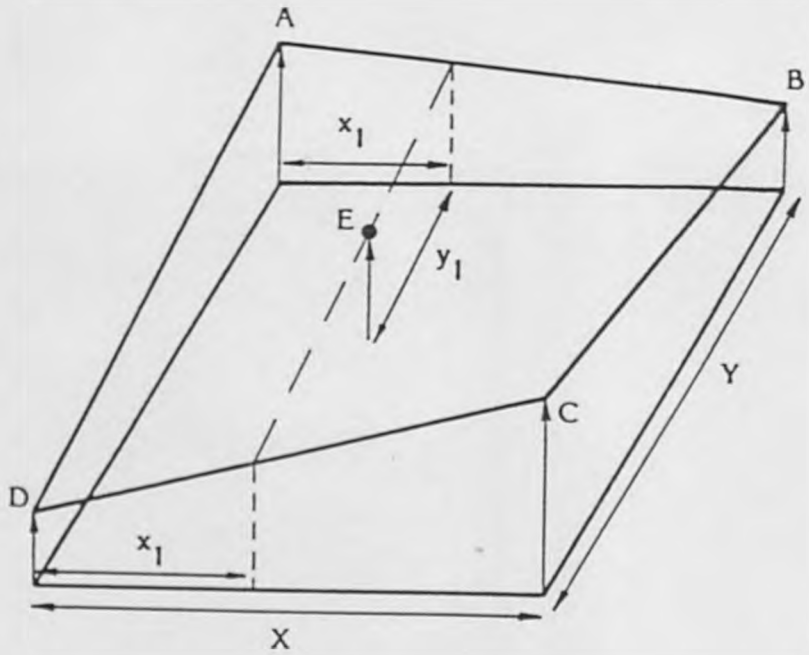

$$E = A\left(1 - \frac{x_1}{X} - \frac{y_1}{Y} + \frac{x_1}{X}\cdot\frac{y_1}{Y}\right) + B\frac{x_1}{X}\left(1 - \frac{y_1}{Y}\right) + C\frac{x_1}{X}\cdot\frac{y_1}{Y} + D\frac{y_1}{Y}\left(1 - \frac{x_1}{X}\right),$$

where A, B, C and D are the relevent node points

Figure 7.9. BILINEAR INTERPOLATION.

(a) Mean local threshold nodal points

(b) Median local threshold nodal points

Figure 7.10. Example of bilinear interpolation binary thresholding.

Figure 7.11. Example of the complete binary segmentation process.

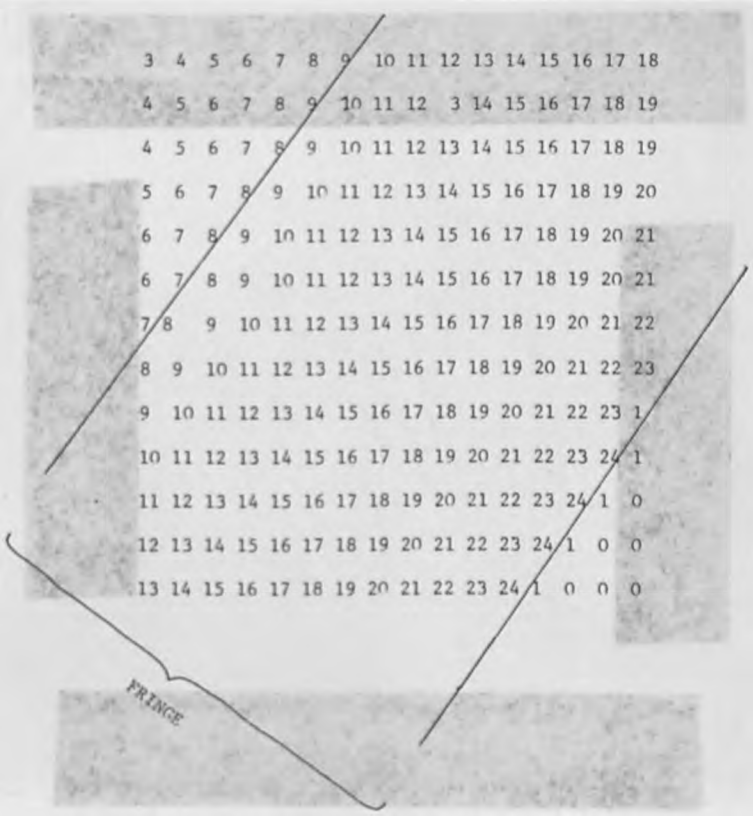

Figure 7.12. Assigned pixel order in a serial thinning process.

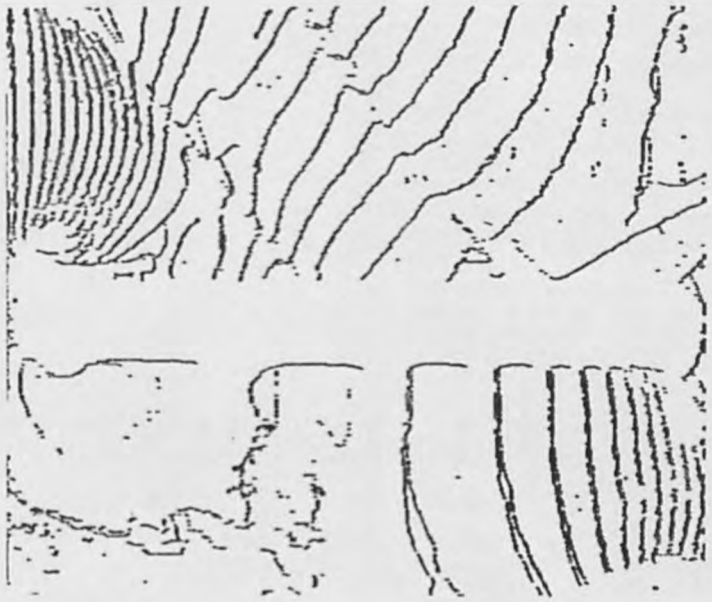

Figure 7.13. Example of a serial thinning operation.

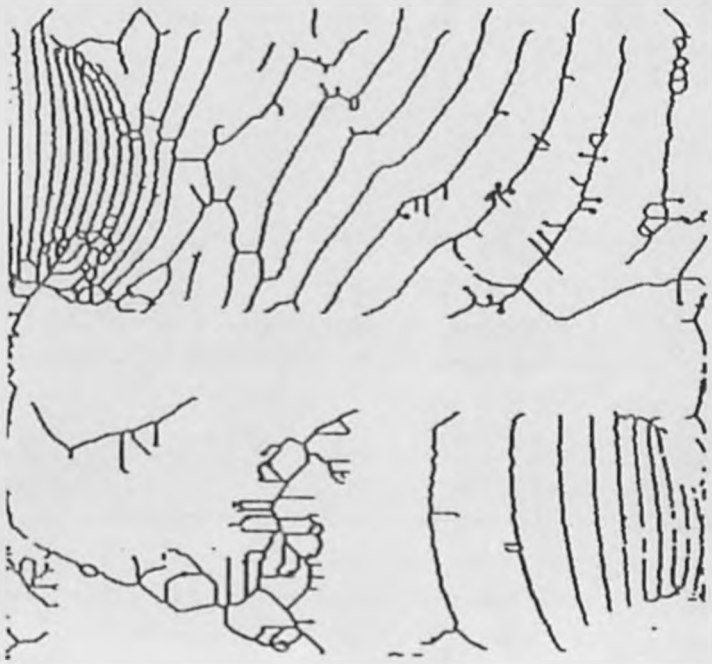

Figure 7.14. Example of a parallel thinning operation.

```
X  Y  X
              Where at least one Y must be
Y 200 Y       equal to 0, and at least
              three X and Y's must equal 200.
X  Y  X
```

Figure 7.15. The edge detection mask utilised.

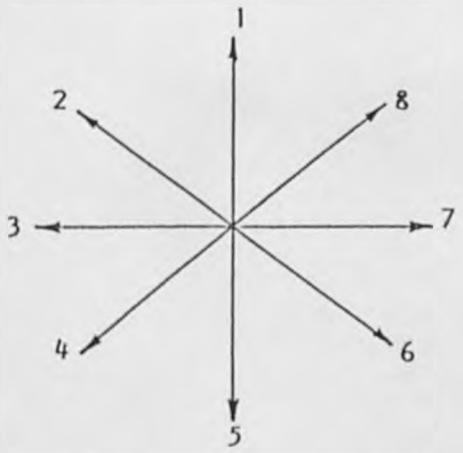

(a). A move to any one of the possible eight neighbours resulted in a bias value being set in accordance with the figure

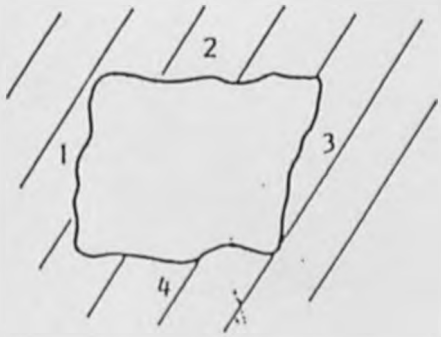

(b). Each edge pixel was checked to see if it was a right or left hand edge, or a top or bottom edge, and labelled accordingly

Figure 7.16. The bias and prefer criteria used in the fringe tracking procedure.

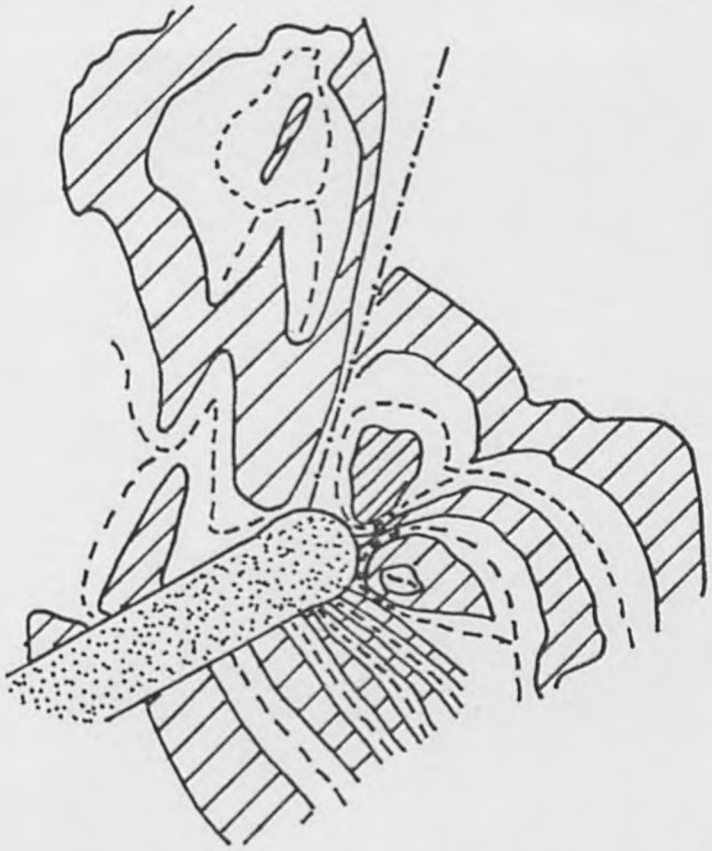

Figure 7.17. Proof for non-branching of fringe edges.

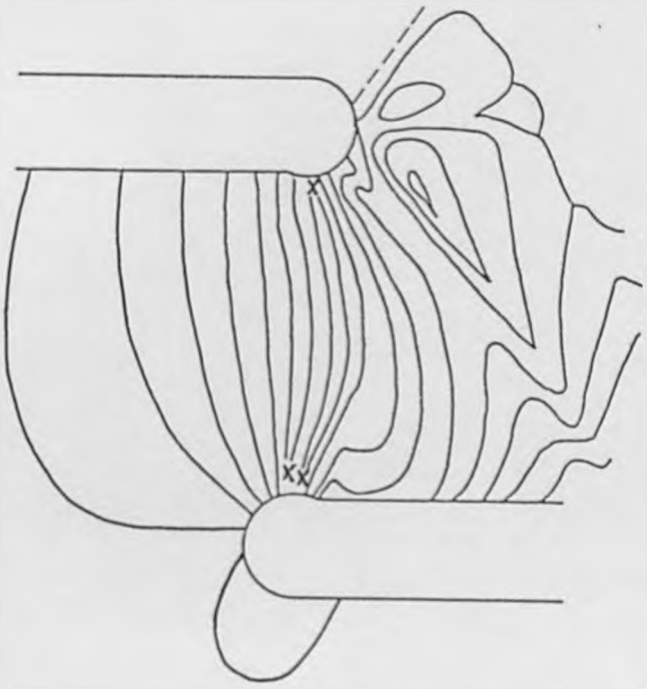

Figure 7.18. Typical cut-points.

Figure 7.19. Example of detected cut-points.

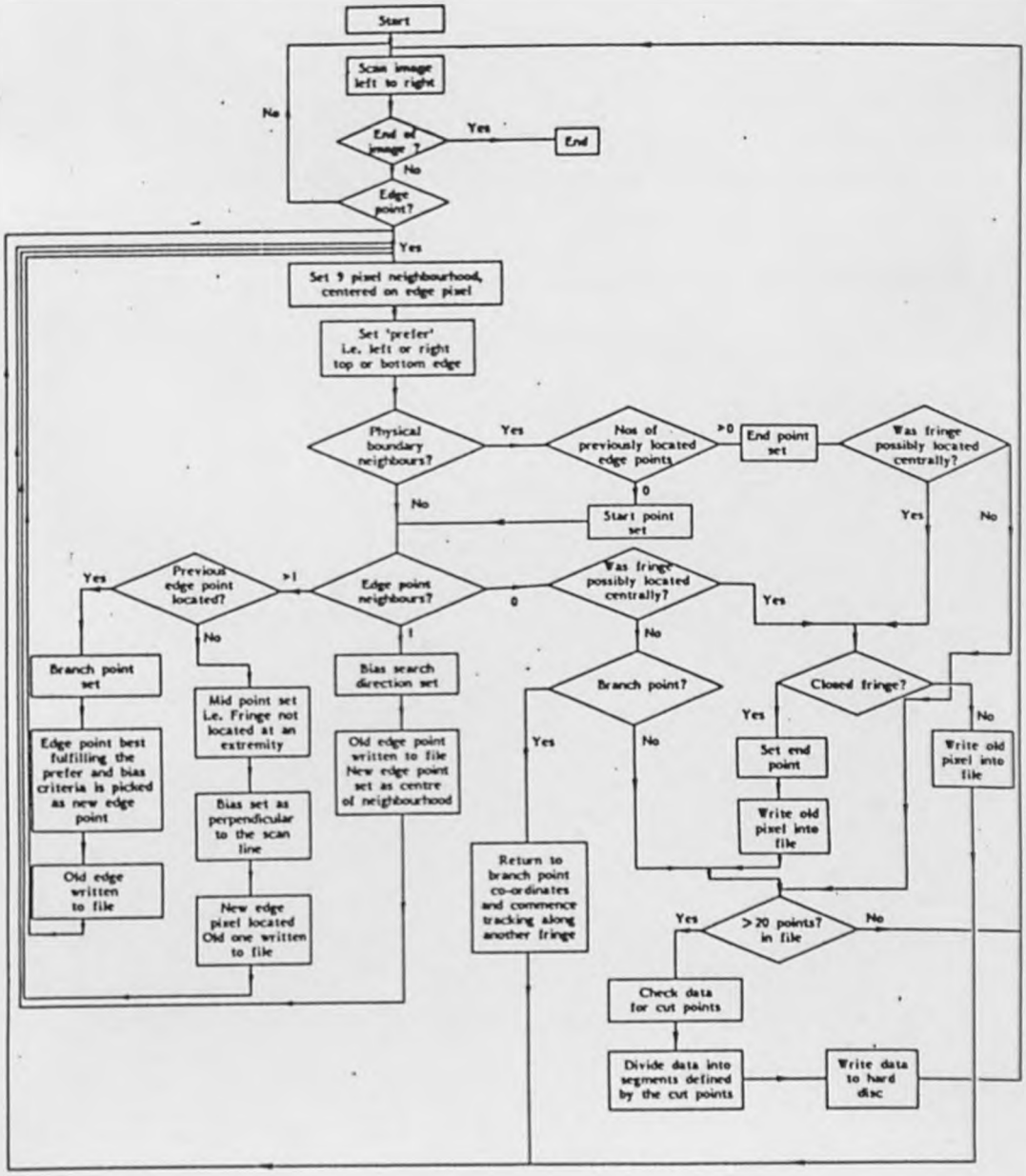

Figure 7.20. Flow dingram of fringe tracking algorithm.

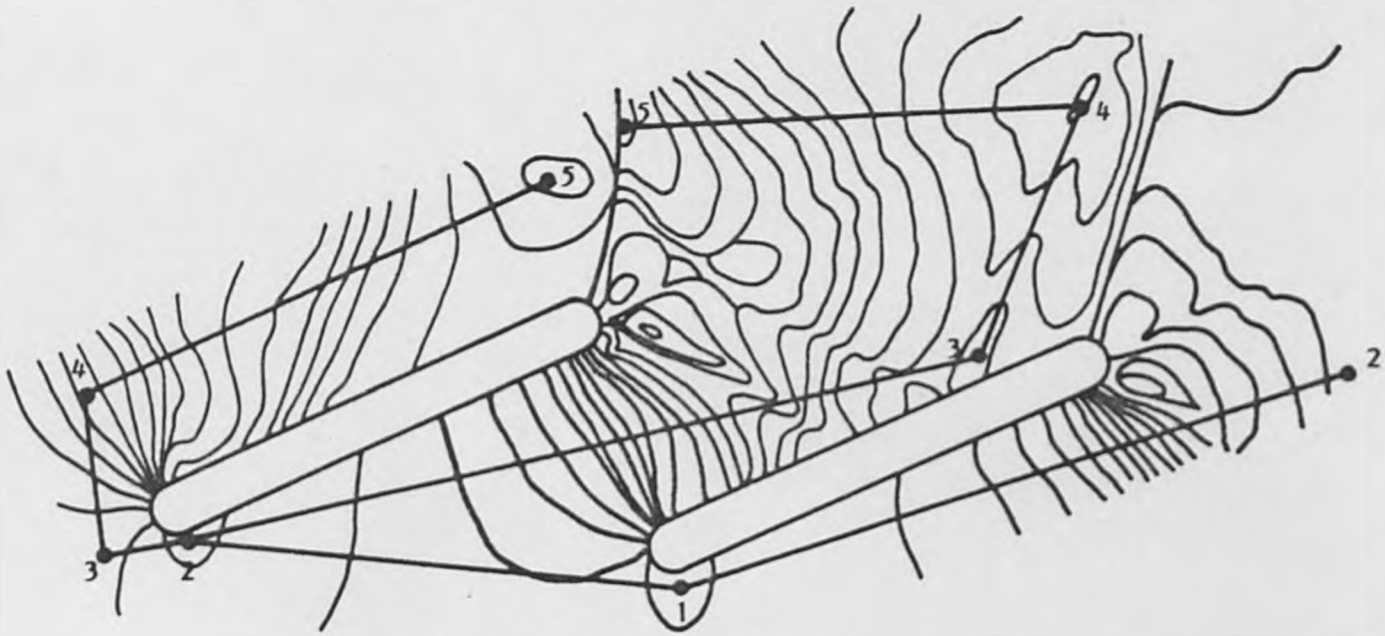

Figure 7.21. TYPICAL CURSOR POSITIONING BY THE OPERATOR WHEN ORDERING A FRINGE FIELD.

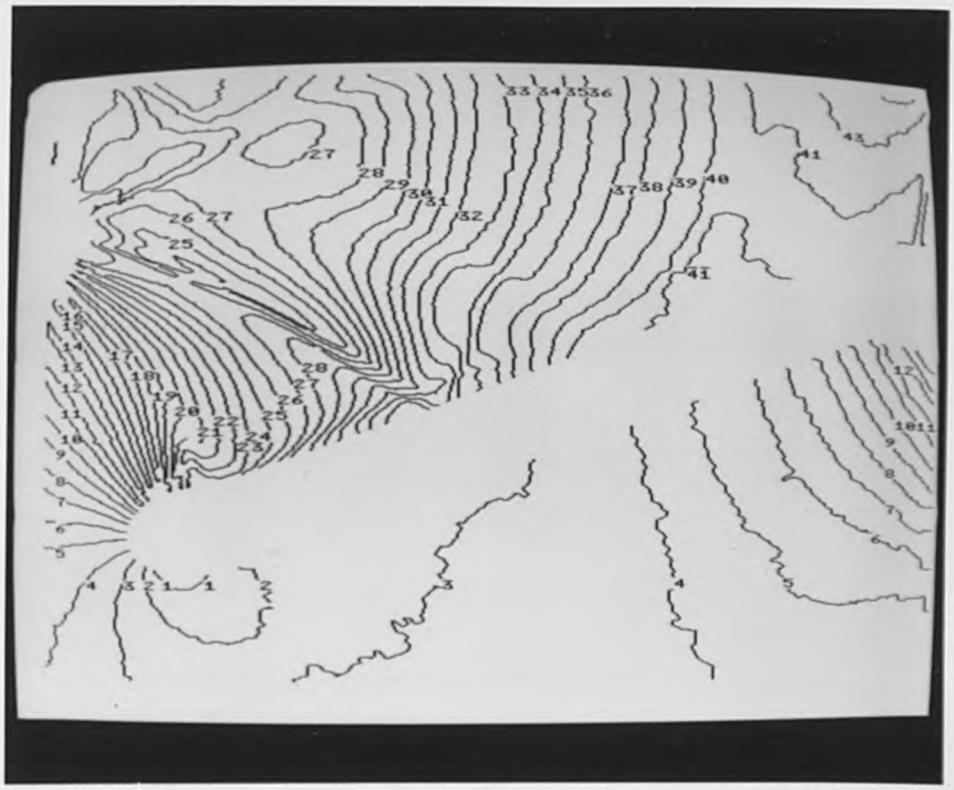

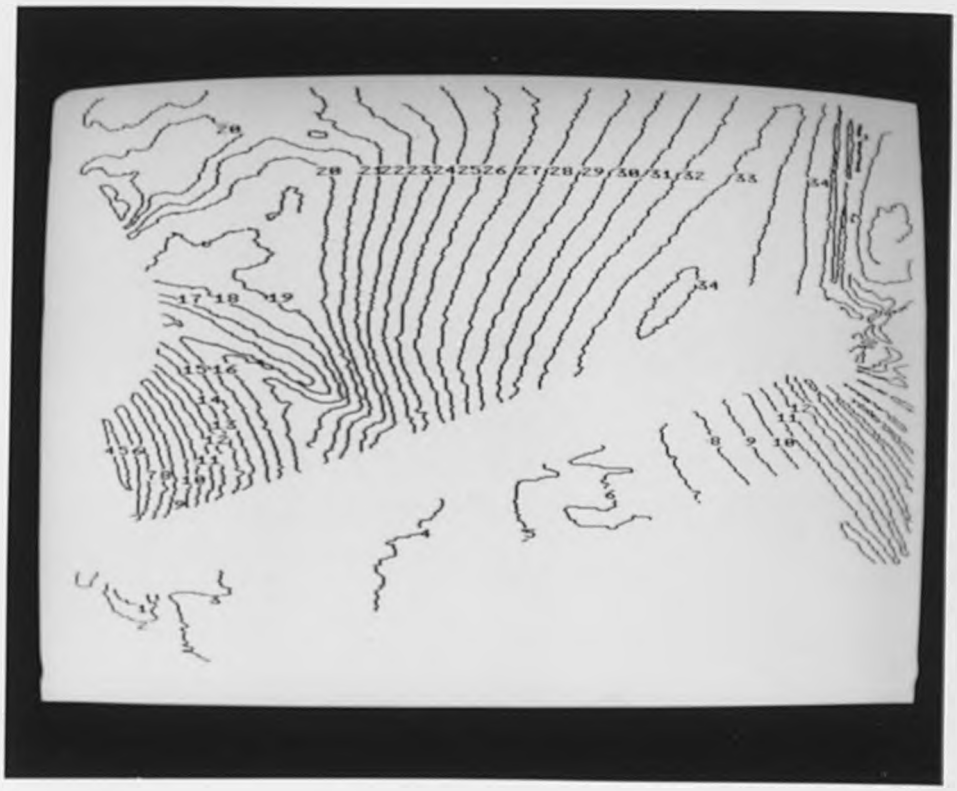

Figure 7.22. Ordered fringe fields.

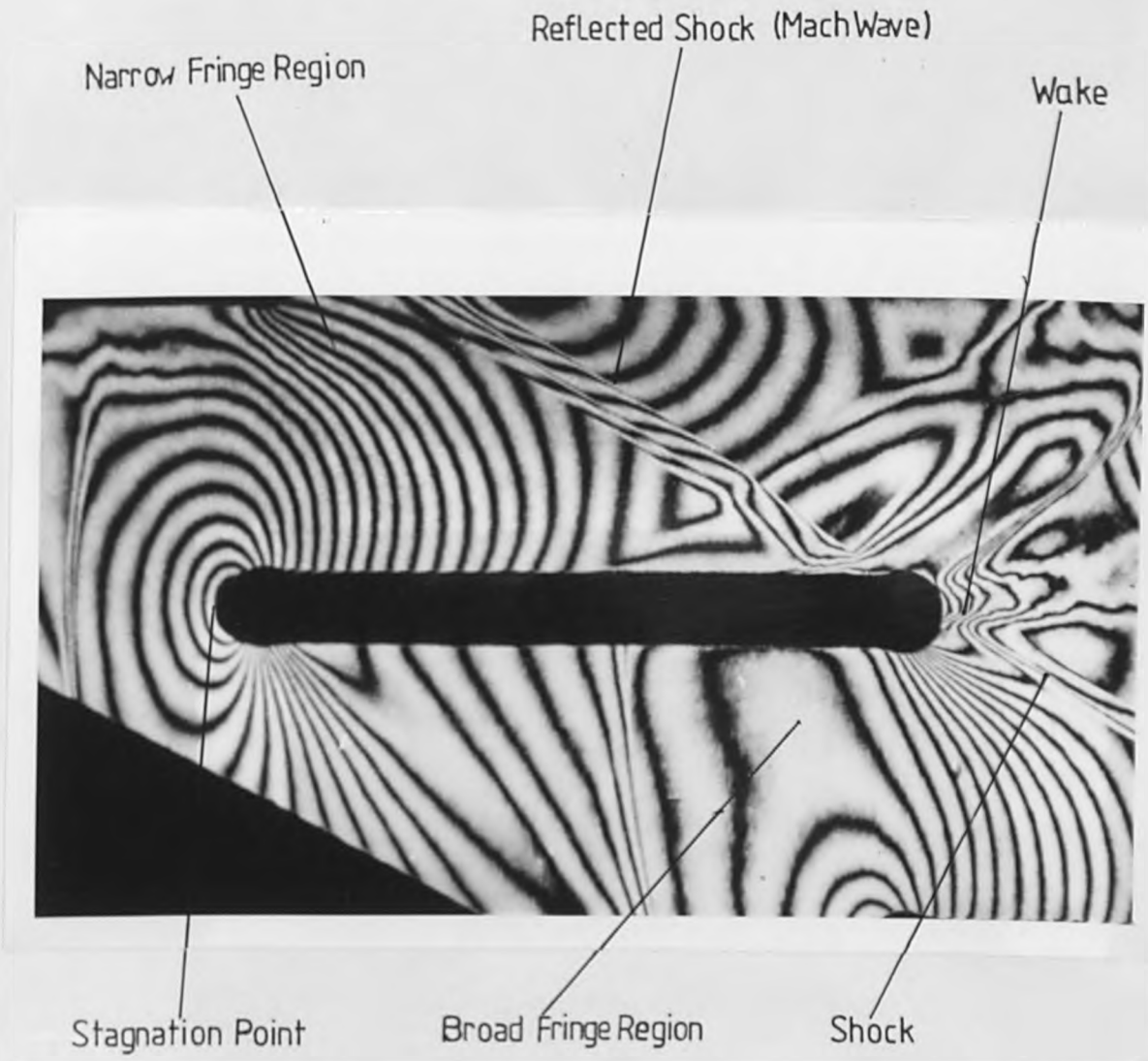

Figure 7.23. A single flow passage showing the major regions of interest.

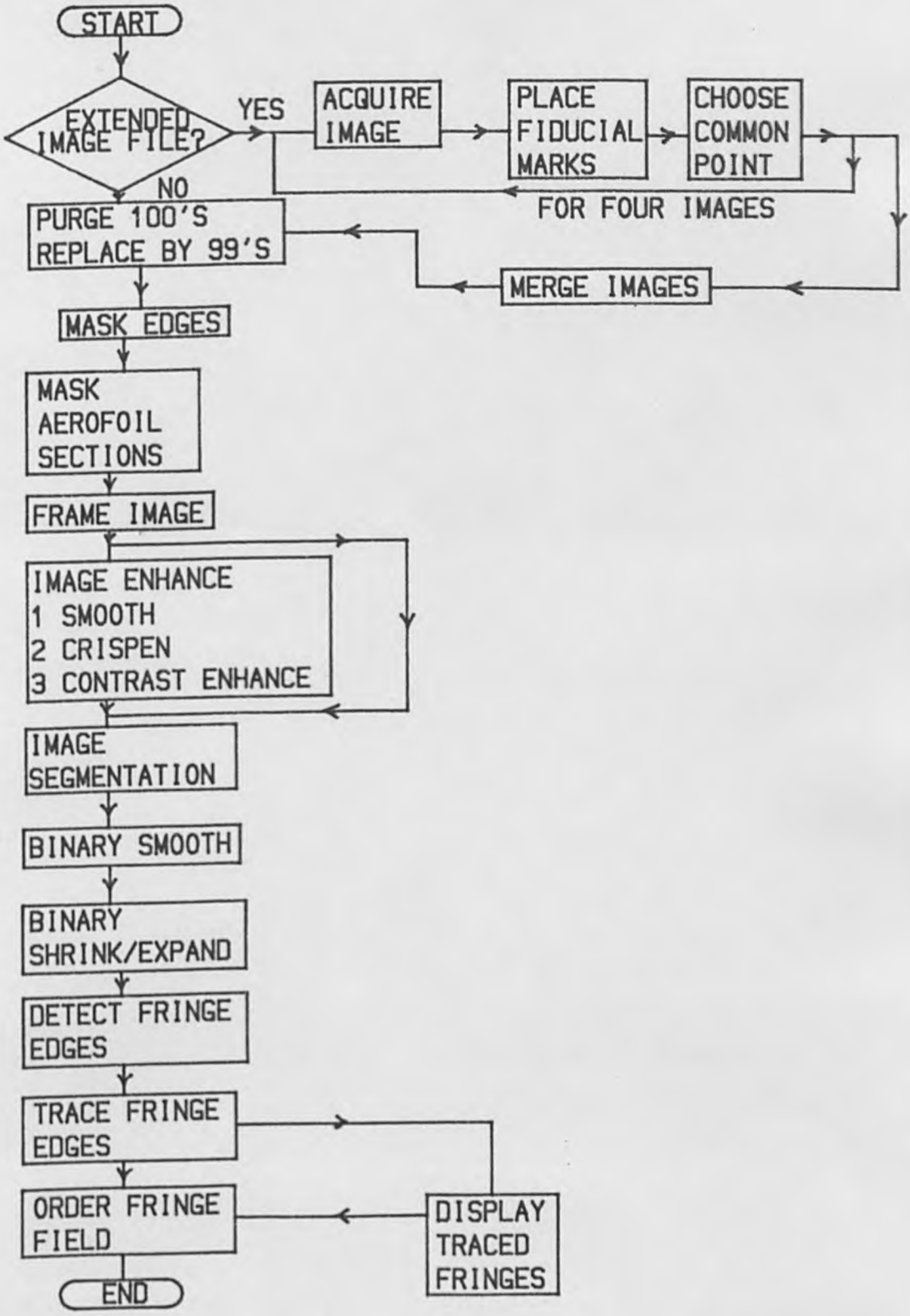

Figure 7.24. Flow diagram for the fringe analysis system.

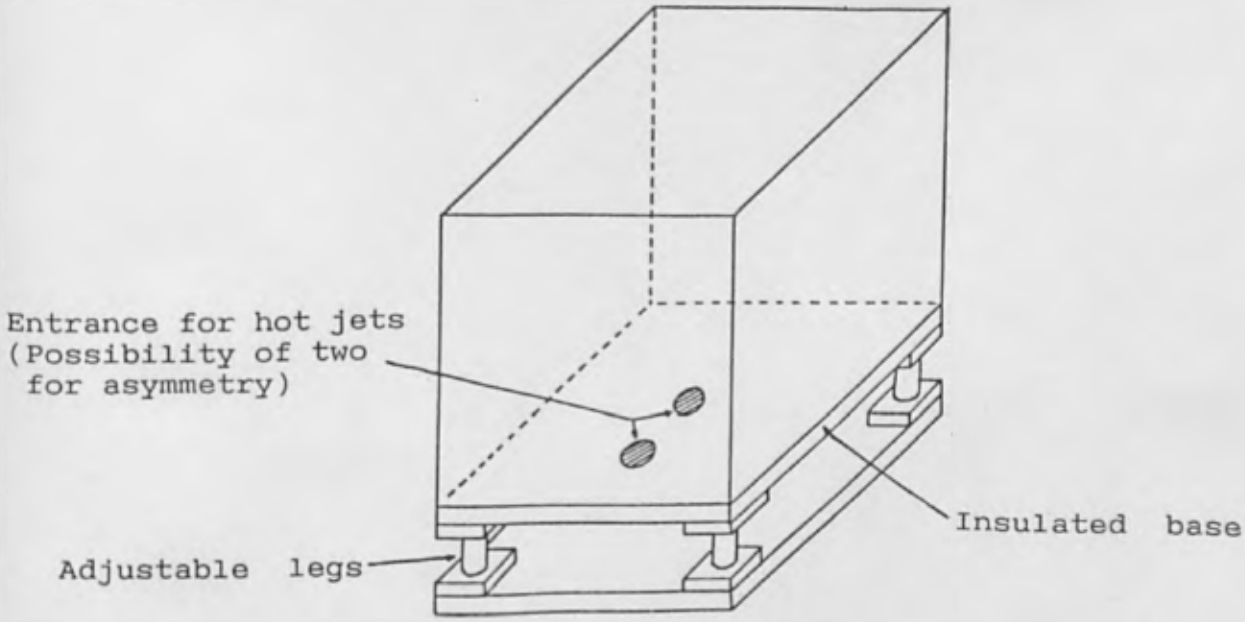

Figure 8.1. Simple forced convection test-rig.

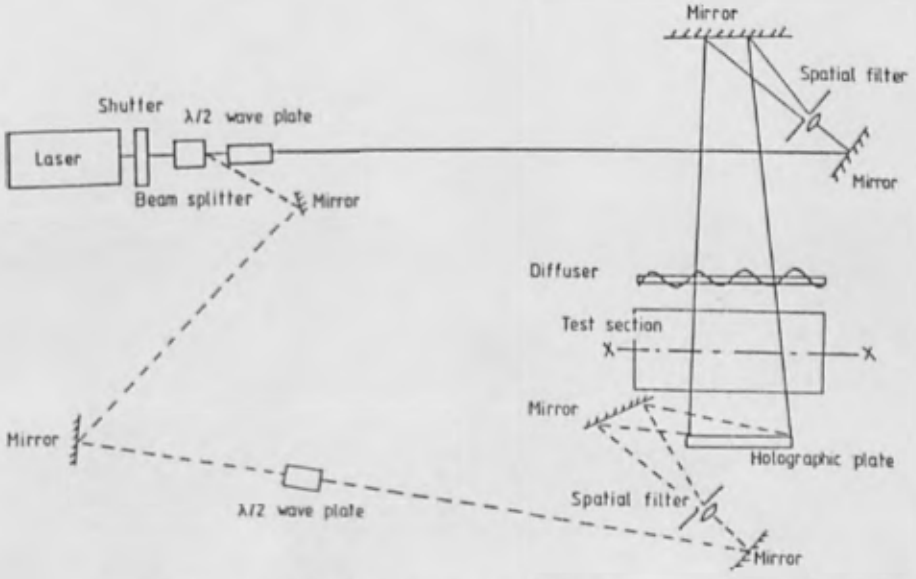

The 3D holographic set-up. ——, object beam; – – –, reference beam.

Figure 8.2. Example Three-dimensional interferometric lay-out.

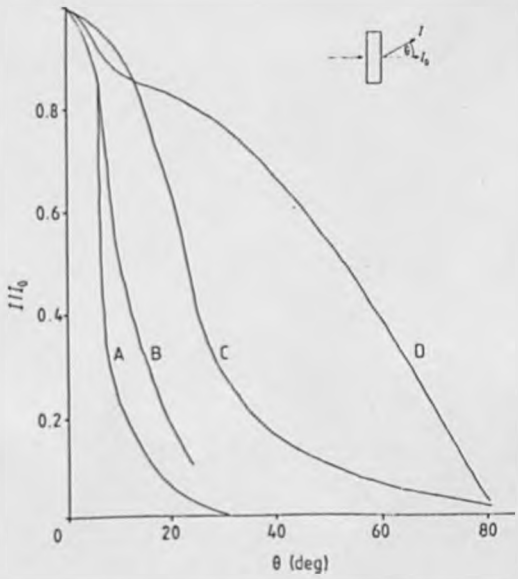

. Goniometric curves for various diffusers: A, ground glass 500 grit polish; B, ground glass 80 μm grit; C, ground glass coarse grit (used experimentally); D, opal glass 500 μm thick.

Figure 8.3. Goniometric curves for various diffuser types.

Figure 8.4. Schematic example of a multi-directional interferometric lay-out.

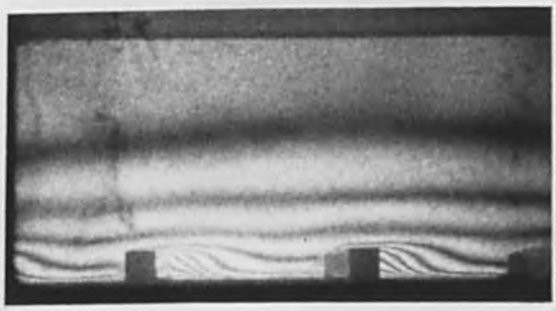

(a) Straight on.

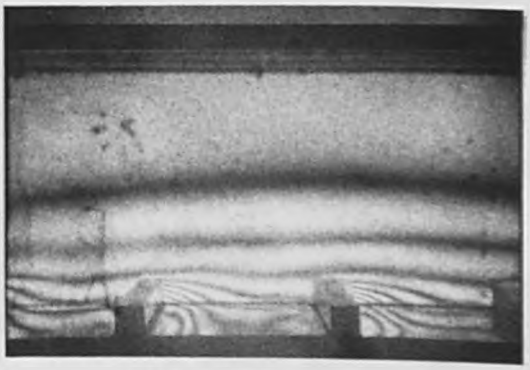

(b) 5 degrees above

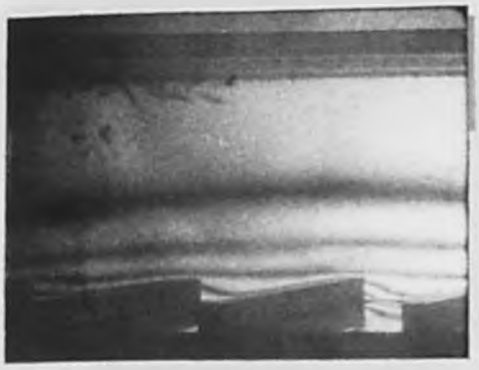

(c) 10 degrees from the right

(d) 10 degrees from the left

Figure 8.6. Three-dimensional Heat Transfer examples for a rib-roughened surface.